Ulrich Heiner Nikolaus Dürr

Solid-state ^{19}F-NMR studies on fluorine-labeled model compounds and biomolecules

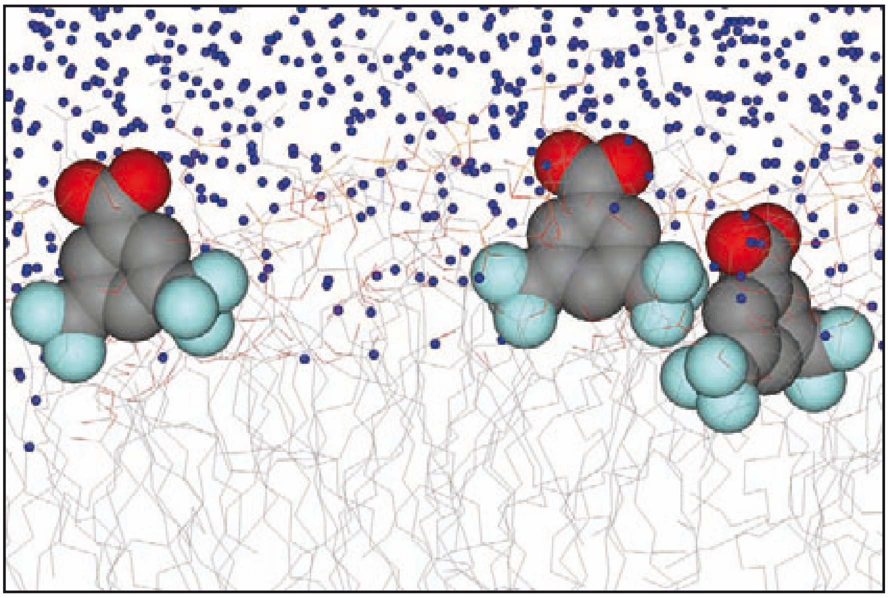

universitätsverlag karlsruhe

Ulrich Dürr

Solid-state ^{19}F-NMR studies on fluorine-labeled model compounds and biomolecules

Solid-state ^{19}F-NMR studies on fluorine-labeled model compounds and biomolecules

by
Ulrich Dürr

universitätsverlag karlsruhe

Dissertation, Universität Karlsruhe (TH)
Fakultät für Chemie und Biowissenschaften, 2005

Impressum

Universitätsverlag Karlsruhe
c/o Universitätsbibliothek
Straße am Forum 2
D-76131 Karlsruhe
www.uvka.de

SOME RIGHTS RESERVED

Dieses Werk ist unter folgender Creative Commons-Lizenz
lizenziert: http://creativecommons.org/licenses/by-nc-nd/2.0/de/

Universitätsverlag Karlsruhe 2006
Print on Demand

ISBN 3-86644-046-4

Solid-state ^{19}F-NMR studies on fluorine-labeled model compounds and biomolecules

Zur Erlangung des akademischen Grades eines

DOKTORS DER NATURWISSENSCHAFTEN
(Dr. rer. nat.)
der Fakultät für Chemie und Biowissenschaften der
Universität Karlsruhe (TH)

vorgelegte

DISSERTATION

von
Dipl.-Phys. Ulrich Heiner Nikolaus Dürr
aus Hamburg

Dekan:	Prof. Dr. Manfred Kappes
Referent:	Prof. Dr. Anne S. Ulrich
Korreferent:	Prof. Dr. Stefan Bräse
Tag der mündlichen Prüfung:	12. Juli 2005

Solid-state ^{19}F-NMR studies on fluorine-labeled model compounds and biomolecules

Biomembranes

Solid-state NMR spectroscopy
of membrane associated molecules

Table of contents

I.	Introduction	1
II.	Best-fit analysis of solid-state NMR data	29
III.	Amino acids with a single ^{19}F-label	47
IV.	^{19}F-NMR of CF_3-groups	61
V.	Six-spin system	71
VI.	Fusogenic peptide B18	95
VII.	Gramicidin S: β-sheet antimicrobial peptide	111
VIII.	PGLa: α-helical antimicrobial peptide	135
IX.	Summary	159
Appendices		163
A.	List of abbreviations	
B.	Sample *Mathematica* notebook (^{19}F-analysis of gramicidin S)	
C.	Publication on B18 in *Magnetic Resonance in Chemistry*	
D.	Publication on PGLa in *Journal of Magnetic Resonance*	
E.	Publication on PGLa in *Biophysical Journal*	
F.	Statement of contributions	
G.	Curriculum vitae	
H.	Acknowledgements	

Abstract

The fluorine nucleus, when introduced as a reporter group in membrane-associated proteins or peptides, offers a highly sensitive alternative to conventional isotope labels in solid-state NMR spectroscopy. The study presented here is concerned with the development of ^{19}F-NMR methods, as well as data analysis schemes to extract the wealth of structural and motional information from the spectra. Several applications to representative membrane-active peptides are illustrated.

In the first part of this dissertation, simple model compounds were investigated in order to establish basic methodology and spectroscopic parameters. Amino acids labeled with single ^{19}F or CF_3-substituents were investigated in polycrystalline form to establish a database of chemical shifts and dipolar coupling parameters for future ^{19}F-NMR studies. In the case of CF_3-groups, additional attention had to be paid to experimental pulse sequences. Contrary to common belief, usage of a single-pulse experiment proved feasible and advisable for all further experiments.

Next, several more complicated model substances carrying two CF_3-groups in close spatial proximity were investigated in a model membrane environment. Remarkably complex dipolar coupling patterns were found in CPMG experiments on macroscopically oriented lipid bilayer samples, which could be successfully analyzed and interpreted in terms of anisotropic molecular mobility. Additional information was obtained from a molecular dynamics simulation. The motional behavior of these small organic model compounds was found to differ qualitatively from the more confined dynamic behavior of typical membrane-active peptides.

The final chapters contain applications of the previously gained know-how to several membrane-active peptides, illustrating how the structural and motional information can be extracted from solid-state ^{19}F-NMR data. For three different membrane-active peptide systems, several analogues were prepared with single ^{19}F-labels or CF_3-groups, and their structures were determined from spectra obtained with macroscopically aligned lipid bilayer samples. It proved possible to interpret the NMR data in terms of basic models and theory, but close attention had to be paid to details of the local molecular conformation and mobility. The fusogenic peptide B18 was found to have a helix-loop-helix structure in the membrane, which is in good agreement with the amphiphilic properties of the molecule and suggests an explanation for its destabilizing effect on membranes. The two antimicrobial peptides gramicidin S and PGLa represent two very different types of structure, namely a β-sheet and an α-helix. For both types of peptide, a concentration-dependent re-alignment had been observed by ^{19}F-NMR, which could be interpreted here in structural terms. These results support and significantly extend the currently discussed two-state model of membrane permeabilization by antimicrobial peptides, and they indicate differing modes of action for both peptides. For PGLa, additional NMR data from ^{2}H- and ^{15}N-isotope labeled analogs was available to complement the ^{19}F-data, which allowed for a confirmation of the ^{19}F-NMR analysis by non-disturbing labels and provided an assessment of the accuracy of this approach.

In summary, valuable methodological ^{19}F-NMR experience on simple model systems was gathered in the present work. This experience was subsequently transferred and applied to more complex membrane-active peptide systems of high biological and pharmaceutical interest.

Zusammenfassung

Als Markierung in membranständigen Proteinen oder Peptiden bietet sich der Fluor-Kern als hochempfindliche Sonde an, gegenüber konventionellen Isotopenmarkierungen, die bislang in der Festkörper-NMR Spektroskopie eingesetzt werden. Die hier vorgelegte Arbeit befasst sich mit grundlegenden Entwicklungen der ^{19}F-NMR Methodik sowie der Datenauswertung, um die in den ^{19}F-NMR Spektren vorhandene Information über molekulare Strukturen und Beweglichkeiten in ihrer gesamten Breite zugänglich zu machen.

Im ersten Teil der Arbeit wurden experimentelle Methoden sowie ^{19}F-NMR Parameter anhand einfacher Modellsubstanzen etabliert. Markierte Aminosäuren mit einfachen ^{19}F- sowie CF_3-Substituenten wurden in polykristalliner Form untersucht, um eine Datensammlung der chemischen Verschiebungsanisotropie und dipolaren Kopplungen für zukünftige ^{19}F-NMR Untersuchungen aufzubauen. Die Vermessung von CF_3-Gruppen erforderte dabei spezielle Aufmerksamkeit, doch entgegen der allgemeinen Annahme erwies sich das Ein-Puls-Experiment als möglich und wird für alle weiteren Experimente empfohlen.

Mehrere komplexere Modellsubstanzen, die zwei CF_3-Gruppen in großer räumlicher Nähe tragen, wurden in Modellmembran eingebettet und untersucht. Ausgesprochen komplizierte dipolare Kopplungsmuster wurden in CPMG-Experimenten an makroskopisch orientierten Lipiddoppelschichten erhalten, konnten aber erfolgreich unter Annahme anisotroper molekularer Beweglichkeit analysiert und interpretiert werden. Zusätzliche Informationen ergaben sich aus Molekulardynamik-Simulationen. Die molekulare Beweglichkeit dieser kleinen organischen Substanzen unterscheidet sich qualitativ vom dynamisch stärker eingeschränkten Verhalten von typischen membran-aktiven Peptiden.

Der zweite Teil der Dissertation umfaßt mehrere Anwendungsbeispiele an membran-aktiven Peptiden, und zeigt, wie deren Struktur und Beweglichkeit aus den Festkörper-^{19}F-NMR Spektren zugänglich gemacht wurde. Drei verschiedene Peptid-Systeme wurden mit einzelnen ^{19}F-Markierungen oder CF_3-Gruppen hergestellt und in makroskopisch orientierten Lipiddoppelschichten vermessen. Die Daten konnten mit Hilfe grundlegender Modelltheorie ausgewertet werden, wobei jedoch der lokalen molekularen Konformation und Beweglichkeit große Aufmerksamkeit gewidmet werden mußte. Das fusogene Peptids B18 ergab eine geknickte helikale Struktur im membrangebundenen Zustand, was gut mit dem amphiphilen Charakter des Peptids übereinstimmt und eine Erklärung für dessen Membran-destabilisierende Wirkung nahelegt. Die beiden antimikrobiellen Peptide Gramicidin S und PGLa repräsentieren zwei sehr unterschiedliche molekularen Strukturen, nämlich ein β-Faltblatt und eine α-Helix. In beiden Fällen wurde eine konzentrationsabhängige Umlagerung mittels ^{19}F-NMR beobachtet, die in dieser Arbeit strukturell erklärt wird. Die Ergebnisse unterstützen das aktuelle Zwei-Zustands-Modell antimikrobieller Funktion und erweitern es um wesentliche strukturelle Aspekte. Die Art, wie die beiden Peptide eine Durchlässigkeit der Membran verursachen, scheint auf unterschiedliche Wirkungsweisen zu beruhen. Für PGLa waren zusätzliche ^{2}H- und ^{15}N-markierter Analoga verfügbar, die die ^{19}F-NMR Auswertung anhand dieser nicht-störende Markierungen bestätigten und es gleichzeitig ermöglichten, die Genauigkeit dieser neuen Strategie einzuschätzen.

Insgesamt wurden in der vorliegenden Arbeit wertvolle methodische Erfahrungen anhand von kleinen Modellsystemen gesammelt. Diese Erfahrungen ließen sich anschließend auf mehrere kompliziertere membran-aktive Peptidsysteme von hohem biologischem und pharmazeutischem Interesse übertragen und anwenden.

I. Introduction

Aims and structure of this study

This thesis is concerned with the development of solid-state ^{19}F-NMR as a versatile tool for structural measurements on ^{19}F-labeled biomolecular systems. The unifying theme of this thesis is the exploitation of anisotropic ^{19}F-NMR interactions for the determination of molecular parameters, namely molecular structure, orientation, and mobility.

Method development was pursued on a number of different systems that either served as models for novel experimental strategies to be used in future studies, or that represented biomolecular systems of considerable biological interest in themselves. Still, the connecting 'red line' of the thesis chapters is provided by the methodology rather than the individual systems used for developing that methodology. To do justice to this situation, each concrete system is treated in single unified chapters, where an introduction is given, experimental details are described, and the obtained results are presented. The common habit of grouping all 'introduction' and 'material and methods' information into dedicated chapters was not followed here, since it would have resulted in unnaturally large chapters and would have torn apart information that can be fully appreciated only in a coherent context. Instead, the thesis sets out with a very general introduction.

The introductory chapter I delineates the current situation of structural biology of membrane proteins and describes the relevance of solid-state ^{19}F-NMR in that context. In addition, it provides the general physical background and a few technical aspects.

The deduction of molecular properties from ^{19}F-NMR spectroscopic evidence is the focus of this thesis. Consequently, chapter II collates the mathematical tools for the description and prediction of NMR resonance frequencies and splittings. The chapter can thus be seen as a prolongation of the introduction, or it can be thought of as representing the 'Methods'-chapter of the thesis. This proceeding seems to be especially justified, given the situation that (to our knowledge) the current literature does not offer a concise presentation which is at the same time exact *and* readily understandable to non-physicists. In addition, chapter II describes the special implementations chosen for the analyses presented in subsequent chapters, as well as the experience gained with different technical approaches, i.e. the chapter does already contain results.

After having presented the theoretical framework for determining molecular orientations by use of anisotropic ^{19}F-NMR interactions, the thesis moves on to the results achieved. Solid-state ^{19}F-NMR methodology was advanced in two different ways: On the one hand, simple model substances were investigated in polycrystalline form in order to gain experience with ^{19}F-NMR material parameters and spectrometer-related technical questions. On the other hand, more complex ^{19}F-labeled substances and peptides were investigated in model lipid bilayer environment in order to access the wealth of information present in their ^{19}F-NMR spectra.

As most simple model systems, amino acids carrying F- or CF_3-substituents were investigated in pure polycrystalline form. They were characterized to establish a framework of material NMR-parameters, which will serve as necessary background database in future analysis of resonance frequencies measured on fluorinated substances in macroscopically aligned lipid

bilayer samples. Chapter III presents the principal values of the ^{19}F CSA tensors observed in a number of mono-fluorinated aromatic as well as aliphatic amino acids, along with data on their relaxational properties.

We expect the CF_3-group as a ^{19}F-NMR label to be superior to mono-F substituents. To gain basic experimental experience with that group, a number of CF_3-labeled amino acids in polycrystalline form were used to investigate the CF_3-group's behavior in common echo experiments, as well as in a phase cycled sequence custom-tailored for the special combination of CSA and dipolar interactions present in that group. Chapter IV presents experimental and simulated spectra from different pulse sequences. The measured spectra allowed for the extraction of CSA principal tensor and dipolar coupling values. In addition, relaxational behavior was characterized over a wide temperature range.

The main aim of using ^{19}F-NMR is to determine molecular properties *in a lipid bilayer environment*. In order to advance ^{19}F-NMR methodology for lipid bilayer samples, four different fluorine labeled systems were addressed in the present study. The common theme in the chapters V to VIII is the attempt at three-dimensional structural analysis.

The first type of system investigated in a lipid bilayer environment consisted of small amphiphilic organic molecules, each carrying two CF_3-groups in close spatial proximity. Containing two interacting CF_3-groups, they represent the most demanding spin system of the thesis, and they were found to give remarkably complex ^{19}F-NMR spectra. For their nuclear magnetic properties, these systems are termed 'six-spin systems' here. One question in the investigation of the six-spin systems was whether the dipolar interaction between two CF_3-groups can be exploited for distance or orientation measurements. A potential application may be found in peptide oligomers, where single CF_3-labels on each monomer make spatial contact only upon oligomerization. Therefore, the six-spin systems can be regarded as a model for advanced fluorine labeling strategies. At the same time they represent more than a model, since their spectroscopic properties give direct insight into the mobility properties of lipid bilayers, which are of high biophysical interest in themselves. Chapter V presents the results obtained on several related six-spin systems.

Three peptides known to possess membrane-associated functions make up the final three chapters of the thesis. For each, solid-state ^{19}F-NMR data from a number of fluorinated analogues in macroscopically aligned lipid bilayer samples was to be analyzed. In the case of the fusogenic peptide B18, it was possible to determine the overall orientation of the two helical segments from data acquired on nine 4F-Phg labeled analogues, as described in chapter VI. The antimicrobial peptide gramicidin S was investigated by means of two 4F-Phg labeled analogues, which allowed to discover its concentration- and temperature-dependent re-orientation in the membrane, *cf.* chapter VII.

The antimicrobial peptide PGLa demonstrates the first application of the CF_3-group as label in a membrane-active peptide system. Here, the peptide's orientation was to be determined from dipolar couplings observed on macroscopically aligned lipid bilayer samples. In addition, data obtained on ^{2}H- and ^{15}N-isotope labels was to be analyzed and compared, in order to assess the reliability of ^{19}F-NMR. The results obtained are presented as chapter VIII.

The principal aim of the present thesis was the advancement of ^{19}F-NMR methodology. This was pursued using a number of polycrystalline model substances, in order to lay the foundations for biomolecular systems. Subsequently, a number of membrane-active peptides was investigated in model membrane environment. To reach these goals, a large amount of

collaborative work in a highly inter-disciplinary environment was necessary, where chemistry, biology, physics and computer science equally contributed. The author's particular contribution as a physicist consisted in experimental questions related to the acquisition of ^{19}F-NMR spectra, as well as in the exploration of suitable analysis schemes for the obtained data. On the experimental side, the author ensured the availability and reliability of the spectrometer hardware for solid-state ^{19}F-NMR, which is not yet routinely available in commercial spectrometers. For the analysis of the obtained data, a robust and user-friendly implementation of the computational best-fit scheme of analysis had to be established and needed to be tested for its accuracy. In some instances, additional input from molecular dynamics simulations was necessary for successful data analysis. A detailed account of which particular tasks were carried out by whom is given as appendix F of the thesis.

On the whole, the thesis draws a line from purely physical experimental questions towards biological applications, where experimental technology steps back to serving as a fully applicable versatile tool. This gives an idea of the impressive width of the solid-state NMR field of research. The highly inter-disciplinary nature makes this field at the same time highly challenging, but also exceedingly attractive and fruitful.

I. Introduction

Biological background

Structural biology today has reached a point of maturation where mechanistic explanations of most biochemical processes can already be given at an atomic scale, or are actively searched for. The biological membrane poses one of the remaining challenges for molecular biology, with integral membrane proteins being of primary interest. Membrane-associated peptides are of great interest as well, not only in themselves but also as tractable model systems for method development. Solid-state NMR spectroscopy is evolving as a promising tool for the study of biological membranes. Isotope labeling and preparation of macroscopically aligned samples open a path to determination of their structure, dynamics, and function.

Biological membranes

Biological membranes not only form the interface between a cell and the outside world by protecting the cell from mechanical and chemical stress, by providing for selective transport, and by transducing molecular signals. They also serve numerous purposes as major constituents of the cell's organelles, where membranes are essential in energy metabolism, protein synthesis and modifications, vesicular trafficking, enzymatic catalysis, and anchoring of the cytoskeleton.

The 'fluid mosaic' model introduced by Singer and Nicolson[1], depicted in figure 1.1, represents the current structural view of biological membranes. It describes the membrane as two leaflets of lipid molecules that are ordered according to their hydrophobicity properties. Thus, the membrane faces its aqueous environment with two hydrophilic surface regions, and maintains a hydrophobic core in its middle. Within this fluid lipid matrix, membrane proteins are either integrally embedded or peripherally associated, thereby constituting the 'mosaic'. As a currently discussed advancement of the fluid mosaic model, there are strong indications that super-structured assemblies, called lipid rafts, exist in biological membranes.[2-4]

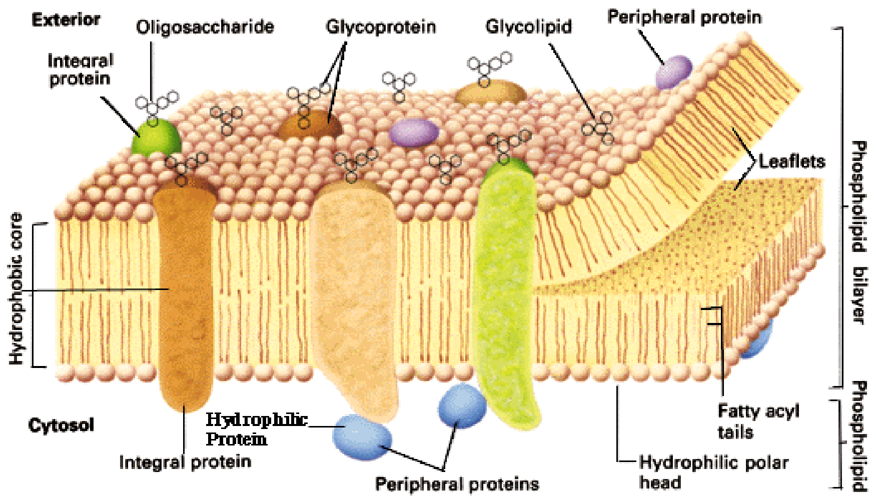

Figure 1.1: Fluid mosaic model of the biological membrane according to Singer and Nicolson[1].

Pure lipid molecules in aqueous environment are known to spontaneously form lamellar bilayer structures around 4 to 5 nm thick. Bilayer formation is driven by the amphipathic properties of the lipids, which possess hydrophilic headgroups and (in most cases two) hydrophobic fatty acyl chains. In nature, an enormous number of different lipid classes and species is found, which vary in the chemical nature of their headgroups as well as in the nature of the fatty acyl chains. The lipid composition of biological membranes is very different in different types of membranes, as found in different organisms and organelles, and may also differ between the two leaflets of an individual bilayer. Numerous biophysical properties of biological membranes can, however, be mimicked in model membrane systems. By proper choice of only a handful of lipid constituents, naturally occurring conditions regarding e.g. bilayer thickness, overall charge, curvature tendency, or cholesterol content can be reproduced.

In 2001, the human genome was completely sequenced.[5;6] Analysis of smaller genomes showed that 20 to 30% of open reading frames code for membrane proteins.[7] Beyond the mere numbers, the central role of membrane proteins in biology becomes even more evident from the functions they fulfill. Aside from the vital roles for the individual cell, membrane proteins also serve to make a complex multi-cellular organism functional. Namely, membrane-located receptor systems in signaling cascades are involved in all higher physiological functions, integrating billions of cells into a higher organism. Likewise, neuronal signaling is based on membrane-located protein machineries. Malfunctions of membrane receptors are at the core of many diseases, the most prominent of which being cancer. Important steps in viral lifecycles are located at membranes as well. As a prominent pharmaceutical implication, membrane proteins constitute highly promising drug targets.

In contrast to their high relevance, comparatively little is known about membrane proteins. A striking example is the marginal number of elucidated three-dimensional structures. There are only 50 unique high-resolution structures of membrane proteins,[8] a continually updated catalogue of which can be found at www.mpibp-frankfurt.mpg.de/michel/public/memprotstruct.html. In comparison, there is a total of approximately 28300 protein structures deposited in the Brookhaven protein data bank (http://www.rcsb.org/pdb/holdings.html, as of May 2005). This situation reflects the fact that established methods for protein structure elucidation usually fail in membrane systems. X-ray crystallography is only applicable to proteins that form crystals of reasonable quality, which membrane proteins usually refuse to do as a consequence of their highly hydrophobic nature.[9]

Nuclear magnetic resonance (NMR) spectroscopy[10] is the other well-established technique for studying protein structure. *Solution-state* NMR is traditionally restricted to proteins of moderate size <50kDa[11] and high molecular mobility, as found in proteins in aqueous solution. The second condition is usually not met in membrane-bound proteins. Still, methods of solution-state NMR can be adapted to membrane proteins solubilized in sufficiently small detergent micelles. A number of systems has been treated in this way.[12] In parallel, a completely new approach based on *solid-state* NMR spectroscopy is currently evolving. Here, approaches are developed to make membrane proteins tractable in their native environment by novel NMR methods.

To conclude, the biological membrane represents a scientific frontier from the structural biology, from the methodological, as well as from a very general point of view.

Membrane-active peptides

Some membrane protein complexes range among the largest protein machineries found (e.g. F_0F_1-ATPase[13], photosystem I and II[14], fatty acid synthase[15;16]), but—at the other extreme of the molecular size scale—also peptides with a chain length of only very few amino acids are found to be highly active in biological membranes (*per se* or as part of larger proteins). These membrane-active peptide systems encompass signal peptides (e.g. encephalins, neurotensin, growth factors), surface proteins of bacteriophages (e.g. M13, Pf1 coat proteins), ionophores (e.g. valinomycine, δ-hemolysine), and fusogenic sequences as well as antimicrobial peptides. Representatives of the latter two classes were investigated here.

Membrane fusion is a fundamental process in many intra- and intercellular events such as fertilization, viral infection, vesicular trafficking and synaptic transmission. Complex protein machineries control the recognition between the two apposing membranes, and trigger their fusion at the correct point in time and space.[17-19] Short amphiphilic protein sequences, called fusogenic peptides (or 'fusion peptides' when derived from viral fusion machineries), mediate the actual merging of the bilayers.[20;21] Even as isolated peptides these fusogenic sequences are able to induce vesicle fusion *in vitro*, hence their structural description promises a better understanding of the fundamental mechanism. In the present study, the fusogenic peptide B18 from the sea urchin fertilization protein bindin was investigated using solid-state ^{19}F-NMR.

Antimicrobial peptides, which kill bacteria and fungi, are another class of membrane-active peptides. They are part of the innate immunity of multi-cellular organisms.[22-25] Important examples are defensins[26] and cathelins[27] found in humans, and magainins[28;29] found in frog skin. The antimicrobial peptides found in higher organisms are cleaved from genetically coded precursors, and are speculated to also have signaling function.[30] Other antimicrobial peptides are excreted by microbes, where they are synthesized non-ribosomally. The ubiquitous importance of antimicrobial peptides becomes evident from their large number and great chemical diversity, as can e.g. be seen in a dedicated database for gene-encoded animal and plant antimicrobial peptides, http://www.bbcm.units.it/~tossi/amsdb.html. This database had 893 entries as of May 2005. Antimicrobial peptides are under active investigation as potential new antibiotic drugs, which are urgently needed since infective microbes develop increasing resistance to common antibiotics.[31] A specific protein receptor is not involved in the action of antimicrobial peptides,[32] hence it is unlikely that bacteria will develop resistance against such peptides.

Due to their cationic nature, antimicrobial peptides preferentially bind to bacterial membranes, which tend to be negatively charged. This renders their action specific against bacteria and reduces hemolytic side-effects on uncharged eukaryotic cells. It is observed in electrophysiological experiments[33] that antimicrobial peptides permeabilize membranes, i.e. make them 'leaky' and thereby destroy electrophysiological gradients. It is commonly accepted that after electrostatically driven membrane association, the peptides assume a surface-bound, so-called 'S-state'. It has been suggested that only after changing into a second, membrane-spanning 'I-state', the peptides kill the bacterium by permeabilizing its membrane. This two-state model and nomenclature were introduced by Huang[34]. They allude to the two-state model of Popot and Engelman[35], which was originally derived to explain the folding and membrane insertion of large integral membrane proteins such as bacteriorhodopsin.

For a mechanistic explanation of membrane permeabilization, a number of structural models for the I-state are under debate. Figure 1.2 gives an overview of the suggested mechanisms for the action of an antimicrobial peptide in its I-state. In (A), the electrostatically driven association of the peptide to the membrane is illustrated, which will make the peptide adopt a well-defined folded structure and which is the starting point for any further action. Panel (B) illustrates the 'carpet' model, which suggests that antimicrobial peptides form a dense carpet on the membrane and lead to non-specific breakthrough. The 'barrel-stave' model (C) suggests that the peptides orient upright within the lipid bilayer, self-assemble in a parallel fashion and thereby open a pore through the membrane which causes the observed conductivity events. Finally, the 'wormhole'-model (D) also proposes upright orientation and pore formation, but here the surrounding lipids participate in the lining of the pore. The debated structural models were reviewed by e.g. Strandberg and Ulrich[36], Bechinger[37;38], and Epand and Vogel[39].

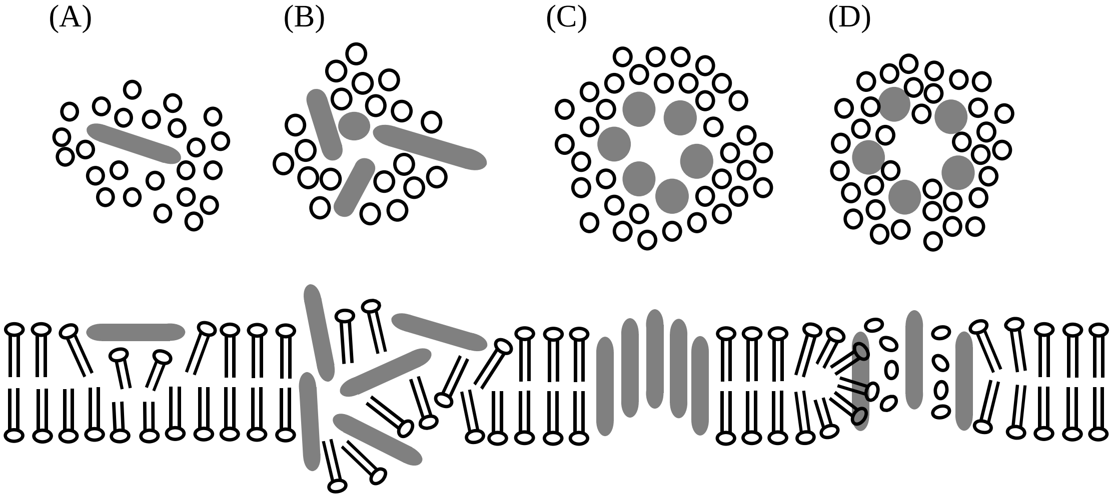

Figure 1.2: Proposed mechanisms for action of antimicrobial peptides (top) when looking down onto membrane surface, (bottom) side view from within membrane. (A) Initial membrane association, (B) carpet, (C) barrel-stave, and (D) wormhole model.

Obviously, the peptides and lipids show very different (distributions of) orientations in the lipid bilayer according to the different models. Knowledge about their orientational behavior can thus be key to a distinction between the concurring models. Experimental measurements of molecular orientations are possible by solid-state NMR spectroscopy of isotope labeled peptides. This technique is described in the following section and was applied here to gramicidin S and PGLa, two typical representatives of antimicrobial peptides.

NMR on isotope-labeled peptides and proteins

The native state of proteins and peptides in membranes is physically very different from the conditions under which proteins in solution are commonly investigated in traditional solution-state NMR spectroscopy. In the membrane, proteins are severely restricted in their molecular mobility, thereby making the anisotropy of certain nuclear magnetic interactions fully effective. This was earlier believed to be a prohibitive obstacle in NMR spectroscopy of systems with reduced molecular mobility, since it makes NMR lineshapes of those systems very broad and 'featureless'. But today, a number of approaches has been developed to

overcome those obstacles and to put anisotropic interactions in motionally restricted systems to good use. These techniques, as well as the whole field of study, are commonly termed 'solid-state NMR spectroscopy'. Solid-state NMR is applied to solid bodies in the strict physical sense of the word as well as to 'soft' polymer systems and biological membranes, which strictly speaking are not solid bodies, but much rather like special liquid crystals.

Solid-state NMR studies typically rely on isotope labels that are either uniformly or selectively introduced into the system of interest. These labels are then used to measure structural or orientational constraints from anisotropic nuclear magnetic interactions. A single label can already give orientational information via the anisotropy of its chemical shielding. This is indicated on the right side of figure 1.3, which shows a hypothetical protein carrying a number of different isotope labels. By use of the orientation- and distance-dependent dipolar coupling between a pair of isotope labels, orientational as well as distance information may be obtained, as indicated on the left of figure 1.3.

The restraints measured on individual isotope labels can then be integrated to yield a structure or orientation determination for the whole molecule. Since to date only a limited number of constraints can routinely be measured on one molecule, additional input is usually necessary. Especially, model structures of the molecule of interest, as determined e.g. in NMR studies in solution, are often used as starting point for orientation determinations.

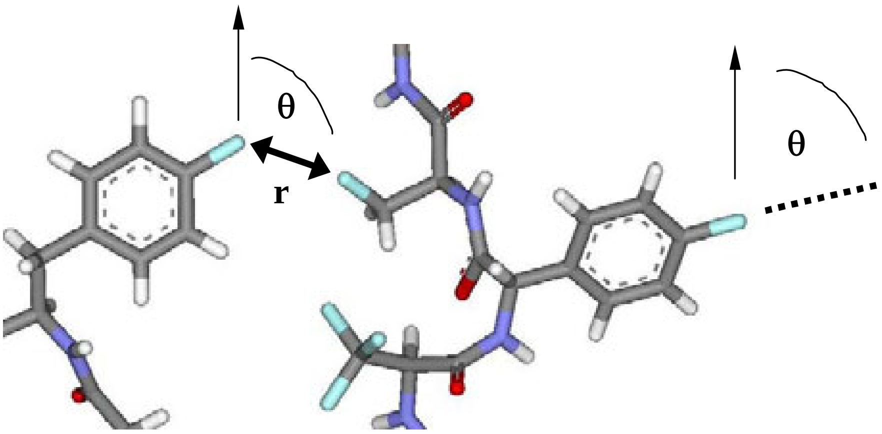

Figure 1.3: Illustration of a hypothetical protein carrying fluorine-19 labels (light blue). A single isotope label allows to determine the orientation θ of the molecular segment (right), while a pair of labels in spatial proximity allows additional determination of their internuclear distance **r** (left).

Fluorine-19 as isotope label

Solid-state NMR studies of membrane-associated proteins and peptides generally suffer from low sensitivity of the isotope labels that are commonly incorporated and observed. The ^{19}F nucleus, on the other hand, has an exquisitely high NMR sensitivity,[40;41] which saves material and instrument time up to several orders of magnitude compared with ^{2}H, ^{13}C or ^{15}N. Only small amounts of ^{19}F-labeled peptide (down to 20 nmol) need to be incorporated in macroscopically oriented membrane samples to be observable in short acquisition times (minutes to hours). As the fluorine nucleus is normally absent in proteins, there is no natural abundance background. At the same time, there is no need for intricate isotope-enrichment, since the NMR-active ^{19}F isotope is virtually the only isotope present.

On the other hand, this approach necessitates introduction of non-natural ^{19}F-labeled amino acids into the system of interest.[41;42] After fluorine labeling is achieved by either solid-phase peptide synthesis, biosynthetic incorporation or chemical linkage via e.g. a disulfide bridge, any potential distortion effected by the label needs to be individually assessed for each labeled site. Fluorine was successfully introduced into biological systems in numerous NMR spectroscopic studies in solution.[43-45] Aliphatic and aromatic side chains without functional groups constitute suitable targets for fluorination. Especially ^{19}F-labeled alanine derivatives were used in membrane-associated systems, namely an alanine carrying a CH_2F-group was used in two studies by Toke *et al*.[46;47], and an alanine carrying a CF_3-group was investigated by Bravo *et al*.[48;49] Another aliphatic labeling target is the unusual amino acid α-aminoisobutyric acid, where sophisticated schemes for the synthesis of CF_3-labeled analogues were developed,[50] which were subsequently introduced into (among numerous others) the peptide alamethicin.[51] Fluorinated aromatic amino acids, such as 4-F-phenylalanine, 3-F-tyrosine, or 5-F-tryptophan provide another class of possible labeling sites and were already used in membrane-associated GB1[52] and membrane-embedded gramicidin A[53].

In the present study, two fluorinated analogues of the unusual amino acid phenylglycine were employed. The first one, 4-fluoro-L-phenylglycine (4F-Phg) carries a fluorine in the *para* position of the phenyl ring, while the second, 4-trifluoromethyl-L-phenylglycine (CF_3-Phg), carries a CF_3-group in the same position. It was recently demonstrated that both labels are suitable ^{19}F-NMR labels in peptides for structural studies.[54;55] They tend to racemize during solid-phase peptide synthesis, but in all cases separation and identification of stereoisomeric products was possible. In three different peptides, 4F- and CF_3-Phg were thus used to substitute for a hydrophobic amino acid and caused hardly any perturbation of conformation and biological function.[54]

The two ^{19}F-labeled amino acids are depicted in figure 1.4, where their most important geometrical properties are indicated as well. Both offer the advantage of a rigid connection of the fluorine label to the peptide backbone, allowing measurement of global structural parameters of the secondary structure element rather than local aspects of the side chain conformation. In 4F-Phg, the phenyl ring assumes a specific orientation with respect to the peptide backbone, characterized by the torsion angle χ_1 as indicated This phenyl torsion is difficult to determine reliably but absolutely necessary for the analysis of NMR data acquired on 4F-Phg. Naturally, the phenyl torsion is also present in CF_3-Phg, but here it does not enter NMR data analysis, since the rotational diffusion of the CF_3-group will average all NMR interactions onto the rotation axis. Therefore, a noticeably simplified data analysis is expected for CF_3-Phg.

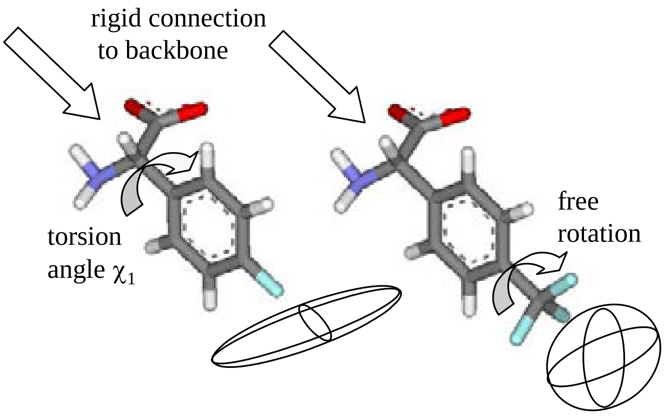

Figure 1.4: The two fluorine analogues 4-F-Phg (left) and 4-CF_3-Phg (right) of the unusual amino acid phenylglycine (Phg) that were used in the present study.

Macroscopically aligned samples

Once fluorine labeled proteins or peptides are synthesized and their structural and functional integrity is proven, they can be reconstituted into a quasi-native membrane environment to allow for solid-state ^{19}F-NMR spectroscopic studies. The orientation dependence of certain NMR interactions, which is conserved in motionally restricted samples, was mentioned above. To exploit it for the determination of structural parameters, two methodological approaches are commonly pursued. The first and more common one, magic angle sample spinning (MAS), is usually applied to un-ordered (often termed 'powder') samples, e.g. polycrystalline powders, peptide lyophilates, or lipid dispersions. Rapid spinning of the sample around the magic angle initially suppresses anisotropic interactions altogether, allowing to observe isotropic chemical shifts and J-couplings in solid samples. In addition, by use of sophisticated pulse sequences, it is possible to selectively re-introduce and measure anisotropic interactions of interest in MAS experiments.

The second approach was used in the present thesis. It employs macroscopically aligned membrane samples[56] to fix the molecular orientation of lamellar lipid bilayers with respect to the magnetic field. Figure 1.5 shows a schematic representation of a macroscopically aligned sample. It consists of a stack of typically 15 to 20 very thin glass plates, between which the protein or peptide of interest is situated immersed in the desired lipid environment. As lipid environment, either an extract of biological lipids or a properly chosen lipid model system may be used. Dispersed between glass plates, the lipid system will spontaneously form lamellar bilayers aligned with the plates, as shown by the inset in figure 1.5. Typically a few thousand bilayers are accommodated between two glass plates, giving a height that is comparable to the 60 μm thickness of a glass plate. In oriented samples, spectra are simplified to a tractable complexity, and spectral resolution and sensitivity are decisively improved. The spectra shown in tables 6.1 and 6.2 of this thesis give a good impression of the broad powder lineshapes observed in non-oriented samples, and of the narrow resonances from oriented samples, respectively. The 'mosaic spread' describes the quality of alignment in an oriented sample, which limits spectral resolution.

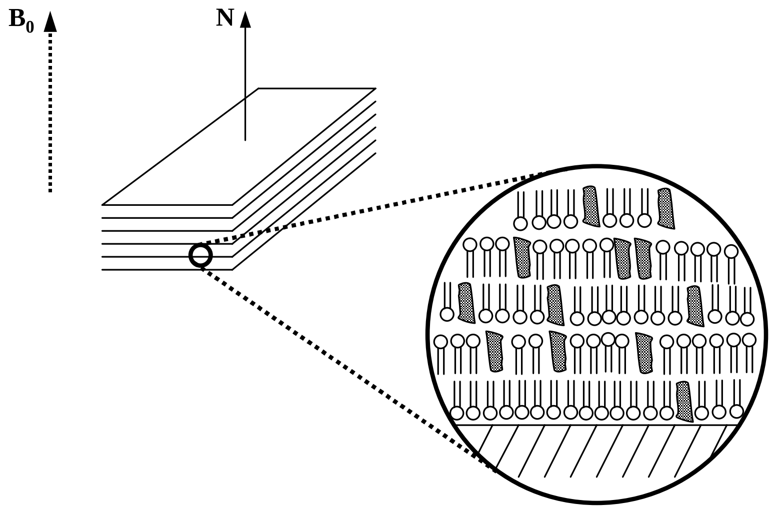

Figure 1.5: Macroscopically aligned lipid bilayer sample made up from a stack of glass plates (left), and providing a lamellar microscopic order of lipid bilayers and proteins (right). The membrane normal N is usually aligned parallel to the static magnetic field direction B_0.

By macroscopically fixing the orientation of the incorporated proteins along with the lipid bilayers, the samples allow for experimentally adjusting any desired angle between the lipid bilayer and the external magnetic field. Thus, observed NMR resonances can now directly be set into relation with the bilayer geometry, making use of the orientation dependence of these resonances. That way, the three-dimensional structure of a membrane-associated peptide can be calculated from a number of individual orientational constraints.[57] Measuring an oriented sample at several different tilt angles with respect to the magnetic field provides additional information about the rotational diffusion of the molecules around the membrane normal.

Once a number of structural or orientational constraints have been measured by either MAS or in oriented samples, these data points need to be integrated to give a conclusive picture of the system at hand. In solution-state NMR, multi-dimensional methods allow determination of hundreds of constraints from a single set of spectra. Well-developed computer methods exist to calculate molecular structures from the large amount of data. Solid-state NMR is not yet routinely able to supply comparable amounts of data, but methods may sufficiently evolve to provide a comparable wealth of information.

At the moment, structure analysis of solid-state NMR experiments relies heavily on additional input, as provided by molecular coordinates determined in solution or idealized model conformations. Advanced computer methods, especially geometry optimization and molecular dynamics simulations, can also provide supplementary input in solid-state NMR studies (including this one).

NMR spectroscopy

Atomic nuclei, as well as most elementary particles, have a property called spin. Nuclear spin is a form of angular momentum, which is described by the vectorial quantity $\vec{I}$. Nuclear spin is linked to a magnetic moment $\vec{\mu}_n$, which is proportional to nuclear spin angular momentum: $\vec{\mu}_n = \gamma \cdot \vec{I}$. The constant of proportionality is the gyromagnetic ratio, γ. In the classical picture, the observed nuclear magnetic moment can be understood as the effect of a rotating charged particle. Quantum mechanics, however, shows the classical picture not to be fully appropriate. Most importantly, a quantum mechanical spin is not able to take any given orientation with respect to an external magnetic field. Instead, only a very limited number of relative orientations are observed. They are characterized by the integer or half-integer magnetic quantum number *m*, which is limited to $-|I| \le m \le |I|$.

Nuclear magnetic moments are approximately 1000 times smaller then electronic magnetic moments which give rise to the ferro-, para- and diamagnetic properties of matter. Measurement of nuclear magnetic resonance effects became possible with the advent of radiofrequency technology in the 1940s. In the following sections, some physical background relevant for this work along with the employed measurement technology shall be presented.

Nuclear magnetic resonance

The spin of an atomic nucleus is composed of the spins of the protons and neutrons which make up the nucleus. All integer and half-integer spins between *I*=0 and *I*=9 (^{180}Ta) are observed. Most common and useful in biomolecular NMR are nuclei with *I*=1/2 (^{1}H, ^{13}C, ^{15}N, ^{19}F, ^{31}P) and *I*=1 (^{2}H, ^{14}N).

When a nucleus carrying a spin is brought into a strong external magnetic field, the possible orientation states of the nuclear spin with respect to that field are no longer identical in energy. The effected splitting of energy levels allows the nucleus to perform transitions between spin states that are connected to absorption or emission of radiation in the radio-frequency wavelength range. The relationship between the field strength B_0 and the observed transition frequency is given by

$$\omega_0 = -\gamma \cdot B_0, \tag{1.1}$$

where the linearity constant γ is called the gyromagnetic ratio and is a fundamental property of each nucleus. The transition frequency ω_0 is referred to as the Larmor frequency, and can be interpreted as the angular frequency at which the spin precesses around B_0, driven by the perpendicular torque that B_0 exerts.

Figure 1.6 is an attempt to summarize these facts for a nuclear spin I=1/2. On the right hand side, its two possible orientations with respect to the external magnetic field, B_0, are shown. The energy of the parallel orientation ('spin-up', m=+1/2, often denoted α) decreases linearly as a function of B_0, while the anti-parallel orientation ('spin-down', m=-1/2, β) becomes less favorable energy-wise. The splitting is strongest for ^{1}H (and even stronger for practically irrelevant ^{3}H), as determined by γ, closely followed by ^{19}F. A spin flipping transition at a field strength of 11.7 T, as used in most of the presented experiments, is indicated. The

proton frequency $\omega_0 = \Delta E / \hbar = 500\,\text{MHz}$ is often given as a measure of field strength employed.

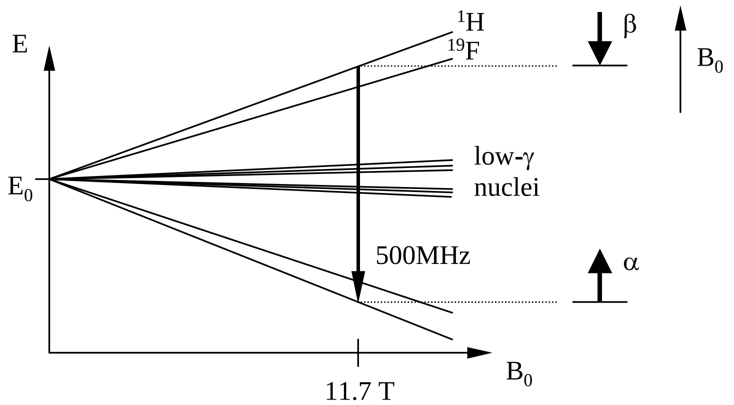

Figure 1.6: Linear dependence between external magnetic field B_0 strength and energy levels of different spin states for nuclei with different gyromagnetic ratio γ. ($\gamma_{^1H} > \gamma_{^{19}F}$ >> other nuclei).

In more detail, the effective field strength acting on a specific nucleus is dependent on the local electronic environment of that nucleus. The surrounding electron clouds may enhance or counteract the external magnetic field, thereby slightly shifting the resonance frequency observed. This effect is called chemical shielding, and it allows conclusions about the chemical surrounding of that nucleus and explains the paramount usefulness of nuclear magnetic resonance for chemistry. Chemical shielding is described by the formula

$$\omega = (1 - \sigma)\,\omega_0\,, \tag{1.2}$$

with σ describing the extent by which a nucleus is shielded by the surrounding electron cloud, which shifts its fundamental Larmor frequency ω_0 to the observed frequency ω. Since the spectral effects to be observed are very small, the values for the shielding $\sigma = (\omega_0 - \omega)/\omega_0$ are typically given multiplied by a factor of 10^6, which is denoted by the suffix ppm (parts-per-million—a factor, not a unit!).

An NMR spectrometer does not monitor individual quantum-mechanical spin states, but measures the bulk magnetization of a macroscopic sample. The observable macroscopic magnetization is made up of all the microscopic nuclear magnetic moments. Due to the very small energy difference between nuclear α- and β-states, both of them are almost equally populated. The Boltzmann distribution predicts the difference between α- and β-populations to be only 10^{-6}, explaining why only a very weak bulk magnetization is induced by the strong external magnetic field. Bulk magnetization is typically denoted by a vector **M** and, by use of the Bloch equations, can be treated in a classical manner. This is the basis for the vector diagrams presented along with the pulse sequences in the following sections. Although not fully correct, the classical picture is sufficient for all thoughts presented in this work.

Single-pulse experiment

NMR spectra today are measured by means of Fourier transform spectroscopy, based on the application of a strong, short radiofrequency (r.f.) pulse via a coil onto the sample. The pulse response—usually termed 'free induction decay' (FID)—of the sample is recorded, which yields the NMR spectrum as its Fourier transform. Figure 1.7 shows this procedure, along with the vector diagram of the time evolution of bulk magnetization **M**. On the top, the pulse sequence is given in a schematic fashion, while the lower panels show the evolution of magnetization.

At the start of the experiment (A), the equilibrated bulk magnetization is lined up with the external magnetic field B_0. In a so-called single-pulse experiment—the most simple of all NMR pulse sequences—a single r.f. pulse is applied. The r.f. pulse generates a temporary additional magnetic field B_1 in the xy-plane. The bulk magnetization rotates around the B_1 field, and if the r.f. pulse is terminated after a proper time (giving a so-called 90°-pulse), the magnetization has reached the xy-plane (B). There, it starts to precess around B_0 according to its Larmor frequency. This precession in turn induces an oscillating voltage in the receiver coil, which gives the FID acquired (ACQ) by the NMR spectrometer. Due to different interactions, there is a distribution of Larmor frequencies, hence the magnetization will fan out (C and D) until it is completely dephased and no macroscopic magnetization is detectable any more (E). This dephasing of the magnetization is called spin-spin or transverse relaxation and is characterized by the T_2 relaxation time. Eventually, the equilibrium magnetization will build up again (F). This process is called spin-lattice or longitudinal relaxation and is quantified by the T_1 relaxation time.

In panels (A) and (B) of figure 1.7, the effect of a 90°-pulse on bulk magnetization **M** was shown. In this example, the B_1-rotation was carried out around the y-axis, and therefore the pulse is denoted a $90°_y$-pulse. By proper choice of the phase of the carrier frequency of the r.f. pulse, any axis φ in the xy-plane may act as the B_1-rotation axis, giving a manifold of differently phased $90°_\varphi$-pulses. Pulses of different phases and pulse trains with systematically shifted phases are commonly employed to compensate for instrumental imperfections or to enhance or suppress certain evolutions of a spin system. A particular application of this 'phase cycling' technique will be discussed below.

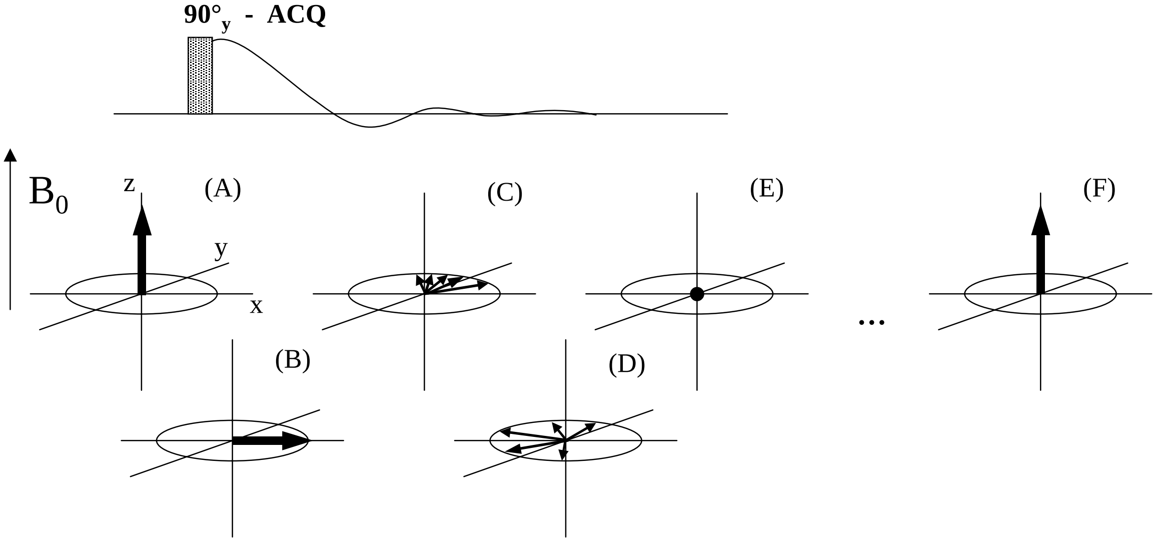

Figure 1.7: Single-pulse experiment (top) and effected time evolution and relaxation of bulk magnetization (bottom).

Orientation dependence of chemical shift: CSA

It is obvious that the shielding effected by the electron cloud surrounding a nucleus will be different for different orientations of the molecule with respect to the external magnetic field. However, such anisotropic effects become evident in NMR spectra only when the sample is sufficiently solid. In fully mobile molecules, e.g. in solution, anisotropic effects are hidden by stochastic thermal motions of the molecules, which make only the time-averaged isotropic chemical shift values observable.

Whenever the molecules in a sample are motionally restricted, the anisotropy of the electron cloud is reflected in NMR spectra. Especially the chemical shift σ—described by equation (1.2)—is highly anisotropic. Therefore, it needs to be written as a function of orientation of the molecule, $\sigma = \sigma(\vartheta, \varphi)$, where the molecular orientation is given by polar coordinates ϑ and φ. This effect is called chemical shift anisotropy (CSA).

Figure 1.8 uses a fluoro-phenyl group to exemplify the effect of chemical shift anisotropy.[58-61] Here, the highly anisotropic geometry of the phenyl π-electron system makes the effect especially pronounced. When the phenyl ring plane is aligned perpendicular to the external magnetic field, the π-electrons will cause a very effective shielding of the fluorine nucleus, and therefore a very low value of chemical shift around –155 ppm is observed. If, on the contrary, the fluoro-phenyl ring is oriented with the ring normal and the long axis both perpendicular to B_0, shielding will be very ineffective and a comparably high chemical shift around -60 ppm is observed. For the third geometrically distinct case, where the C_ω-F connecting bond lines up with the magnetic field, an intermediate shielding causing a chemical shift of approximately –125 ppm is observed.

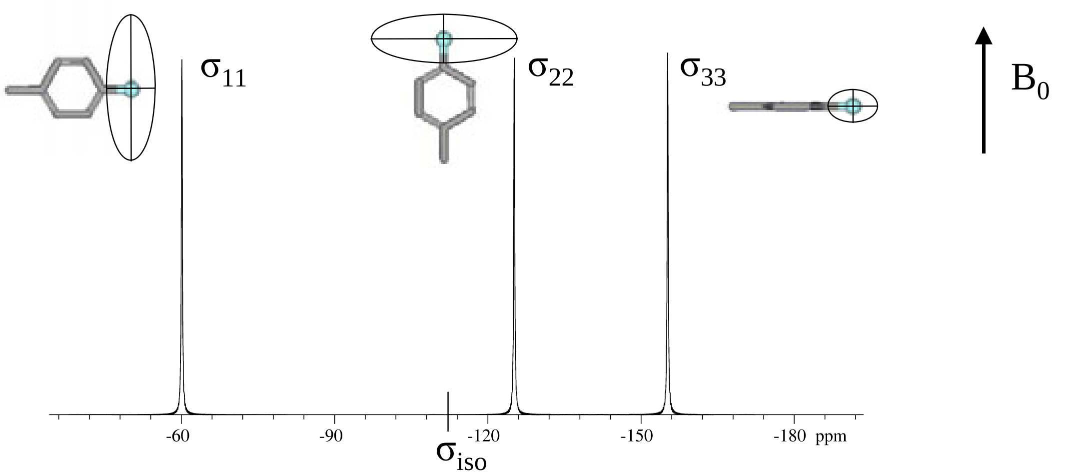

Figure 1.8: Anisotropic ^{19}F-NMR resonance frequencies observed on a fluoro-phenyl group in three different orientations with respect to the magnetic field B_0. The CSA tensor is indicated in ellipsoid representation.

A tensor needs to be employed in the mathematical description of CSA. When represented by a 3x3-matrix in the laboratory frame of reference, the CSA tensor is denoted as $\boldsymbol{\sigma}^{\mathrm{LAB}}$. It allows the prediction of experimentally observed chemical shifts σ_{obs} as

$$\sigma_{obs} = \left(\boldsymbol{\sigma}^{LAB}\right)_{zz}, \tag{1.3}$$

meaning that the observed chemical shift is given as the zz-component of the CSA tensor, i.e. the component that is lined up with the external magnetic field, B_0.

The CSA tensor may be diagonalized, yielding three principal values σ_{ii}, i=1,2,3, that make up the tensor's main diagonal in matrix representation. The feasibility of matrix diagonalization is ensured since the CSA tensor is a *mathematically* symmetric tensor. The numbering of the three principal elements needs some attention. In the most simplistic approach that was chosen for this thesis, the principal elements are ordered by their magnitude:

$$\sigma_{11} \leq \sigma_{22} \leq \sigma_{33} . \qquad (1.4)$$

Another convention orders the principal elements according to their proximity to the isotropic chemical shift position.[62;63] The isotropic chemical shift, $\sigma_{iso} := (\sigma_{11} + \sigma_{22} + \sigma_{33})/3$, is the fully averaged chemical shift that would be observed in a fully mobile molecule, e.g. in solution. The CSA tensor elements are then ordered by definition according to the modulus of their difference to σ_{iso}:

$$|\sigma_{22}' - \sigma_{iso}| \leq |\sigma_{11}' - \sigma_{iso}| \leq |\sigma_{33}' - \sigma_{iso}| . \qquad (1.5)$$

This is a mathematical prescription which ensures that σ_{22}' is located between σ_{11}' and σ_{33}', and that σ_{11}' is the principal value closer to σ_{22}'. As a result, σ_{33}' may be the most as well as the least shielded component, depending on its proximity to the isotropic chemical shift. In particular, for the case of two coinciding principal values, this convention always identifies the unique principal axis as the 3-axis, irrespective of the sign of δ. In the case of the fluoro-phenyl group illustrated in figure 1.8, this convention calls for an inversion in the assignment of the 1- and 3-principal components: $\sigma_{11}'=\sigma_{33}$ and $\sigma_{33}'=\sigma_{11}$.

The eigenvectors corresponding to the principal values form a special orthogonal coordinate system, the principal axis system (PAS) of the CSA tensor. This coordinate system is the basis for the ellipsoid visualization[64] of a tensor that is indicated alongside the fluorine labels in figures 1.4 and 1.8. In this representation, a three-dimensional ellipsoid has its half-axes lined up with the tensor's principal axis system, and the magnitude of each half-axis is determined by the inverse of the square root of the modulus of each principal value σ_{ii}.

The three principal values σ_{ii} fully characterize the magnitudes observed on the tensor. Another set of three values is commonly employed to give an alternative characterization. The first characteristic value is the isotropic chemical shift that was already mentioned,

$$\sigma_{iso} := (\sigma_{11} + \sigma_{22} + \sigma_{33})/3 , \qquad (1.6)$$

where the := sign denotes an equation giving a definition. The values for the two additional parameters are independent of the numbering convention, but the definitions are far simpler when expressed in the second numbering convention, (1.5). Therefore, they shall be given in that convention, but please keep in mind that in general this thesis adheres to the first convention, (1.4). The anisotropy parameter δ describes the tensor's overall width, although it is not identical to the overall width, but is defined as the difference between σ_{33}' and σ_{iso}:

$$\delta := \sigma_{33}' - \sigma_{iso} . \qquad (1.7)$$

Finally, the tensor's deviation from rotational symmetry is described by the asymmetry parameter η, defined as

$$\eta := \frac{\sigma_{22}' - \sigma_{11}'}{\sigma_{33}' - \sigma_{iso}}. \tag{1.8}$$

The ordering of the principal values given in equation (1.5) results in $0 \le \eta \le 1$. In the case of two main elements of the tensor being degenerate, i.e. having equal values, the asymmetry parameter evaluates to η=0. This sort of tensor is termed a 'symmetric' tensor *in the context of NMR tensors*. Note that this usage of 'symmetric' is more rigid than the mathematical usage, where any NMR tensor will qualify as 'symmetric'.

The set of three values (σ_{iso}, δ, η) is equivalent to the set of three principal values σ_{ii}. It allows a second formulation for the observed chemical shift,

$$\sigma_{obs}(\theta,\varphi) = \sigma_{iso} - \delta \cdot \left[\frac{3\cos^2\theta - 1}{2} + \eta \frac{\sin^2\theta \cos 2\varphi}{2} \right], \tag{1.9}$$

where ϑ, φ are the polar coordinates of the magnetic field vector B_0 in the PAS frame of reference. This formula is equivalent to (1.3), but is easier to handle since it involves only an ordinary function instead of a full tensor. Thus, it is useful in hands-on calculations in simple coordinate systems, but is hard to transform into different frames of reference.

In poly-crystalline samples as well as in lipid dispersions, all possible molecular orientations in space and thus all possible frequencies given by formula (1.9) are present. Therefore, very broad NMR lineshapes are observed in these samples. The observed broad lines possess characteristic shapes that are termed 'powder patterns' or 'tensor lineshapes'. Figure 1.9 presents the powder pattern observed in a non-oriented sample containing the fluoro-phenyl group considered in figure 1.8. The powder pattern allows a direct determination of the tensor principal values.

For the labeling and data analysis scheme used here, knowledge of the characteristic tensor values is as important as knowledge of the resonance position to be analyzed. Once σ_{iso}, δ, and η are known, a σ_{obs} value measured on an oriented sample will allow to extract possible ranges for θ and φ following equation (1.9). The characteristic tensor values were determined for a number of fluorinated amino acids in chapter III of this thesis, before the strategy was applied to several membrane systems for structure analysis.

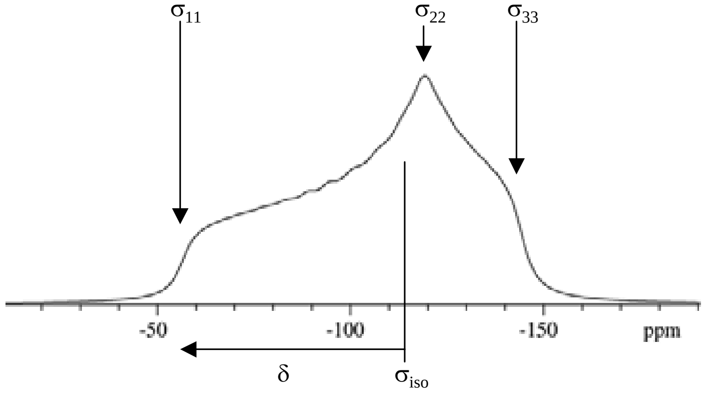

Figure 1.9: Powder spectrum observed on fluoro-phenyl groups in a fully non-oriented sample with all orientations equally present

The Hahn echo sequence

The broad spectra typically observed in solid-state NMR are reflected in the rapidly decaying FIDs seen in those samples. The very short FIDs prohibit use of the basic single-pulse sequence presented above, since receiver dead-times and probe ring-down make it impossible to acquire immediately after a high-power r.f. pulse. To overcome this problem, echo experiments are commonly employed in solid-state NMR. They cause the formation of a second signal, called the echo, after application of a second r.f. pulse.

The type of the second 'echo pulse' needs to be chosen differently in spin systems showing different interactions. In the case of individual nuclei experiencing only CSA interaction, the second pulse applied has to be a 180°-pulse. This sequence is known as the Hahn echo sequence. It is given schematically in figure 1.10, together with the time development of bulk magnetization. First, a 90°-pulse rotates magnetization into the xy-plane (A,B), as described above. There, magnetization will start to precess at different speeds (C), depending on the chemical shift of the respective group of spins. In figure 1.10 (C), faster and slower spins are schematically represented by different magnetization vectors marked F and S. After an 'echo delay' time τ, the echo pulse is applied. It is a $180°_x$-pulse which will flip all the nuclear magnetic moments within the xy-plane around the x-axis, returning all of them into the xy-plane (D). After the pulse, the magnetic moments continue their Larmor precession, with the important difference that now the slow spins S are ahead, while the fast spins F lag behind. Thus, after waiting for another delay time τ, the fast spins will have caught up with the slow ones (E), theoretically returning the spin system exactly to the state (B) it was in directly after the initial 90°-pulse. This is called refocussing, and the resulting signal shown above (E) is called the echo signal. The echo can easily be acquired by the spectrometer's receiver and, after Fourier transformation, gives the desired NMR spectrum.

In practice, instrument imperfections, especially inhomogeneities in B_0, will inhibit perfect refocussing. Also, due to electronic run-time effects, the echo is always observed to form a few μs later than expected from the τ value chosen (S. Antonijevic, personal communication, and own experience).

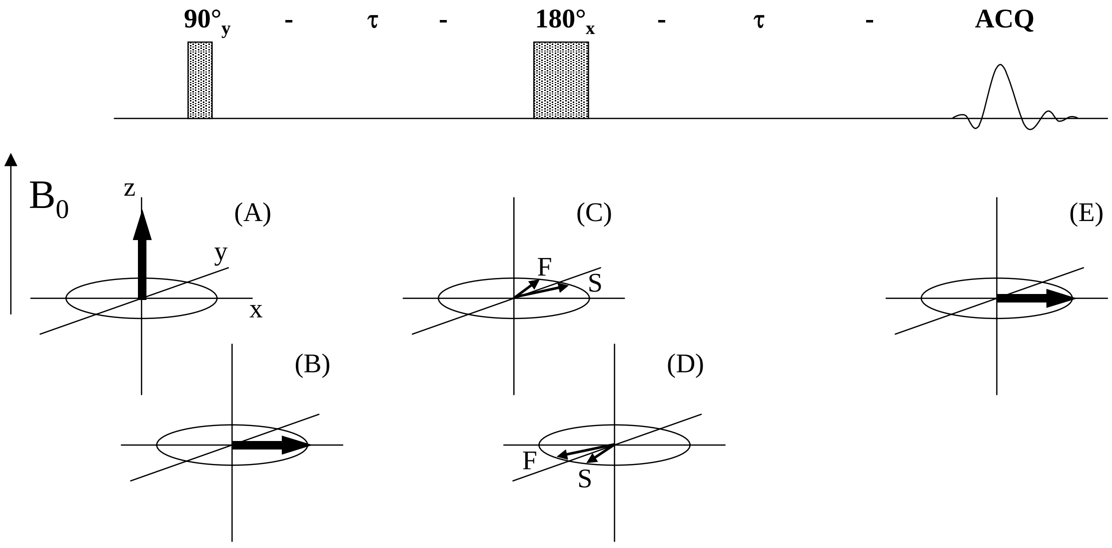

Figure 1.10: Hahn echo pulse sequence (top) and effected time evolution of spin magnetization (bottom) corresponding to two signals with different chemical shifts.

Dipolar coupling

The second nuclear magnetic interaction relevant in this study involves two nuclei. It is found that the α and β energy levels of one nucleus are influenced by the spin state of the other nucleus when they are close in space. This effect is called dipolar coupling. As a result, the β→α transition of the first nucleus splits up into two lines, one of them corresponding to the α or β state, respectively, of the coupled second nucleus. The resulting spectral doublet is shown in the right panel of figure 1.11, where also the splitting D_{ij} is noted down. The strength of dipolar coupling changes with molecular geometry. It depends on the distance between the two nuclei as well as on the angle that their internuclear connection vector encloses with the external magnetic field. When using the definition of variables given in the left panel of figure 1.11, the observed dipolar coupling between two nuclei denoted i and j behaves according to

$$D_{ij} = D_{ij}^{0} \cdot \frac{3\left\langle \cos^2 \theta \right\rangle - 1}{2} . \qquad (1.10)$$

Here, the angular brackets denote a time average, taking into account fast molecular motions. From the formula it can be seen that the dipolar coupling will vanish at a certain angle of $\theta_{m.a.}$=54.7°, which is referred to as the 'magic angle'. Maximum dipolar splitting D_{ij}^0 is observed when both nuclei line up with the magnetic field at θ=0°. Its magnitude can be calculated from natural constants as

$$D_{ij}^{0} = 2 \cdot f \cdot \hbar \gamma_i \gamma_j \cdot \frac{\mu_0}{4\pi} \cdot \frac{1}{2\pi rad} \cdot \frac{1}{r_{ij}^{3}} \quad , \qquad (1.11)$$

with

$$\hbar = 1.05459 \cdot 10^{-34} Js,$$
$$\gamma_H = 2.6752 \cdot 10^{8} radT^{-1}s^{-1},$$
$$\gamma_F = 2.5181 \cdot 10^{8} radT^{-1}s^{-1},$$
$$\frac{\mu_0}{4\pi} = 10^{-7} Hm^{-1},$$

for the values of Planck's constant ħ, proton and fluorine gyromagnetic ratios γ_H and γ_F, and magnetic field constant $\mu_0/4\pi$. The distance r_{ij} between the two nuclei enters as the inverse of its third power. Moreover, a factor *f* is introduced to distinguish between homo- and heteronuclear coupling. In the heteronuclear case *f*=1 holds, while in the homonuclear case an exchange contribution from the undistinguishable nuclei needs to be considered, which necessitates *f*=1.5. (A practical hint: The SIMPSON spectral simulation package does not take *f* as a part of D_{ij}^0, but adds it only in equation 1.10.)

From formula (1.10) it is evident that dipolar coupling, in contrast to CSA, is an intrinsically axially symmetric interaction. It does not scale with the strength of the magnetic field, as the chemical shift does, and is therefore given on an absolute Hz scale rather than on a relative (ppm) scale.

In addition, the right panel of figure 1.11 also shows the powder lineshape seen in a non-oriented sample where all orientations θ are equally present. Here, the maximum splitting D_{ij}^0 corresponds to $\theta = 0°$, it can directly be read from the spectrum, and will allow determination of r_{ij} using equation (1.11). Together with D_{ij} as determined from a macroscopically aligned sample, this will in turn allow extraction of θ via equation (1.10).

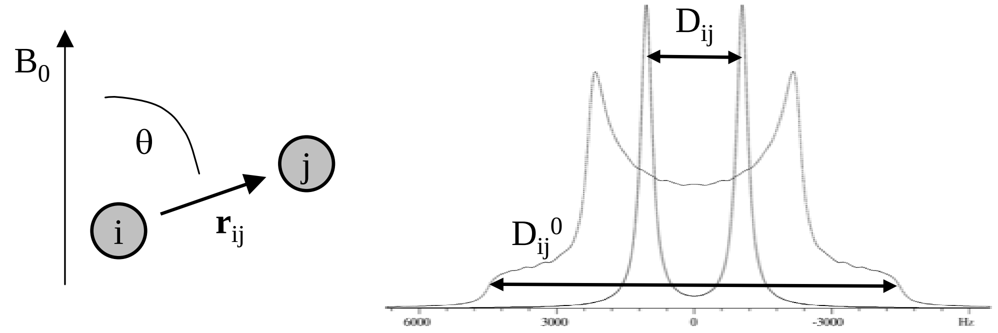

Figure 1.11: Dipolar coupling between two nuclei labeled i and j is determined by inter-nuclear connecting vector $\mathbf{r}_{ij}$ and angle θ between $\mathbf{r}_{ij}$ and external magnetic field B_0 (left). Doublet showing splitting D_{ij}, as observed in macroscopically oriented sample, along with powder pattern observed in a non-oriented sample (right).

Other magnetic nuclear interactions

This section briefly introduces the nuclear magnetic interactions not yet mentioned. The first interaction to be presented is that of a nucleus' quadrupolar electrical moment with the gradient of the surrounding electric field distribution. This interaction is observed for nuclei with a spin $I \geq 1$. The most relevant quadrupolar nucleus in biomolecular NMR is the deuteron ^{2}H, a heavier isotope of hydrogen.[65] It has a nuclear spin of I=1 and shows a so-called quadrupolar line splitting of

$$\Delta\nu = \Delta\nu_0 \cdot S_{mol} \cdot \frac{3\langle\cos^2\theta\rangle - 1}{2}, \qquad (1.12)$$

with $\Delta\nu_0$ giving the maximum observable splitting when the electric field gradient lines up with the external magnetic field B_0 at θ=0°. In the case of a rotating CD_3-group, as presented below, a value of $\Delta\nu_0$=84.0 kHz is appropriate.[66] Mathematically, the functional form of formula (1.12) is perfectly identical to that of the dipolar coupling interaction (1.10). Therefore, NMR data from deuterium measurements can easily be used to complement fluorine measurements, as done in chapter VIII of this thesis.

Another interaction of high importance in solution-state NMR is indirect or J-coupling between two nuclei. As in dipolar coupling, the energy level of one spin depends on the spin orientation of the other, but here the interaction is mediated by the electrons of covalent bonds or hydrogen bridges between both nuclei. The typical magnitude of this interaction is only several to several tens of Hz. Since this is two or three orders of magnitude below typical CSA or dipolar interactions, J-couplings are very rarely observed and utilized in solid-state NMR spectroscopy to date.

The isotropic chemical shift was mentioned before. Here, it should be noted that its absolute value may also contain valuable structural information in solid-state systems,[67;68] just as it does in solution. The isotropic chemical shift is readily accessible by fast MAS experiments.

The quadrupolar echo sequence

For refocussing homonuclear dipolar interaction, a second kind of echo sequence needs to be employed. It is called either the 'solid' or the 'quadrupolar' echo sequence and differs from the Hahn echo sequence presented in figure 1.10 only in the fact that a 90°-pulse is applied as the second pulse, as opposed to the 180° pulse used in the Hahn echo sequence. The name indicates that it was originally designed for NMR spectroscopy of quadrupolar nuclei.

The quadrupolar echo sequence is given schematically in figure 1.12, along with its effect on the magnetic moments within the sample. The figure is taken from a pioneering paper[69] by E. Hahn. After the bulk magnetization is turned into the xy-plane by the initial 90°-pulse (B), the microscopic magnetic moments precess and fan out as described for the Hahn echo sequence. As the 'echo' pulse, now a second 90°-pulse is applied, which turns the plane of the dephased magnetization vectors into the xz-plane (D), where they continue their Larmor precession and eventually dephase over the whole three-dimensional sphere (E). Following the echo delay time τ, they will organize in a complicated pattern (F), which Hahn likens to the written number '8'.

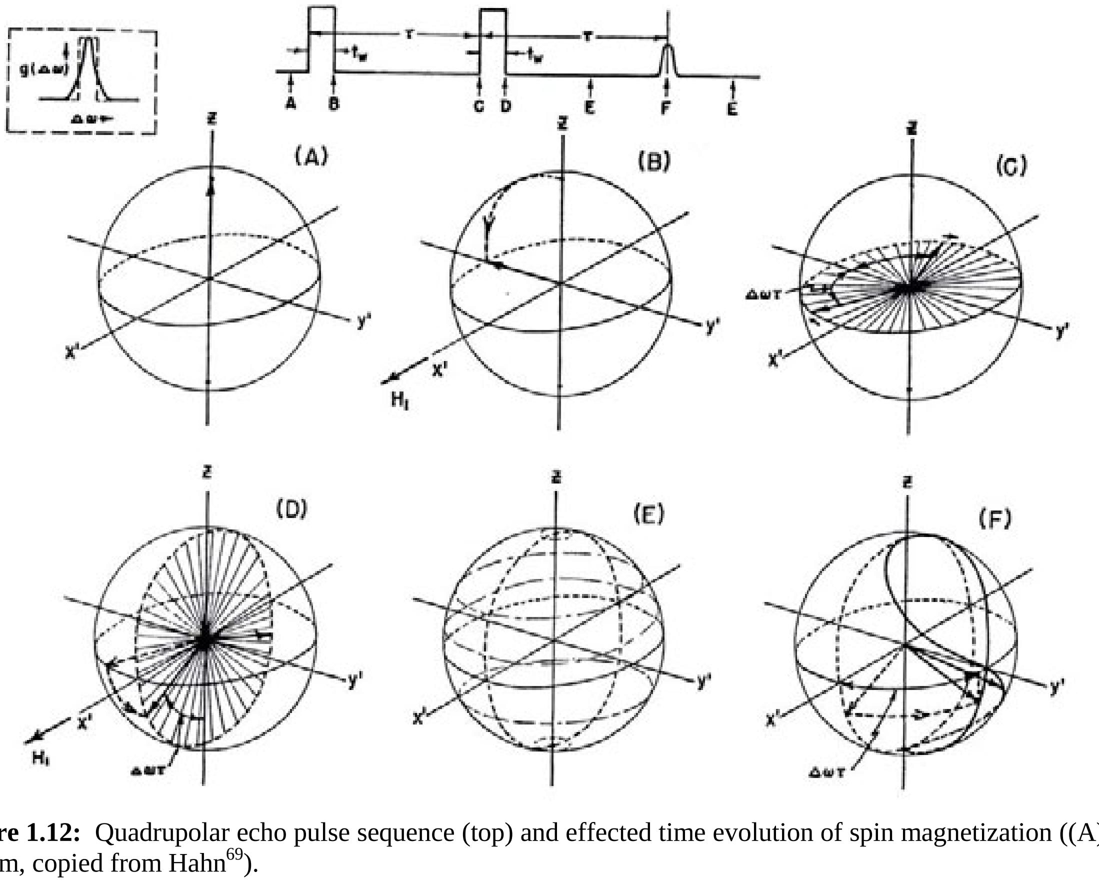

Figure 1.12: Quadrupolar echo pulse sequence (top) and effected time evolution of spin magnetization ((A)-(F), bottom, copied from Hahn[69]).

It is important to note that this 'number 8'-pattern does not represent a perfect refocussing of the magnetic moments to their initial state (B) after the initial 90°-pulse. Rather, it gives a distribution of magnetic moments with an optimized component in the xy-plane, thereby maximizing the observable signal.

Problem of simultaneous CSA and dipolar interaction

It was stated that different echo sequences are needed for samples showing either CSA or dipolar interactions. In the case of the CF_3-group, whose viability as an NMR isotope label shall be explored, both interactions are present with comparable magnitude. Each of the three fluorine nuclei experiences CSA from the surrounding electronic environment, and each pair of fluorine nuclei shows dipolar coupling. Antonijevic and Wimperis[70] have shown that a phase cycled version of the quadrupolar echo sequence is appropriate in this case.

The physical reason for the necessity of two different re-focussing echo sequences is found in the different mathematical form of the quantum-mechanical interactions involved. For the exact quantum-mechanical description of a spin system, the time-dependent Schrödinger equation needs to be solved. (That's what a spectral simulation program like SIMPSON does.) Here, the interactions form part of the Hamilton operator which describes the system as a whole. The parts of the Hamiltonian describing the CSA and dipolar coupling interactions—introduced in the classical approximation above—are given as

$$\begin{aligned} \hat{\mathbf{H}}_{CSA} &= \omega_{CSA}(\theta,\varphi)\cdot\hat{\mathbf{I}}_z \\ \hat{\mathbf{H}}_{DD} &= \Delta_0\cdot\hat{\mathbf{I}}_z^1\cdot\hat{\mathbf{I}}_z^2, \end{aligned} \qquad (1.13)$$

where the operators $\hat{\mathbf{I}}_z$ represent the z-component of the spin angular momentum of the nuclei involved. It can be seen from equation (1.13) that in the CSA Hamiltonian only one angular momentum operator $\hat{\mathbf{I}}_z$ enters linearly, while the dipolar Hamiltonian has two, i.e. this Hamiltonian is bi-linear in the angular momentum operators. This different mathematical form causes their fundamentally different behavior in the echo sequences.

To overcome the problems imposed by the different behavior of CSA and dipolar interactions, Antonijevic and Wimperis[70] have proposed a specially designed pulse cycling scheme for the quadrupolar echo sequence in the presence of chemical shift effects. It represents a new application of the well-known EXORCYCLE[71;72] phase cycling scheme, and is given in table 1.1. In their paper, they have shown experimentally as well as theoretically in the appropriate irreproducible 9-dimensional operator base, that this sequence will effect a perfect re-focussing of any system showing CSA as well as dipolar coupling. In chapter IV of this dissertation, the behavior of an actual CF_3-group in the aforementioned sequences was investigated theoretically and experimentally.

Table 1.1: Phase cycling scheme for quadrupolar echo sequence according to Antonijevic and Wimperis[70]

phase cycle step number	phase of initial 90° pulse	phase of second 90° pulse	phase of receiver
1	x	x	x
2	x	y	-x
3	x	-x	x
4	x	-y	-x

Multi-pulse experiments

Figure 1.13 summarizes the pulse sequences introduced in the preceding paragraphs. In addition, it shows the CPMG multi-pulse sequence,[73] which is another relevant experiment in this study. In the CPMG sequence, a 90° pulse is followed by repeated application of 180° pulses. In each 'window' between two 180° pulses an echo is formed, of which only the maximum point is acquired and stored by the NMR spectrometer. This procedure can be understood as a continuous repetition of the Hahn echo sequence. Since the Hahn echo sequence refocuses CSA interactions, so does the CPMG sequence, allowing only dipolar interactions to evolve freely. Therefore, in a CPMG spectrum only the so-called 'dipolar spectrum' of a sample is observed after Fourier transformation of the stroboscopically observed pseudo-FID, while anisotropic chemical shifts are suppressed.

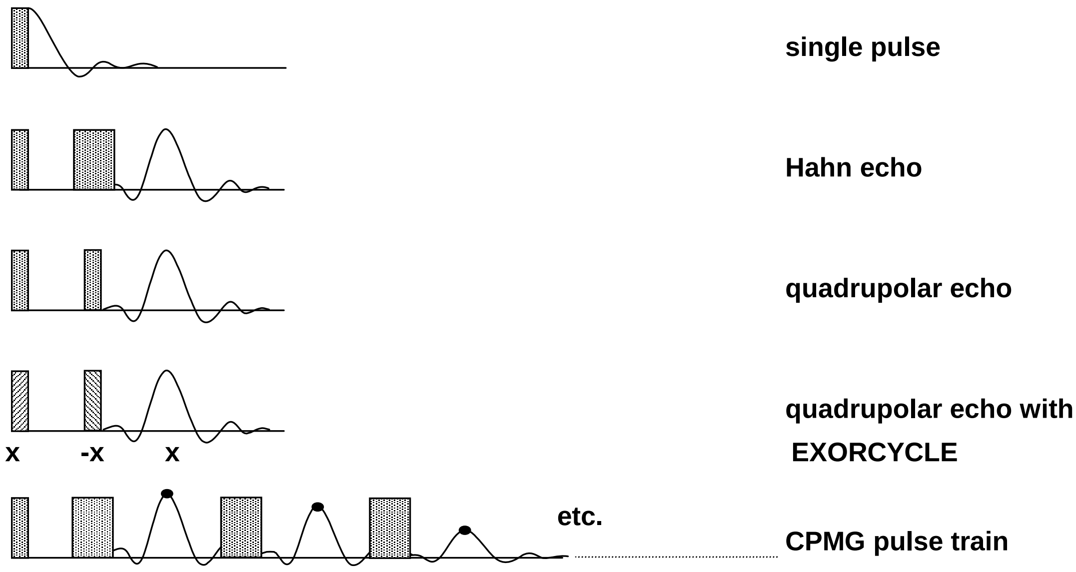

Figure 1.13: An overview of the pulse sequences relevant in this thesis. Hatching denotes pulses where phase cycling is essential.

This concludes the description of nuclear magnetic resonance and the overview of NMR interactions that formed the second portion of chapter I. The following chapter will describe how the anisotropy of these interactions can be utilized for structural studies. Pictorially speaking, chapter I introduced how structural parameters influence the strength of nuclear magnetic interactions, while chapter II will reverse the direction of reasoning by demonstrating how measured interactions can be exploited to yield structural insight into biomolecular systems.

Reference List

(1) Singer, S. J.; Nicolson, G. L. *Science* **1972**, *175*, 720-731.

(2) Maxfield, F. R. *Curr.Opin.Cell Biol.* **2002**, *14*, 483-487.

(3) Kurzchalia, T. V.; Parton, R. G. *Curr.Opin.Cell Biol.* **1999**, *11*, 424-431.

(4) Brown, D. A.; London, E. *Annu.Rev.Cell Dev.Biol.* **1998**, *14*, 111-136.

(5) Venter, J. C.; et al. *Science* **2001**, *291*, 1304-1351.

(6) The international human genome mapping consortium *Nature* **2001**, *409*, 934-941.

(7) Wallin, E.; von Heijne, G. *Protein Sci.* **1998**, *7*, 1029-1038.

(8) Curran, A. R.; Engelman, D. M. *Curr.Opin.Struct.Biol.* **2003**, *13*, 412-417.

(9) Garavito, R. M.; Picot, D.; Loll, P. J. *J.Bioenerg.Biomembr.* **1996**, *28*, 13-27.

(10) Wüthrich, K. *Science* **1989**, *243*, 45-50.

(11) Clore, M. G.; Gronenborn, A. M. *Science* **1991**, *252*, 1390-1399.

(12) McDonnel, P. A.; Opella, S. J. *J.Magn.Reson.B* **1993**, *102*, 120-125.

(13) Zhou, Y.; Duncan, T. M.; Cross, R. L. *Proc.Natl.Acad.Sci.U.S.A.* **1997**, *94*, 10583-10587.

(14) Ben-Shem, A.; Frolow, F.; Nelson, N. *FEBS Letters* **2004**, *564*, 274-280.

(15) Brink, J.; Ludtke, S. J.; Yang, C.-Y.; Gu, Z.-W.; Wakil, S. J.; Chiu, W. *Proc.Natl.Acad.Sci.U.S.A.* **2002**, *99*, 138-143.

(16) Fromme, P.; Melkozernov, A.; Jordan, P.; Krauss, N. *FEBS Letters* **2003**, *555*, 40-44.

(17) Lentz, B. R.; Malinin, V.; Haque, M. E.; Evans, K. *Curr.Opin.Struct.Biol.* **2000**, *10*, 607-615.

(18) Skehel, J. J.; Wiley, D. C. *Cell* **1998**, *95*, 871-874.

(19) Pécheur, E. I.; Sainte-Marie, J.; Bienvenüe, A.; Hoekstra, D. *J.Membrane Biol.* **1999**, *167*, 1-17.

(20) Martin, I.; Ruysschaert, J.-M. *Biosci.Rep.* **2000**, *20*, 483-500.

(21) Tamm, L. K.; Han, X. *Biosci.Rep.* **2000**, *20*, 501-518.

(22) Boman, H. G. *Scand.J.Immunol.* **1998**, *48*, 15-25.

(23) Henzler Wildman, K. A.; Lee, D.-K.; Ramamoorthy, A. *Biochemistry* **2003**, *42*, 6558.

(24) Barra, D.; Simmaco, M.; Boman, H. G. *FEBS Letters* **1998**, *430*, 130-134.

(25) Zasloff, M. *Nature* **2002**, *415*, 389-395.

(26) Bauer, F.; Schweimer, K.; Klüver, E.; Conejo-Garcia, J.-R.; Forssmann, W.-G.; Rösch, P.; Adermann, K.; Sticht, H. *Protein Sci.* **2001**, *10*, 2470-2479.

(27) Gudmundsson, G. H.; Agerberth, B.; Odeberg, J.; Bergman, T.; Olsson, B.; Salceldo, R. *Eur.J.Biochem.* **1996**, *238*, 325-332.

(28) Matsuzaki, K. *Biochim.et Biophys.Acta* **1998**, *1462*, 1-10.

(29) Matsuzaki, K. *Biochim.et Biophys.Acta* **1998**, *1376*, 391-400.

(30) Dürr, M.; Peschel, A. *Infection and Immunity* **2002**, *70*, 6515-6517.

(31) Neu, H. C. *Science* **1992**, *257*, 1064-1073.

(32) Wade, D.; Boman, A.; Wåhlin, B.; Drain, C. M.; Andreu, D.; Boman, H. G.; Merrifield, R. B. *Proc.Natl.Acad.Sci.U.S.A.* **1990**, *87*, 4761-4765.

(33) Wu, M.; Maier, E.; Benz, R.; Hancock, R. E. W. *Biochemistry* **1999**, *38*, 7235-7242.

(34) Huang, H. W. *Biochemistry* **2000**, *39*, 8347-8352.

(35) Popot, J.-L.; Engelman, D. M. *Biochemistry* **1990**, *29*, 4031-4037.

(36) Strandberg, E.; Ulrich, A. S. *Concepts Magn.Res.* **2004**, *23A*, 89-120.

(37) Bechinger, B. *J.Membrane Biol.* **1997**, *156*, 197-211.

(38) Bechinger, B. *Biochim.Biophys.Acta* **1999**, *1462*, 157-183.

(39) Epand, R. F.; Vogel, H. J. *Biochim.Biophys.Acta* **1999**, *1462*, 11-28.

(40) Ulrich, A. S. High resolution solid state NMR, ^{1}H, ^{19}F; In *Encyclopedia of spectroscopy and spectrometry*; Lindon, J. C., ed. Academic Press: 2000; pp 813-825.

(41) Ulrich, A. S. *Prog.NMR Spectr.* **2004**, *46*, 1-21.

(42) Ulrich, A. S.; Wadhwani, P.; Dürr, U. H. N.; Afonin, S.; Glaser, R. W.; Strandberg, E.; Tremouilhac, P. P. Y.; Sachse, C.; Berditchevskaia, M.; Grage, S. L. Solid-state ^{19}F-NMR analysis of membrane-active peptides; 2004.

(43) Danielson, M. A.; Falke, J. J. *Annu.Rev.Biophys.Biomol.Struct.* **1996**, *25*, 163-195.

(44) Gakh, Y. G.; Gakh, A. A.; Gronenborn, A. M. *Magn.Reson.Chem.* **2000**, *38*, 551-558.

(45) Gerig, J. T. *Prog.Nucl.Magn.Reson.Spectrosc.* **1994**, *26*, 293-370.

(46) Toke, O.; Maloy, W. L.; Kim, S. J.; Blazyk, J.; Schaefer, J. *Biophys.J.* **2004**, *87*, 662-674.

(47) Toke, O.; O'Connor, R. D.; Weldeghiorhis, T. K.; Maloy, W. L.; Glaser, R. W.; Ulrich, A. S.; Schaefer, J. *Biophys.J.* **2004**, *87*, 675-687.

(48) Bravo, P.; Capelli, S.; Valdo Meille, S.; Viani, F.; Zanda, M.; Kukhar, V. P.; Soloshonok, V. A. *Tetrahedr.Asym.* **1994**, *5*, 2009-2018.

(49) Bravo, P.; Bruché, L.; Pesenti, C.; Viani, F.; Volonterio, A.; Zanda, M. *J.Fluor.Chem.* **2001**, *112*, 153-162.

(50) Koksch, B.; Sewald, N.; Jakubke, H. D.; Burger, K. Synthesis and incorporation of α-trifluoromethyl-substituted amino acids into peptides; In *Biomedical frontiers of fluorine chemistry*; Ojima, I., McCarthy, J. R., Welch, J. T., eds. American Chemical Society: Washington DC, 1996; pp 42-58.

(51) Wenschuh, H.; Beyermann, M.; Haber, H.; Seydel, J. K.; Krause, E.; Bienert, M. *J.Org.Chem.* **1995**, *60*, 405-410.

(52) Campos-Olivas, R.; Aziz, R.; Helms, G. L.; Evans, J. N. S.; Gronenborn, A. M. *FEBS Letters* **2002**, *517*, 55-60.

(53) Grage, S. L.; Wang, J.; Cross, T. A.; Ulrich, A. S. *Biophys.J.* **2002**, *83*, 3336-3350.

(54) Afonin, S.; Glaser, R. W.; Berditchevskaia, M.; Wadhwani, P.; Gührs, K.-H.; Möllmann, U.; Perner, A.; Ulrich, A. S. *Chembiochem* **2003**, *4*, 1151-1163.

(55) Glaser, R. W.; Sachse, C.; Dürr, U. H. N.; Wadhwani, P.; Ulrich, A. S. *J.Magn.Reson.* **2004**, *168*, 153-163.

(56) Moll III., F.; Cross, T. A. *Biophys.J.* **1999**, *57*, 351-362.

(57) Cross, T. A. *Methods Enzymol.* **1996**, *289*, 672-696.

(58) Griffin, R. G.; Yeung, H.-N.; LaPrade, M. D.; Waugh, J. S. *J.Chem.Phys.* **1973**, *59*, 777-783.

(59) Hiyama, Y.; Silverton, J. V.; Torchia, D. A.; Gerig, J. T.; Hammond, S. J. *J.Am.Chem.Soc.* **1986**, *108*, 2715-2723.

(60) Mehring, M. *High Resolution NMR of Solids*; Springer: Berlin, 1976.

(61) Nehring, J.; Saupe, A. *J.Chem.Phys.* **1970**, *52*, 1307-1310.

(62) Mason, J. *Solid State Nucl.Magn.Reson.* **1993**, *2*, 285-288.

(63) Schmidt-Rohr, K.; Spiess, H. W. *Multidimensional Solid-State NMR and Biopolymers*; Academic Press: San Diego, CA, 1994.

(64) Radeglia, R. *J.Magn.Reson.* **1995**, *4*, 317-321.

(65) Ulrich, A. S.; Grage, S. L. Solid state ^{2}H-NMR; In *Solid state NMR of polymers*; Ando, I., Asakura, T., eds. Elsevier: Amsterdam, 1998; pp 190-211.

(66) Davis, J. H. *Biochim.Biophys.Acta* **1983**, *737*, 117-171.

(67) Sternberg, U. *Mol.Phys.* **1988**, *63*, 249-267.

(68) Wishart, D. S.; Sykes, B. D. *Methods Enzymol.* **1994**, *239*, 363-392.

(69) Hahn, E. L. *Phys.Rev.* **1950**, *80*, 580-594.

(70) Antonijevic, S.; Wimperis, S. *J.Magn.Reson.* **2003**, *164*, 343-350.

(71) Bodenhausen, G.; Freeman, R.; Turner, D. L. *J.Magn.Reson.* **1977**, *27*, 511-514.

(72) Vold, R. L.; Vold, R. R. *J.Magn.Reson.* **1981**, *42*, 173-176.

(73) Grage, S. L.; Ulrich, A. S. *J.Magn.Reson.* **2000**, *146*, 81-88.

I. Introduction

II. Best-fit analysis of solid-state NMR data

For the structural evaluation of orientation-dependent chemical shifts and dipolar couplings, a molecular model needs to be fitted to the experimental NMR data. The present chapter first introduces the concept of model theory and best-fit analysis. It then presents the influence of molecular orientation and mobility on NMR spectral properties, laying the mathematical basis for prediction of NMR data from a given model. For the present thesis, the best-fit analysis scheme was implemented in dedicated programs written in the computer algebra package *Mathematica* (www.wolfram.com), which was successfully applied to the actual analysis of solid-state NMR data measured on isotope labeled peptides. The chapter finishes with a description of the *Mathematica* implementation and comments on the practical experiences that were made with it. It is the basis for all following chapters, where necessary input parameters for the calculations are gathered (chapters III and IV), and best-fit analysis is applied to actual membrane-associated systems (chapters V to VIII). An exemplary *Mathematica* program is given as appendix B of this thesis.

Model theory and penalty functions

For the structural interpretation of observed solid-state NMR anisotropic chemical shifts σ_{exp}, a mathematical model needs to be specified which can predict theoretical frequencies σ_{model}. (The same applies for observed dipolar coupling values, which for the sake of readability are neglected for the time being). The model usually contains free parameters, for which best-fit values are searched for to generate (in the best case perfect) agreement between measured and predicted values. In the present case, a model predicts anisotropic chemical shift values $\sigma_{model} = \sigma_{model}(\rho, \tau, S_{mol})$ that are determined by three free parameters: The overall orientation of the molecule under investigation is characterized by a pair of angles (ρ,τ), and its molecular mobility is characterized by the molecular order parameter S_{mol}. The meaning of these three parameters is illustrated in figure 2.1 and will be introduced in detail in the course of this chapter. For the moment it suffices to note that molecular orientation and mobility are equally important to predict model chemical shift values.

In the framework of model theory,[1] experimental data and predicted chemical shift values are tested against each other by means of a penalty function, also called error function. The smaller the value of the penalty function, the better the agreement between model and experiment. If the penalty function reaches a value of zero, the model predicts exactly the values found in experiment.

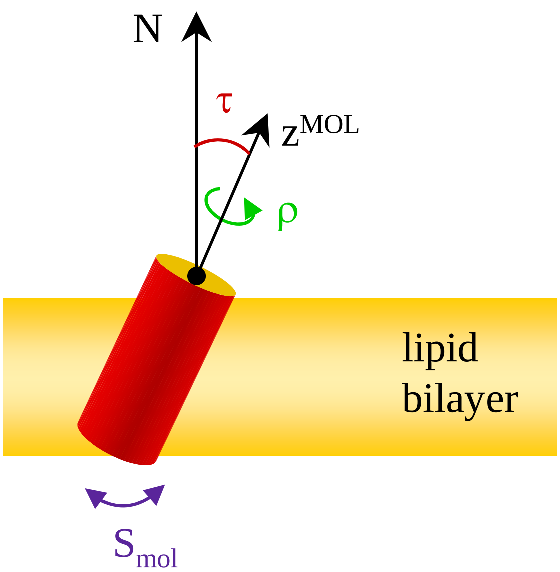

Figure 2.1: The situation of a peptide in a lipid bilayer is characterized by three parameters: The angles ρ and τ, where τ gives the angle between molecular z-axis and bilayer normal N, and ρ describes the peptide's azimuthal rotation. In addition, molecular mobility is measured by the molecular order parameter, S_{mol}.

Two penalty functions are in common use, called *rmsd* and χ^2. The former one, root mean square deviation (*rmsd*), is defined as

$$rmsd := \sqrt{\frac{1}{N}\sum_{i=1}^{N}\left(\sigma_{i,model}\left(\rho,\tau,S_{mol}\right)-\sigma_{i,\exp}\right)^2}\ , \qquad (2.1)$$

where the index *i* numbers individual experimental data points and N is the total number of data points $\sigma_{i,exp}$, i.e. $1 \le i \le N$. As the name indicates, *rmsd* gives the square root of the average of the squared differences between the experimental and predicted data. It is therefore measured in the same units as the observed quantity, being units of frequency in the present case. The second common penalty function is called χ^2 and is defined as

$$\chi^2 := \sum_{i=1}^{N}\left(\frac{\sigma_{i,model}\left(\rho,\tau,S_{mol}\right)-\sigma_{i,\exp}}{\Delta\sigma_i}\right)^2, \qquad (2.2)$$

where $\Delta\sigma_i$ is the experimental error of the *i*-th data point that needs to be estimated from the accuracy of the performed experiment. Important in the present case are uncertainties in referencing the chemical shift,[2] and the mosaic spread found in the sample, which will be reflected in observed linewidth. By normalizing the squared deviation to $\Delta\sigma_i$, the χ^2-function becomes unitless. At the same time, it becomes especially easy to interpret. If a predicted resonance position is within experimental error of the observed one, then the squared deviation will rest ≤ 1. Therefore, a value of $\chi^2 \le N$ indicates perfect coincidence between model and experiment *within experimental error*.

Both penalty functions have slightly differing interpretations. As explained, the χ^2-function gives *overall* error in quadratic form, while *rmsd* gives *mean* deviation, i.e. deviation *per input parameter*. Therefore, *rmsd* typically gives much smaller numbers and a 'high' value (say, larger than 1.0 ppm) of *rmsd* is much less acceptable than the same value in χ^2. (Example: For a peptide carrying N=4 labels, $\Delta\sigma$=1ppm, a minimum of χ^2=2.0 would correspond to a value of $rmsd = \sqrt{\chi^2/N}\cdot\Delta\sigma = \sqrt{2/4}\cdot 1\,\text{ppm} = 0.224\,\text{ppm}$. This solution would be acceptable within experimental error, for as long as $\chi^2 \le 4$ in this case.)

Because χ^2 is normalized to experimental error, χ^2 values from different types of nuclei (here: ^{19}F, ^{2}H, and ^{15}N) can directly be compared and may even be added, while *rmsd* values must not. Therefore, *rmsd* was used to analyze data from the sixspin systems and for B18 (chapters V and VI), where only ^{19}F labels were employed, while a χ^2-analysis was necessary for gramicidin S and PGLa (chapters VII and VIII), where data from different isotope labels had to be integrated.

After defining a penalty function, a best-fit data analysis of experimental data is performed by finding minima in the penalty function. Any minimum will give two pieces of information. By its value, it will show whether the solution found is acceptable, i.e. whether the corresponding fit explains the data within experimental error. It has to be noted that model theory will never give a certain *proof* for a given model, but can only rule out non-acceptable ones. If the quality of the fit (or 'goodness-of-fit') is acceptable, then the corresponding values of the free parameters may be extracted and analyzed. In the present case, each acceptable minimum will give a set of ρ, τ, and S_{mol} that may be interpreted in structural terms.

Orientational analysis of anisotropic NMR interactions

In the following sections, the influence of the global molecular orientation in the membrane —parameterized by a pair of angles (ρ,τ)—on predicted chemical shift values $\sigma_{model} = \sigma_{model}(\rho,\tau,S_{mol})$ is presented. The influence of molecular mobility—parameterized by the molecular order parameter S_{mol}—is individually treated later on. The geometry of various molecular properties is mathematically captured by corresponding frames of reference. The relative orientation between two frames of reference is quantified by transformations. Comprehensive treatments of the mathematics involved can be found in most NMR textbooks.[3-6] A brief description of the computational details, which is somewhat parallel to the present one, can be found in a recent review by Bechinger and Sizun[7].

Transformations between frames of reference

In the introductory chapter I, it has become evident that different frames of reference are needed to describe and understand NMR data. The CSA tensor is most easily described in its principal axis system PAS, while a measurement observes the zz-component of the CSA tensor in the laboratory frame of reference, LAB. Neither frame of reference carries any interesting information on the molecule under investigation. Hence the ultimately interesting frame of reference is a third one, MOL, which is rigidly connected to the molecule of interest, and whose orientation is to be determined from the NMR data.

It is evident that different frames of reference are needed to properly describe different situations, and transformations are needed to change between them. In NMR, the necessary transformations are restricted to rotations, since global translations do not influence any NMR-relevant parameters. Generally, rotations are given by 3x3-matrices R, which allow transformations of vectors v and tensors $\boldsymbol{\sigma}$ to be carried out according to the transformation formulae

$$\begin{aligned} v' &= R \cdot v \\ \boldsymbol{\sigma}' &= R \cdot \boldsymbol{\sigma} \cdot R^{-1}, \end{aligned} \tag{2.3}$$

where the primes denote the transformed values. Both formulae are relevant here, since the employed interactions are given by CSA *tensor* and internuclear connection *vector*.

To predict a CSA resonance frequency, a transformation from PAS to LAB is needed, so equation (2.3) can be given more precisely with the transformation matrix written as $R = R^{PAS \to LAB}$. From the resulting CSA tensor in LAB, $\boldsymbol{\sigma}^{LAB}$, the chemical shift resonance frequency can then directly be calculated according to equation (1.3) as

$$\sigma_{\exp} = \left(\boldsymbol{\sigma}^{LAB}\right)_{zz} = \left(R^{PAS \to LAB} \cdot \boldsymbol{\sigma}^{PAS} \cdot \left(R^{PAS \to LAB}\right)^{-1}\right)_{zz}. \tag{2.4}$$

For dipolar couplings, the mathematical problem is essentially the same. Again, the relevant characteristic—the connecting vector between the coupled nuclei—is needed in LAB. Here, only a vector instead of a tensor needs to be transformed, which calls for the same transformation matrix, and only requires the simpler first transformation formula in equation (2.3). The predicted resonance frequencies or splittings can then be tested against experimental values, as described above.

Relevant frames of reference

In practice, the transformation PAS→LAB is done by a number of intermediate steps between intermediate frames of reference, which were either already mentioned or shall be defined in the following.

As described in chapter I, the CSA tensor is characterized by three principal values, σ_{ii}. The eigenvectors connected to these principal values form an orthogonal coordinate system, the principal axis system PAS. This 'magnetic geometry' of the nucleus now needs to be put in relation to the 'chemical geometry' of the direct molecular environment.

The chemical surrounding of an isotope label is described by another frame of reference, PPL. It needs to be individually defined for each chemical labeling situation. For the situation of a ^{19}F nucleus in a fluoro-phenyl group, it is defined in figure 6.3. Due to the symmetry of the fluoro-phenyl group, it is found to coincide with PAS. For the case of a ^{15}N nucleus in a Peptide PLane, the definition of PPL is given in figure 7.3. This is actually one of the most relevant molecular situations in solid-state NMR of biomolecules, which made me choose the abbreviation. Measuring or predicting the exact relationship between PAS and PPL is not a trivial task. It either calls for single crystal measurements,[5] sophisticated experimental NMR schemes,[8-11] or involved quantum-mechanical calculations.[12]

The molecular coordinate system MOL is rigidly connected to the molecule of interest, thereby describing its spatial orientation. It needs to be individually defined for each molecule under investigation. For the four membrane-active substances investigated in chapters V to VIII of the present thesis, this will be done in the respective introductory sections. In each case, MOL was chosen to be coinciding with special features of the molecular geometry (α-helix axis, C_2 symmetry axis) to later make the interpretation of results more intuitive. When comparing the four molecular situations, one notices that they are completely different among each other, but all of them are funneled into exactly the same mathematical framework by a proper choice of MOL.

For the description of MAS experiments, an additional intermediate coordinate system ROT needs to be employed, which is rigidly connected to the MAS rotor. Since we are dealing with static samples only, it is of no relevance here.

The laboratory frame of reference, LAB, is given by the direction of the external magnetic field B_0. As is common practice in NMR spectroscopy, the z axis of LAB is defined to be parallel to B_0. For x^{LAB} and y^{LAB}, no definition needs to be given since they do not enter any NMR-relevant formulae.

The intermediate frames of reference described can now be used to decompose the overall transformation into intermediate ones:

$$R^{PAS\rightarrow LAB} = R^{MOL\rightarrow LAB} \cdot R^{PPL\rightarrow MOL} \cdot R^{PAS\rightarrow PPL}\,. \tag{2.5}$$

Next, the rotations used in the intermediate transformations need to be quantified.

Euler angles quantify rotations

To quantify rotations, a set of three independent rotation angles, called Euler angles, is most commonly employed. Figure 2.2 shows the Euler angle definition used in this study. For obvious reasons, a fluoro-phenyl group in the molecular coordinate system MOL is used for illustration. The illustrations were generated by *Mathematica*, with a sphere representing the fluorine atom and one aromatic bond being colored red to break the phenyl group's symmetry. Dots indicate the arcs along which the consecutive rotations take place.

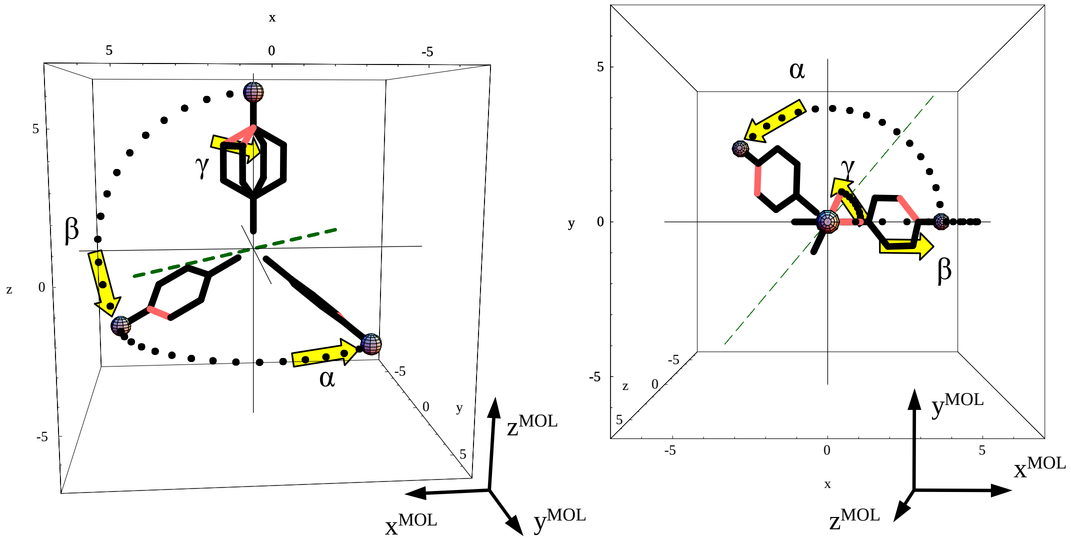

Figure 2.2: Demonstration of the Euler angle definition used in this study, exemplified on a fluoro-phenyl group. Front (left) and side (right) views of the intermediate positions, connected by dotted arcs that show the three elementary rotations. The dashed green line is the 'node line', which is perpendicular to both z- and z'-axis.

Initially, the fluoro-phenyl group (i.e. the coordinate system PPL characterizing its local geometry) is aligned with MOL, which here is shown space-fixed. In the first step, the fluoro-phenyl group is rotated by an angle γ around the z^{MOL}-axis. Next, it is rotated around the y^{MOL}-axis by an angle β, and finally around the z^{MOL}-axis, by an angle α. This convention allows any rotation or orientation of an object to be described by the Euler angles α, β, and γ, which can take values of $0° \le \alpha < 360°$, $0° \le \beta < 180°$, and $0° \le \gamma < 360°$, respectively. The sign of the angles is given by the right-hand rule around the positive direction of each axis. In the example of figure 2.2, values of γ=65°, β=120°, and α=140° (characteristic of a 4F-Phg residue in an α-helix) were used.

The set of three Euler angles is one parameterization (out of many) of the group SO(3) of rotations in three-dimensional real space. Using the Euler angle parameterization, the full rotation matrix R can be decomposed into three elementary rotations, one for each Euler angle: $R(\alpha,\beta,\gamma) = R_z(\alpha)R_y(\beta)R_z(\gamma)$. This definition is consistent with most of solid-state NMR textbooks.[3-6] It has to be noted, though, that in a number of other applications the second rotation is carried out around the *x*-axis, resulting in completely different formulae. Also, in a many other contexts passive transformations are more appropriate than the active ones used here. The following section discusses the difference between active and passive transformations. Afterwards, the discussion will turn back to the practical details of actual calculations.

Transformations may be active or passive

The definition of the three Euler angles given above is different from the more rigorous definition used in theoretical physics. There, the transformation parameterized by Euler angles is defined as a passive transformation, while the transformation described above is an active one. In an active transformation, an *object* is rotated with respect to a single coordinate system that does not change. In a passive transformation, on the contrary, the (tripod that defines the) initial untransformed *coordinate system* is subjected to rotations. This relationship is schematically depicted in figure 2.3.

For passive transformations, a different set of transformation rules than those of equation (2.3) applies. If the coordinate system is transformed by a rotation R, then vectors v and tensors $\boldsymbol{\sigma}$ transform according to

$$\begin{aligned} v' &= R^{-1} \cdot v \\ \boldsymbol{\sigma}' &= R^{-1} \cdot \boldsymbol{\sigma} \cdot R, \end{aligned} \tag{2.6}$$

i.e. the transformation rules now contain the inverse of the transformation, R^{-1}. The difference in transformation rules can be understood by a hand-waving interpretation: Whenever an object is turned 'right' (in the widest sense, shown on the right side in figure 2.3), then this transformation is equivalent to the coordinate system being turned 'left' (again in the widest sense). The resulting relationship between object and coordinate tripod is identical and cannot be distinguished, as can also be seen upon closer examination of figure 2.3.

In the case of rigorous Euler angles, the initial coordinate system is (actively) transformed by three consecutive rotations to give the new coordinate system. First, the coordinate system is rotated by an angle α around the 'old' z-axis until the y-axis lines up with the 'node line', which is defined to be perpendicular to both old and new z-axes. It is indicated by a dashed green line in figure 2.2. The second rotation, β, rotates the old z-axis around the node line (intermediate y'-axis) onto the new z"-axis. The third rotation γ is performed around the new z"-axis to line up the intermediate y'-axis with the final y"-axis. Thus, the actual passive transformation is given by three rotations around intermediate axes, as written down in the first line of

$$\begin{aligned} R(\alpha,\beta,\gamma) &= R_{z''}(\gamma) R_{y'}(\beta) R_z(\alpha) \\ &= R_z(\alpha) R_y(\beta) R_z(\gamma). \end{aligned} \tag{2.7}$$

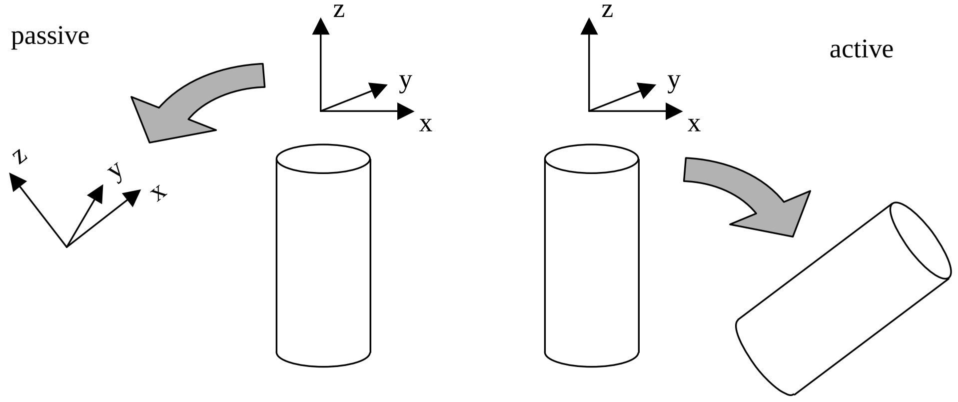

Figure 2.3: Schematic comparison of passive and active transformations

Unfortunately, matrix algebra requires a single fixed coordinate system to make matrix multiplications meaningful, i.e. the first line of equation (2.7) is hard to carry out practically. Luckily, a simple relationship between the mathematically complicated rotations in intermediate coordinate systems and simple active rotations in a fixed single coordinate system exists. It is given as the second line in equation (2.7), and states that the passive definition results in a rotation matrix exactly identical to the one derived from the active definition given in the previous section. This important relationship is tacitly assumed (or overlooked) in most NMR textbooks, only Mehring's textbook[5] mentions it explicitly (p. 218f). It explains the order of rotation angles (*first* γ, then β, then α), which the reader may have found surprising in the active definition of the Euler angles.

Passive transformations would actually be the proper choice for our purposes, since we want to describe a peptide's *orientation*. An active rotation implicitly suggests that an actual *motion* takes place, with the peptide actively moving from the untransformed towards the transformed orientation. This rather academic consideration was quickly dropped since passive transformations were found to considerably decrease the clarity and interpretability of the calculations. The resulting conceptual confusion of the programmer makes the whole calculation error-prone and is easily avoided by sticking to active transformations.

Explicit form of transformation matrices

In the active definition $R(\alpha,\beta,\gamma) = R_z(\alpha)R_y(\beta)R_z(\gamma)$ of the Euler angles introduced above, the symbol $R_z(\alpha)$ denotes an elementary rotation of α degrees around the z-axis, while R_y denotes a rotation around the y-axis. Mathematically, a rotation in three-dimensional space is given by a 3x3-matrix. Elementary rotation matrices R_z and R_y around the z- and y-axes of the laboratory frame of reference are given by[3]

$$R_z(\alpha) = \begin{pmatrix} \cos\alpha & -\sin\alpha & 0 \\ \sin\alpha & \cos\alpha & 0 \\ 0 & 0 & 1 \end{pmatrix}, \quad \text{and} \quad R_y(\beta) = \begin{pmatrix} \cos\beta & 0 & \sin\beta \\ 0 & 1 & 0 \\ -\sin\beta & 0 & \cos\beta \end{pmatrix},$$

where α and β again denote the respective rotation angles. Using these elementary matrices, the required rotation can be composed:

$$R(\alpha,\beta,\gamma) = \begin{pmatrix} \cos\alpha & -\sin\alpha & 0 \\ \sin\alpha & \cos\alpha & 0 \\ 0 & 0 & 1 \end{pmatrix} \cdot \begin{pmatrix} \cos\beta & 0 & \sin\beta \\ 0 & 1 & 0 \\ -\sin\beta & 0 & \cos\beta \end{pmatrix} \cdot \begin{pmatrix} \cos\gamma & -\sin\gamma & 0 \\ \sin\gamma & \cos\gamma & 0 \\ 0 & 0 & 1 \end{pmatrix}$$

$$= \begin{pmatrix} \cos\alpha\cos\beta\cos\gamma - \sin\alpha\sin\gamma & -\cos\alpha\cos\beta\sin\gamma - \sin\alpha\cos\gamma & \cos\alpha\sin\beta \\ \sin\alpha\cos\beta\cos\gamma + \cos\alpha\sin\gamma & -\sin\alpha\cos\beta\sin\gamma + \cos\alpha\cos\gamma & \sin\alpha\sin\beta \\ -\sin\beta\cos\gamma & \sin\beta\sin\gamma & \cos\beta \end{pmatrix} \qquad (2.8)$$

This is the explicit form of the Euler transformation matrix which was used in all calculations presented in this thesis. To use it in calculations following formula (2.4), explicit values for the Euler angles used in each transformation in formula (2.5) need to be found.

For the structural interpretation of NMR data, the relationship between the molecular and laboratory coordinate systems is of direct interest. Therefore, the Euler angles used in this MOL→LAB transformation are given special symbols:

$$R^{MOL\rightarrow LAB} := R(0°,\tau,\rho)\,, \tag{2.9}$$

where ρ is the molecule's rotation around its z^{MOL}-axis, and τ the tilt of that z^{MOL}-axis against the laboratory z-axis z^{LAB}. The membrane's bilayer topology restricts τ to half its usual range: $0° \le \tau < 90°$. For the most relevant case of an α-helix, ρ and τ are shown explicitly in figures 2.1 and 6.2.

So far, the symbols α, β, and γ were used to denote Euler angles in general. In the following, their usage will be restricted purely to describing the relation between molecular segments and the whole molecule. This relation is given by the rotation matrix

$$R^{PPL\rightarrow MOL} := R(\alpha,\beta,\gamma)\,. \tag{2.10}$$

The exact values of the angles need to be determined from the molecular model structure at hand, a process described in detail in the next section. The ranges of the angles may be reduced by molecular symmetry. For example, the C_2-symmetry of the fluoro-phenyl group reduces the necessary range of γ to $0° \le \gamma < 180°$.

For the ^{15}N CSA tensor, PPL and PAS are not coinciding. Therefore, an additional transformation is needed in the analysis of nitrogen data:

$$R^{PAS\rightarrow PPL} := R(0°,\theta,0°)\,, \tag{2.11}$$

where θ is the angle between the nitrogen CSA tensor's most shielded axis and the NH-bond axis, which defines the z^{PPL}-axis. In the literature an average value of θ=-16.7° is reported,[13] which we used as well. Some authors also found the third Euler angle to differ from zero, e.g. Wu *et al.*[10] report 20°. In all of our calculations, it proved to have only very minor influence on the results and was therefore set to zero in the presented calculations.

Model building

As described in the previous section, the relationship between PPL and MOL depends on the molecular geometry, which is therefore needed as additional input in predicting resonance frequencies $\sigma_{model}(\rho,\tau,S_{mol})$. Therefore, molecular models had to be created for each of the systems investigated. Here, molecular model means a geometrical model representing the three-dimensional structure, usually given in pdb or COSMOS data format. Details of model building for each system investigated will be reported in the materials and methods sections of the respective chapters. Here, it is noted that this process requires no specialized software at all, as the wide spectrum of software available for viewing, manipulating, and presenting molecular structures can fully be used. As a result, model building is not restricted to any perfectly idealized model structure as used in the B18 analysis (chapter VI), but can directly be extended to highly irregular structures as the one used to analyze gramicidin S (chapter VII). Of special interest here are software functionalities that allow to introduce arbitrary

imperfections in idealized structure elements. Especially influences from thermal fluctuations and local deviations from idealized structure are highly expected for membrane-active systems. By using geometry optimization and molecular dynamics, which are implemented in a number of modeling programs, such imperfections could be introduced in the model structures. Their influence on the quality of fit was investigated systematically in the analysis of PGLa data (chapter VIII).

When a model structure was satisfying all demands it was used to extract the parameters necessary for best-fit analysis. The required input parameters are the sets of Euler angles α, β, γ that describe the location of each isotope label within the molecular frame of reference, i.e. give the transformation PPL$\rightarrow$MOL as introduced in equation (2.10). In a first approach, these angles were measured directly on the model structures—which obviously need to be given in their MOL coordinate system—using angle measurement tools implemented in most molecular viewing programs.

As an example, consider the Euler angles for the ^{19}F CSA tensor in an idealized α-helix carrying 4F-Phg labels. Since the molecular coordinate system MOL is chosen to have its z-axis along the helix axis, the Euler angles take readily intuitive values. The values for γ and β should be identical for all residues, while α should change by 100° between consecutive residues. And indeed, measurements on idealized structures yielded values of

$$\begin{aligned} \alpha &= 140° + (j-1)\cdot\omega \\ \beta &= 120° \\ \gamma &= 65°, \end{aligned} \qquad (2.12)$$

where the C_α of residue j=1 defines the y^{MOL}-axis, and the pitch angle ω=100° describes the angle between two adjacent residues j and j+1 in an α-helix. The value of β=120° indicates that the 4F-Phg residues (or more generally, the C_α-C_β bonds) point 'down' the helix in the direction of the N-terminus. At the same time, they point into the helical direction of screw, as described by a positive α=140°. The side chain torsion is given by the angle γ=65°, which differs from χ_1 by a constant because γ is measured against the node line. (*Cf.* figure 2.2, where exactly the values (2.12) were chosen.) These intuitive values of the Euler angles allow easy generation of 'non-perfect' α-helices by slightly varying the angle values. Here, 'non-perfect' means a perfectly regular structure, but with slightly varied values of helix diameter and pitch. This is of biophysical interest, since there are indications that α-helices in lipid membranes tend to be more rigid and better ordered than those known from solution NMR structures.[14]

Although the Euler angles have a comparatively simple form and can easily be interpreted, we did not find them to be advantageous in routine calculations. Especially the process of measuring them within molecular viewing programs was found to be tedious and error-prone. To circumvent the determination of Euler angles, we resorted to an alternative way of determining the matrix (2.10) describing the PPL$\rightarrow$MOL transformation. It is known from basic vector analysis that the columns of the transformation matrix are given by the transformed unit vectors of the original coordinate system, PPL. These can easily be constructed from a few atomic positions: In the 4F-Phg case, the vectors C_ζ-^{19}F and $C_{\delta1}$-$C_{\delta2}$ give two of the three PPL axis directions, the third one is constructed as their vectorial product (see figure 6.3). In the case of the ^{15}N-labeled peptide plane, z^{PPL} is defined by the vector ^{15}N-H_N, and the position of C_α will then define the peptide plane and thereby the

remaining vectors (see figure 7.3). Since the molecular model is given in its MOL coordinate system, the named atomic coordinates will immediately give the transformed unit vectors sought for.

Therefore, second-generation *Mathematica* programs were written to carry out best-fit analysis according to the procedure described. They take sets of atomic coordinates as input which can easily be extracted from the model structures ($C_{\delta 1}$, $C_{\delta 2}$, C_{ζ} and ^{19}F for each fluorine label; ^{15}N, C_{α}, H_N for each nitrogen label). The unit vectors of the respective local coordinate systems are calculated from these positions, and the transformation matrix (2.10) is generated having the unit vectors as its columns. The transformation matrix is thus directly determined from pdb-coordinates given in the MOL frame of reference, hence the Euler angles relating PPL and MOL coordinate systems are not determined explicitly anymore as they are actually completely hidden in the calculation. This procedure proved to be far easier to handle and far more reliable than explicit Euler angle determination.

Influence of molecular mobility on NMR spectra

It was stated repeatedly above that molecular mobility strongly influences NMR spectra. Different modes of molecular mobility are distinguished by characteristic time scales on which thermal molecular or segmental reorientation happens, measured by the correlation time τ_{corr}. In solution, molecular reorientations typically take place on the ns time scale. In comparison, the time span of a typical NMR experiment covers several μs to ms, in solution-state NMR even up to seconds, meaning that it is several orders of magnitude longer than the molecular correlation time: $\tau_{corr} \ll \tau_{NMR}$. In solution-state NMR fast molecular reorientations average all anisotropic components of the interactions, giving the typical narrow and well-resolved lineshapes.

Whenever molecular mobility is restricted, as is the case in solid bodies, polymers, liquid crystals or biological membranes, typical correlation times reach the order of magnitude of the NMR time scale: $\tau_{corr} \cong \tau_{NMR}$. This limit constitutes the realm of solid-state NMR studies, where reduced mobility makes anisotropic interactions fully effective and extremely broad spectra are observed. For the lineshape and width of these spectra, another characteristic of molecular mobility becomes relevant: the order parameter, which characterizes the spatial amplitude and preferred axis of molecular motions.

Long-axial rotation

Under ambient conditions—especially in liquid crystalline membranes—there are many modes of mobility, all of which lead to a partial averaging of the NMR interactions. A typical example that is easy to deal with is a methyl group, which shows unrestricted rotational mobility around its axis of symmetry at room temperature.[15] Relevant in the context of this thesis are CF_3- and CD_3-groups, that are also found to rotate freely around their axis of symmetry. This mode of mobility projects the respective NMR interaction tensors onto the axis of rotation. For axially symmetric interactions such as the homonuclear dipolar coupling,

the quadrupolar interaction, or a CSA with η=0, the averaging can be expressed in terms of an order parameter S_ζ

$$\left\langle \frac{3\cos^2\theta - 1}{2} \right\rangle = \frac{3\cos^2\zeta - 1}{2} \cdot \left\langle \frac{3\cos^2\beta - 1}{2} \right\rangle = S_\zeta \cdot \left\langle \frac{3\cos^2\beta - 1}{2} \right\rangle . \tag{2.13}$$

Here, ζ is the angle between the relevant spin interaction tensor and the axis of averaging, and β denotes the angle between the latter and B_0. In the case of a CF_3-group, the direction of dipolar coupling between each pair of nuclei forms an angle of ζ=90° with the rotational axis, hence the fast rotation of the CF_3-group reduces the original static dipolar coupling by a factor of $S_\zeta=(3\cos^2 90°-1)/2=-1/2$, and the observed magnitude of dipolar splitting is now governed by the angle β between magnetic field and the methyl rotational axis. The appropriate scaling factor is different for a CD_3-group, where the relevant direction of (quadrupolar) interaction is given by the C-D-bond, which forms an angle of ζ=109.5° with respect to the axis of rotation. The corresponding factor of S_ζ=–1/3 is already contained in the value for $\Delta\nu_0$ given after equation (1.12).

An analogous effect is found when CSA tensors are averaged around a single axis of rotation at a rate that is faster than the NMR time scale. The observed fluorine CSA tensors of typical peptides in lipid bilayers are usually symmetric due to rotational diffusion of the whole peptide around the bilayer normal. This mode of mobility will leave only the tensor component that is lined up with the bilayer normal unchanged, and will mix all other tensor components to an average value, in analogy to equation (2.13) that is applicable to the more simple case of a symmetric interaction.

Molecular wobbling

The rotational order parameter S_ζ is concerned with the local averaging of specific molecular segments or in fact any rotation around a well-defined axis. A different problem is posed by the global wobbling motions of the whole molecule around an equilibrium position. From a phenomenological point of view, this kind of molecular mobility often leads to a partial reduction of the spectral width of NMR spectra, while (more or less) retaining their spectral lineshape. The degree of narrowing can then be described by a single number, which allows for a pragmatic definition for S_{mol} as a simple scaling factor. In the case of dipolar splittings, it can be calculated from the observed NMR spectrum by changing equation (1.10) into

$$S_{mol} := \frac{D_{ij}}{D_{ij}^0} = \left\langle \frac{3\cos^2\theta - 1}{2} \right\rangle . \tag{2.14}$$

In the static case of a completely immobilized molecule, S_{mol} evaluates to 1 and no reduction of dipolar splitting is observed. At the other extreme, for a fully mobile molecule, the splitting collapses to zero and S_{mol} = 0. Neither complete immobility nor full mobility are typically found in membrane-associated systems. These systems show partial averaging such that $0 \le S_{mol} \le 1$. Note that S_{mol} contains no information on the average orientation of an individual molecular segment nor about the overall amplitude of motion of the whole molecule. Specifically, a vanishing dipolar splitting may have two different causes: Either,

the internuclear vector rotates fast around a well-defined axis that is aligned at the magic angle, $S_\zeta(54.7°)$ or the molecule is internally rigid but globally fully mobile such that $S_{mol}=0$.

In the case of the CSA tensor, mobility will scale down only the anisotropic parts $\sigma^{0,aniso}$, so here the phenomenological definition (2.14) of S_{mol} needs to be adapted to

$$\sigma_{ii} = \sigma_{iso} + S_{mol} \cdot \sigma_{ii}^{0,aniso} . \tag{2.15}$$

Side chain oscillations

In the present work, the segmental mobility of the fluoro-phenyl side chain in the 4F-Phg label was of special interest. Clear spectroscopic evidence was found that the fluoro-phenyl side chain does not rotate freely, but oscillates about an equilibrium value of the torsion angle χ_1. Not only this angle was needed for the analysis of spectral data, but also the amplitude of thermal libration around it.

Thermal oscillations of the fluoro-phenyl side chain will leave the σ_{22} component of the ^{19}F CSA tensor unchanged, while the σ_{11} and σ_{33} components are averaged. To quantify the degree of tensor narrowing, a pragmatic definition was used to define a local order parameter, analogous to the one of equation (2.14), which calculates the order parameter as the ratio of observed to maximum possible difference between σ_{11} and σ_{33}. The symbol S_{Phg} was used to denote its limited applicability to only the 4F-Phg situation:

$$S_{Phg} := \frac{\sigma_{11}^{obs} - \sigma_{33}^{obs}}{\sigma_{11}^{0} - \sigma_{33}^{0}} , \tag{2.16}$$

where the indices '*obs*' and '*0*' distinguish the observed from the non-averaged principal CSA tensor components, respectively. This is a special instance of a more general definition of a rotational order parameter.[16;17]

Our implementation of best-fit analysis

This chapter has so far described the mathematical details for calculating model resonance frequencies as a function of molecular orientation and molecular mobility. Molecular orientation is described by the transformation matrices between PAS and LAB coordinate systems, while molecular mobility directly affects the CSA tensors or dipolar couplings. Consequently, the result of the preceding sections can be summarized in the formula

$$\sigma_{model}(\rho,\tau,S_{mol}) = R^{-1}(\rho,\tau)\cdot \boldsymbol{\sigma}(S_{mol})\cdot R(\rho,\tau), \qquad (2.17)$$

which in some cases needs refinement by an additional order parameter S_{Phg} describing side chain oscillation. Equation (2.17) is now ready to be applied using penalty functions according to equations (2.1) and (2.2) for best-fit analysis of resonance frequencies observed in oriented bilayer samples, which will be carried out repeatedly in chapters VI to VIII. The remaining two sections of the present chapter introduce the graphical representation of orientation-dependent functions and the experiences that were made in the software implementation of the best-fit analysis scheme.

Graphical representation of orientational dependencies

Most of the results of this thesis are presented in the form of so-called ρ-τ-plots. They show properties changing with rotation ρ and tilt τ. The pair (ρ,τ) of Euler angles describes a molecule's orientation with respect to the laboratory frame of reference, LAB, as shown in figure 2.1. Figure 2.4 gives a cartoon of which molecular orientation is described by which pair (ρ,τ). The right hand side shows the reference frame LAB, which is usually aligned with

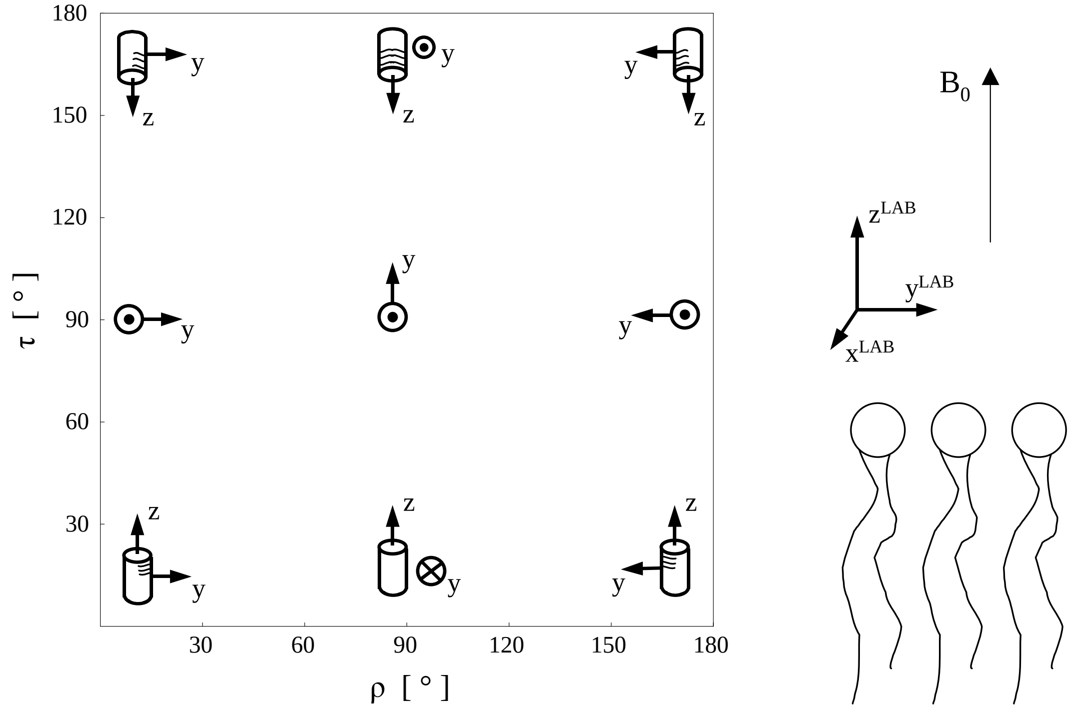

Figure 2.4: Graphical representation of different molecular orientations with respect to the lipid bilayer, as represented by the different regions of the ρ-τ-plane.

the schematically represented lipid bilayer and the external magnetic field B_0. The row of cartoon α-helices displayed e.g. in the bottom of the left panel shows the case of tilt τ=0°. The background of the panel is a ρ-τ- plane, where, by convention, we always show ρ on the abscissa and τ on the ordinate. In the τ=0° case, the molecular z-axis lines up with the LAB z-axis, and ρ describes the rotation of the helix around its long axis. The middle and upper rows of cartoon helices show values of tilt τ=90° and 180°, respectively, representing helices that are either perpendicular or anti-parallel to the LAB z-axis.

In figure 2.4 the range for ρ was already reduced from the mathematically meaningful [0°, 360°] to half that range, which is the non-redundant range for NMR spectroscopy. An equivalent representation could choose the range of ρ as the full [0°,360°], but reduce τ to [0°, 90°]. The meaningful range of ρ and τ may further be reduced by the symmetry of the investigated molecule.

The ρ-τ-plane can now be used to plot a function f(ρ,τ) of ρ and τ. Mathematically, plotting an orientation-dependent function onto a rectangular area is an instance of the 'orange-peel problem' of projecting the surface of a sphere onto a plane, meaning that areas are not meaningful here. A function f is represented in a ρ-τ-plot by contours of identical value, f(ρ,τ)=*const*. This is demonstrated in figure 2.5 for the anisotropic chemical shift, equations (1.3) and (1.9). The panels to the right give the contour representation in the ρ-τ-plane, while the left-side panels show identical functions in a three-dimensional plot. Upper and lower panels show differently aligned CSA tensors. In the upper panels, PAS is aligned with MOL, while for the lower panel Euler angles of α=140°, β=120°, γ=65° (typical for 4F-Phg in an α-helix) were used for the alignment between PAS and MOL. The plots show the full ranges for ρ and τ, proving that these ranges are actually redundant for NMR data, as reflected in the symmetry visible in the plots.

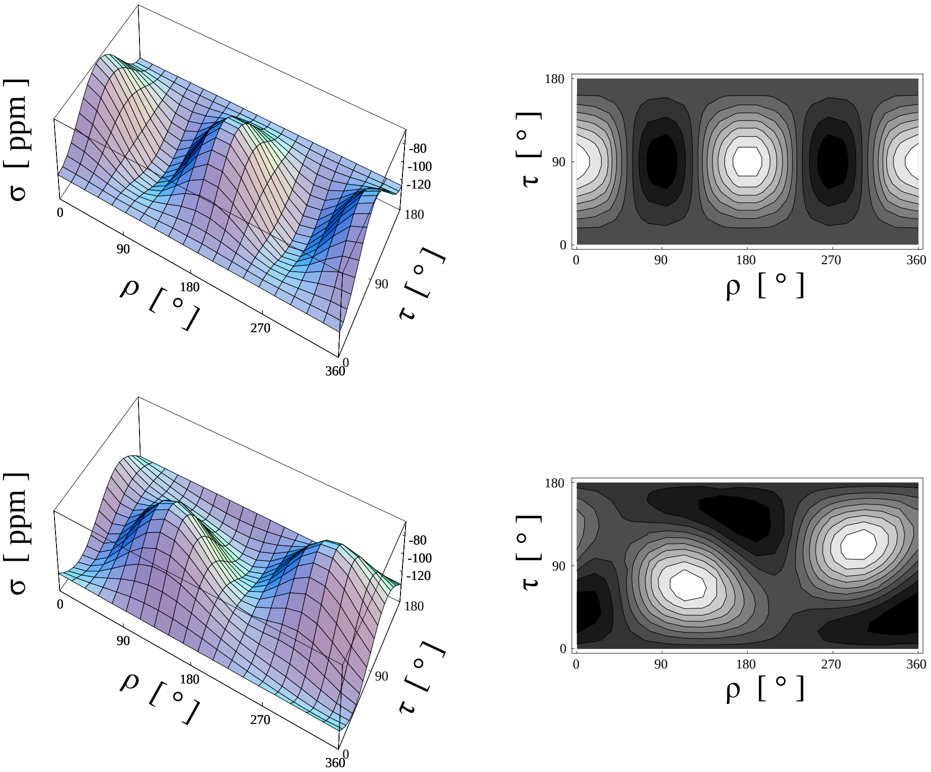

Figure 2.5: Orientation dependence of CSA resonance frequency in different molecular situations (top: PAS coincides with MOL, bottom: PAS different from MOL), presented as surface plots (left) and contour plots (right).

Software platform

For model building, most commercial and non-commercial molecular modeling software was found to be useful, each program having individual advantages and drawbacks.

For the best-fit analysis scheme, which is the consecutive and final step in analysis of oriented solid-state NMR data, the computer algebra package '*Mathematica*' (www.wolfram.com) was found to be most appropriate. *Mathematica* provides large sets of tools, including programming, algebraic, analytical, statistical and graphics tools. Within a *Mathematica* file (called a ‘notebook’), the analysis can be split up into functional pieces of code, which may be run individually or consecutively. This approach allows interactive assessment, treatment and evaluation of data, while at the same time every step is documented, and publication-quality graphical output can be generated. Since *Mathematica* is very much math-oriented, programming is kept simple which in turn makes it easy to learn step-by-step, 'as you go'. This may seem to be time-consuming, but is has to be noted that the analysis process is not completely trivial, but every step takes some attention of the operator. Therefore, it has to be seen as an advantage that a *Mathematica* notebook always confronts the user with the full computational code. In conclusion, *Mathematica* was found to be the ideal tool to do the best-fit analysis necessary for the evaluation of our solid state NMR data. The appendix of this thesis presents a sample Mathematica notebook that was used in the analysis of ^{19}F-NMR data acquired on gramicidin S. Additional notebooks are available on our internet site (www-ifia.fzk.de/IFIA_Webseiten/Webseiten_Ulrich/index.html) as supplementary material to the published results on PGLa.[18;19]

Parallel to the programming of the best-fit data analysis scheme, substantial effort was made to visualize the respective models within the data analysis environment of *Mathematica*. Thereby, a method of control was introduced that permitted *intrinsic* checks on all orientational results. Figure 2.6 presents two examples of the graphic output that was generated: Two views of the idealized α-helix that was used in the analysis of B18 and PGLa data, and a side view of the gramicidin S model employed. Although these visualizations may not meet aesthetic demands, they proved to be very helpful in performing, controlling and understanding the described calculations.

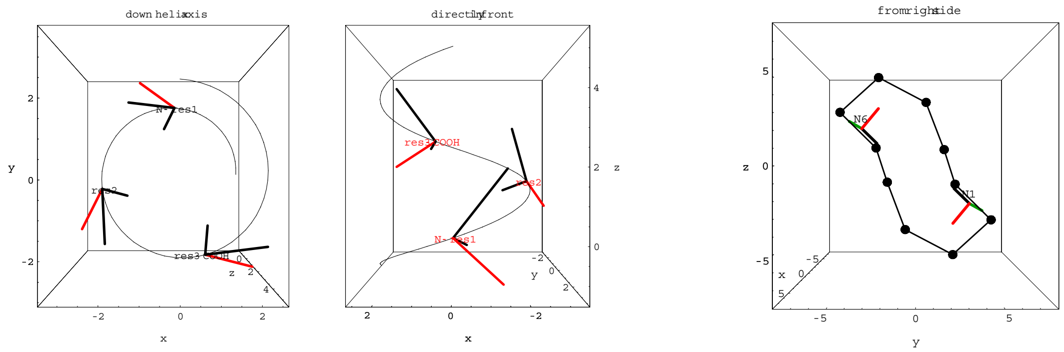

Figure 2.6: *Mathematica* renderings of the molecular models employed. (Left and middle) Top and side view of an idealized α-helix, ^{19}F-CSA tensors represented by tripods localized on C_α positions, backbone indicated by a spiral. (Right) Structure of gramicidin S[20], with the ^{19}F CSA tensors represented by tripods localized on ^{19}F positions, and the backbone indicated by connected C_α positions.

Similar to the approach presented here, a number of other researchers have previously chosen a combination of NMR-specific code in a powerful general software environment. Jacco van Beek developed the software package 'matNMR 3' (matnmr.sourceforge.net/) for spectral analysis, which is based on MATLAB (www.mathworks.com/products/matlab/), another computer algebra environment. The package 'nmrtools' (www.nmrtools.com) offers a similar tool package based on the data analysis software ORIGIN (www.originlab.com).

An alternative approach involves custom-tailored computer programs that are fully coded in a compiled universal programming language, such as C or C++. This was done e.g. in the analysis of deuterium labeled WALP model peptides.[21;22] Such fully coded programs are far less user-friendly than the proposed *Mathematica* approach, since the user needs to be fluent in a compiled computer language. Such fluency does not offer any advantage as computational speed is not an issue in the present problem. Instead, use of a compiled language necessitates programming of all the additional functionalities (such as evaluation and plotting of functions) that are already present in *Mathematica*. Interfacing also calls for major attention in any compiled program. For example, the most powerful computational tool available for solid-state NMR spectroscopy, SIMPSON[23], is controlled via a simple scripting language, Tcl[24]. In addition, a subsidiary program, SIMMOL[25], is provided to generate SIMPSON formatted input from molecular models.

All mentioned methods are hands-on tools and require quite some craftsmanship. For the future, it seems desirable to have a software tool that can be handled in a more routine fashion. Especially, a software solution combining molecular modeling and NMR data analysis—as known from solution state NMR—would noticeably ease the analysis process.

Reference List

(1) Press, W. H.; Teukolsky, S. A.; Vetterling, W. T.; Flannery, B. P. *Numerical recipes in C*; Cambridge University Press: Cambridge, 1992.

(2) Glaser, R. W.; Ulrich, A. S. *J.Magn.Reson.* **2003**, *164*, 104-114.

(3) Duer, M. *Solid State NMR Spectroscopy*; Blackwell Science: 2002.

(4) Haeberlen, U. *High Resolution NMR in Solids--Selective Averaging*; Academic Press: New York, San Francisco, London, 1976.

(5) Mehring, M. *High Resolution NMR of Solids*; Springer: Berlin, 1976.

(6) Schmidt-Rohr, K.; Spiess, H. W. *Multidimensional Solid-State NMR and Biopolymers*; Academic Press: San Diego, CA, 1994.

(7) Bechinger, B.; Sizun, C. *Conc.Magn.Reson.A* **2003**, *18A*, 130-145.

(8) Brender, J. R.; Taylor, D. M.; Ramamoorthy, A. *J.Am.Chem.Soc.* **2001**, *123*, 914-922.

(9) Lee, D.-K.; Ramamoorthy, A. *J.Magn.Reson.* **1998**, *133*, 204-206.

(10) Wu, C. H.; Ramamoorthy, A.; Gierasch, L. M.; Opella, S. J. *J.Am.Chem.Soc.* **1995**, *117*, 6148-6149.

(11) Grage, S. L.; Wang, J.; Cross, T. A.; Ulrich, A. S. *Biophys.J.* **2002**, *83*, 3336-3350.

(12) Sternberg, U.; Witter, R.; Ulrich, A. S. *Annu.Rep.NMR Spectr.* **2004**, *52*, 53-104.

(13) Straus, S. K.; Scott, W. R. P.; Watts, A. *J.Biomol.NMR* **2003**, *26*, 283-295.

(14) Kim, S.; Cross, T. A. *Biophys.J.* **2002**, *83*, 2084-2095.

(15) Beshah, K.; Olejniczak, E. T.; Griffin, R. G. *J.Chem.Phys.* **1987**, *86*, 4730-4736.

(16) Hyberts, S. G.; Goldberg, M. S.; Havel, T. F.; Wagner, G. *Protein Sci.* **1992**, *1*, 736-751.

(17) Detlefsen, D. J.; Thanabal, V.; Pecoraro, V. L.; Wagner, G. *Biochemistry* **1991**, *30*, 9040-9046.

(18) Glaser, R. W.; Sachse, C.; Dürr, U. H. N.; Wadhwani, P.; Afonin, S.; Strandberg, E.; Ulrich, A. S. *Biophys.J.* **2005**, *88*, 3392-3397.

(19) Glaser, R. W.; Sachse, C.; Dürr, U. H. N.; Wadhwani, P.; Ulrich, A. S. *J.Magn.Reson.* **2004**, *168*, 153-163.

(20) Xu, Y.; Sugár, I. P.; Krishna, N. R. *J.Biomol.NMR* **1995**, *5*, 37-48.

(21) Strandberg, E.; Özdirekcan, S.; Rijkers, D. T. S.; van der Wel, P. C. A.; Koeppe II, R. E.; Liskamp, R. M. J.; Killian, J. A. *Biophys.J.* **2004**, *86*, 3709-3721.

(22) van der Wel, P. C. A.; Strandberg, E.; Killian, J. A.; Koeppe II, R. E. *Biophys.J.* **2002**, *83*, 1479-1488.

(23) Bak, M.; Rasmussen, T.; Nielsen, N. C. *J.Magn.Reson.* **2000**, *147*, 296-330.

(24) Ousterhout, J. K. *Tcl and the Tk toolkit*; Addison-Wesley: Reading, MA, 1994.

(25) Bak, M.; Schultz, R.; Vosegaard, T.; Nielsen, N. C. *J.Magn.Reson.* **2002**, *154*, 28-45.

III. Amino acids with a single ^{19}F-label

A comprehensive database of fundamental ^{19}F-NMR spectroscopic parameters was determined for a wide range of mono-fluorinated amino acids. These are interesting in themselves and are needed as input and reference framework for the analysis of ^{19}F-NMR data acquired on ^{19}F-labeled peptides in macroscopically aligned lipid bilayer samples.

Introduction

The proposed scheme of orientational analysis of membrane-associated biomolecules in macroscopically oriented lipid bilayer samples was introduced in chapter I, the mathematical details of the envisaged data analysis scheme were demonstrated in chapter II. The present chapter focuses on material parameters that characterize the fluorine nucleus in ^{19}F-labeled amino acids. These are necessary to make the data analysis scheme applicable to ^{19}F-labeled biomolecules. It became evident in chapter I that knowledge of the CSA tensor's principal axis elements is vital for the proposed analysis scheme. Anisotropic chemical shift values measured on oriented samples can only be analyzed in structural terms once the principal elements of the corresponding CSA tensor are known.

A wide variety of ^{19}F-labeled amino acids can be incorporated into polypeptides by solid-phase peptide synthesis, and there are several amino acids which may even be used for biosynthetic labeling in *Escherichia coli*, such as fluoro-tryptophan[1;2], fluoro-phenylalanine, fluoro-tyrosine, and fluoro-leucine. Selective ^{19}F-labels in side chains may thus be used as highly sensitive probes to characterize the local conformation and dynamics. For certain cases, where a well-defined relation between the ^{19}F-label and the polypeptide backbone can be established, it is even possible to describe the orientation and mobility of a given secondary structure element in a lipid membrane. In order to make use of the advantages of ^{19}F-NMR detailed knowledge about the NMR parameters of the labels is necessary, which in most cases is not yet available. As a fundamental basis for further solid-state ^{19}F-NMR studies in biological systems we have therefore recorded and compiled the chemical shift anisotropies, isotropic chemical shifts, and relaxation properties of the most prominent polycrystalline amino acids.

The investigated polycrystalline fluoro-amino acids can be divided into three different categories: First, monoaromatic amino acids similar to the naturally occurring amino acid phenylalanine (Phe). Two derivatives of Phe, with fluorine substituted in *para*- and *meta*-positions, respectively, were investigated. Of principal interest in this study is the amino acid phenylglycine (Phg), which is not naturally incorporated into proteins and peptides, but offers

4-F-Phg 4-F-Phe 3-F-Phe 3-F-Tyr

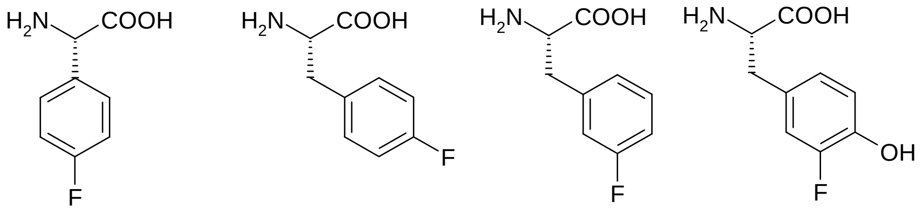

Figure 3.1: Structures of the investigated mono-fluorinated analogues of phenylglycine (Phg), phenylalanine (Phe), and tyrosine (Tyr, shown in each case are the L-stereoisomers).

the advantage of a rigid connection between the ^{19}F-label on the side chain and the peptide backbone (*cf.* chapter I, esp. figure 1.3 and 1.4). One analogue of Phg with fluorine substituted in ring position 4 was available. The last representative amino acid in this group is 3-fluoro-tyrosine, which differs from 3-F-Phe by an additional OH-substituent in *para*-position. The structures of the members of the first group are given in figure 3.1, together with the abbreviated names used to denote the substances in the following.

The second group comprises fluoro-derivatives of the naturally occurring amino acid tryptophan, which has the heteroaromatic indole group as its side chain. Tryptophan analogs with fluorine substituents in 5- and 6-position were available, both as L-isomer as well as in DL-racemic mixture. Figure 3.2 gives the molecular structures and shorthand nomenclature.

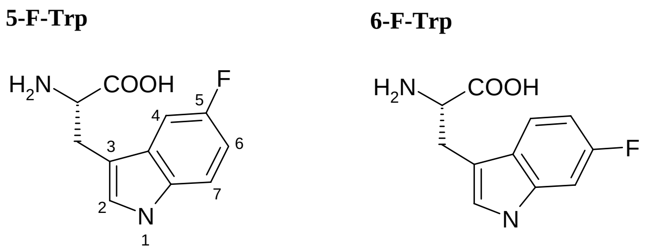

Figure 3.2: Structures of the investigated mono-fluorinated tryptophan analogs (shown are the L-stereoisomers)

The third and final set of fluoro-amino acids investigated here comprises a number of aliphatic derivatives. One analog each of alanine and valine was available with fluorine substituents in the side chain methyl groups. Of leucine, a number of analogs with fluorine or deuterium substituents or both in one side chain methyl group were kindly provided by D. Young (Univ. of Sussex, UK). Comparison with the deuterated analogs allowed to estimate the influence of heteronuclear dipolar coupling on the spectra. It could be assessed whether dipolar coupling to protons or to deuterons has more deleterious effect on ^{19}F-NMR spectra, and which influence is easier to suppress by continuous-wave decoupling on the respective frequency band. In addition, a fluorinated leucine with an additional Fmoc-protection group was included to determine the influence of the protecting group, especially the presence of a peptide bond, on fluorine nuclear magnetic properties. Figure 3.3. presents molecular structures of all investigated substances together with the names to be used in the following.

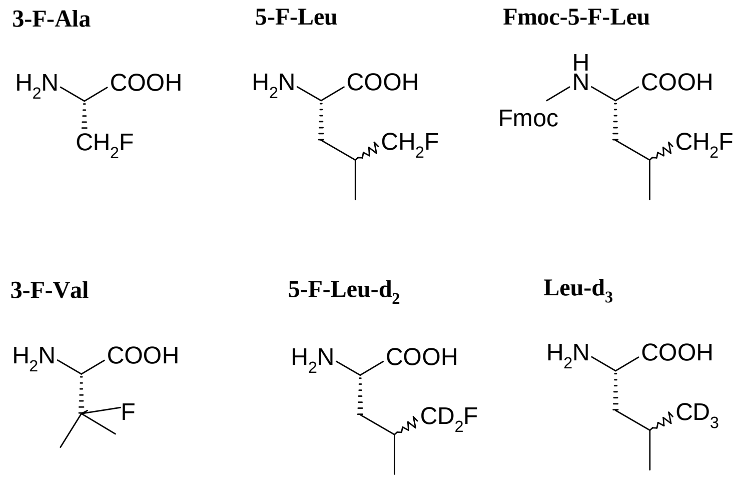

Figure 3.3: Structures of investigated mono-fluorinated aliphaticamino acids (shown are the L-stereoisomers)

Materials and methods

^{19}F-NMR spectroscopy

All polycrystalline ^{19}F-labeled amino acids were used as obtained from the suppliers cited in table 3.1. The leucine derivatives were synthesized by J.-D. Charrier and D. Young, as described previously.[3;4] 5-F-L-tryptophan was provided by T. A. Cross (Tallahassee, FL, USA) and 3-F-DL-phenylalanine was a gift from T. Asakura (Tokyo, Japan). Whenever multiple spectral components were found in ^{19}F-MAS spectra, purity was checked by ESI at the Institute of Organic Chemistry, Univ. Karlsruhe, and in all cases confirmed.

Solid-state ^{19}F-NMR spectra were recorded at 20°C on a wide-bore Bruker Avance spectrometer (Bruker Biospin GmbH, Rheinstetten, Germany) operating at a ^{19}F resonance frequency of 564.7 MHz. The double-tuned (^{19}F/^{1}H) Bruker 4 mm MAS probe allowed for 90°-pulses of 2.0 μs length and for proton decoupling at 40 kHz B_1 field strength. Static spectra were recorded using a Hahn echo sequence with an echo delay time of 25 μs, while MAS spectra were recorded at 12.5 kHz MAS frequency in a saturation recovery sequence. The spectral width was chosen to be 200 kHz. All ^{19}F-NMR spectra are referenced against $CFCl_3$.

Relaxation measurements (as well as the spectra of re-crystallized compounds in figure 3.4) were performed at 470.3 MHz ^{19}F resonance frequency on a Varian UnityInova spectrometer equipped with an Oxford instruments wide bore magnet. A double-tuned (^{1}H/^{19}F) static flat-coil probe from Doty Scientific (Columbia, SC, USA) with a typical ^{19}F 90°-pulse length between 2 and 3 μs was used. The T_1 values were mostly determined by inversion recovery (only in the case of very long T_1 by saturation recovery), and the T_2 data was measured from a standard Hahn echo experiment. A temperature range was covered from –60°C to +60°C with an accuracy of ±2°C.

Solution-state ^{19}F-NMR spectra were recorded on the same Varian UnityInova 500 MHz spectrometer at 25°C using a single-pulse sequence on a 5mm Varian solution probe.

Solid-state ^{2}H-NMR spectra were recorded at 76.8 MHz ^{2}H resonance frequency (corresponding to 500 MHz proton resonance frequency) on a Varian UnityInova wide bore spectrometer. A quadruple-tuned (^{1}H/^{19}F/X/Y) 5 mm MAS probe from Doty Scientific (Columbia, SC, USA) was used to apply a quadrupolar echo with 4.8 μs 90° pulse width and 25 μs echo delay time.

Spectral simulations

For spectral simulation of MAS lineshapes, the dedicated solid-state NMR software DMfit[5] was found to be less appropriate than the general, but more developed and reliable data analysis software Origin 7 (www.originlab.com). This was not due to DMfit's general design, which is very convincing, but to the imperfect and unreliable implementation. Origin, on the other hand, reaches its limits when too many lines need to be fitted to a MAS band, but was found to give sufficient performance for all spectra at hand. After import of data using

Origin's ONMR module (www.nmrtools.com), MAS spectra were fitted using an appropriate number of either Gaussian or Lorentzian lineshapes. The determined intensities of the MAS sideband patterns were subsequently analyzed to yield principal tensor components by means of the Herzfeld-Berger algorithm[6] as implemented in the program 'HBA', Version 1.2, written by Klaus Eichele (http://casgm3.anorg.chemie.uni-tuebingen.de/klaus/soft/).

Results

Solution-state ^{19}F-NMR of aqueous solutions

A list of all ^{19}F-labeled amino acids that were characterized in this study is compiled in table 3.1, together with information about their stereochemistry and source. Additionally, the ^{19}F-NMR parameters obtained in aqueous solution are summarized. The isotropic chemical shift values (σ_{iso}), J-coupling constants, and the types of multiplet were determined. The isotropic chemical shifts of ^{19}F cover a wide range from –60 ppm to –220 ppm, in accordance with literature values on related aliphatic and aromatic compounds.[7;8]

Table 3.1: Properties of the investigated ^{19}F-labeled amino acids in aqueous solution

Substance	Stereoch.	Source	σ_{iso} [ppm]	^{1}J [Hz]	^{2}J [Hz]	type of spectrum
Phe, Phg, Tyr						
4-F-Phe	L	Fluka	-115.76	8.5	4.5	triplet of triplets
	DL	Fluka	-115.67	./.	./.	not resolved[a]
3-F-Phe	not det.	T. Asakura	-113.33	9.8	6.8	doublet of triplets
4-F-Phg	DL	Fluka	-112.55	8.8	4.5	triplet of triplets
3-F-Tyr	DL	Lancaster	-136.70	8.8	3.6	doublet of doublets
Trp						
5-F-Trp	L	T.A. Cross	-124.91	9.6	4.6	triplet of doublets
	DL	Lancaster	-124.82	./.	./.	not resolved[a]
6-F-Trp	L	T.A. Cross	-122.18	./.	./.	not resolved[a]
	DL	Acros	-121.70	9.4	5.3	triplet of doublets
aliphatic						
3-F-Ala	DL	Bachem	-229.20	47	29	triplet of doublets
5-F-Leu	(2S,4S)	D. Young	-221.62	48	20	triplet of doublets
5-F-Leu	(2S,4R)	D. Young	-220.83	46	21	triplet of doublets
Fmoc-5-F-Leu	(2S,4S)	D. Young	-221.10	47	20	triplet of doublets
5-F-Leu-d_2	(2S,4S)	D. Young	-222.94	6.8	--	octet
Leu-d_3	L	Cambridge Isotopes	--	--	--	--
3-F-Val	DL	Lancaster	-141.04	./.	./.	not resolved[a]

[a]data acquired on a 400 MHz spectrometer (IOC, Univ. Karlsruhe) did not provide necessary resolution as obtained at 500 MHz (Inst. of Mol. Biology, Univ. Jena).

Fluorine substituents on the phenyl rings of Phe or Phg resonate around –112 to –116 ppm. Whether fluorine is substituted in *para*- or *meta*-position has only a minor influence on the observed chemical shift. Also, the chemical shifts observed on Phe and Phg do not show strong variation. In the situation of tyrosine, where the phenyl ring carries an additional hydroxyl group, the resonance shifts to –137 ppm. Fluorine substituents in the heteroaromatic inositol side chain of tryptophan resonate between frequencies of σ_{iso}=–121 ppm and –124 ppm. When substituted into a methyl group of an aliphatic amino acid, the isotropic chemical shift of the fluorine nucleus is observed between σ_{iso}= –220 ppm and –230 ppm. In the case of 3-F-Val, on the other hand, the chemical shift value of σ_{iso}=–141 ppm is caused by the fact that fluorine is substituted at a tertiary carbon site. The observed J-coupling values are also listed in table 3.1. Wherever they could be resolved on the two accessible spectrometers, the type of the observed multiplets meets the character expected from the molecular structures.

Polycrystalline powders show crystal polymorphism

Initially, the solid-state ^{19}F-NMR spectra of the polycrystalline powders of the fluorinated amino acids were recorded statically, using a flat-coil probe designed for macroscopically aligned lipid bilayer samples. Repeatedly, the recorded ^{19}F-NMR spectra did not exhibit the expected powder pattern or tensor spectral lineshape that were introduced in chapter I and are depicted in figure 1.9. This was especially worrying for most Trp-derivatives, of which a representative spectrum is shown in figure 3.4 at the bottom.

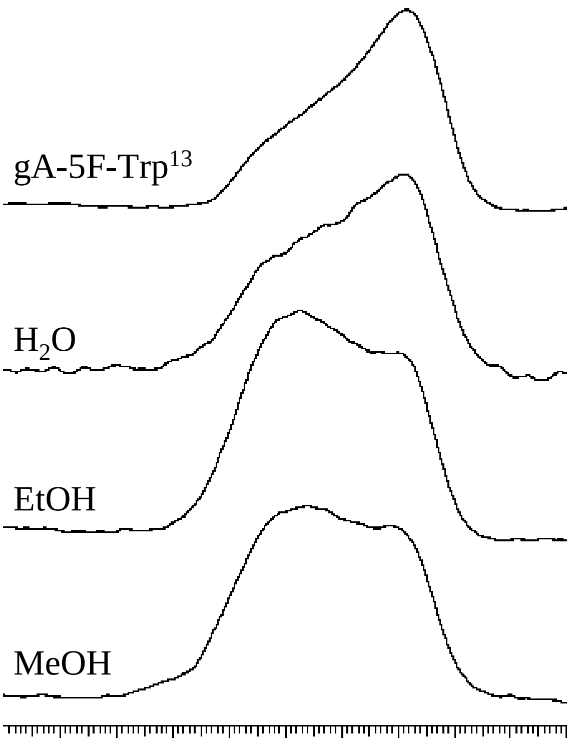

Figure 3.4: ^{19}F-NMR spectra of polycrystalline 5F-DL-Trp crystallized from different solvents, namely methanol, ethanol and water (bottom to top). At the very top, the spectrum of a lyophilized gramicidin A analog labeled with 5F-Trp in position 13 is shown for comparison and to demonstrate the far better lineshapes observed on peptide lyophilates.

To determine the origin of the unusual lineshapes, lyophilization was attempted for a few fluorinated amino acids in order to homogenize the samples. This process did not improve the spectra but yielded completely shapeless spectral lineshapes, reflecting an even more erratic atomic environment in a lyophilate. It has to be noted, though, that this observation does not hold true for lyophilized *peptide* samples. The topmost spectrum in figure 3.4 shows the ^{19}F-NMR spectrum of a lyophilized 5F-Trp-labeled analog of the antimicrobial peptide gramicidin A, which exhibits an almost perfect (although strongly broadened) tensor lineshape.

Another approach taken to generate homogeneous samples was re-crystallization from different solvents. Figure 3.4 shows ^{19}F-NMR spectra of polycrystalline 5F-DL-Trp recrystallized from three different solvents, namely methanol, ethanol, and water. The three spectra show strongly

deviating lineshapes, with at least two distinguishable spectral components present. Only the material re-crystallized from H_2O resembles the spectrum of 5F-Phg in the lyophilized peptide shown at the top. It can be concluded that different crystal modifications are present in the polycrystalline material and are the cause of the multi-component lineshape. This is in consistence with a previous report that phenylalanine forms different crystals when re-crystallized from H_2O or MeOH/H_2O, respectively.[9]

Other possible causes for an involved spectral shape include complex motional properties of 5F-Trp molecules in their crystal sites and dipolar coupling between ^{19}F nuclei that are in close spatial proximity in the crystal lattice. The latter would be consistent with a crystal structure determined on unlabeled tryptophan, where the corresponding carbons in 6-position were found to be in close spatial proximity of 4.05 Å.[10] Since the structure was determined in X-ray crystallography, no hydrogen positions are resolved. But from inspection of the unit cell, the H_6 nuclei should be in even closer spatial proximity than their respective carbons. No exact distance is reported for the C_5 position, but visual inspection shows both C_5 to be further apart, at around 5 to 6 Å distance. However, motional properties and dipolar coupling can be ruled out in the present case, since they should not be changed after re-crystallization. Dipolar coupling is also considered unlikely, since a co-crystallization assay of 5F-DL-Trp with unlabeled Trp at a molar ratio of 1:10 still yielded comparable involved lineshapes.

The initial hope to isolate a single 'good' crystal modification by re-crystallization was not further pursued since none of the modifications would be in any way preferable to or more meaningful than the other ones. Also re-crystallization was found to be a time-consuming task which does not necessarily lead to perfectly clean tensor spectra, as evident from figure 3.4.

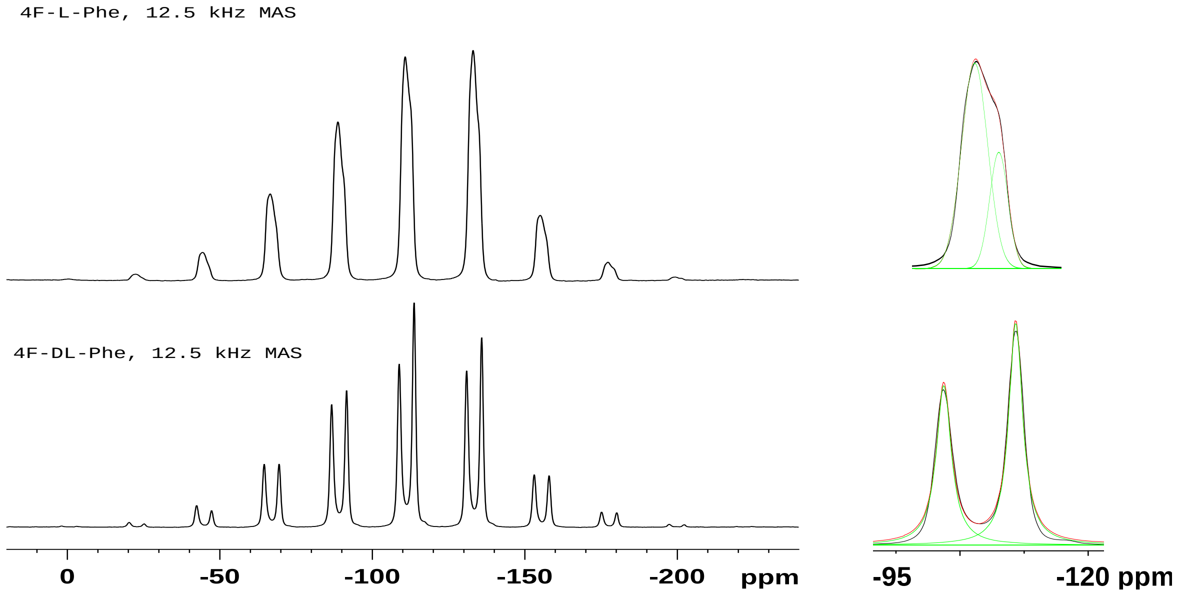

Figure 3.5: (Left) ^{19}F-NMR MAS spectra of 4F-Phe in pure L form and racemic mixture, showing presence of multiple components that could be resolved in MAS spectra at 564.7 MHz ^{19}F resonance frequency. (Right) Best-fit analysis of central lines using Gaussian (top) or Lorentzian (bottom) model lineshapes (central lines shown only).

MAS spectra allow for separation of multiple ^{19}F-CSA tensors

Instead of preparing an individual defined crystal modification, it proved possible to separate different spectral components by use of MAS ^{19}F-NMR. An essential prerogative was the availability of a high-field magnet at 14.1 T, giving a ^{19}F resonance frequency of 564.7 MHz. Figure 3.5 shows MAS spectra of 4F-Phe both as pure L-enantiomer and as DL-racemic mixture, where multiple sets of MAS sideband patterns are sufficiently resolved. Hodgkinson and Emsley[11] have shown that the CSA tensor principal values are most reliably determined by fitting MAS spectra with two or three spinning sidebands on either side of the isotropic line. Therefore, ^{19}F-NMR spectra were recorded at 12.5 kHz MAS and fitted using the Origin 7 data analysis software. Shown to the right of figure 3.5 are fits of Gaussian lineshapes to the central lines of the spectra.

Extracted ^{19}F-NMR parameters of polycrystalline powders

The sideband intensities were further analyzed to determine CSA tensor principal components by use of the Herzfeld-Berger algorithm.[6] The characteristic values thus determined are compiled in table 3.2, both as principal tensor components and in terms of isotropic chemical shift δ_{iso}, anisotropy δ, and asymmetry η, as introduced in equations (1.6-8). Given are the values obtained in fits with a Gaussian lineshape. The results from each individually resolved sideband pattern are reported in a separate line of the table, where appropriate. Alternative fits using Lorentzian lines gave deviations below 0.5 ppm wherever three or more sidebands could be fitted on each side of the isotropic line. The error inherent in the spectral signal-to-noise and other imperfections will add to this, so we estimate the overall error to be in the order of ± 2 ppm. In the case of fluorinated leucine analogs, only two sidebands were available, with the outmost one having only very little intensity. Here, deviations between Gaussian and Lorentzian linefits produced deviations of around 10% relative error. We assign this to the unsatisfactory number of fitted sidebands rather than to the different model lines fitted.

The isotropic chemical shift values determined in the solid-state and in aqueous solution tend to be very similar within a couple of ppm in most cases, but they may differ by up to 10 ppm. For other isotopes a closer agreement between NMR in the solid-state and in solution is usually observed, but the ^{19}F nucleus is known to be particularly sensitive towards its local environment.[7] The three lone pairs of electrons of the ^{19}F-substituent are strongly affected by the packing in a crystalline environment, by the polarity and type of solvent, by hydrogen-bonding effects, and by temperature.

The isotropic chemical shift values of the Phe-type fluorinated amino acids are centered around σ_{iso}=-110 ppm, with the exception of Tyr, where the additional OH-substituent moves the value to σ_{iso}=-135.1 ppm, in good agreement with the data in aqueous solution. Large spectral widths are found, characterized by an anisotropy δ ranging from 55 to 75 ppm. The asymmetry η of the CSA tensors has fairly large values between 0.65 and 0.97. For all parameters, the differences are found to be more pronounced between crystal modifications than between different related substances, indicating that the crystal environment has as dominant an influence as the chemical structure.

Table 3.2: Solid-state ^{19}F-NMR parameters extracted from MAS spectra at 20°C using Herzfeld-Berger analysis based on Gaussian linefits of sideband patterns.

Substance	Stereo-chem.	σ_{11} [ppm]	σ_{22} [ppm]	σ_{33} [ppm]	δ_{iso} [ppm]	δ [ppm]	η	T_1 [s]	T_2 [µs]
Phe-like									
4-F-Phe	L	-51.9	-118.4	-162.0	-110.8	58.9	0.74	352± 12[a]	33.8± 0.8
		-41.6	-124.5	-171.4	-112.5	70.9	0.66		
	DL	-48.4	-114.2	-164.0	-108.9	60.5	0.82	75.5±3.0	40.6±7.2
		-56.7	-120.9	-163.8	-113.8	57.1	0.75		
3-F-Phe	not det.	-54.7	-115.2	-156.5	-108.8	54.1	0.76	91± 11	39.4± 3.8
		-55.7	-121.3	-158.4	-111.8	56.1	0.66		
		-57.6	-123.4	-159.6	-113.5	55.9	0.65		
4-F-Phg	L	-46.6	-109.3	-168.8	-108.2	61.6	0.97	7.68±0.27	37.8±3.2
		-51.6	-117.5	-162.7	-110.6	59.0	0.77		
		-55.4	-125.8	-161.7	-114.3	58.9	0.61		
	DL	-53.1	-118.7	-165.0	-112.2	59.2	0.78	36.6± 4.7	23.6± 1.2
3-F-Tyr	DL	-79.9	-115.7	-209.7	-135.1	-74.6	0.48	14.9± 0.7[a]	25.4± 5.4
Trp									
5-F-Trp	L	-70.9	-146.8	-148.7	-122.1	51.2	0.04	133.6± 4.5	37.6± 0.8
	DL	-77.5	-148.2	-148.2	-124.6	47.1	0.00	27.5± 1.2	42.0± 1.1
6-F-Trp	L	-66.9	-127.5	-162.6	-119.0	52.1	0.67	52.3±5.4	31.4±5.2
	DL	-67.7	-125.7	-163.9	-119.1	51.4	0.74	104.8± 6.3	26.7± 1.7
aliphatic									
3-F-Ala	DL	-200	-235	-263	-232.7	-33	0.84	19.5± 1.1 17.3± 1.6	14.7± 0.3
5-F-Leu	(2S,4S)	-205	-218	-240	-221.4	-19	0.68	0.38± 0.03	54.0± 5.1
5-F-Leu	(2S,4R)	-213	-224	-231	-222.4	10	0.72	0.52± 0.03	41.4± 3.2
Fmoc-5-F-Leu	(2S,4S)	-175	-200	-240	-204.9	-4	0.71	3.3± 0.6	33.6± 1.4
5-F-Leu-d_2	(2S,4S)	-216.1	-226.5	-253.1	-231.9	-21.2	0.49	1.62± 0.03	36.2± 3.1
		-215.6	-235.0	-260.6	-237.1	-23.5	0.82		
3-F-Val	DL	-117.6	-131.6	-176.5	-141.9	-34.6	0.40	2.05±0.04	36.0±0.3

[a]obtained at 0°C

In the fluoro-derivatives of Trp, isotropic chemical shift values around σ_{iso}=-120 ppm were observed, each being about 2 ppm higher than the value in aqueous solution. All anisotropies δ amount to around 50 ppm. For the value of η, however, a remarkable difference between the analogues substituted in 5- and 6-position is found. The 5-flourine labeled analogues display a very small asymmetry $\eta\approx0$ (as reflected in the almost symmetric tensor lineshapes of figure 3.4), while both 6-labeled analogues have a rather high asymmetry around $\eta\approx0.7$. In both 6F-Trp analogues the MAS lines consist of two components, which are heavily overlapped and could not be resolved by linefitting. Therefore, here the error found in the tensor principal values is considerably larger than for the other amino acids. Still, static spectra clearly confirm the higly asymmetric nature of the corresponding ^{19}F CSA tensors. Considering this fact, an new explanation may be offered for the peculiar lineshapes of figure 3.4: Two superimposed powder lineshapes of $\eta\approx0$ and $\eta\approx1$ with comparable intensities may lead to the unusual spectral lineshapes.

In all analogues of aliphatic amino acids, a small anisotropy parameter δ was found, which made the determination of principal tensor components less reliable. Only in the case of 5F-Leu-d_2, a sufficient number of MAS sidebands was achievable. Therefore, for the other Leu-analogs a linefit to static tensor spectra was necessary, making the results less accurate. The isotropic chemical shifts of singly-labeled alanine and leucine derivatives are centered around –220 ppm, their anisotropy parameters range between 10 and 30 ppm, and asymmetries are found between 0.4 and 0.9.

Polycrystalline vs. proteinaceous environment: 4F-Phg and 5F-Trp

Two of the ^{19}F-labeled amino acid derivatives investigated here were already successfully used as isotope labels in biomolecular solid-state ^{19}F-NMR studies, namely 4F-L-Phg and 5F-DL-Trp.[12;13] The former label plays a central role in the present thesis, since data acquired on two different membrane-active peptides carrying that label are investigated in chapters VI and VII. Here, some results of subsequent chapters are given in advance to allow for a comparison between CSA tensor characteristics observed in polycrystalline and in proteinaceous environment. In table 3.3 the parameters determined in polycrystalline pure 4F-Phg (indicated by gray shading in the table) are compared to chemical shift data found in the two mentioned antimicrobial peptides. Moreover, values predicted by the chemical shift prediction functionality of the COSMOS program (www.cosmos-software.de) are given for an isolated fluoro-phenyl side chain and for 4F-Phg in gramicidin S (*in vacuo*).

The isotropic chemical shift δ_{iso} of the 4F-Phg label covers a range of approx. 6 ppm and shows a stronger variability between the different crystal modifications than between the values found in proteinaceous environments. The anisotropy parameter δ is only somewhat reduced in the peptide environment, indicating that local molecular mobility within a peptide is surprisingly similar to the mobility within a crystal that is generally considered to be rigid. The anisotropy δ is larger in the α-helical structure of B18 than in the β-sheet environment of gramicidin S. This appears consistent with reduced mobility due to the far deeper energy profiles for the χ_1-torsion angle found for an α-helix, indicative of stronger steric hindrance. Note also that the δ_{22}-component in the more mobile gramicidin S side chain is shifted *away*

Table 3.3: CSA values measured on 4F-Phg as polycrystalline powder as well as incorporated in peptide-lyophilates or pdb-files

Substance	Condition	σ_{11} [ppm]	σ_{22} [ppm]	σ_{33} [ppm]	δ_{iso} [ppm]	δ	η
4F-L-Phg	polycryst.	-46.6 ... -55.4	-109.3 ... -125.8	-161.7 ... -168.8	-108.2 ... -114.3	58.9 ... 61.6	0.61 ... 0.97
	aq. sol.	--	--	--	-115.7	--	--
B18-(4F-L-Phg) [a]	lyophilized	-60.1	-124.3	-155.3	-113.2	53.1	0.58
gS-(4F-L-Phg) [b]	membrane-bound	-65.5	-126.5	-153.0	-115.0	49.5	0.54
F-phenyl [c]	COSMOS (*in vacuo*)	-45.6	-116.0	-164.0	-108.5	62.9	0.76
gS-(4F-L-Phg) [c]	COSMOS (*in vacuo*)	-53.8	-113.5	-174.0	-113.8	60.0	1.00

[a] *cf.* chapter VI, [b] Salgado J. *et al.*[13], [c] Dr. habil. Ulrich Sternberg, FZ Karlsruhe, personal communication

from the isotropic position, indicating that it is not affected by increased mobility. This indicates that the most prominent mode of mobility here is an oscillation about the $C_\alpha C_\beta$-bond,which does not influence the (parallel) δ_{22} component. COSMOS predicts δ for a fluoro-phenyl group to be almost identical for an isolated side chain when compared to a side chain attached to a gS molecule. This is not a contradiction to the reduction in spectral width just reported, since COSMOS does not account for molecular mobility. Therefore, it can be concluded that the reduction of δ observed in a peptide environment is due to the motional properties of that environment rather than to subtle changes in the shielding orbitals. The most strongly varying parameter is the tensor asymmetry η, which covers the whole range between η=0.5 and the maximum η=1.

Another fluorinated amino acid, 5F-L-Trp, was previously investigated in proteinaceous environment. The powder spectrum of lyophilized gramicidin A containing 5F-Trp (from Grage S. *et al.*[12]) was shown at the top of figure 3.4. Table 3.4 compiles the available data, including a recent study on the 5F-Trp-labeled protein GB1 from our lab.[1;14] The observed isotropic chemical shift positions cover a range of 4 ppm. The tensor asymmetry in the proteinaceous environment is again only slightly reduced when compared to polycrystalline values. The asymmetry parameter η shows strong variability.

Table 3.4: CSA values measured on 5F-L-Trp as polycrystalline powder as well as incorporated in peptide-lyophilates or pdb-files

Substance	Condition	σ_{11} [ppm]	σ_{22} [ppm]	σ_{33} [ppm]	δ_{iso} [ppm]	δ	η
5F-L-Trp	polycryst.	-70.9	-146.8	-148.7	-122.1	51.2	0.04
	aq. sol.	--	--	--	-124.9	--	--
gA-13(5F-L-Trp)[a]	membrane-bound	-80.0	-141.5	-156.5	-126.0	46.0	0.33
gA-15(5F-L-Trp)[a]	membrane-bound	-81.0	-141.0	-157.5	-126.5	45.5	0.36
GB1-(5F-L-Trp)[b]	aq. sol.	--	--	--	-124.2	--	--
	lyophilized	-82.7	-140.2	-151.8	-124.9	-42.2	0.27

[a]Grage S. *et al.*[12], [b]Müller S.[14]

^{2}H-NMR of substituted methyl groups reveals rotational properties

The rotational mobility of a monofluoromethyl-group is further investigated by ^{2}H-NMR spectroscopy of two deuterated leucine analogues. Besides 5F-Leu-d_2, a leucine analogue carrying a tri-deutero-methyl group CD_3 was available, referred to as Leu-d_3 (molecular schemes are given in figure 3.3). The ^{2}H-NMR spectra of both compounds are shown in figure 3.6 (*cf.* the CF_3-group in 5,5,5-F_3-Leu in the next chapter). The deuterium relaxation times of 5F-Leu-d_2 are T_1=12.5 s ± 0.6 s and T_2=164.0 μs ± 5.0 μs, for Leu-d_3 they are T_1=57.5 ms and T_2=91 μs ± 18 μs.

It is clear from the size of the deuterium quadrupole splitting of around 120 kHz that the monofluoro-methyl group in polycrystalline 5F-Leu-d_2 is not engaged in any uniaxial rotation faster than the 10 μs timescale, in agreement with the non-vanishing value of the asymmetry parameter, η=0.49...0.82, found in ^{19}F CSA tensors. In contrast, however, Leu-d_3 undergoes fast rotational diffusion, confirming earlier results on alanine-d_3.[15] These different mobilities are attributed to the broken symmetry of the monofluoro-methyl rotor, which is distorted by the heavy ^{19}F substituent.

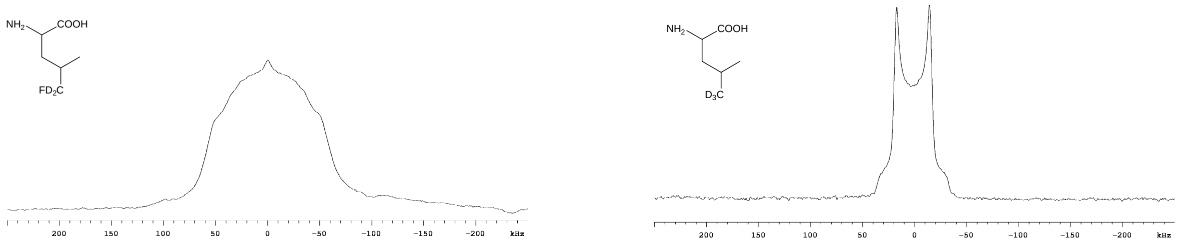

Figure 3.6: ^{2}H-NMR spectra of deuterated leucine analogs 5F-(2S,4S)-Leu-d_2 (left) and Leu-d_3 (right).

Since ^{1}H-decoupling of ^{19}F-NMR spectra is technically rather demanding in view of the close proximity to the ^{19}F resonance frequency, the substitution of geminal protons by deuterons seems a promising alternative to achieve line-narrowing. However, we found that ^{1}H-decoupling with only 40 kHz produced much better line-narrowing in the ^{19}F-NMR spectra of 5F-Leu than the effect of deuteration in 5F-Leu-d_2. This observation is not unexpected in view of the close packing of many protons around any ^{19}F-label in a crystal lattice. Furthermore, it turned out that neither ^{1}H-decoupling nor ^{2}H-decoupling alone had much impact on the linewidth in the ^{19}F-spectra of deuterated 5F-Leu-d_2. The spectra of protonated 5F-Leu, on the other hand, were significantly narrowed by ^{1}H-decoupling. Therefore, even at the comparatively low decoupling field strengths available on the probe used in this work, ^{1}H-decoupling of adjacent protons yields better results than partial deuteration, in accordance with earlier observations by Grage *et al.*[12]

Spin-spin- and spin-lattice relaxation of polycrystalline powders

The longitudinal relaxation times T_1 are displayed as a function of temperature in the range of –60°C to +60°C in figure 3.5 for the aromatic and in figure 3.6 for the aliphatic ^{19}F-labeled amino acids. The values of T_1 and T_2 at 20°C are explicitly stated in table 3.2. For the T_2 relaxation times, no significant temperature dependence was found, and the T_2 values do not

differ much amongst the various amino acids. They are most likely dominated by the strong dipolar couplings to the ubiquitous protons.

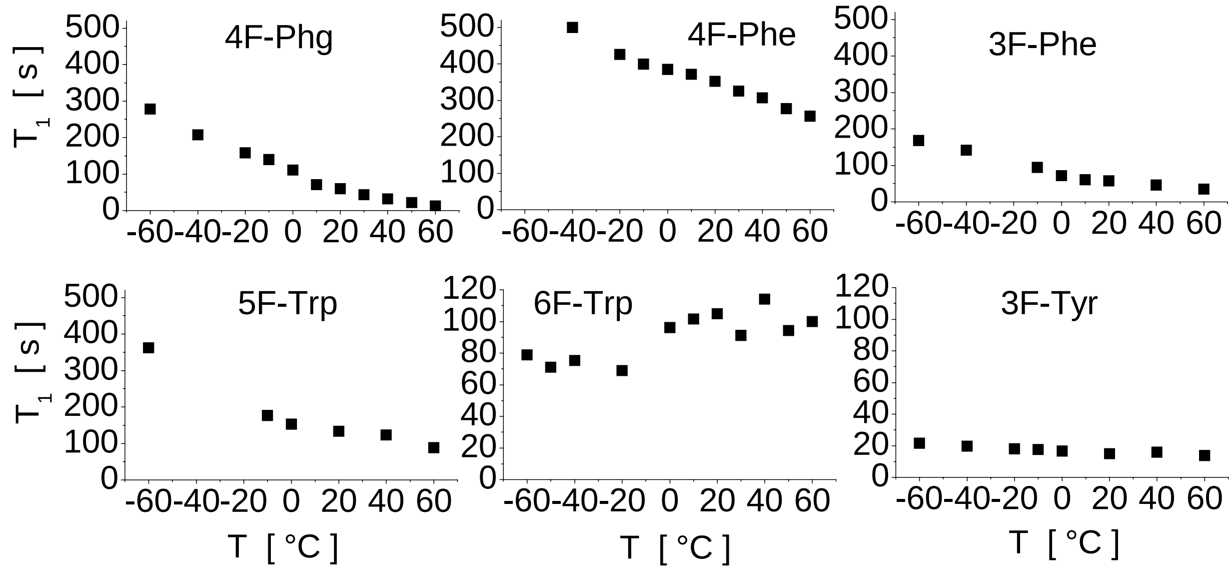

Figure 3.7: Temperature dependence of spin-lattice-relaxation in fluoro-derivatives of aromatic amino acids

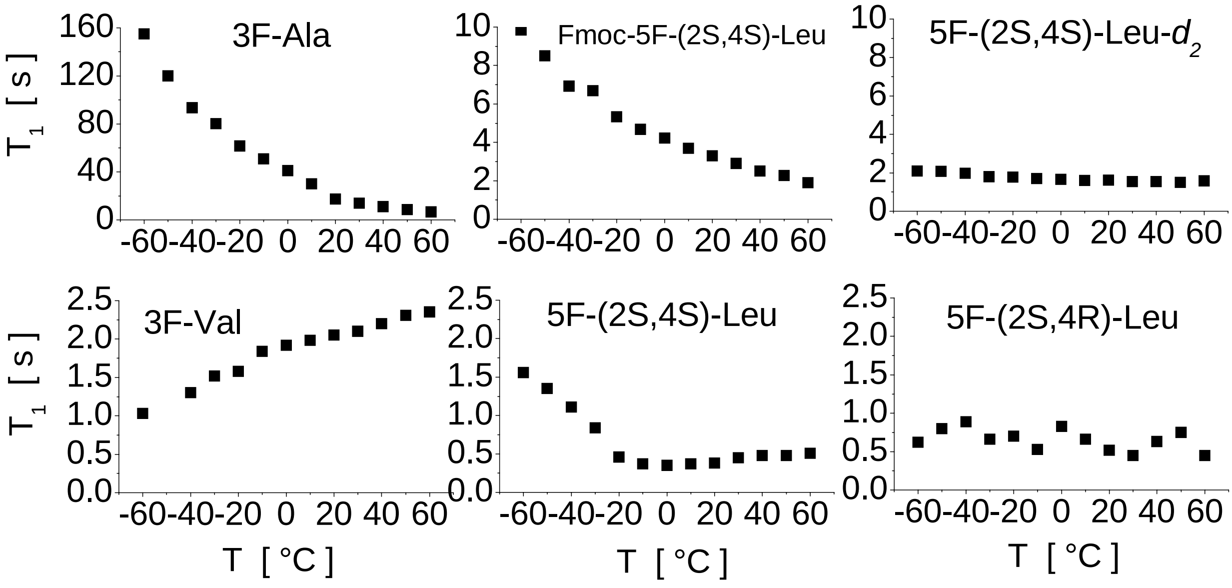

Figure 3.8: Temperature dependence of spin-lattice-relaxation in aliphatic amino acid derivatives

In contrast, the T_1 relaxation times possess a pronounced temperature dependence and vary over two orders of magnitude amongst the different types of amino acids investigated here. Particularly long T_1 relaxation times were observed for some of the aromatic ^{19}F substituents, especially at low temperature. These long T_1 values of several 100 s suggest a virtually complete lack of motion of the stacked aromatic rings. The singly-labeled aliphatic amino acids also show decreasing T_1-values with decreasing temperature. The terminal ^{19}F-substituent on the various leucine analogs has rather short relaxation times around 1s, being considerably more mobile than the substituent on alanine. On lyophilized and membrane-bound peptides, similar or even shorter T_1 relaxation times around or below 1 s are typically observed. The dominant mechanism for T_1 relaxation is found in the broad range of chemical shifts experienced by each ^{19}F nucleus. Dipolar coupling can be excluded as relaxation mechanism, since heteronuclear coupling to protons is suppressed by continuous wave

decoupling, and no evidence of homonuclear coupling is found in the spectra. The width of CSA fluctuations experienced by a fluorine nucleus is of comparable width for most compounds. Therefore, the reason for the strongly differing T_1 values needs to be sought in strongly differing mobility properties within the investigated polycrystalline material.

Summary and discussion

A database of NMR parameters for the most prominent ^{19}F-labeled amino acids was compiled to lay the grounds for further biological applications of solid-state ^{19}F-NMR. The reported values of the principal CSA components as well as the isotropic chemical shifts were found to be very similar to values in polypeptides in the case of 4F-Phg and 5F-Trp, showing that these values are directly transferable with considerable accuracy. An exception was found in the case of 6F-Trp, where the tensor asymmetry η exhibits a strongly differing high value. Taken on its own, this database has already provided some useful insight into the typical scatter and accuracy of ^{19}F-NMR parameters in different environments. For example, polycrystalline powders were compared with aqueous solutions, different stereoisomers of the same compound were compared that are affected by different crystal packing effects, and the subtle influence of protonated vs. deuterated neighbors was assessed.

In a considerable number of the investigated polycrystalline powders, strong crystal polymorphism was found, which caused stronger changes in tensor values than compared to the values found in proteinaceous environment. In the case of T_1 and T_2 relaxation times, it will not be possible to transfer the data from polycrystalline amino acids directly to the side chains in polypeptides, but the database provides a valuable reference for examining the different relaxation mechanisms of ^{19}F in the solid state.

The principal CSA values and isotropic chemical shifts can now be used to design solid state ^{19}F-NMR experiments, where it is essential to assess the feasibility of the measurement before producing any labeled material. For example, the distance measurements using rotational resonance rely on the spectral overlap of the chemical shift tensors and on the matching of the spinning speed to the isotropic chemical shift difference of the two labels. Similarly, to study the mobility of ^{19}F-labeled side chains in polypeptides by analysis of their CSA widths, it is straightforward to compare the resulting data with the immobilized CSA tensors provided here. Likewise, the orientation of a side chain with respect to the plane of a biological membrane can be extracted by lineshape analysis of oriented samples on the basis of the CSA data provided here. Suitable ^{19}F-labels can thus be incorporated into peptides and proteins by solid phase synthesis or biosynthetically, according to the demands of the experiment and the structural questions to be addressed.

Reference List

(1) Campos-Olivas, R.; Aziz, R.; Helms, G. L.; Evans, J. N. S.; Gronenborn, A. M. *FEBS Letters* **2002**, *517*, 55-60.

(2) Gakh, Y. G.; Gakh, A. A.; Gronenborn, A. M. *Magn.Reson.Chem.* **2000**, *38*, 551-558.

(3) Feeney, J.; McCormick, J. E.; Bauer, C. J.; Birdsall, B.; Moody, C. M.; Starkmann, B. A.; Young, D. W.; Francis, P.; Havlin, R. H.; Arnold, W. D.; Oldfield, E. *J.Am.Chem.Soc.* **1996**, *118*, 8700-8706.

(4) Charrier, J.-D.; Hadfield, D. S.; Hitchcock, P. B.; Young, D. W. *Org.Biomol.Chem.* **2004**, *2*, 797-802.

(5) Massiot, D.; Fayon, F.; Capron, M.; King, I.; Le Calvé, S.; Alonso, B.; Durand, J.-O.; Bujoli, B.; Gan, Z.; Hoatson, G. *Magn.Reson.Chem.* **2002**, *40*, 70-76.

(6) Herzfeld, J.; Berger, A. E. *J.Chem.Phys.* **1980**, *73*, 6021-6030.

(7) Berger, S.; Braun, S.; Kalinowski, H.-O. *NMR-Spektroskopie von Nichtmetallen; Band 4: 19F-NMR Spektroskopie*; Georg Thieme Verlag: Stuttgart, 1992.

(8) Brey, W. S.; Brey, M. L. Fluorine-19 NMR; In *Encyclopedia of NMR*; Grant, D. M., Harris, R. K., eds. Wiley: New York, 1996; pp 2063-2071.

(9) Frey, M. H.; DiVerdi, J. A.; Opella, S. J. *J.Am.Chem.Soc.* **1985**, *107*, 7311-7315.

(10) Bakke, O.; Mostad, A. *Acta Chem.Scand.B* **1980**, *34*, 559-570.

(11) Hodgkinson, P.; Emsley, L. *J.Chem.Phys.* **1997**, *107*, 4808-4816.

(12) Grage, S. L.; Wang, J.; Cross, T. A.; Ulrich, A. S. *Biophys.J.* **2002**, *83*, 3336-3350.

(13) Salgado, J.; Grage, S. L.; Kondejewski, L. H.; Hodges, R. S.; McElhaney, R. N.; Ulrich, A. S. *J.Biomol.NMR* **2001**, *21*, 191-208.

(14) Müller, S. *In vivo* Markierung der Proteine GB1 und TatA mit Fluorderivaten aromatischer Aminosäuren. Diploma thesis, Universität Karlsruhe (TH), 2004.

(15) Beshah, K.; Olejniczak, E. T.; Griffin, R. G. *J.Chem.Phys.* **1987**, *86*, 4730-4736.

IV. ^{19}F-NMR of CF_3-groups

This chapter extends the collection of fundamental fluorine material parameters started in the previous chapter towards amino acids substituted with a CF_3-group. In addition, experimental challenges are addressed which are posed by simultaneous presence of CSA and dipolar interaction within the CF_3-group.

Introduction

As an alternative to a single fluorine substituent, a CF_3-group may also serve as an isotope label in solid-state ^{19}F-NMR of biomolecular systems. Compared to the isolated fluorine nucleus, a number of advantageous properties are expected from this group. Aside from its 3-fold increased sensitivity, it offers the advantage of fast rotational averaging around the CF_3-axis of symmetry. The motional averaging projects the anisotropic interaction tensors onto the symmetry axis and makes the observed interaction independent of the side chain conformation given by the torsion angle χ_1 (*cf.* chapter I, esp. figure 1.4).

A complex lineshape is expected for the static ^{19}F-NMR spectrum of a CF_3-group in an unoriented polycrystalline or genererally unordered sample. Figure 4.1 gives a prototypical powder spectrum simulated for a single-pulse experiment, i.e. free from spectrometer distortions. Its convoluted lineshape is governed by the simultaneous presence of CSA and homonuclear dipolar coupling. Indicated in the figure are the characteristic 'landmark' frequencies, i.e. characteristic features of the spectrum that are governed by the strength of the respective interaction. The underlying CSA interaction is displayed at the bottom of figure 4.1 in black. It obeys the $(3\cos^2\theta\text{-}1)/2$ dependency of equation (1.9) for an asymmetry of $\eta=0$. The 0°- and 90°-edges of the corresponding powder pattern are marked as $\sigma_{\parallel}$ and $\sigma_{\perp}$ in figure 4.1, respectively. In addition to the CSA, the ^{19}F-^{19}F dipolar coupling leads to a splitting whose magnitude follows the same functional dependency as given by equation (1.10). Spectral features corresponding to the underlying triplets defining the edges of the 0°

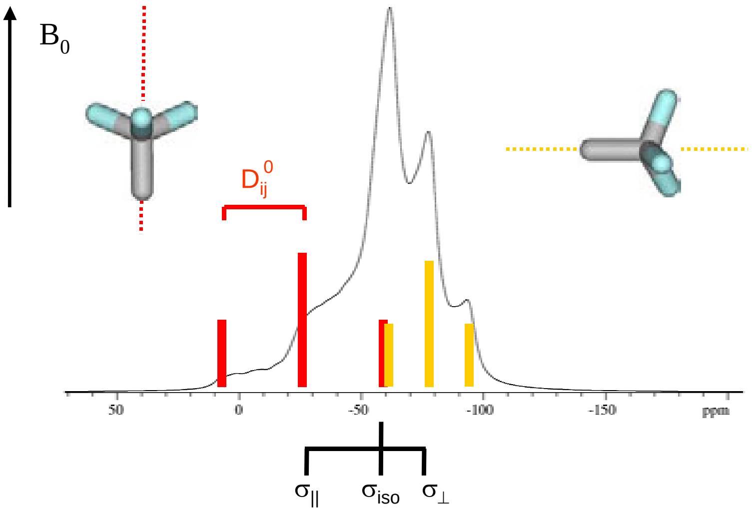

Figure 4.1: Prototypical spectrum of a CF_3-group in a hypothetical one-pulse experiment, calculated using the SIMPSON simulation package.

and 90° orientations of the CF_3-groups can easily be identified. Dipolar coupling reaches its maximum value, D_{ij}^{0}, when the CF_3-axis of symmetry is aligned parallel to the external magnetic field, B_0. This maximum coupling value on the '0°-edge' of the spectrum is indicated in red color in figure 4.1. On the other edge of the 'CSA spectrum', the '90°-edge', an equivalent triplet at half the splitting is observed, marked in yellow in the figure. It is caused by CF_3-groups whose symmetry axis is aligned perpendicularly to the magnetic field. Statistically, this orientation is found most often, therefore the spectrum shows maximum intensity on the 90°-edge.

Due to the presence of both interactions at almost equal magnitude, the center line is almost fixed in its resonance frequency at σ_{iso} because CSA and dipolar interaction cancel, while the outmost line of the spectrum covers a spectral range of approximately 120 ppm between the two extreme orientations, because CSA and dipolar interaction add up. Note that the interaction magnitudes in figure 4.1 were chosen corresponding to the ones reported for actual CF_3-groups below, where they were extracted by spectral analysis of convoluted lineshapes. The fact that CSA and dipolar interaction are present at equal strength is by no means self-evident, but is a peculiar coincidence that is closely related to the special field strengths of 500 and 600 MHz used in the available spectrometers. The equal magnitude of CSA and dipolar coupling gives rise to the effect of differential relaxation described in detail in chapter VIII.

One of the main objectives of this thesis is to explore the viability of the CF_3-group as biomolecular label. The subsequent chapter V will explore the physical properties of two CF_3-groups interacting over an intermedia te distance, while the closing chapter VIII presents a first three-dimensional structure analysis based on CF_3-labeling of a membrane-active peptide, PGLa labeled with 4-CF_3-Phg. In the current chapter, we want to extend the aim of the preceding chapter to the CF_3-group, i.e. to determine fundamental ^{19}F-NMR parameters on polycrystalline CF_3-labeled amino acids, to provide a data collection to be used as reference in future studies. Additionally, the experiments to measure static specta of CF_3-groups need to be optimized.

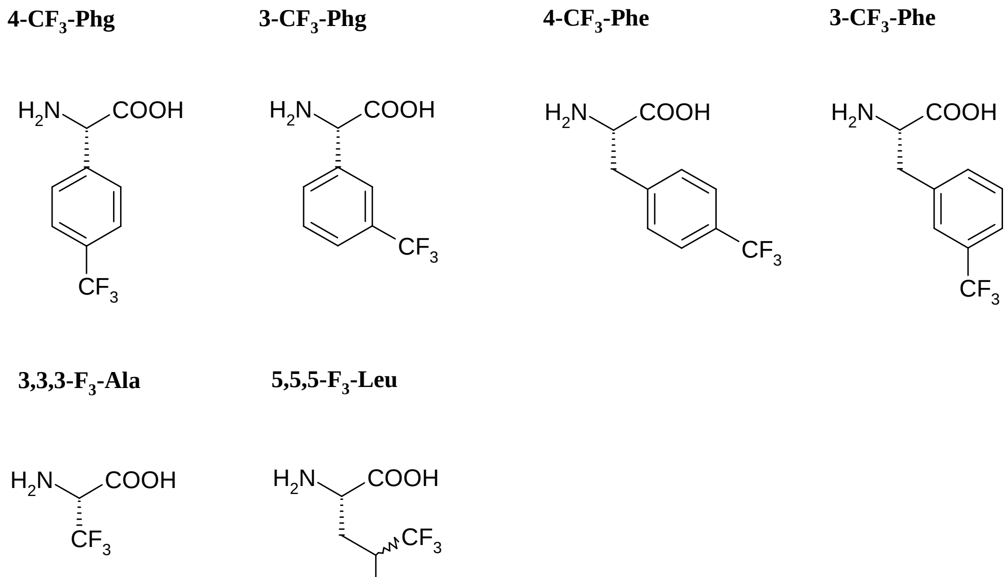

Figure 4.2: Molecular schemes of investigated CF_3-labeled amino acids (shown are the L-stereoisomers)

Under investigation were six CF_3-labeled amino acid derivatives, as shown in figure 4.2. Four of them are derivatives of aromatic amino acids, namely the naturally occurring phenylalanine (Phe) and its uncommon analog phenylglycine (Phg). Phg is of principal interest here, since its rigid stereochemistry with respect to the peptide backbone makes it an ideal NMR label to study the overall structural and conformational properties of a peptide. Both Phe and Phg were investigated with CF_3-substituents in *para*- and *meta*-positions on the phenyl group. Here, the influence of the slightly different chemistry as well as the effect of different substituent positions can be compared. In addition, CF_3-analogs of the two aliphatic amino acids alanine (Ala) and leucine (Leu) were investigated. 3,3,3-F_3-Ala- offers the same advantage of a rigid connection of the label to a peptide backbone and is currently used in our group for first labeling studies.

These six CF_3-carrying amino acids were examined as pure polycrystalline powders in static and MAS experiments, and relaxation properties were recorded. The simultaneous presence of CSA and dipolar coupling at equal magnitude complicates the application of common echo sequences to the CF_3-group, as described in detail in chapter I. Therefore, the polycrystalline CF_3-substituted amino acids were additionally used as model systems to study the behavior of the CF_3-group in different echo experiments. The principal components of the CSA tensor were extracted from the spectra by lineshape simulation and compared. In addition, the homonuclear dipolar coupling between the fluorine nuclei within a CF_3-group needed to be determined to completely describe the observed spectra.

Materials and methods

^{19}F-NMR spectroscopy

All investigated substances were obtained as racemic mixtures from the suppliers listed in table 4.1 and used without further purification. Whenever multiple spectral components were found in ^{19}F-MAS spectra, purity was checked by ESI and in all cases confirmed.

Solid-state ^{19}F-NMR spectra were recorded at 25°C on two Bruker Avance spectrometers (Bruker Biospin GmbH, Rheinstetten, Germany) operating at ^{19}F resonance frequencies of 564.7 MHz (all MAS spectra) and 470.3 MHz (spectra shown in figure 4.3 to test different pulse sequences). Measurements at 564.7 MHz were carried out as described in the preceding chapter III. Measurements at 470.3 MHz employed a triple-tuned (^{1}H/^{19}F/X) Bruker 2.5 mm HFX-MAS probe with a 90°-pulse width of 1.8 μs and proton decoupling was feasible at 40 kHz B_1 field. The tested pulse sequences were described in detail in chapter I. Solution-state ^{19}F-NMR and ^{19}F relaxation measurements were acquired as described in the preceding chapter III.

Spectral simulations

Spectral simulations were done using the SIMPSON spectral simulation package[1], which combines a compiled, speed-optimized back-end with a user-friendly front-end. The front-end requires the simulator to be familiar only with the simple, easy-to-learn scripting language Tcl[2], instead of an intricate compiler language such as C++. (Initial attempts were

undertaken to utilize the C++ library GAMMA[3] for spectral simulations, but this effort was not pursued further, since it calls for intricate C++ programming and it was not compatible with a new version of the gcc-compiler.)

The spectrum presented in figure 4.4 was simulated using a single-pulse experiment with a pulse-length of 2.0 μs, and powder averaging was performed using 678 crystallite orientations. An FID of 256 points was recorded at 4 μs dwell time, giving a spectral width of 250 kHz in the transformed spectrum. The recorded FID was elongated by zero-filling up to 8192 points and Fourier-transformed using exponential line broadening of 2.7 kHz.

MAS lineshapes were simulated by fitting Gaussian and Lorentzian lines using Origin 7 and subsequent analysis of intensities using the Herzfeld-Berger algorithm,[4] as described in detail in chapter III.

Results

Solution-state ^{19}F-NMR

All CF_3-labeled amino acids under investigation are listed in table 4.1, together with information on their chirality and supplier. Additionally, ^{19}F-NMR data obtained in aqueous solution are summarized. Isotropic chemical shift values (σ_{iso}), J-coupling constants, and the types of multiplet were determined. The isotropic chemical shifts of all CF_3-substituents on phenyl are found around –62 ppm with little variability, and around –72 ppm for CF_3-labeled aliphatic amino acids, in accordance with literature values on related compounds.[5;6] The observed J-coupling values and multiplets meet the character expected from the molecular structures.

Table 4.1: Properties of the investigated CF_3-labeled amino acids in aqueous solution (all as racemic D/L mixtures).

Substance	Source	σ_{iso} [ppm]	^1J / ^2J [Hz]	type of spectrum
4-CF_3-Phg	ABCR	-62.68	--	single line
3-CF_3-Phg	Ulrich lab	-62.57	--	single line
4-CF_3-Phe	ABCR	-62.35	--	single line
3-CF_3-Phe	T. Asakura	-62.38	--	single line
3,3,3-F_3-Ala	Chempur	-70.61	10	doublet
5,5,5-F_3-Leu	Lancaster	-73.43	140 / 19	doublet of doublets

4-CF_3-Phg gives best spectra in a single-pulse experiment

Unlike in solution, solid-state NMR spectra are usually acquired with echo experiments to overcome the problems associated with receiver dead-times and ringing. However, as outlined in detail in chapter 1, different echoes are required to refocus the CSA (180° Hahn echo) and the homonuclear coupling (90° quadrupolar echo), which are of comparable size in the CF_3-group. Therefore, to determine the lineshapes of the CF_3-group resulting from different types of pulse sequences, 4-CF_3-Phg was chosen as model substance since it is of most interest in the subsequent applications. Figure 4.3 shows ^{19}F-NMR spectra obtained on polycrystalline 4-CF_3-Phg in a single-pulse experiment as well as a Hahn and quadrupolar echo experiment. In addition, the quadrupolar echo sequence with EXORCYCLE phase cycling was tested, as proposed by Antonijevic and Wimperis[7] to deal with the simultaneous presence of CSA and dipolar coupling.

Application of the Hahn echo sequence to polycrystalline 4-CF3-Phg resulted in a heavily distorted spectrum, shown at the bottom of figure 4.3. Use of a quadrupolar echo did not show dispersive distortions, but yields a comparatively featureless spectrum, where especially the low-field 0°-edge is not sufficiently resolved. Application of EXORCYCLE phase cycling to the quadrupolar echo did not improve the spectrum (middle spectra in the figure). Unexpectedly, the application of a simple one-pulse experiment (with high power proton decoupling) yielded the most convincing lineshape, shown topmost in figure 4.3. Note that an important prerogative for this clear spectral shape was the availability of very short 90°-pulses of 1.8 μs in a Bruker 2.5 mm MAS probe. It does show slight distortions from the expected perfect lineshape given in figure 4.1, but clearly gives the best resolution of the spectral landmarks and has no dispersive distortions.

In conclusion, a basic single-pulse experiment was found to give far superior spectra when compared to any echo sequence. This alleviates common concerns that the transmitter dead time following a high-power r.-f. pulse prohibits acquisition of a satisfactory FID. The spectrum presented here demonstrates that spectrometer hardware today has overcome that obstacle.

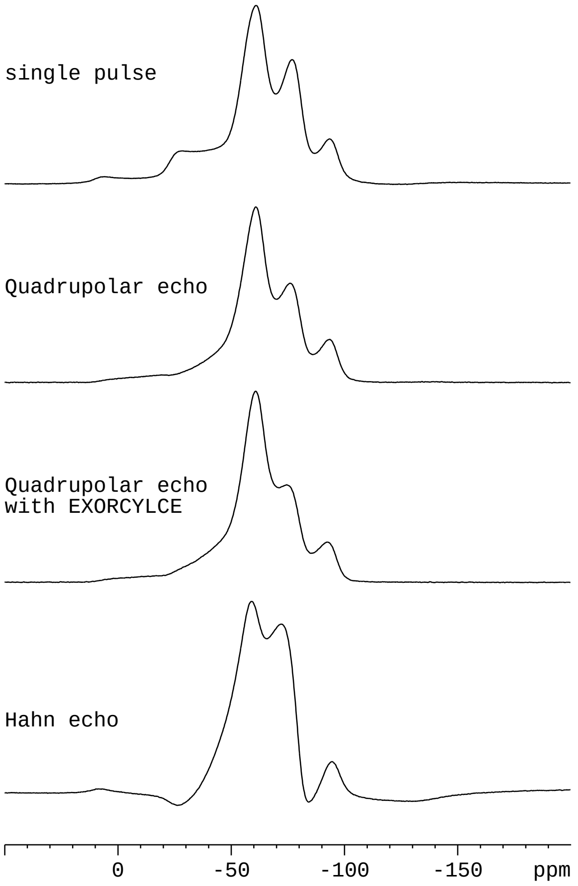

Figure 4.3: Spectra obtained on poly-crystalline 4-CF_3-Phg in different types of experiments

Spectral simulation of the 4-CF_3-Phg ^{19}F-NMR spectrum

The SIMPSON spectral simulation package was used to calculate the ^{19}F-NMR spectrum of 4-CF_3-Phg corresponding to a single-pulse experiment.[1] Fitting had to be done by visual inspection, since iterative fitting did not converge due to the low spectral intensity in the 0°-edge. This edge does not enter the error function sufficiently and thereby prohibits that the fit reproduces this core feature of the lineshape. Figure 4.4 shows experimental and simulated spectra in comparison. Obviously, the simulated lineshape reproduces the experimental one well, but not perfectly. This deviation is not due to pulse sequence imperfections, as systematic investigation of the influence of pulse sequence parameters on the simulated spectrum revealed. Neither an inclusion of transmitter dead time, nor consideration of the width of real pulses, nor carrier frequency were able to perfectly reproduce the experimental lineshape. Neither are crystal imperfections the cause, as MAS spectra (figure 4.5) did not reveal any crystal polymorphism, and lyophilization of the material severely deteriorated the original spectra. Therefore, we conclude that statistical distributions in crystal properties, especially a distribution in CSA principal values and dipolar coupling values, cause the deviation from the theoretically expected spectrum. This hypothesis is supported by the unusually high value of exponential linebroadening of 2.7 kHz that needs to be chosen in the simulation to reproduce the experimental spectrum. Another possible cause for the non-perfect fit may be found in relaxational properties that SIMPSON is not able to take into account. Nonetheless, the simulation adequately reproduces the landmark features of the experimental spectrum, and thus gives a reliable determination of the mean values of the polycrystalline material.

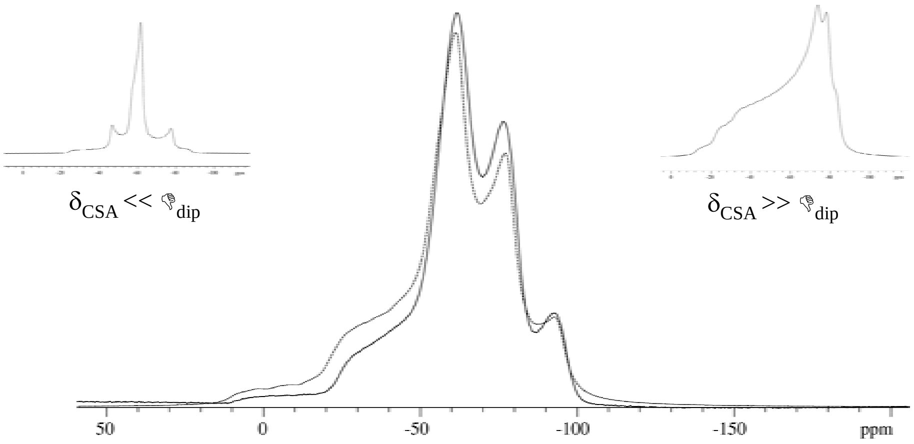

Figure 4.4: Comparison of the experimental single pulse ^{19}F-NMR spectrum of 4-CF_3-Phg (solid line) and simulated spectral lineshape (dotted line). Two insets show less convoluted spectra, where one of the two anisotropic interactions dominates the spectral lineshape.

The SIMPSON simulation yielded an isotropic chemical shift value of –60 ppm. For the CSA tensor, the anisotropy was determined as δ=38 ppm and asymmetry as η=0.0, while the dipolar coupling constant was found to be D_{ij}^0=15.0 kHz. At 470 MHz ^{19}F-NMR frequency δ=38 ppm corresponds to 17.8 kHz, hence the two interactions are equally dominant. Two other cases that would be expected at much lower ($\delta_{CSA} \ll \Delta_{dipolar\ coupling}$) and much higher ($\delta_{CSA} \gg \Delta_{dipolar\ coupling}$) B_0 fields strength are illustrated as insets in figure 4.4 for comparison. The fundamental values of δ and D_{ij}^0 are almost identical to the ones found in analysis of ^{19}F-NMR MAS spectra of the same material (next section, 4-CF_3-Phg values are given in table 4.2 and highlighted by gray shading to stress their importance for the present study).

Comparison of CF_3-labeled amino acid analogs

Following the experience gained on monofluorinated amino acids and 4-CF_3-Phg, the remaining five CF_3-labeled substances were investigated in MAS experiments at 12.5 kHz MAS, where dipolar coupling is sufficiently suppressed to determine the CSA principal tensor values. Figure 4.5 shows static and MAS ^{19}F-NMR spectra recorded for all six polycrystalline amino acid derivatives. Note that the spectrum of 4-CF_3-Phg differs from the one in figure 4.4, since here it was measured at 600 instead of 500 MHz field strength. The corresponding static spectra of substances other than 4-CF_3-Phg show rather more shapeless spectra but with essentially identical CSA and dipolar coupling landmarks. The MAS spectra reveal crystal polymorphism in only cases, 3-CF_3-Phe and 5,5,5-F_3-Leu. Remarkably, this fact is not reflected in the static spectra, whose quality does not seem to correlate with the presence of crystal polymorphism.

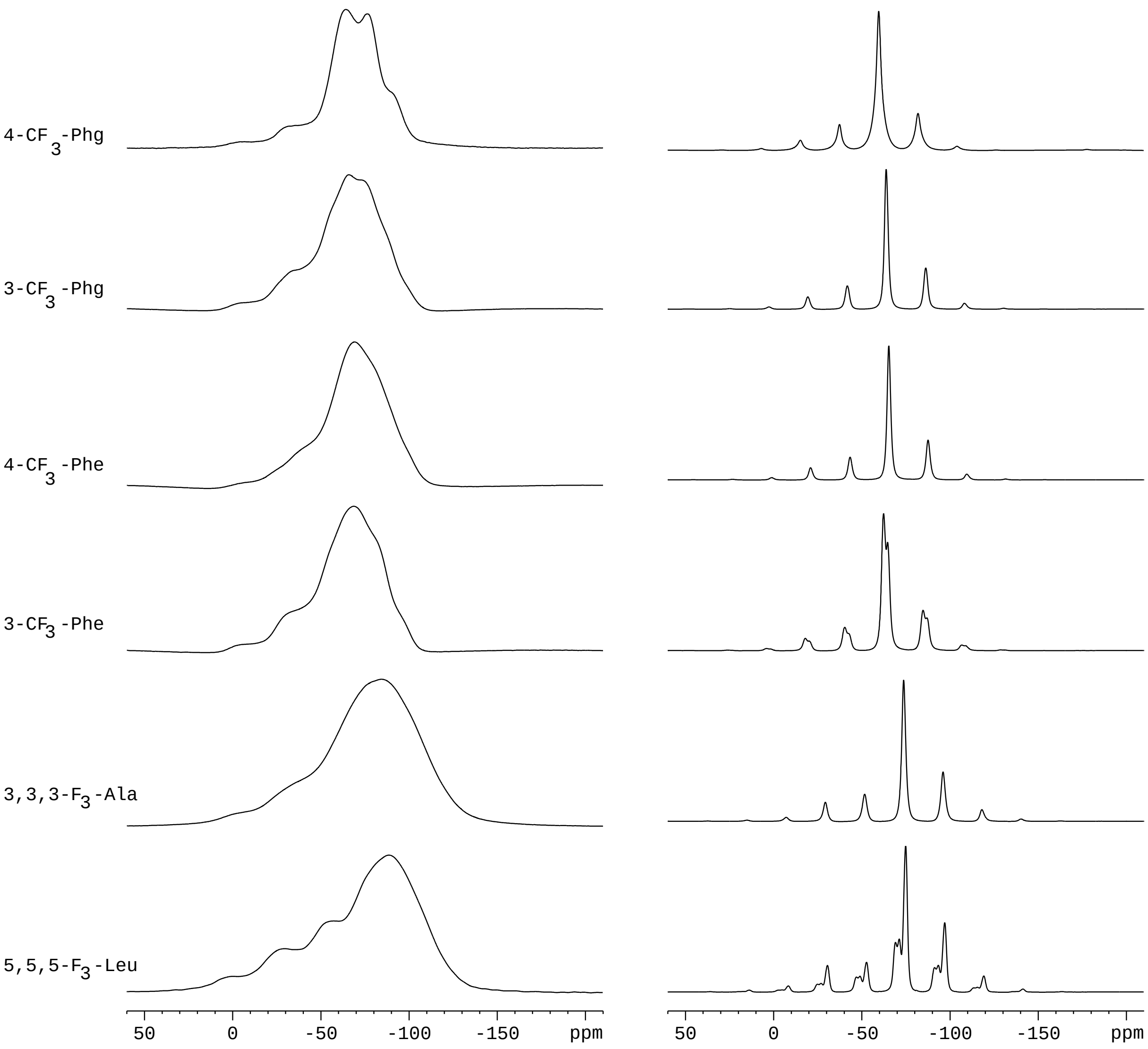

Figure 4.5: Single-pulse spectra of all CF_3-labeled substances in static experiments (left) and at 12.5 kHz MAS.

The MAS spectra were analyzed analogous to the procedure described in the preceding chapter for mono-fluorinated amino acid analogs. At least two sidebands on either side of the central lines were fitted, according to the work of Hodgkinson and Emsley.[8] Comparison of

Gaussian and Lorentzian linefits revealed that Lorentzians better describe the observed spectral shapes. The CSA tensor principal components were determined using the Herzfeld-Berger algorithm[4] from MAS spectra, while the dipolar coupling values were estimated from the landmarks of the static spectra. All results are compiled in table 4.2. It has to be noted that in the case of 3,3,3-F_3-Ala and 5,5,5-F_3-Leu the Herzfeld-Berger algorithm did not fully explain the sideband intensities, maybe indicating that at 12.5 kHz MAS the dipolar coupling (D_{ij}^0≈15-20 kHz!) is not fully suppressed. Working at higher MAS speeds is not feasible, since then the number of observed sidebands will not allow a reasonable Herzfeld-Berger-fit any more. Still, the extracted values are sufficiently close to the data in aqueous solution and to the values of the other five substances to rule out any major systematic error here.

Table 4.2: CSA principal components and dipolar coupling values extracted from the spectra of figure 4.5, along with spin-lattice- and spin-spin-relaxation times.

Substance	σ_{11} [ppm]	σ_{22} [ppm]	σ_{33} [ppm]	σ_{iso}^{MAS} [ppm]	δ [ppm]	η	D^0 [kHz]	T_1 [s]	T_2 [μs]
4-CF_3-Phg	-23.4	-77.9	-77.9	-59.7	36.3	0.00	15.4	5.7 ±0.4	31.4 ± 2.2
3-CF_3-Phg	-24.0	-83.6	-83.8	-63.8	39.8	0.01	17.5	(a)	(a)
4-CF_3-Phe	-25.3	-85.2	-85.7	-65.4	40.1	0.01	18.5	1.86 ±0.07	23.5 ±0.7
3-CF_3-Phe	-23.7	-76.9	-86.6	-62.4	38.7	0.25	16.5	(a)	(a)
	-26.0	-83.7	-84.4	-64.7	38.7	0.02			
3,3,3-F_3-Ala	-30.8	-92.2	-98.3	-73.8	43.8	0.14	19.5	0.32 ±0.01	39.6 ±2.8
5,5,5-F_3-Leu	-24.4	-80.0	-103.2	-69.2	44.8	0.52	16.5	1.08 ±0.03	24.0 ±4.0
	-23.1	-82.3	-108.5	-71.3	48.2	0.54			
	-27.6	-95.7	-101.3	-74.9	47.3	0.12			

(a) not measured

Isotropic chemical shift values σ_{iso} are found around –62 ppm for the aromatic amino acid derivatives, and around –72 ppm for both aliphatic amino acid analogues. All values are within 2 ppm of the values in aqueous solution, again showing the limited influence of the far environment on isotropic chemical shifts. Tensor anisotropies δ are found between 35 and 45 ppm, as could already be estimated from visual inspection of the static spectra of figure 4.5. Asymmetries η are in five cases very close to zero, indicating that the CF_3-group in a crystalline environment undergoes rapid rotational diffusion around its axis of symmetry. 5,5,5-F_3-Leu forms an exception, since asymmetries of η≈0.5 are observed. The dipolar couplings are very similar in all substances, ranging between 15 and 21 kHz.

Evidently, the characteristic parameters of CF_3-groups do not show much difference when attached to either aromatic or aliphatic scaffolds. Therefore, a distinction between aromatic and aliphatic substances as made in the previous chapter III is pointless here. On the other hand, any comparison of F- and CF_3-substituents on identical scaffolds (e.g. 4F-Phe vs. 4-CF_3-Phe), does not yield any insight, since they are too different (i.e. apples and oranges).

An important aspect when working with ^{19}F-labels in methyl-groups is their motional behaviour. Fast uniaxial rotation about the threefold symmetry axis renders the three

fluorines of a CF_3-group chemically and magnetically equivalent, and it reduces their homonuclear dipolar coupling by a factor of –1/2. From the size of the dipolar splitting of around 20 kHz (at the 0°-edges of the convoluted powder lineshapes) within the CF_3-group it is concluded that this substituent undergoes fast axial rotation in all of the polycrystalline amino acids studied here. The fact that all ^{19}F CSA tensors of CF_3-labeled amino acids are found to be symmetric further proves that the CF_3-group is engaged in free rotational diffusion. Summarizing, we find that methyl groups substituted symmetrically with three identical substituents, i.e. the groups CD_3 and CF_3, are free for rotational diffusion, while the asymmetrically substituted CFD_2- and CFH_2-groups shows only restricted rotational mobility, as demonstrated in the previous chapter III.

Spin-spin- and spin-lattice relaxation of CF_3-labeled amino acids

The longitudinal and transversal ^{19}F-NMR relaxation times T_1 and T_2 as a function of temperature in the range of –60°C to +60°C were determined for four representative CF_3-labeled substances under investigation. Figure 4.6 gives the resulting curves for T_1, explicit values of T_1 and T_2 at 20°C are included in table 4.2. Compared to the values found in mono-fluorinated amino acids in chapter III, the CF_3-labeled substances all show rather short T_1 times, on the order of magnitude of a second.

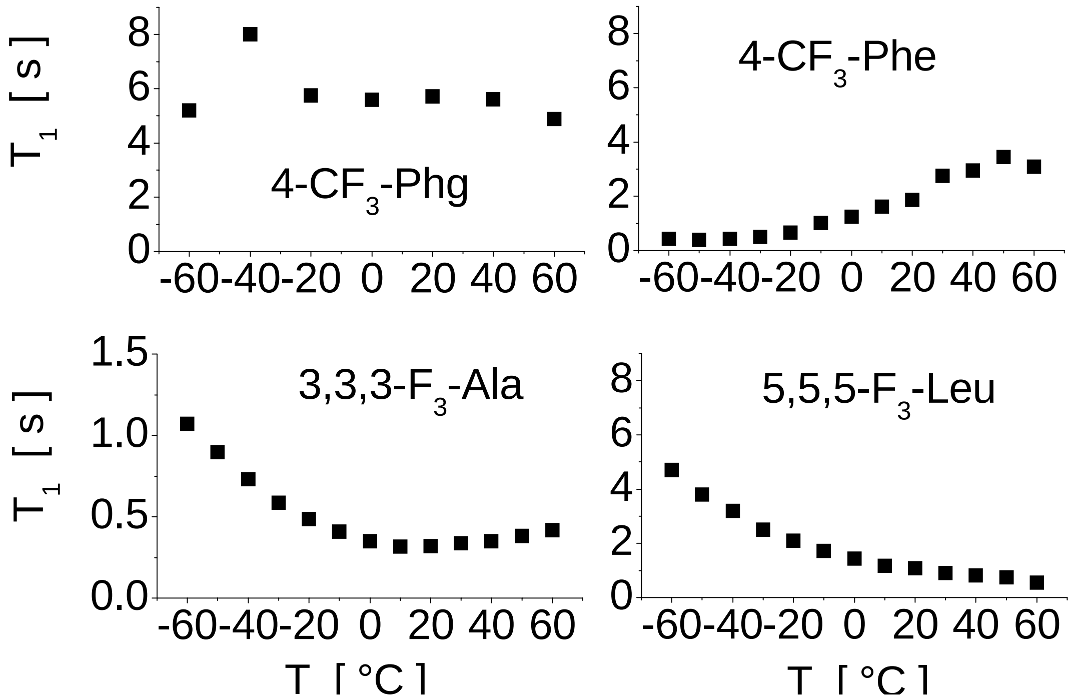

Figure 4.6: Temperature dependence of T_1 spin-lattice relaxation times observed in CF_3-labeled amino acids

As was the case in the mono-fluorinated amino acids of the previous chapter, T_2 relaxation does not significantly vary, neither with temperature nor amongst the various amino acids. In contrast, T_1 relaxation times exhibit a more interesting temperature dependence, as the series observed on 3,3,3-F_3-Ala shows an interesting T_1-minimum. At this temperature, the rate of axial rotation passes through the regime of most efficient relaxation by fluctuating fields with the same correlation time.

Summary and discussion

The ^{19}F-NMR properties of polycrystalline CF_3-labeled amino acids were characterized. A single-pulse experiment gave the best spectral lineshapes, although it was previously deemed technically not feasible due to receiver dead times. It was thus possible to overcome the problem of the simultaneous presence of CSA and dipolar coupling of equal magnitude in the CF_3-group, which causes common echo spectra to be heavily distorted. A phase-cycled quadrupolar echo sequence[7] designed to deal with this challenge gave inferior spectra than the single-pulse experiment.

It was possible to extract CSA principal tensor values and dipolar coupling parameters from static single-pulse spectra in combination with MAS spectra taken at 12.5 kHz spinning speed. The properties found for the CF_3-group in aromatic and aliphatic environment differ only slightly. Comparing ^{19}F- and ^{2}H-NMR spectral properties of CF_3-, CFH_2-, CFD_2-, and CD_3-groups (see chapter III) gave insight into their motional properties. The free rotation found in CH_3-groups around their axis of symmetry[11;12] is also present in the symmetrically substituted CF_3- and CD_3-groups, but is hindered whenever only a single ^{19}F-substituent is present in the methyl groups of the investigated crystals.

This work forms a point of reference for future biomolecular applications of CF_3-NMR and already provided input in the analysis of data obtained on a CF_3-labeled antimicrobial peptide, PGLa, presented in chapter VIII.

Reference List

(1) Bak, M.; Rasmussen, T.; Nielsen, N. C. *J.Magn.Reson.* **2000**, *147*, 296-330.

(2) Ousterhout, J. K. *Tcl and the Tk toolkit*; Addison-Wesley: Reading, MA, 1994.

(3) Smith, S. A.; Levante, T. O.; Meier, B. H.; Ernst, R. R. *J.Magn.Reson.A* **1994**, *106*, 75-105.

(4) Herzfeld, J.; Berger, A. E. *J.Chem.Phys.* **1980**, *73*, 6021-6030.

(5) Berger, S.; Braun, S.; Kalinowski, H.-O. *NMR-Spektroskopie von Nichtmetallen; Band 4: ^{19}F-NMR Spektroskopie*; Georg Thieme Verlag: Stuttgart, 1992.

(6) Brey, W. S.; Brey, M. L. Fluorine-19 NMR; In *Encyclopedia of NMR*; Grant, D. M., Harris, R. K., eds. Wiley: New York, 1996; pp 2063-2071.

(7) Antonijevic, S.; Wimperis, S. *J.Magn.Reson.* **2003**, *164*, 343-350.

(8) Hodgkinson, P.; Emsley, L. *J.Chem.Phys.* **1997**, *107*, 4808-4816.

(9) Beshah, K.; Olejniczak, E. T.; Griffin, R. G. *J.Chem.Phys.* **1987**, *86*, 4730-4736.

(10) Grage, S. L.; Wang, J.; Cross, T. A.; Ulrich, A. S. *Biophys.J.* **2002**, *83*, 3336-3350.

(11) Nicholson, L. K.; Kay, L. E.; Baldisseri, D. M.; Arango, J.; Young, P. E.; Bax, A.; Torchia, D. A. *Biochemistry* **1992**, *31*, 5253-5263.

(12) Schmidt-Rohr, K.; Spiess, H. W. *Multidimensional Solid-State NMR and Biopolymers*; Academic Press: San Diego, CA, 1994.

V. Six-spin system

In order to characterize the complex homonuclear interactions between multiple ^{19}F spins, three simple model substances carrying two CF_3-groups in *meta*-position on a phenyl ring were incorporated in DMPC membranes. Pure dipolar spectral patterns were measured by use of the CPMG multi-pulse sequence and could be analyzed to yield intra-CF_3 and inter-group dipolar coupling values. Since the inter-fluorine distances are known, the anisotropy of the dipolar couplings allowed for a subsequent analysis of orientational and mobility properties of the molecules. Findings were confirmed by a molecular dynamics (MD) simulation.

Introduction

To establish solid-state ^{19}F-NMR as a highly sensitive and versatile method for studying biomembranes it is necessary to start with simple model systems. In particular we carried out studies on small molecules carrying two ^{19}F nuclei[1] or a trifluoro-methyl group[2], respectively, which were incorporated in macroscopically aligned lipid bilayer samples. These systems allowed us to establish and validate experimental techniques for determining molecular distances and orientations by measuring dipolar couplings in a CPMG pulse sequence. In parallel, fluorine labeling was performed on a number of membrane active peptides, thus tackling the synthetical challenges of fluorine labeling and gaining first exciting insights into the structure and function of those systems.[3-6]

The work presented here aims at extending these studies in the direction of a more complex spin system consisting of six ^{19}F-nuclei, referred to as 'six-spin system' in the following. As molecular scaffold, we chose three related substances carrying two trifluoro-methyl groups in *meta*-position on an aromatic ring system. All three substances additionally possess a carboxyl group, giving the molecules a polar region that may assist in attaching and orienting the molecules in macroscopically aligned membranes of DMPC. The three molecules differ in their size and symmetry, which should influence their motional and alignment properties within the membrane. The molecules are depicted in figure 5.1 and shall be referred to as BA-F_6, PhA-F_6 and BBA-F_6 (listed in order of increasing size, abbreviations chosen according to the non-fluorinated analogs benzoic acid, phenylacetic acid, and benzoyl-benzoic acid). The largest and least symmetric molecule, BBA-F_6, is very similar to flufenamic acid, which played a central role in a previous study.[2;7] The smaller and more symmetric molecules BA-F_6 and PhA-F_6 were chosen for their less complex geometry.

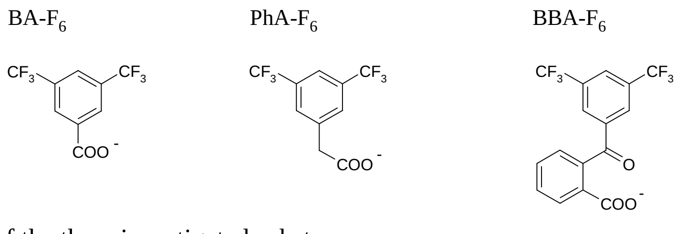

Figure 5.1: Structures of the three investigated substances

We consider this situation of two CF_3-groups, interacting over an intermediate distance by dipolar coupling, as a good model for CF_3-labeled biomolecules to be addressed in the future. The CF_3-group in itself has valuable properties as a selective NMR label for determination of segmental orientation from the anisotropy of dipolar couplings in oriented membranes (*cf.* chapters I and VIII of this work). Moreover, we envisage CF_3-groups as promising reporters of spatial proximity. Due to the high sensitivity of the fluorine nucleus, dipolar coupling between two CF_3-groups may be detectable at distances up to 15 Å.[8-10] Two CF_3 groups on two independent molecules could thereby give direct evidence of oligomerization. More sophisticated 'spin-counting' experiments[11] may then allow to determine the exact number of monomers involved. By establishing the described hexafluorinated substances as model systems, we hope to gain experience with complex dipolar coupling patterns between two CF_3-groups at intermediate distance.

It is known from liquid crystal chemistry that ^{1}H-NMR spectra of organic substances dissolved in nematic liquid crystals are extremely complex and can show hundreds of lines.[12;13] Still, valuable information can be deduced on the dissolved molecule's orientation and conformational properties.[14-18] From the point of view of the mentioned liquid crystal studies our systems are very similar, since they contain an organic solute within a smectic liquid crystal, i.e. the lipid bilayer. From the NMR point of view, our hexafluorinated model systems differ from this situation, since their ^{1}H-NMR spectra cannot be observed over the background of the lipid proton signal, unless costly per-deuterated lipids are employed. On the other hand, the directly observable ^{19}F-NMR spectra of the hexafluorinated systems are very similar to ^{1}H-NMR spectra of solutes in liquid crystals. Therefore, we hope to learn valuable lessons from liquid crystal chemistry about the application of ^{19}F-NMR to biological membranes, and to establish a link between liquid crystal structure analysis and membrane biophysics.

Materials and methods

Sample preparation

The hexafluorinated substances 3,5-bis-(trifluoromethyl)benzoic acid (BA-F_6, Acros Organics); 3,5-bis-(trifluoromethyl)phenylacetic acid (PhA-F_6, Aldrich); 2-[3,5-bis-(trifluoromethyl)benzoyl]benzoic acid (BBA-F_6, Fluorochem) were purchased at purity >98% and used without further purification.

Oriented lipid bilayer samples were produced by co-dissolving the hexafluorinated compounds (typically 0.1 mg) at a molar ratio of 5% with DMPC (Avanti Polar Lipids, Alabaster, AL, USA) in $CHCl_3$. The solution was then spread on 15 glass plates, allowed to dry in air and subsequently under vacuum overnight. To obtain oriented samples, the glass plates were stacked and incubated for 24 h at 48°C under an atmosphere of 98% relative humidity obtained over a saturated solution of K_2SO_4. The achieved quality of orientation in the oriented bilayer samples was controlled by solid-state ^{31}P-NMR and was usually very high (>90%). When following the described protocol, all prepared samples showed highly reproducible fluorine spectra. No aging of samples was observed, even after months of storage at –20°C.

When establishing this protocol for the acidic molecules, in the initial experiments a modification was considered in which defined amounts of 1...10μl of concentrated buffers at different pH were added to the glass plates prior to stacking, in order to control pH in the samples. This alternative protocol was not pursued further since it did not have noticeable effect on the spectral patterns of interest, while it severely deteriorated the quality of bilayer orientation. In addition, pH-control is not expected to severely influence the samples, since pK values of BA-, PhA- and BBA-F_6 are reported to have the low values of pK=3.3, 3.4, and 3.2, respectively (www.cas.org/SCIFINDER/). Therefore, only the de-protonated form of the hexafluorinated substances is expected to be found even in the hydrophobic environment of a lipid bilayer.

Solid-state NMR spectroscopy

All solid-state NMR measurements were carried out on a 500 MHz Varian Unity Inova spectrometer (Varian, Palo Alto, CA, USA) equipped with a second, home-built high frequency channel for the fluorine observe frequency of 470 MHz. For the ^{19}F-ssNMR measurements a double-tuned flat-coil probe (Doty Scientific Inc., Columbia, SC, USA) was used which allowed for proton decoupling while observing fluorine spectra.

Typical pulse lengths for fluorine 90°-pulses were 2.5 μs, proton decoupling was applied at a B_1 field strength of 15 kHz in single pulse experiments. In CPMG multi-pulse experiments, dwell times of τ=44μs were used, acquiring 2400 data points and composite 90°-pulses of the type $90°_x$-$180°_y$-$90°_x$were used to increase the width of spectral excitation and compensate for pulse imperfections.[19;20] Typically, a few hundred scans were acquired per 1D and 1000-2000 for a CPMG spectrum

CPMG scaling factor

Typically, multi-pulse sequences not only suppress certain interactions, but also make the evolving interactions appear smaller than they actually are.[21;22] This property, which is related to finite pulse widths, is described by a so-called scaling factor, denoted α in the following. In the case of the CPMG experiment, a scaling behavior according to

$$\Delta_{\exp} = (1-\alpha D)\Delta_0 \qquad (5.1)$$

is expected from theory.[1;2] Here, Δ_{exp} denotes the dipolar splitting observed in a multi-pulse experiment, while Δ_0 is the unscaled dipolar splitting corresponding to a basic one-pulse experiment. The additional factor D is the pulse train's duty cycle, taking into account the finite width of the pulses. The duty cycle is calculated from an individual pulse's finite width t_w and the time τ between two pulses' mid-points as $D= t_w/\tau$.

In CPMG, the applicable scaling factor α is dependent on the type of spin system investigated. It also differs when composite pulses are used rather than simple pulses in order to enhance the width of spectral excitation. For our case of an extended system of six spins I=1/2 under composite pulses, to our knowledge, there was no previous determination of the appropriate scaling factor α. Therefore, we determined the scaling factor in an experimental way by extrapolating the fluorine CPMG spectra of the substances investigated.[2;23]

To determine the CPMG experiment's scaling factor α according to formula (5.1), CPMG spectra of oriented samples of BA-F_6 and PhA-F_6 were recorded over a significant range of different duty cycles D. Picking eight lines that are narrow, well-resolved and can be distinctively identified in each spectrum allowed to determine α by linear regression. The splittings observed on the selected eight line pairs are shown as a function of D in figure 5.2. The scaling factor for the six-spin system was thus determined to be α=1.10±0.05 in a CPMG experiment using $90°_x$-$180°_y$-$90°_x$ composite pulses.

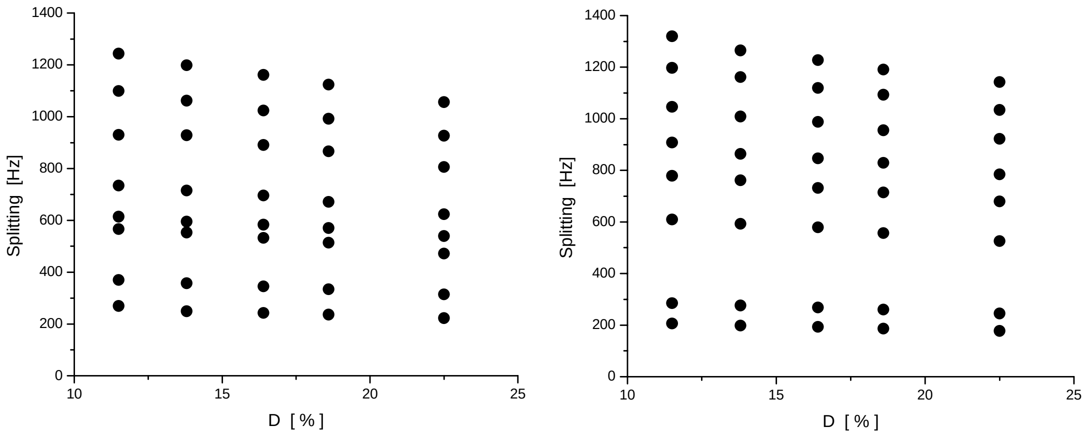

Figure 5.2: CPMG-splittings observed on eight prominent resonances as a function of duty cycle D, in BA-F_6 (left) and PhA-F_6 (right)

We note that at certain values of D the overall resolution and quality of the CPMG spectra deteriorated dramatically. We believe this to be a general interference effect which had to be avoided in the present experiments, but might be utilized in future ones. On the whole, the quality of the six-spin CPMG spectra is highly dependent on the quality of the experimental settings, so much that they can be used as a control for proper hardware functioning.

Analysis of CPMG spectra

The complexity of ^{1}H-NMR spectra of organic substances dissolved in liquid crystals is due to 'strong coupling' operator terms $\hat{\vec{I}}^i\hat{\vec{I}}^j$ in the homonuclear dipolar coupling terms of the Hamiltonian (given in 'high-field approximation'). The same is true for our system, where ^{19}F is the nucleus of interest. Here, the relevant Hamiltonian is given by two sums of homo- and heteronuclear dipolar interaction terms:

$$\hat{H} = \sum_{i<j} D_{ij}^0 \cdot \frac{3\cos^2\theta_{ij} - 1}{2} \cdot \left(3\hat{I}_z^i\hat{I}_z^j - \hat{\vec{I}}^i\hat{\vec{I}}^j\right) + \sum_{k<l} D_{kl}^0 \cdot \left(3\cos^2\theta_{kl} - 1\right) \cdot \hat{I}_z^k\hat{S}_z^l \qquad (5.2)$$

However, this complicated Hamiltonian is significantly simplified when taking into account motional properties. Caused by the angular dependence of dipolar coupling on the angle θ_{ij}, an effective value D_{ij} will be observed instead of the maximum dipolar splitting D_{ij}^0 (*cf.* equation (2.14)). Since the CF_3-groups rotate freely around their connecting bonds to the phenyl ring—which, however, may be aligned at different angles with respect to the magnetic field—there exist only three fundamentally different homonuclear dipolar couplings, two being the couplings between any two neighboring fluorine nuclei within one and the same CF_3-group (termed D_{11} and D_{22} in the following), along with the coupling D_{12} between any two fluorine nuclei belonging to different CF_3-groups. These three parameters fully suffice to determine the highly complicated spectra, but are hard to extract from them.

In addition, motional averaging around the membrane normal will average all interaction tensors to be parallel to the membrane normal, which in turn is aligned parallel with the external magnetic field B_0. Thus, no angular dependence has to be taken into account in the Hamiltonian (5.2). Further simplified by omitting heteronuclear interaction, which is suppressed in the CPMG experiment, the Hamiltonian now reads

$$\hat{H} = D_{11}\sum_{\text{intra,1}}\left(3\hat{I}_z^i\hat{I}_z^j - \hat{\vec{I}}^i\hat{\vec{I}}^j\right) + D_{22}\sum_{\text{intra,2}}\left(3\hat{I}_z^i\hat{I}_z^j - \hat{\vec{I}}^i\hat{\vec{I}}^j\right) + D_{12}\sum_{\text{inter}}\left(3\hat{I}_z^i\hat{I}_z^j - \hat{\vec{I}}^i\hat{\vec{I}}^j\right). \qquad (5.3)$$

In order to extract the three dipolar coupling constants from experimentally observed spectra, theoretical spectra need to be calculated from the Hamiltonian (5.3) and iteratively fitted to the experimental spectrum. Most commonly, theoretical spectra are calculated from the time evolution effected by the Hamiltonian (5.3) on the spin system. In the case at hand, the complexity of the spin system allows a single spectrum to be calculated in around 10 minutes, which makes iterative fitting prohibitively time-consuming.

To fit experimental spectra in a computationally less demanding, interactive manner, the program package ARCANA[24-26] was developed in the group of Prof. M. Longeri (University of Calabria, Rende, Italy). The spectral calculations are simplified in ARCANA by restriction to energy levels E_i, which can be calculated by a straightforward representation and diagonalisation of the Hamiltonian (5.3), thereby solving the time-independent Schrödinger equation, $\hat{H}\psi_k = E_k\psi_k$. Once the set of energy eigenstates ψ_k of the Hamiltonian is known, the spectrum can easily be calculated as superposition of lines with frequencies $\nu_{kl} = (E_k - E_l)/h$ given by the energy eigenvalues. The iterative fitting procedure requires the user to interact by pinpointing peaks, linewidths, and intensities that are already reproduced correctly. It is described as a time-consuming procedure which allows for

listening to loud music in parallel (M. Carravetta, personal communication). The analysis was carried out for the CPMG spectra of the three hexafluorinated substances in collaboration with Dr. Giuseppina de Luca of Prof. Longeri's group.

For cross-checking and presentation purposes, the spectra corresponding to the extracted D_{ij} values were re-calculated in our laboratory using SIMPSON[27]. Interactions other than homonuclear dipolar coupling were not taken into account, allowing for the use of an ideal single-pulse experiment in the simulation. Also, ideal orientation, i.e. absence of mosaic spread, was assumed by the restriction of the simulation to a single crystallite aligned with the magnetic field. This approach reduced processor times to around 10 min per spectrum on a 1.5 GHz processor running under Windows XP. An FID of 1024 points was generated at 100 µs dwell time, giving a spectral width of 10 kHz in the transformed spectrum. The recorded FID was elongated by zero-filling up to 8192 points and Fourier-transformed using exponential line broadening of 20 Hz for BA- and PhA-F_6, and 50 Hz for BBA-F_6.

Analysis of orientation and mobility

The molecular geometry of the 3,5-bis-CF_3-phenyl group common to all three systems was modeled as an idealized structure. Ideal tetrahedral bond angles and standard bond lengths were used, as implemented in the InsightII molecular modeling package (Accelrys Inc., www.accelrys.com). For collectively modeling the fluorine nuclei within a rapidly rotating CF_3-group, pseudo-atoms were introduced in the middle of the equilateral triangle described by the three fluorine nuclei. Thus, the relevant interaction distances were found to be r_{intra}=2.25Å between two nuclei *within* a CF_3-group, and r_{inter}=5.90Å between the two pseudo-atoms representing the rotating CF_3-groups. The molecular coordinate system MOL was chosen as shown in figure 5.3, with the z-axis pointing along the C_2-symmetry axis of the 3,5-bis-CF_3-phenyl group, the x-axis perpendicular to it within the plane of the phenyl ring, and the y-axis perpendicular to both and forming a right-handed coordinate system.

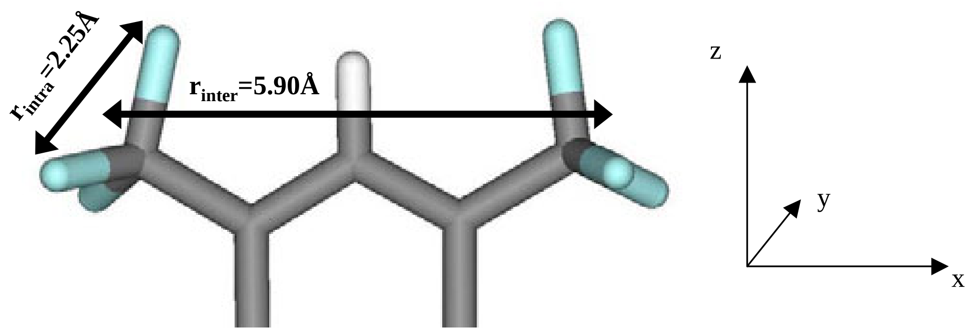

Figure 5.3: Bis-CF_3-phenyl geometry with definition of molecular coordinate system

Since the maximum dipolar splittings D_{ij}^0 play a central role in the following analysis in terms of the Saupe ordering matrix, they needed to be determined with some accuracy. Special attention was paid to the distances r_{ij} between fluorine nuclei, as shown for an idealized geometry in figure 5.3, since according to equation (1.11) they enter D_{ij}^0 to the third power.

To compare idealized distances to more realistic ones, we examined two crystal structures of molecules containing the bis-CF_3-phenyl group. These were downloaded from the Cambridge structural database (CSD, www.ccdc.cam.ac.uk), where they are deposited under accession

codes ALBA20 and STRIA0. In addition, an *ab initio* calculation was available where the geometry of a CF_3-group in trifluoro-acetic acid had been determined (Dr. habil. Ulrich Sternberg, FZ Karlsruhe GmbH, personal communication). An experimental NMR study by Brouwer *et al.*[28] determined r_{intra} also in an isolated CF_3-group, confirming the idealized value. All accessible fluorine-fluorine distances are compiled in table 5.1.

Table 5.1: Fluorine-fluorine-distances within CF_3 groups (r_{intra}) and between two CF_3 pseudo-atoms (r_{inter}) in the investigated structures

structure	r_{intra} [Å]	r_{inter} [Å]
idealized	2.25	5.89
ALBA20	2.10	5.82
STRIA0	2.13	5.86
ab initio	2.17	not det.
Brouwer *et al.*[28]	2.25	not det.

It appears that the fluorine-fluorine distances found in more realistic CF_3-geometries have a slight tendency to be shorter than expected from an idealized geometry. This finding is somewhat counter-intuitive, since fluorine has a larger nuclear radius than hydrogen, and should therefore force apart the near-perfect tetrahedral geometry seen in methyl groups.

The distance found between two pseudo-atoms representing two CF_3-groups in *meta*-position is almost identical to the one in idealized geometry. An additional source of error may be the calculation of inter-CF_3 dipolar couplings from pseudo-atom positions. A rough estimation taking into account a detailed averaging of the pairwise inter-group couplings due to rotating CF_3-groups was performed. It showed that pseudo-atom calculation actually under-estimates the inter-CF_3 coupling D_{12} by less than 10%.

In conclusion, deviations of more realistic molecular geometries from ideal tetrahedral geometry were found to be very small, and the idealized molecular model was retained in the following. From the relevant distances of 2.25 Å and 5.90 Å reported above, the maximum expected dipolar splittings D_{ij}^0 are calculated according to formula (1.11) and were found to be 28005 Hz and 1561 Hz, respectively. For the maximum coupling within the rotating CF_3-group, a value scaled by a factor of –1/2 due to rotation has to be taken into account, *cf.* equation (2.13), resulting in the employed value of $D_{11}^0 = D_{22}^0 = -14003\,\text{Hz}$.

Molecular dynamics simulation

Molecular dynamics simulations on the BA-F_6/DMPC system were performed in collaboration with Dr. Barbara Hoff of the group 'Bioverfahrenstechnik' at the Institute of Mechanical Process Engineering and Mechanics (MVM) of the University of Karlsruhe. The GROMOS force field was used as implemented in the GROMACS 3.0 software package[29], see also http://www.gromacs.org. The simulation box contained a double layer of 128 DMPC molecules and 3655 water molecules and was downloaded from http://moose.bio.ucalgary.ca/Downloads/files/dmpc_npat.pdb. Lipid parameters were chosen according to Berger et al.[30] Water molecules were modeled as single point charge molecules.[31] Six molecules of BA-F_6 were inserted by hand into the simulation box, where the necessary voids were generated by a tool supplied in GROMACS. A steepest-descent energy-minimization of 100 steps was

performed prior to simulations. The simulation covered 20 ns, using 2 fs time steps and a leap-frog integration algorithm. Temperature and pressure were kept constant at a temperature of 343 K and an anisotropic pressure of 1 bar, respectively, by weak coupling according to Berendsen et al.[31], with coupling constants of τ_T=0.1 ps and τ_p=1 ps. Long-distance interactions were treated with a twin-range cut-off, using a cut-off radius of 1.8 nm for Coulomb interactions and 1 nm for van der Waals interactions.

Results

Single-pulse experiments

The three six-spin model substances were incorporated in macroscopically aligned bilayers of DMPC. Single-pulse ^{19}F-NMR spectra obtained on these samples at temperatures of 10°C and 35°C are depicted in figure 5.4. Spectra acquired without proton decoupling show broad 'humps' ca. 6 kHz wide, with only few spectral features resolved. At 35°C, due to increased motional spectral averaging, slightly more spectral detail becomes apparent than at 10°C, especially the BBA-F_6 spectrum now shows four resolved components.

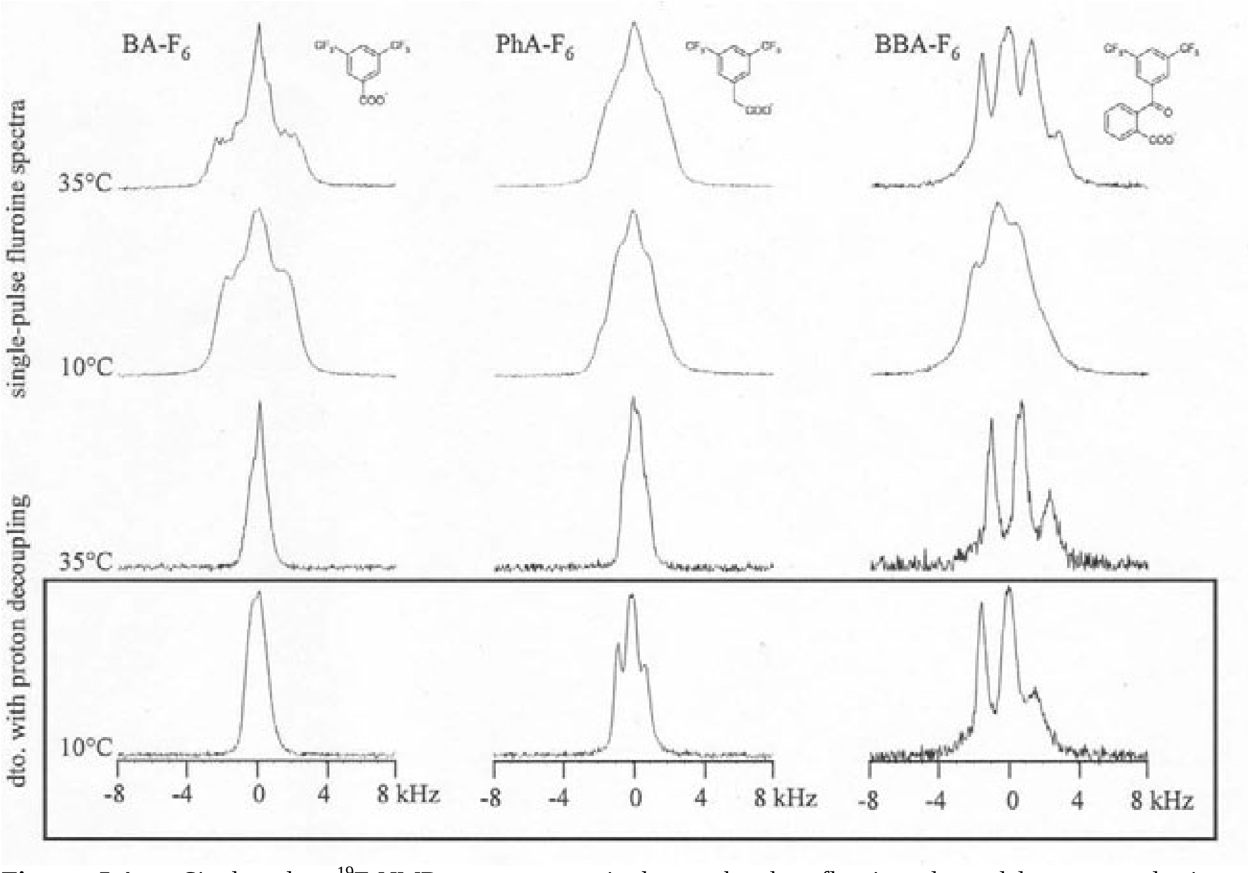

Figure 5.4: Single-pulse ^{19}F-NMR spectra acquired on the hexafluorinated model compounds in macroscopically oriented DMPC bilayers. (Top) Spectra without proton decoupling at 35°C and 10°C temperature. (Bottom) Spectra with 15 kHz proton decoupling applied at 35° and 10°C.

When applying proton decoupling during acquisition, the spectra become even more shapeless, or differently put, more simple. BA-F_6 has a single line approx. 2 kHz wide, while PhA-F_6 and BBA-F_6 show triplets of 3 and 5 kHz width, respectively. The increase of spectral width with molecular size (BBA-F_6 has twice the spectral width of the other two) can be understood in terms of molecular mobility: A larger molecule is expected to be less mobile in the lipid bilayer, and should therefore show larger spectral width due to reduced motional averaging. Different alignments of the CF_3-groups may also contribute to different intrinsic strengths of anisotropic interactions. The lineshapes become slightly broader at a lower temperature of 10°C, thereby resolving the PhA-F_6 spectrum to a clear triplet. These are not the perfect triplets known from textbooks, but seem to have different linewidths for

each component. This situation is reminiscent of the spectra observed in CF_3-labeled PGLa, described in chapter VIII of this thesis. There, different linewidth is caused by different relaxational properties effected by dipolar and CSA interactions on the same order of magnitude.

The proton-decoupled single-pulse spectra at 10°C (highlighted by a box in figure 5.4) are qualitatively very similar to the ones observed in low-temperature CPMG spectra, presented in the following section. Spectra acquired in Hahn-echo experiments were found to be practically identical to the single-pulse spectra presented here (data not shown).

CPMG experiments

Subsequently, we investigated our systems using the CPMG multi-pulse sequence[1;2], which suppresses all interactions except for homonuclear dipolar couplings (and thus makes proton decoupling unnecessary as a highly welcome side-effect). Figure 5.5 presents spectra acquired on our six-spin systems with the CPMG-sequence. They show a complex pattern of numerous lines of very different intensities and linewidths. The increased resolution is due to the suppression of ^{19}F-CSA interaction, which was giving additional linebroadening in the single-pulse spectra presented above. The complicated dipolar pattern is effected by the presence of strong coupling between the non-equivalent ^{19}F-nuclei.

Upon tilting the oriented sample perpendicular to the magnetic field, the spectra retain their individual shape, but are scaled down in width by a factor of 0.5 (data not shown). This behavior is as expected for dipolar coupling tensors averaged around the membrane normal equation (2.13), as small molecules in liquid crystalline bilayers do. It indicates that the samples are uniformly oriented and only minor isotropic components (arising from non-oriented lipid portions or hexafluorinated molecules not embedded in the lipid bilayer) are present.

At 10°C, the CPMG spectra are very similar to the single-pulse spectra presented in figure 5.4. Since the CPMG sequence suppresses all asymmetric interactions, especially the CSA interaction, the spectra are now perfectly symmetric around 0 Hz. For the BA-F_6 system, a doublet of two very broad components at a splitting around 500 Hz is observed, while PhA- and BBA-F_6 show broad triplets of approx. 800 Hz and 1200 Hz splitting, respectively.

Upon raising temperature, the spectra reveal more and more spectral detail, eventually showing up to 20 resolved lines. For BA- and PhA-F_6, the full complexity of the six-spin dipolar pattern is fully revealed already at 40°C, while BBA-F_6, due to its larger molecular size and smaller mobility, does not appear to give comparable spectral resolution even at 70°C. For the sake of chemical stability of the lipids, the temperature was not raised beyond that point. The width of all spectra decreases slightly with temperature, as expected from increased molecular wobbling.

It has to be noted that the main lipid phase transition, which in DMPC occurs at 23°C, is not reflected in the temperature series of the embedded compounds. Rather, the spectra show a smooth temperature dependence. This behavior may be understood from the nature of the main lipid phase transition, where the lipid acyl chains change from an all-*trans* to an unordered high-temperature state. Since the phase transition relates to the order state of the lipid acyl chains, it appears that there is only little hydrophobic interaction with the

hexafluorinated molecules. Hence, the acyl chain melting is not reflected in our CPMG spectra. We did not observe any hysteresis effects either, as even repeated passage of the main phase transition between gel and liquid crystalline state did not change the observed spectra, similar to the behavior observed for flufenamic acid in DMPC bilayers.[2]

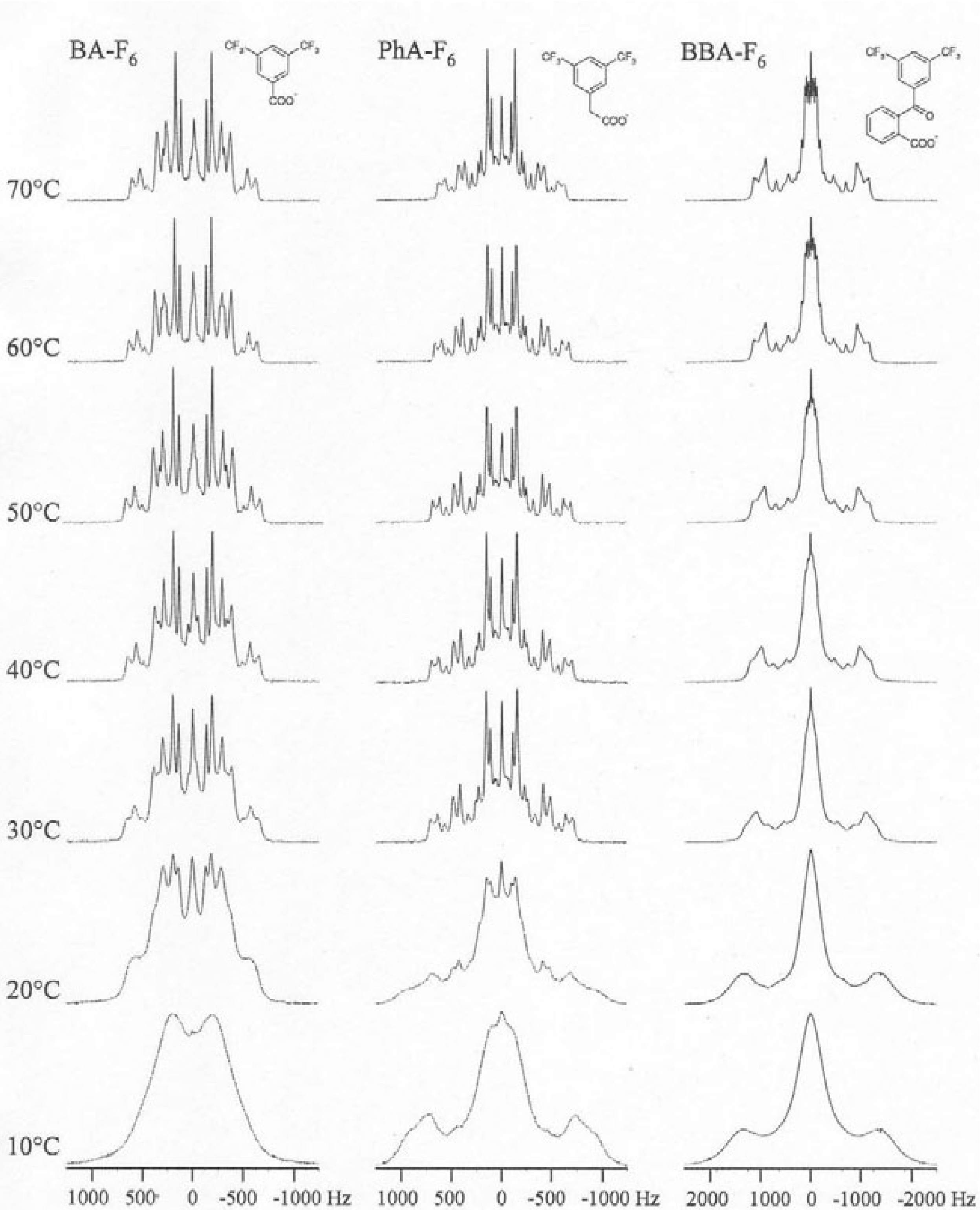

Figure 5.5: ^{19}F-CPMG spectra of the BA-, PhA-, and BBA-F6 systems (left to right), temperature series ranging from 10°C to 70°C.

Analysis of CPMG-spectra

It is known from theory that the complex CPMG spectra acquired on the hexafluorinated systems are described by three dipolar couplings only. These are the two intra-group couplings D_{11} and D_{22} within each CF_3-group, and the inter-group coupling D_{12}. They are orientation dependent, and their definition is given in equation (5.3). Using the ARCANA[24-26] program package described in the methods section, it was possible to extract the three relevant dipolar couplings from the CPMG spectra acquired at 70°C, which showed best spectral resolution. The extracted values are given in table 5.2, alongside with corresponding segmental order parameters S_{ij} calculated according to formula (2.15). It is interesting that for BA- and PhA-F_6 the extracted values for D_{11} and D_{22} are identical, while in the case of BBA-F_6 they are not.

Table 5.2: Homonuclear dipolar couplings between fluorine nuclei as extracted from CPMG spectra, and corresponding segmental order parameters.

System		D_{11} [Hz]	D_{22} [Hz]	D_{12} [Hz]	S_{11}	S_{22}	S_{12}
BA-F_6	70°C	-123.96	-123.96	89.35	0.009	0.009	0.057
PhA-F_6	70°C	-149.62	-149.62	68.42	0.011	0.011	0.044
BBA-F_6	70°C	-340.58	-177.60	57.80	0.024	0.013	0.037

As an independent confirmation of the dipolar analysis, the coupling values given in table 5.2 were used to reproduce our spectra using the SIMPSON[27] spectral simulation package. Figure 5.6 shows calculated spectra in comparison to experimental ones. Lines in the experimental spectra become increasingly narrow the closer they are to the 0 Hz splitting in the center of the spectrum. This observation is attributed to the sample's mosaic spread, which will be more dominant in the outer parts of the spectrum, where the orientation-dependence of the splitting is strongest in absolute terms. The effect is not reproduced in the simulations, as they assume perfect orientation of the sample.

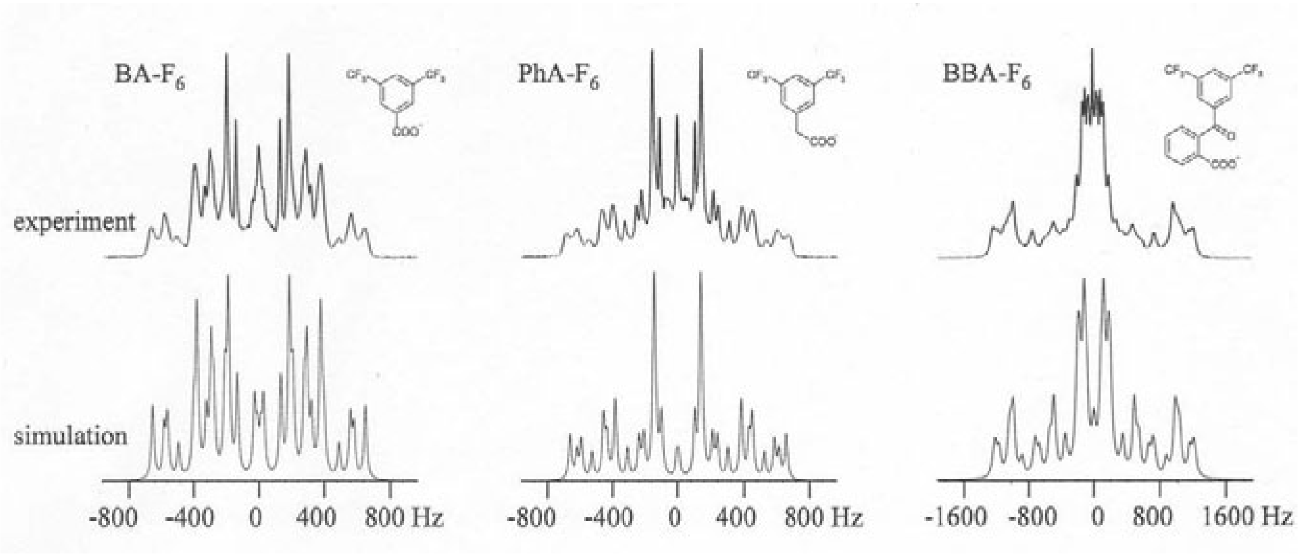

Figure 5.6: Comparison of experimental CPMG spectra to simulated spectra calculated from extracted dipolar coupling values.

The simulations demonstrate that the observed spectra can be fully explained by a single Hamiltonian, ruling out any initial speculations that the complicated lineshapes might be caused by different molecular species (protonated and de-protonated) within the samples. In addition, the spectral components observed around 0 kHz in BA-F_6 and PhA-F_6 are proven to be part of the spectral pattern of the oriented six-spin systems, and are *not* due to CPMG imperfections.

Analysis by Saupe ordering tensor

In the present case, a structure analysis cannot be carried out in purely orientational terms, since the very small molecules at hand do not show much ordering. Their high degree of motional averaging is evident from the exceedingly small segmental order parameters S_{11}, S_{22}, S_{12} that can be inferred from the very narrow CPMG spectra (*cf.* table 5.2). The concept of a well-defined molecular orientation characterized by two Euler angles ρ and τ and a single molecular order parameter S_{mol} is no longer appropriate, since the situation of the molecule is now a complex (probability) distribution over a wide range of orientations.

As a consequence, the dipolar couplings cannot be calculated any more from a single order parameter, as was the case in equation (2.14):

$$D_{ij} = S_{mol} \cdot D_{ij}^{0} ,$$

where the molecular order parameter S_{mol} was defined as the time average over the angle θ that the internuclear connecting vector forms with the external magnetic field:

$$S_{mol} := \frac{3\left\langle \cos^2\theta \right\rangle - 1}{2} .$$

Instead, molecular order now needs to be described by a symmetric 3x3-matrix, the Saupe ordering matrix $\mathbf{S}=(S_{\alpha\beta})$, $\alpha,\beta=x,y,z$.[32-34] Its elements can be calculated from the 'direction cosines' $\cos\theta_\alpha$ of the angles θ_α that the molecular α-axis encloses with the external magnetic field direction, z^{LAB}, according to

$$S_{\alpha\beta} := \left\langle \frac{3\cos\theta_\alpha \cos\theta_\beta - \delta_{\alpha\beta}}{2} \right\rangle , \qquad (5.4)$$

where $\delta_{\alpha\beta}$ is the Kronecker delta function, which is 1 if α=β, and 0 otherwise. It is always possible to find a coordinate system in which the ordering matrix is diagonal, though this need not be coincident with the local molecular geometry. The elements of the ordering tensor allow the calculation of observed dipolar coupling values, given that the orientational relationship between the molecular coordinate system and the pair of nuclei showing dipolar coupling is known. This relationship is measured by a set of three angles θ_{ij}^{α} , α=x,y,z, for each pair i,j of nuclei, which gives the angle between the internuclear connecting vector with respect to the molecular α-axis. The observed dipolar coupling is then given by[15]

$$D_{ij} = D_{ij}^0 \cdot \left[S_{zz} \frac{3\cos^2\theta_{ij}^z - 1}{2} + \left(S_{xx} - S_{yy}\right) \cdot \frac{\cos^2\theta_{ij}^x - \cos^2\theta_{ij}^y}{2} + 2S_{xz}\cos\theta_{ij}^x \cos\theta_{ij}^z \right]. \quad (5.5)$$

The maximum dipolar splitting D_{ij}^0 is calculated according to equation (1.11) as described in the methods section of this chapter. The relevant angles θ_{ij}^α for the case at hand are illustrated in figure 5.7. Due to our choice of the molecular coordinate system (*cf.* methods section), θ_y is always 90° and therefore, its cosine vanishes and the corresponding term does not need to be considered. θ_x evaluates to 0° and 30° for inter- and intra-CF_3-group dipolar coupling, respectively. Values for θ_z are 90° and 60°, respectively.

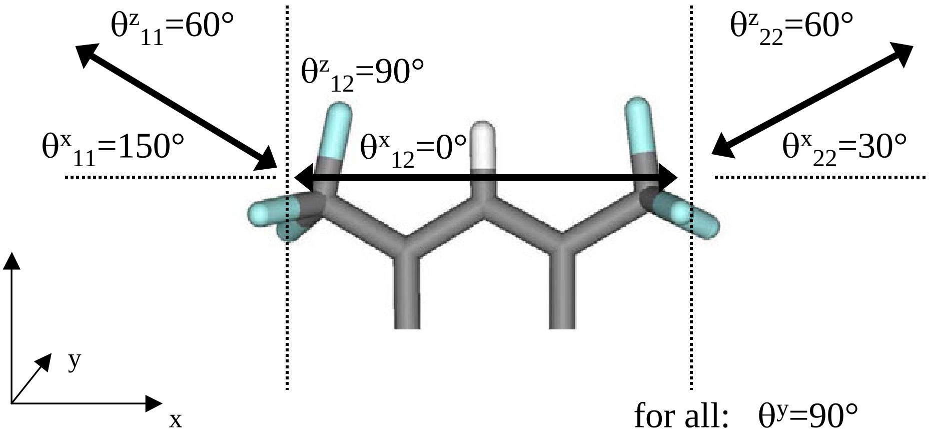

Figure 5.7: Definition and values of angles θ_{ij} relating relevant directions of dipolar coupling to the molecular frame of reference, MOL.

Given the appropriate values for θ_{ij}^α in the bis-CF_3-phenyl geometry, as illustrated in figure 5.7, equation (5.5) evaluates to a set of three equations:

$$\begin{aligned} D_{11} &= D_{11}^0 \cdot \left[-\frac{1}{8}S_{zz} + \frac{3}{8}\left(S_{xx} - S_{yy}\right) - \frac{\sqrt{3}}{2}S_{xz} \right] \\ D_{22} &= D_{22}^0 \cdot \left[-\frac{1}{8}S_{zz} + \frac{3}{8}\left(S_{xx} - S_{yy}\right) + \frac{\sqrt{3}}{2}S_{xz} \right] \\ D_{12} &= D_{12}^0 \cdot \left[-\frac{1}{2}S_{zz} + \frac{1}{2}\left(S_{xx} - S_{yy}\right) + 0 \right] \end{aligned} \quad (5.6)$$

In the case of BA- and PhA-F_6, the molecules possess C_{v2} symmetry (obvious for BA-, and present as effective averaged symmetry for PhA-F_6, see below), which allows for a further simplification. For a molecule having C_{2v} symmetry, it is impossible to be situated obliquely within the membrane, since there is no reason for such an asymmetry, neither from the symmetry properties of the molecule nor those of the membrane. Therefore, in the case of the BA-F_6 molecule, the C_{v2} symmetry axis is expected to line up with the principal axis system of the ordering matrix, which in turn will line up with the external magnetic field. This behaviour is reflected in the ordering matrix being diagonal, i.e. S_{xz}=0 in the BA- and PhA-F_6 cases, and the last terms in equations (5.6) vanish.

Equations (5.6), with the respective simplifications where appropriate, were used to calculate the values of $S_{\alpha\beta}$ from the dipolar coupling values extracted from the CPMG spectra, as reported in table 5.2. Note that the signs given for D_{ij} in table 5.2 are to some extent ambiguous, since an inversion of *all* signs at once will give the identical simulated spectra of figure 5.6. Therefore, table 5.3 repeats the D_{ij} values of table 5.2, but now lists all possible assignments that are compatible with the observed spectra. For each of these assignments it is possible to calculate a set of $S_{\alpha\beta}$, i.e. determine the Saupe ordering matrix. For molecules having symmetry lower than C_{v2}, the analysis is complete once the values of $S_{\alpha\beta}$ have been determined. The low values attained in the present case prove that our molecules are highly mobile in the lipid bilayer, and an analysis only in terms of molecular orientation (as will be done for peptides in chapters VI to VIII) is not appropriate here.

Table 5.3: Values for diagonal elements of the Saupe ordering matrix extracted from the dipolar ^{19}F-NMR data.

system	D_{11} [Hz]	D_{22} [Hz]	D_{12} [Hz]	S_{zz}	S_{xx}-S_{yy}	S_{xx}	S_{yy}	S_{xz}	ε_{zz} [J/mol]	ε_{xx}- ε_{yy} [J/mol]
BA-F_6	124	124	-89	0.1356	0.022	-0.0570	-0.0786	./.	631.19	135.58
	-124	-124	89	-0.1356	-0.022	0.0570	0.0786	./.	-77.13	-91.69
PhA-F_6	150	150	-68	0.0878	0.001	-0.0436	-0.0443	./.	416.63	5.67
	-150	-150	68	-0.0878	-0.001	0.0436	0.0443	./.	-473.41	-4.41
BBA-F_6	341	178	-58	0.0373	-0.0370	-0.0372	-0.0002	0.0067	./.	./.
	-341	-178	58	-0.0373	0.0370	0.0372	0.0002	-0.0067	./.	./.
	178	341	-58	0.0373	-0.0370	-0.0372	-0.0002	-0.0067	./.	./.
	-178	-341	58	-0.0373	0.0370	0.0372	0.0002	0.0067	./.	./.

Probability distribution of BA-F_6 in the membrane

To set out with, it needs to be stated that only the high C_{v2} symmetry of the BA-F_6 molecule makes it possible to analyze its orientational and motional properties further than what has been achieved so far by determining the elements of the Saupe ordering matrix. In the case of the larger molecules PhA- and BBA-F_6, fast interconversion between molecular conformers prohibits the determination of molecular orientation. This is illustrated in figure 5.8 for the case of PhA-F_6. The acyl group on the molecule can interconvert between two conformations, and it needs to be assumed that the rate of interconversion is fast on the NMR timescale. Therefore, only a superposition of both conformers is observed in our experiments. As an effect, the observed dipolar interactions are determined by an intermediate coordinate system that is shown unprimed in figure 5.8, while the molecular coordinate system is shown with primes. The unprimed intermediate coordinate system does possess the high C_{2v} symmetry necessary to simplify equations (5.6). At the same time it prohibits any further interpretation of the results in structural terms, since the intermediate system is the one that

will line up with the bilayer normal for symmetry reasons. Since the relationship between intermediate and molecular coordinate systems is unknown, no information about the molecular coordinate system can be inferred here.

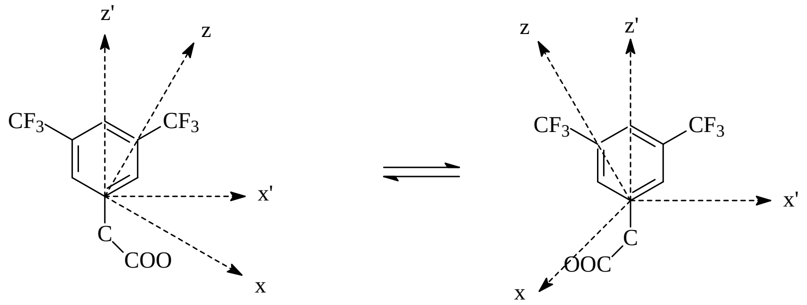

Figure 5.8: PhA- and BBA-F_6 possess a number of molecular conformers, whose interconversion makes the MOL frame of reference (shown primed) inappropriate for a structural interpretation of the NMR data.

Only the smallest molecule, BA-F_6, has actual C_{v2} symmetry. Using the formalism of mean torque,[18] the probability distribution can now be calculated for the orientation of the BA-F_6 molecule in the membrane, thanks to the high symmetry. The values S_{zz} and S_{xx}-S_{yy} reported in table 5.3 allow the calculation of two parameters ε_{zz} and ε_{xx}-ε_{yy} which describe the potential of mean torque that is exerted by the bilayer onto the embedded molecule. [35;36] The potential of mean torque U_{LC} describes the energy that is necessary to turn the molecule away from its equilibrium position. It is given by

$$U_{LC}(\tau',\rho') = -\sqrt{\frac{3}{2}}\left[\varepsilon_{zz}\frac{3\cos^2\tau'-1}{2} + \left(\varepsilon_{xx}-\varepsilon_{yy}\right)\frac{\sin^2\tau'\cos 2\rho'}{2}\right], \qquad (5.7)$$

where the degree of turning is measured by two polar angles τ' and ρ' (corresponding to τ and ρ, respectively, as introduced in chapter II and shown in figure 2.1). The potential of mean torque, $U_{LC}(\tau',\rho')$, determines the probability distribution $P_{LC}(\tau',\rho')$ by means of the Boltzmann distribution:

$$P_{LC}(\tau',\rho') = \frac{\exp\left[-U_{LC}(\tau',\rho')/kT\right]}{\int \exp\left[-U_{LC}(\tau',\rho')/kT\right] d\tau' d\rho'}. \qquad (5.8)$$

$P_{LC}(\tau',\rho')$ gives the probability density that the angle between the axis of symmetry and the lipid bilayer is between τ' and $\tau'+d\tau'$, and the angle between molecular y-axis and the node line is between ρ' and $\rho'+d\rho'$. For the present case of BA-F_6, the parameters ε_{zz} and ε_{xx}-ε_{yy} were determined by G. de Luca from the observed D_{ij} values, and they are given in table 5.3. Note that corresponding to the two possible assignments for the sign of dipolar coupling, two sets of ε_{zz} and ε_{xx}-ε_{yy} are obtained.

The two corresponding probability distributions $P_{LC}(\tau',\rho')$ for BA-F_6 were calculated according to equations (5.7) and (5.8) and are plotted in two different representations in figure 5.9. The distribution derived from the first sign assignment of table 5.3 shows a preferred orientation of the BA-F_6 molecule along the lipid bilayer normal, while the second one shows a weak preference for an alignment perpendicular to the lipid bilayer normal. Since this alignment is biophysically not sensible, we conclude that the distribution illustrated at the top

of figure 5.9 describes our system. This distribution makes perfect biophysical sense, since it describes the molecule to be 'upright' in the membrane, making its amphiphilic properties line up with the hydrophobicity profile of the lipid bilayer.

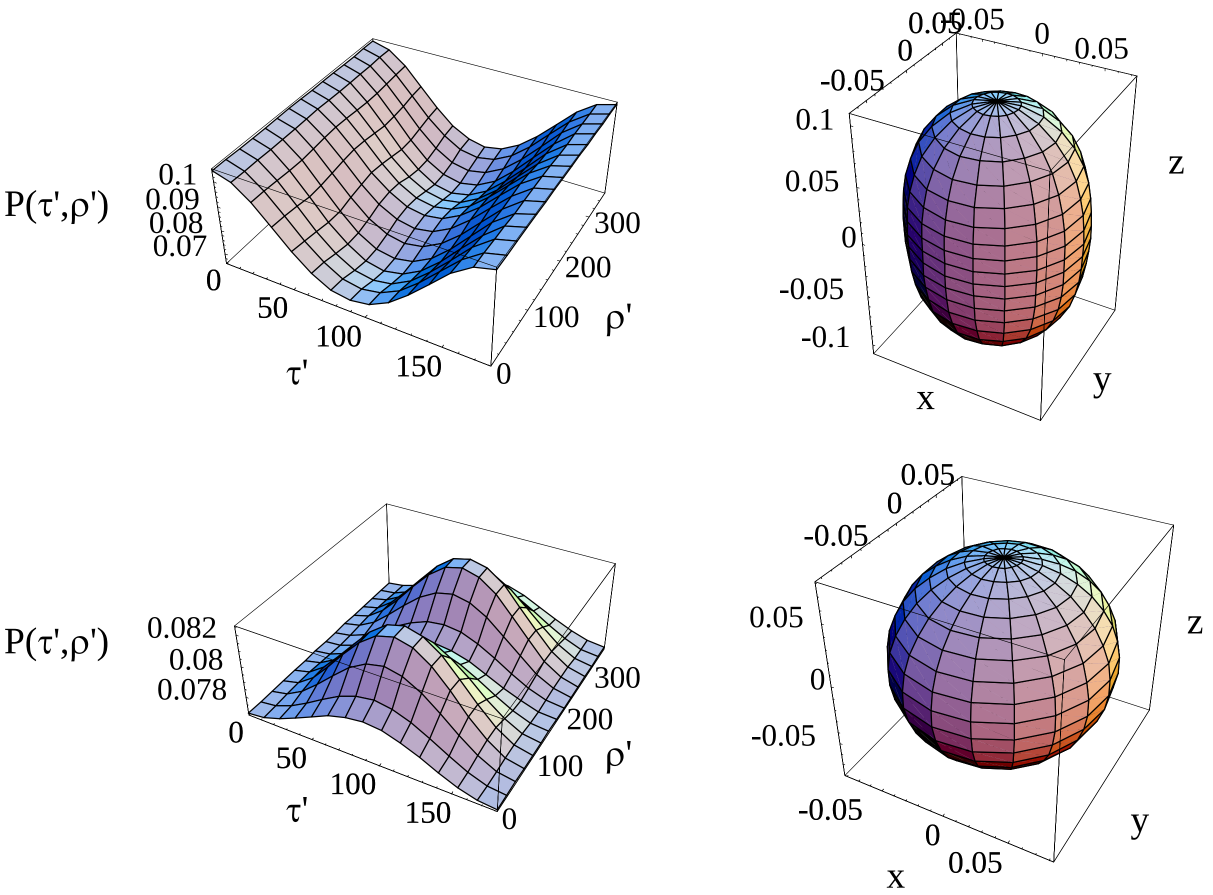

Figure 5.9: Probability distributions $P_{LC}(\beta,\gamma)$ calculated for BA-F_6. (Top) First and (bottom) alternative assignment of signs to dipolar couplings, as given in table 5.3. (Left) Cartesian plots of $P_{LC}(\tau',\rho')$ over the (τ',ρ')-plane, (right) spherical plot with τ' and ρ' as spherical coordinates.

Molecular dynamics simulation

In the preceding section, the BA-F_6 system's dipolar couplings could be explained by strong and strongly anisotropic molecular mobility, and a structural interpretation was given in terms of a probability distribution of the molecular orientation. In order to confirm the results by directly observing the mobility properties, a molecular dynamics simulation of the BA-F_6 system was carried out in collaboration with Dipl.-Ing. Barbara Hoff, MVM, Universität Karlsruhe.

The GROMACS 3.0[29] software package was used to calculate MD trajectories of six BA-F_6 molecules in a box of 128 DMPC molecules. In an initial run, the six molecules were placed into different regions of the box of lipids. Two molecules were placed into the aqueous phase, two into the lipid headgroup region, and two into the hydrophobic region of the lipid acyl chains. During the simulation, all molecules showed a strong tendency to move into the lipid headgroup region. This finding justifies a second run, in which all six molecules were located in the headgroup region from the very start.

In the conclusive MD run, all molecules retained their starting location in the lipid headgroup region. After an equilibration period of ca. 3 ns, all six molecules showed roughly the expected 'upright' orientation, where the hydrophobic phenyl ring carrying the CF_3-groups is pointing towards the bilayer interior, while the hydrophilic carboxyl group is in contact with the membrane lipid headgroups and points in the direction of the membrane normal. It is remarkable that the BA-F_6 molecules are located far up in the lipid headgroup region, almost preventing contact between the CF_3-groups and the lipid acyl chains, consistent with the similarity of ^{19}F-NMR spectra above and below the main lipid phase transition. Figure 5.10 shows a representative snapshot of three BA-F_6 molecules during the simulation. Note that the two molecules visible on the right of figure 5.10 are not in actual proximity, but are

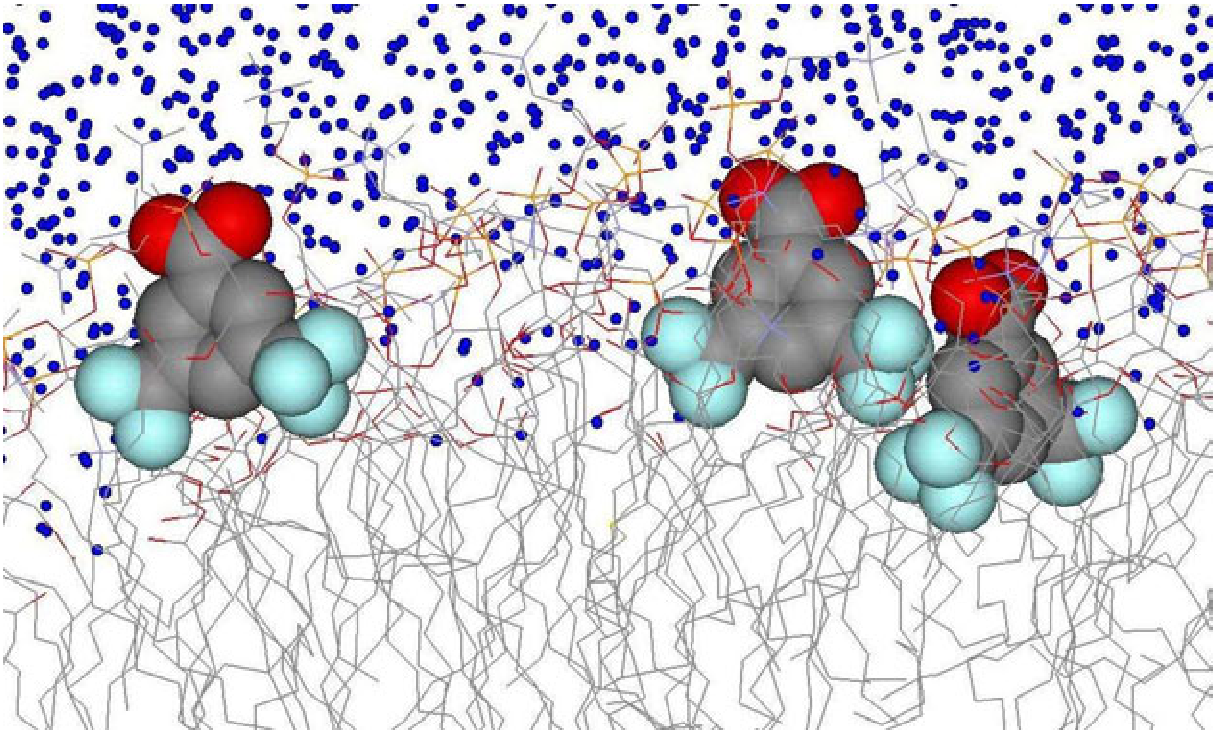

Figure 5.10: Snapshot of MD simulation, showing upright orientation of three of the six simulated BA-F_6 molecules in a cutout of the used box of 128 DMPC molecules. The lipid acyl region is shown to the bottom, headgroup region in the middle, and water as blue spheres on top.

separated in the direction of the paper plane, i.e. the apparent 'contact' is not real. For none of the six BA-F_6 molecules any dimerization or any other contact was observed. The rotational diffusion of the CF_3-groups around their axis of symmetry was clearly reproduced, while the rotational diffusion of BA-F_6 molecules around the membrane normal was not detectable within the 20 ns of our simulation.

In the snapshot of figure 5.10, the BA-F_6 molecules do not seem to be in a perfectly upright orientation. To determine whether this is due to thermal fluctuations or corresponds to a real tilted average orientation, we extracted values for the molecular tilt angle τ from the MD calculations. The tilt angle τ is defined as the angle enclosed by the molecular axis of symmetry and the bilayer normal, while ρ describes the azimuthal rotation of the molecular y-axis (defined as the connecting vector between both CF_3-pseudo-atoms, figure 5.3) with respect to the node line. The obtained τ trajectories are presented as figure 5.11 for the second (fully equilibrated) half of the simulation between 10 and 20 ns.

The two rows of trajectories correspond to the three molecules placed into each leaflet of the lipid bilayer. For this reason, the τ values around 30° in the upper monolayer (and row of panels) are equivalent to the values of 180°-τ=150° reported for the opposing monolayer. The trajectories clearly show that the time average of molecular tilt differs from zero. It has a fairly stable value of τ=27° with a standard deviation of only 6°. Analogous trajectories (data not shown) showed that the azimuthal rotation ρ is restricted to values around 20°. Thus, the BA-F_6 molecules are found to be oriented with a rather well-defined tilt angle with respect to the lipid bilayer.

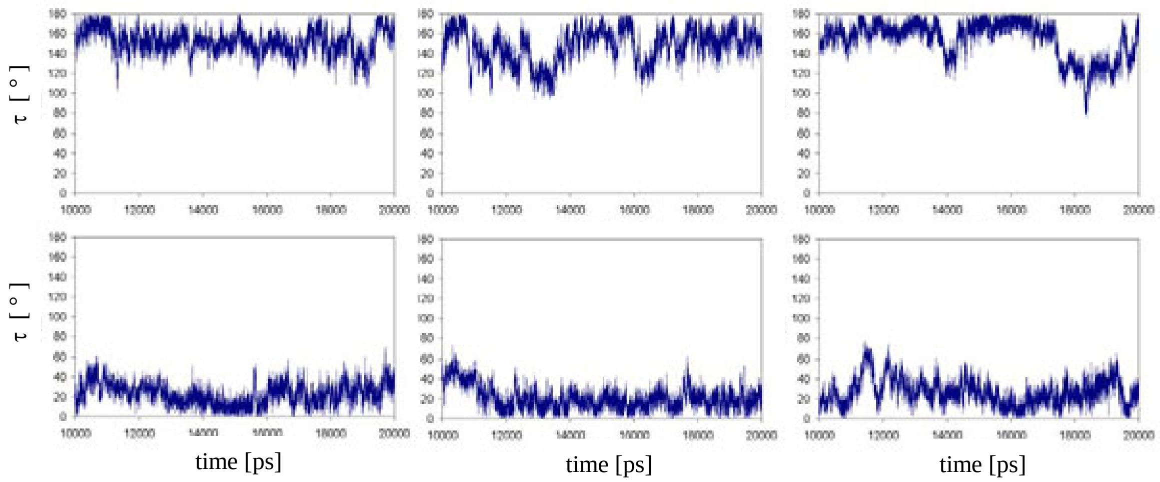

Figure 5.11: Trajectories of tilt angles τ of the six BA-F_6 molecules simulated in a DMPC bilayer

In addition, an unexpected and interesting mode of motion was observed in the trajectories. Some of the BA-F_6 molecules showed a very quick 180°-rotation of the phenyl ring around the molecular z-axis, i.e. the axis of C_2 symmetry. This 'ring-flip' converts the molecule into a symmetry-related identical orientation, but exchanges the positions of the two CF_3-groups. Although the ring-flip occurred only around 5 times in the present simulation, we believe it to be present as a relevant mode of motion in our system. An analogous ring-flip motion was seen at much higher frequency in a similar study of a completely hydrophobic molecule, pyrene, in a POPC bilayer.[37] We conclude that the characteristic times of the ring-flip are longer for systems of higher polarity, and that the ring-flip is present in our BA-F_6 system,

although the elongated characteristic time makes it visible only a few times in the 20 ns MD simulation.

To establish a quantitative connection to our NMR data via equation (2.14), values for the relevant molecular and segmental order parameters were calculated from the trajectories. For the molecular x-, y- and z-axes, as well as for the rotation axes of the CF_3-groups, time averaged order parameters $S_{ij} := \left\langle \left(3\cos^2\theta_{ij} - 1\right)/2 \right\rangle$ were calculated, where θ_{ij} is the angle between the respective axis and the laboratory z-axis. Table 5.4 gives the results.

Table 5.4: Order parameters observed for different molecular segments of the simulated molecules.

molecule	S_{zz}	$S_{xx}=S_{12}$	S_{yy}	S_{11}	S_{22}
1	0.812	-0.401	-0.411	-0.055	-0.141
2	0.662	-0.290	-0.372	0.160	-0.271
3	0.643	-0.238	-0.405	0.364	-0.400
4	0.710	-0.418	-0.292	-0.237	-0.036
5	0.806	-0.393	-0.413	0.033	-0.224
6	0.460	-0.043	-0.417	0.542	-0.381
average of 1...6	0.682	-0.297	-0.385	0.134	-0.242
NMR-relevant		-0.297		-0.054	

The values extracted from equilibrated parts of the six BA-F_6 trajectories show a very broad spread of values, but their averages are in good agreement with typical lipid bilayer values.[38] Also shown (marked by gray shading and labeled 'NMR-relevant') are averaged values $(S_{11}+S_{22})/2$ for the intra-CF_3 segmental order parameters, a procedure justified by the ring-flip motion. This value, along with the inter-group segmental order parameter S_{12}, can now directly be compared to the values obtained in NMR spectroscopy, and is therefore shown shaded in table 5.4.

Discussion

The complicated CPMG dipolar patterns of several related hexafluorinated substances were successfully measured, analyzed, and simulated. The spectral complexity and intricate analysis makes it seem rather challenging to employ two interacting CF_3-groups as molecular reporters on molecular distances and alignments. A special case may be the formation of symmetric oligomers, where the presence of only a single relevant parameter (i.e. distance) should make the spectral complexity tractable. The coupling between two mono-fluorinated positions seems to be a more promising approach for distance measurements, as successfully demonstrated.[6;39] These show a simple doublet lineshape and, in contrast to their CSA analysis, their dipolar coupling is not complicated by side chain torsion.

It was possible to characterize molecular mobility by determining the elements of the ordering matrix from the observed dipolar coupling values, using the Saupe ordering matrix. In the case of the asymmetric PhA- and BBA-F_6 molecules, this ends the analysis. For the symmetric BA-F_6 molecule, a further calculation of the potential of mean torque was possible, which yielded the probability distribution of the preferred molecular alignment in the membrane. However, two possible solutions were found for the probability distribution. One shows the expected result of an 'upright' molecule, with its hydrophilic carboxyl-group pointing towards and immersed in the lipid headgroup region, while the hydrophobic moiety projects into the lipid acyl chain region of the lipid bilayer. The alternative solution gives the unreasonable picture of a molecule oriented perpendicularly within the lipid bilayer and can thus be excluded.

An MD simulation confirmed the intuitive expectation that the BA-F_6 molecules are oriented in the lipid bilayer according to their amphiphilic properties, which allows for energetically favorable hydrogen-bonding to the lipid headgroup region. This finding rules out the unreasonable second probability distribution found in Saupe analysis. Differing from the results of the Saupe analysis, an azimuthally restricted orientation at a slight molecular tilt of τ=27° was found. This does not constitute a contradiction, since even if the potential of mean torque is minimal for τ=0, spherical geometry will require a non-vanishing value for the averaged τ, since the statistical weighting of any particular value of τ increases with that value.

From CPMG spectra as well as from the MD simulation, values for molecular and segmental order parameters could be extracted, as compared in table 5.5. The order parameter values from NMR data are surprisingly low[40], especially when considering that—according to our MD simulation—the molecules are located in the lipid headgroup region, the most ordered region of the lipid bilayer[38]. Due to their small values, no quantitative agreement between experimental and simulated order parameters could be reached. We attribute this finding to the short time span of 20 ns of the simulation, which is not able to fully map all orientations present in a characteristic trajectory, where thermal motions will reach larger amplitudes on longer time scales. Moreover, additional mobility modes with far longer time scales may be present, e.g. a dissociation-association equilibrium[41;42] of the hexafluorinated molecules between the lipid bilayer and interstitial water. Both effects would not become evident in the relatively short time span covered by our simulation.

Table 5.5: Comparison of segmental and principal axis order parameters as determined on BA-F_6 in DMPC by NMR experiment and MD simulation.

	S_{zz}	S_{xx}	S_{yy}	$(S_{xx}-S_{yy})$	$S_{11}=S_{22}$	S_{12}	S_{12}/S_{11}
NMR experiment	0.136	-0.057	-0.079	-0.022	-0.009	-0.057	6.3
MD simulation	0.682	-0.297	-0.385	-0.088	-0.054	-0.297	5.5

From the data in table 5.5 it is evident that anisotropic molecular mobility is clearly present in the MD trajectories. Actually, the asymmetry (S_{xx}-S_{yy}) seen in MD is considerably larger than the one needed to fit the NMR data. The last column in table 5.5 shows the ratio S_{12}/S_{11}, in order to make the NMR data and the MD trajectory comparable despite the differing magnitude of their values. The ratio turns out to be almost identical for the two different approaches, again confirming the role of anisotropic mobility and the overall applicability of the Saupe ordering matrix for small membrane-embedded compounds.

Reference List

(1) Grage, S. L.; Ulrich, A. S. *J.Magn.Reson.* **1999**, *138*, 98-106.

(2) Grage, S. L.; Ulrich, A. S. *J.Magn.Reson.* **2000**, *146*, 81-88.

(3) Afonin, S.; Glaser, R. W.; Berditchevskaia, M.; Wadhwani, P.; Gührs, K.-H.; Möllmann, U.; Perner, A.; Ulrich, A. S. *Chembiochem* **2003**, *4*, 1151-1163.

(4) Afonin, S.; Dürr, U. H. N.; Glaser, R. W.; Ulrich, A. S. *Magn.Reson.Chem.* **2004**, *42*, 195-203.

(5) Glaser, R. W.; Sachse, C.; Dürr, U. H. N.; Wadhwani, P.; Ulrich, A. S. *J.Magn.Reson.* **2004**, *168*, 153-163.

(6) Salgado, J.; Grage, S. L.; Kondejewski, L. H.; Hodges, R. S.; McElhaney, R. N.; Ulrich, A. S. *J.Biomol.NMR* **2001**, *21*, 191-208.

(7) Grage, S. L.; Gauger, D. R.; Selle, C.; Pohle, W.; Richter, W.; Ulrich, A. S. *Phys.Chem.Chem.Phys.* **2000**, *2*, 4574-4579.

(8) Gilchrist Jr, M. L.; Monde, K.; Tomita, Y.; Iwashita, T.; Nakanishi, K.; McDermott, A. E. *J.Magn.Reson.* **2001**, *152*, 1-6.

(9) Smith, S. O.; Aschheim, K.; Groesbeek, M. *Q.Rev.Biophys.* **1996**, *29*, 395-449.

(10) Ulrich, A. S. High resolution solid state NMR, ^{1}H, ^{19}F; In *Encyclopedia of spectroscopy and spectrometry*; Lindon, J. C., ed. Academic Press: 2000; pp 813-825.

(11) deAzevedo, E. R.; Hu, W.-G.; Bonagamba, T. J.; Schmidt-Rohr, K. *J.Am.Chem.Soc.* **1999** , *121*, 8411-8412.

(12) Algieri, C.; Castiglione, F.; Celebre, G.; De Luca, G.; Longeri, M.; Emsley, J. W. *Phys.Chem.Chem.Phys.* **2000**, *2*, 3405-3413.

(13) Emsley, J. W. Liquid crystals: General considerations; In *Encyclopedia of NMR*; Grant, D. M., Harris, R. K., eds. Wiley: New York, 1996; pp 2788-2799.

(14) Diehl, P. Structure of rigid molecules dissolved in liquid crystalline solvents; In *Encyclopedia of NMR*; Grant, D. M., Harris, R. K., eds. Wiley: New York, 1996; pp 4591-4602.

(15) Foord, E. K.; Cole, J.; Crawford, M. J.; Emsley, J. W.; Celebre, G.; Longeri, M.; Lindon, J. C. *Liq.Cryst.* **1995**, *18*, 615-621.

(16) Celebre, G.; Longeri, M.; Emsley, J. W. *Mol.Phys.* **1988**, *64*, 715-723.

(17) Emsley, J. W.; Fung, B. M.; Heaton, N. J.; Luckhurst, G. R. *J.Chem.Phys.* **1987**, *87*, 3099-3103.

(18) Emsley, J. W. Liquid crystalline samples: Structure of nonrigid molecules; In *Encyclopedia of NMR*; Grant, D. M., Harris, R. K., eds. Wiley: New York, 1996; pp 2781-2787.

(19) Levitt, M. H.; Freeman, R. *J.Magn.Reson.* **1979**, *33*, 473-476.

(20) Freeman, R.; Kempsell, S. P.; Levitt, M. H. *J.Magn.Reson.* **1980**, *38*, 453-479.

(21) Haeberlen, U. *High Resolution NMR in Solids--Selective Averaging*; Academic Press: New York, San Francisco, London, 1976.

(22) Mehring, M. *High Resolution NMR of Solids*; Springer: Berlin, 1976.

(23) Engelsberg, M.; Yannoni, C. S. *J.Magn.Reson.* **1990**, *88*, 393-400.

(24) Castiglione, F.; Carravetta, M.; Celebre, G.; Longeri, M. *J.Magn.Reson.* **1998**, *132*, 1-12.

(25) Celebre, G.; De Luca, G.; Longeri, M.; Sicilia, E. *J.Chem.Inf.Comput.Sci.* **1994**, *34*, 539-545.

(26) Longeri, M.; Celebre, G. Liquid crystalline samples: Spectral analysis; In *Encyclopedia of NMR*; Grant, D. M., Harris, R. K., eds. Wiley: New York, 1996; pp 2774-2781.

(27) Bak, M.; Rasmussen, T.; Nielsen, N. C. *J.Magn.Reson.* **2000**, *147*, 296-330.

(28) Brouwer, E. B.; Calloner, R.; Harris, R. K. *Solid State Nucl.Magn.Reson.* **2000**, *18*, 37-52.

(29) Lindahl, E.; Hess, B.; van der Spoel, D. *J.Mol.Model.* **2001**, *7*, 306-317.

(30) Berger, O.; Edholm, O.; Jahnig, F. *Biophys.J.* **1997**, *72*, 2002-2013.

(31) Berendsen, H. J. C.; Postma, J. P. M.; van Gunsteren, W. F.; DiNola, A.; Haak, J. R. *J.Chem.Phys.* **1984**, *81*, 3684-3690.

(32) Englert, G.; Saupe, A. *Z.Naturforsch.* **1964**, *19a*, 172-177.

(33) Saupe, A. *Z.Naturforsch.* **1964**, *19a*, 161-171.

(34) Saupe, A. *Angew.Chem.internat.Edit.* **1968**, *7*, 97-112.

(35) Celebre, G.; De Luca, G.; Longeri, M.; Pileio, G.; Emsley, J. W. *J.Chem.Phys.* **2004**, *120*, 7075-7084.

(36) Emsley, J. W.; Luckhurst, J. R. *Mol.Phys.* **1980**, *41*, 19.

(37) Hoff, B.; Strandberg, E.; Ulrich, A. S.; Tieleman, D. P.; Posten, C. *Biophys.J.* **2005**, *88*, 1818-1827.

(38) Tieleman, D. P.; Marrink, S.-J.; Berendsen, H. J. C. *Biochim.Biophys.Acta* **1997**, *1331*, 235-270.

(39) Afonin, S. Structural studies on membrane-active peptides in lipid bilayers by solid state ^{19}F-NMR. 2003. Friedrich-Schiller-Universität Jena.
Ref Type: Thesis/Dissertation

(40) Hagemeyer, A.; Tarroni, R.; Zannoni, C. *J.Chem.Soc.Faraday Trans.* **1994**, *90*, 3433-3442.

(41) Schwarz, G.; Stankowski, S.; Rizzo, V. *Biochim.Biophys.Acta* **1986**, *861*, 141-151.

(42) Montich, G.; Scarlata, S.; McLaughlin, S.; Lehrmann, R.; Seelig, J. *Biochim.Biophys.Acta* **1993**, *1146*, 17-24.

VI. Fusogenic peptide B18

An orientational analysis for fluorinated analogues of the fusogenic peptide B18 in model lipid bilayers is given. As a prerequisite for this analysis, exact values for the ^{19}F CSA tensor had to be determined. Narrow resonances in macroscopically aligned lipid bilayers could then be used to calculate the well-defined orientation of both helical segments of B18 in the lipid bilayer. It proved necessary to include side chain dynamics as well as overall molecular mobility into the calculations. An unusual mode of membrane binding could thus be described. The results were published in *Magnetic Resonance in Chemistry*[1], the publication is attached to this thesis as appendix C.

Introduction

The fusogenic peptide ‘B18’ investigated here stems from the fully conserved membrane-interacting region of the acrosomal sea urchin protein bindin, which is responsible for merging the membranes of sperm and egg during fertilization.[2;3] The peptide represents the minimal sequence that retains the fusogenic properties of the parent protein,[4] and it has many features in common with viral fusion peptides.[5] B18 has the amino acid sequence

H_2N-L^{103}GLLLRHLRHHSNLLANI^{120}-COOH,
     *   ***   *   ***   *

with numbering given according to *Strongylocentrotus purpuratus* bindin. A ^{1}H-NMR structure of B18 in membrane-mimicking 30% TFE solution, as well as in detergent micelles, was determined by Glaser et al.[6] The peptide was found to assume the well-defined structure presented in figure 6.1. It consists of two α-helices that are shown underlined in the B18 sequence above. The C-terminal helix is found to be less ordered and even shows some characteristics of a 3_{10}-helix. The two sub-helices are connected by a loop which can be thought of as a flexible hinge. It contains three histidine residues, which may interact with Zn^{2+} ions that are essential for B18's function. Apart from the hydrophilic loop region, the structure has a distinct hydrophobicity profile. Each subhelix has a hydrophobic as well as a hydrophilic surface, which will give each subhelix a preferred orientation when attached to amphiphilic lipid bilayers.

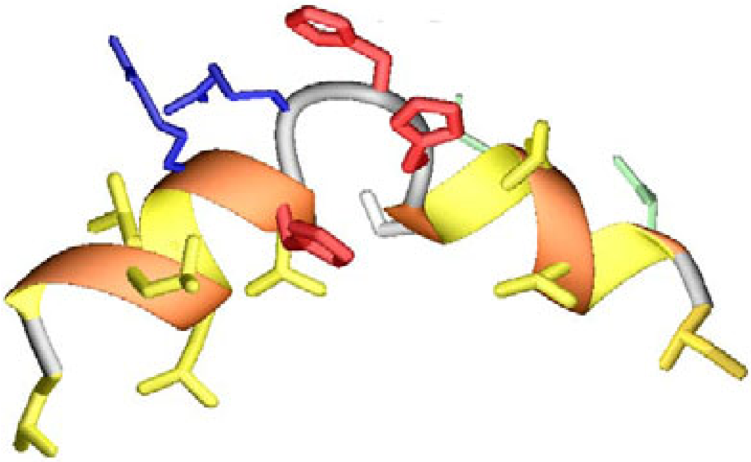

Figure 6.1: Molecular structure of B18 in 30% TFE, as determined by Glaser et al.[6]

In the present study, a more detailed B18 structure in a lipid bilayer was assembled from a series of orientational constraints that were obtained by solid-state ^{19}F-NMR from nine singly 4F-Phg labeled analogues of B18. The labeled positions are indicated by asterisks in the sequence above. Within each half of the sequence a hydrophobic stretch of three amino acids fortuitously occurs (L105-L106-L107 in the N-terminal segment, and L116-L117-A118 in the C-terminal segment). Each of these positions could successfully be replaced by 4F-Phg without losing the fusogenic activity of the peptide. Thus, three positions were labeled within each segment, and three additional labels cover both termini and the hinge region.

Materials and Methods

Peptide synthesis and sample preparation

Nine analogues of B18 labeled with 4F-Phg were synthesized and purified by Sergii Afonin, and their structural and functional similarity to the wild type was verified by circular dichroism spectroscopy (CD) and vesicle fusion assays.[7] Oriented lipid bilayer samples were prepared in a mixture of 1,2-dimyristoyl-*sn*-glycero-3-phosphocholine and 1,2-dimyristoyl-*sn*-glycero-3- [phospho-*rac*-(1-glycerol)] [DMPC-DMPG (80:20, mol/mol)], purchased from Avanti Polar Lipids (Alabaster, AL, USA). Peptide and lipid were co-dissolved in 70% methanol at a peptide:lipid ratio of 1:150, deposited on glass slides (0.06 x 7.5 x 18 mm^3, Marienfeld, Lauda-Königshofen, Germany), vacuum-dried overnight, and hydrated for 1-4 days at 48°C over saturated K_2SO_4 solution (approx. 98% relative humidity at 20°C), wrapped and immediately used for NMR.

^{19}F-NMR spectroscopy

Solid-state NMR experiments were carried out on a wide-bore Unity Inova 500 MHz spectrometer (Varian, Palo Alto, CA, USA). For ^{19}F-NMR, a ^{19}F/^{1}H double-tuned flat-coil probe with a goniometer (Doty Scientific, Columbia, SC, USA) and an external 470 MHz high-power amplifier (Creative Electronics, Los Angeles, CA, USA) were used. ^{1}H-decoupled ^{19}F-NMR spectra were acquired at 35°C with typically 2000 transients, and referenced externally with 100 mM NaF in 10mM HEPES, pH 7.5 (measured at 35°C and set to –120.4 ppm).[8] Continuous-wave proton decoupling was applied at approximately 15 kHz B_1 field strength. The static ^{19}F CSA tensor elements were determined by fitting the powder spectra of the lyophilized peptides with a self-written C++ program and DMfit[9]. Composite pulses[10;11] and long echo delay times were used to obtain ^{19}F-NMR spectra free from off-resonance distortions.

In addition, ^{31}P-NMR experiments were performed on a home-built ^{1}H/X probe equipped with a flat coil. ^{1}H-decoupled ^{31}P-NMR spectra were recorded to judge the quality of lipid orientation in the samples.

Results

^{19}F CSA tensors determined on lyophilized peptides

The proposed experimental scheme for determining molecular orientation relies heavily on the knowledge of the magnitude and molecular situation of the ^{19}F-CSA tensor, as described in the introductory chapter I. In the case of the 4F-Phg side chain, the molecular situation of the ^{19}F CSA tensor was found to conform with molecular symmetry.[12-15] Its magnitude had been determined for 4F-Phg incorporated into the β-sheet peptide gramicidin S previously,[16] but not in an α-helix. Therefore, to obtain reliable tensor values for structural analysis and to assess their variability, we determined the ^{19}F CSA tensor's principal values from lyophilized powders of six of the nine labeled B18 analogues, as summarized in Table 6.1.

In usual Hahn-echo experiments, the lyophilized peptides were found to give noticeably distorted powder lineshapes due to the large overall spectral width of almost 100 ppm. As a remedy, several schemes of composite pulses—designed to improve the spectral excitation profiles of ordinary pulses—were used to replace the initial 90°-pulse as well as the 180°-echo pulse of the Hahn echo sequence. To replace the basic 90°-pulse, composite pulses according to Siminovitch *et al.*[17] (denoted 'S' in the following) and according to Derome[18] (D) were tested. A composite pulse as suggested by Levitt and Freeman[11] (L) was employed as 180°-echo pulse. Observed spectra are shown alongside table 6.1, labeled with two letter codes giving the employed pulse types, with basic pulses labeled 'P'. The echo sequence using S-90° and L-180° composite pulses yielded an almost perfect tensor lineshape, shown boxed in table 6.1.

The optimal choice of composite pulses (SL) was then used to acquire the ^{19}F-NMR spectra of the lyophilized powders of six of the nine investigated ^{19}F-labeled B18 analogues. Extracted principal values of the ^{19}F CSA tensors are given in table 6.1. The static tensor elements are rather similar for all 4F-Phg labels, hence the subsequent data interpretation was based on values of σ_{11}=–60.1(±2.2) ppm, σ_{22}=–124.3(±0.3) ppm, and σ_{33}=–155.3 (±1.2)ppm,

Table 6.1: Principal ^{19}F-CSA tensor elements observed in six ^{19}F-labelled analogues of B18. The panel shows lineshapes observed on lyophilized B18-Leu106(4F-Phg) using different composite pulses in the Hahn-echo sequence. The two letter labels indicate the type of composite pulses used, see text.

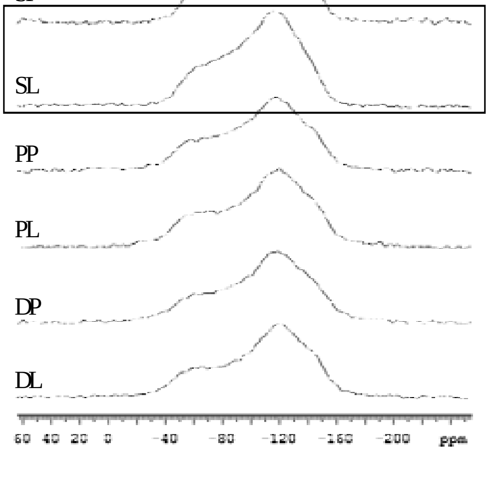

labeled position	principal tensor values in lyophilized powder		
	σ_{11} [ppm]	σ_{22} [ppm]	σ_{33} [ppm]
L 103	./.	./.	./.
L 105	-63.0	-124.5	-154.0
L 106	-63.0	-124.5	-154.0
L 107	-59.0	-124.8	-157.0
L 110	./.	./.	./.
L 116	-58.7	-124.0	-155.5
L 117	-58.6	-124.0	-155.8
A 118	-58.5	-124.1	-155.6
I 120	./.	./.	./.

corresponding to a mean isotropic value of σ_{iso}=–113.2 (±2.2) ppm. These values are also surprisingly close to values found for the polycrystalline free amino acid 4F-Phg in chapter III of this thesis. Table 3.3 gave all values in comparison, with comments in the accompanying text.

^{19}F-NMR of oriented bilayer samples

Afonin[19] showed that macroscopically aligned bilayer samples of 4F-Phg labeled B18 can be prepared in a 80:20 mixture of DMPC and DMPG provided that a peptide to lipid ratio below 1:100 is chosen to avoid aggregation. The macroscopically oriented samples show single resonances in their ^{19}F-NMR spectra, with narrow linewidths around 2 ppm. The panel of table 6.2 shows typical spectra acquired on an oriented bilayer sample of B18-Leu106(4F-Phg) recorded at parallel and perpendicular sample tilt angles of the membrane normal with respect to the magnetic field. The presence of a narrow line also at 90° tilt proves that the peptide undergoes rotational diffusion lipids around the membrane normal, and that the peptide takes part in that rotational diffusion. The resonance frequencies observed at parallel and perpendicular tilt are denoted $\sigma_{||}$ and $\sigma_{\perp}$, respectively. They fully characterize the rotationally averaged, axially symmetric ^{19}F-CSA tensor found in the membrane. The values for $\sigma_{||}$ and $\sigma_{\perp}$ measured on oriented samples of the nine 4F-Phg labeled B18 analogues are compiled in table 6.2.

The respective isotropic chemical shifts were calculated for each labeled position and are given in table 6.2. It is known that the isotropic chemical shifts of ^{19}F-substituents vary to some extent with the chemical and solvent environment, hence the deviations seen here are not surprising (e.g. of the N-terminal amino acid that is not engaged in another peptide bond).

To achieve the highest possible accuracy of ± 1 ppm in the data analysis to be conducted, this variation was explicitly taken into account by basing the analysis on the observed chemical shift anisotropy parameter $\delta^{obs} := \sigma_{||} - \sigma_{iso}$ (*cf.* equation (1.7)) rather than on the absolute

Table 6.2: Resonances observed on oriented membrane samples of the nine fluorinated B18 analogues at parallel and perpendicular tilt with respect to the magnetic field. The panel to the left shows the B18-Leu106(4F-Phg) spectra as illustration.

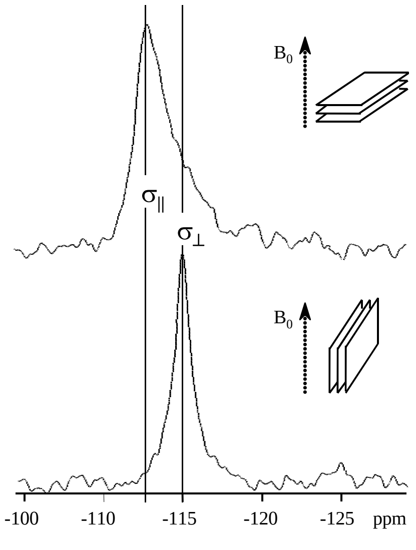

labeled position	^{19}F-NMR resonances in macroscopically aligned bilayers			
	$\sigma_{\|\|}$ [ppm]	$\sigma_{\perp}$ [ppm]	σ_{iso} [ppm]	δ^{obs} [ppm]
L 103	-115.0	-111.1	-112.4	-2.6
L 105	-110.1	-118.0	-115.4	+5.3
L 106	-112.7	-115.1	-114.3	+1.6
L 107	-116.2	-114.8	-115.3	-0.9
L 110	-120.0	-111.1	-114.1	-5.9
L 116	-112.6	-116.7	-115.3	+2.7
L 117	-109.0	-118.6	-115.4	+6.4
A 118	-118.2	-113.6	-115.1	-3.1
I 120	-121.3	-111.1	-114.5	-6.8

values $\sigma_{||}$ and $\sigma_{\perp}$. Values for δ^{obs} calculated from the observed resonances are given in table 6.2. Resorting to δ^{obs} does not alleviate the need for exact chemical shift referencing to minimize susceptibility-induced errors, since the observed range of δ^{obs} values is rather narrow and susceptibility effects are especially pronounced between the parallel and perpendicular orientation of a flat sample.[8;20]

An important aspect in the structural analysis of B18 concerns the question whether the 4F-Phg side chains are able to rotate freely around the C_α-C_β bond, as this would eliminate the need to set the side chain torsion angle χ_1 to any preferred mean value. The energy barrier for phenyl rotation is known to vary significantly in organic molecules, e.g. from 0.96 to 947.7 kJ mol^{-1} in glassy polystyrenes.[21] It is tempting to speculate that free rotation of the fluoro-phenyl group is the cause for the narrow range of δ^{obs} values found in B18 samples. But a closer look at the geometrical and CSA tensor situation will reveal this not to be the case. Free rotational averaging of the phenyl ring would yield an axially symmetric tensor defined by $\sigma_{\perp}=(\sigma_{11}+\sigma_{33})/2=-107.7$ppm and $\sigma_{||}=\sigma_{22}=-124.3$ppm. Since $\sigma_{\perp}$ is averaged from the extreme components of a tensor lineshape with $\eta\approx1$, the residual CSA anisotropy of the averaged tensor is only $\delta^{rot}=\sigma_{||}-\sigma_{iso}=-11.1$ppm. Therefore, given free rotation of the phenyl side chain, the possible values of $\delta^{obs}=\sigma_{||}^{obs}-\sigma_{iso}^{obs}$ would be restricted to an extrememly narrow range from +5.5 ppm downfield to –11.1 ppm upfield of σ_{iso}. Being placed into a liquid crystalline bilayer, long-axial diffusion of the peptide around the bilayer normal will lead to additional motional averaging of the effective CSA tensor by up to a factor of 2, depending on the side chain alignment with respect to the membrane normal. Examining the data observed on B18 analogues, the values of δ^{obs} are in two instances found to be wider than or near the limit of δ^{rot} accessible in the case of free phenyl rotation. The violating values of δ^{obs} are indicated by grey shading in table 6.2. The value observed in B18-Leu105(4F-Phg) is on the very edge of possible values, thus it would only be compatible with a freely rotating phenyl ring if the overall wobbling of the peptide ceases ($S_{mol}=1$), which is not a realistic assumption. Moreover, the δ^{obs} of B18-Leu117(4F-Phg) is clearly outside the allowed spectral range that would be consistent with an unrestricted fluoro-phenyl side chain. Additional violations were found in D-epimeric peptides that were a by-product in the synthesis of 4F-Phg labeled B18, and in doubly 4F-Phg labeled B18 mutants.[7] Hence, there is clear spectroscopic evidence that the 4F-Phg side chain cannot rotate freely in the present peptide-lipid system.

Therefore, the influence of side chain torsion and mobility had to be included into the data analysis. A restricted rotation of the phenyl ring will lead to only partial narrowing of δ^{static} by a concerted shift of σ_{11} and σ_{33} towards $\sigma_{\perp}$, which we quantify by the side chain order parameter S_{Phg} as defined in equation (2.18). By assuming a single uniform value of S_{Phg} for all labeled positions, the alignment of the partially averaged CSA tensor in the membrane becomes accessible, as the model provides a reasonably detailed description of the molecular situation while staying sufficiently simple not to over-interpret the data.

Molecular modeling

The peptide was modeled as two independent molecular units, namely the N- and C-terminal segments, as observed in the ^{1}H-NMR solution structure. Analysis started with the stretches of three consecutive labels occurring in each segment. These core segments were modeled as idealized structural elements. To account for the pronounced structural plasticity found in

fusogenic peptides, all commonly occurring types of secondary structure had to be considered. Namely, model structures in pdb-format were generated to represent ideal backbone conformations of α-helix, 3_{10}-helix, and β-sheet, which were modeled according to IUPAC-IUB-recommended values[22]. For an ideal right-handed α-helix, Ramachandran angles[23] of φ=-57°, ψ=-47°, ω=180° were used. An ideal β-sheet was modeled either in a parallel (φ=-119°, ψ=113°, ω=180°) or anti-parallel (φ=-139°, ψ=135°, ω=-178°) conformation. For the 3_{10}-helix the torsion angles were taken as φ=-49°, ψ=-26°, ω=180°. Whenever an idealized model for the core segments yielded good consistency with experimental data, hinge and/or terminal residues were included into the model to determine whether they participate in a subunit's secondary structure.

The molecular coordinate system MOL was individually defined for each core segment and each type of secondary structure. The long axis of the secondary structure element running from the N- to the C-terminus was defined as the z-axis z^{MOL}. The y^{MOL} axis was defined as the axis perpendicular to z^{MOL} which projects through C_α of the first of three consecutively labeled residues (i.e. C_α of L105 and L116). The x^{MOL}-axis then needs to be defined as orthogonal to y^{MOL} and z^{MOL}, and giving a right-handed coordinate system. The choice of MOL is shown in figure 6.2 for the case of an α-helix. Here, the z^{MOL}-axis coincides with the helix symmetry axis in the direction from N- to C-terminus. This definition is identical to the definitions of Kovacs et al.[24] and van der Wel *et al.*[25] Also illustrated in figure 6.2 are the Euler angles ρ and τ characterizing the orientation of the sub-helix with respect to the lipid bilayer, which is oriented perpendicular to the magnetic field B_0. The angle τ gives the tilt between z^{MOL} and the membrane normal, the azimuthal rotation ρ gives the molecule's polarity as measured between the node line and y^{MOL} (cf. chapter II).

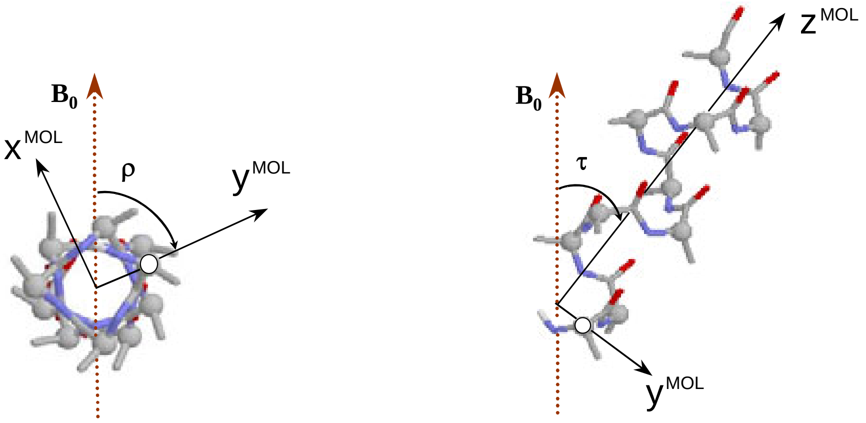

Figure 6.2: Definition of MOL coordinate system, (left) as viewed down the helix axis, and (right) as seen from the side

4F-Phg was placed into a pdb-file as a 'mutation' of the corresponding amino acid (using phenylglycine coordinates from a SYBYL amino acid library). The procedure does not alter the backbone conformation. Next, the conformation of the fluoro-phenyl side chain had to be considered. As shown in the preceding section, there is direct spectroscopic evidence that the fluoro-phenyl group does not show free rotational diffusion, but is restricted in its mobility. Side chain conformation is described by the torsion angle χ_1, defined as the dihedral angle between the N-C_α-C_β-C_γ atoms of 4F-Phg. Figure 6.3 shows χ_1 in a Newman-type projection

of the 4F-Phg residue, looking along the C_β-C_α direction. It is obvious that certain values of χ_1 are very unfavorable, e.g. when they infer a steric clash between H_γ protons and the polar carbonyl group of the backbone. To find the favored values of χ_1, the molecular modeling program packages InsightII (Accelrys Inc., San Diego, CA, USA) and SYBYL (Tripos Inc., St. Louis, MO, USA) were used to calculate the total molecular energy as a function of χ_1 using standard force fields. The resulting 'energy profiles' of the 4F-Phg side chain in idealized poly-Ala structural segments show the most favorable χ_1 angle to be 110° for an α-helix, 115° for a 3_{10}-helix, and 65° for a β-sheet. In helical structures, the minima in χ_1 are found to be far more pronounced than in a β-sheet structure.

The right panel of figure 6.3 presents the situation of the PAS of the ^{19}F CSA tensor within the molecular geometry of the fluoro-phenyl group, which coincides with the local geometry.[12-15] Axis naming is as described in chapter I, with the principal elements of the ^{19}F CSA tensor being ordered by magnitude, $\sigma_{11} \leq \sigma_{22} \leq \sigma_{33}$. Using this PAS definition, inbuilt measuring functions of InsightII and SYBYL were used to determine a set of Euler angles for the transformations from PAS to MOL for each label in the model pdb-structures. The extracted sets of Euler angles are then used as input in the structural analysis outlined in chapter II to yield *rmsd* error functions according to equation (2.1).

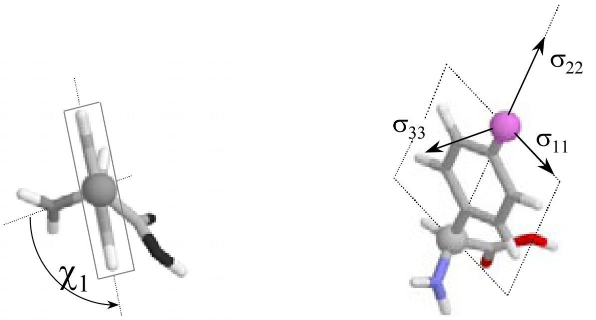

Figure 6.3: Definition of fluoro-phenyl side chain torsion angle χ_1 in 4F-Phg (left), and principal axis system of ^{19}F CSA tensor in the fluoro-phenyl group (right).

Side chain mobility strongly influences the best-fit

The structure of B18 in solution consists of two helical segments connected by a flexible hinge. To take this situation into account, the orientational analysis was first carried out individually for each molecular segment. This section gives a detailed description of fitting an α-helical model to the resonances observed in the 4F-Phg labels introduced in positions 105, 106 and 107, i.e. the core region of the N-terminal segment that had been found to be α-helical in solution. The choice of segment and model is arbitrary, of course, but turns out to be the most instructive one once the results are known.

In the following prototypical fit of an α-helical model to our data, idealized perfect α-helices were employed as described in chapter II. The torsion angle χ_1 of the 4F-Phg side chain was assumed to be fixed to the optimum value described above, which can be determined with reasonable reliability and accuracy from energy profiles. The local rotational mobility of the phenyl ring around that value was accounted for by use of a rotational order parameter S_{Phg}, as defined in equation (2.18). The prediction of simulated values $\delta^{sim} = \sigma_{\parallel}^{sim} - \sigma_{iso}$ according to equation (1.3)—where $\sigma_{\parallel}$ takes the role of σ_{zz}—for use in best-fit analysis obviously does not introduce additional computational challenges. Taking into account all mentioned aspects,

data analysis of the N-terminal segment according to the procedures outlined in chapter II yields the (ρ,τ)-plots of *rmsd* depicted in figure 6.4. Rmsd is now a function of four variables, namely ρ and τ which are presented as usual on the x- and y-axis of the (ρ,τ)-plots of figure 6.4, and of two order parameters, S_{mol} and S_{Phg}.

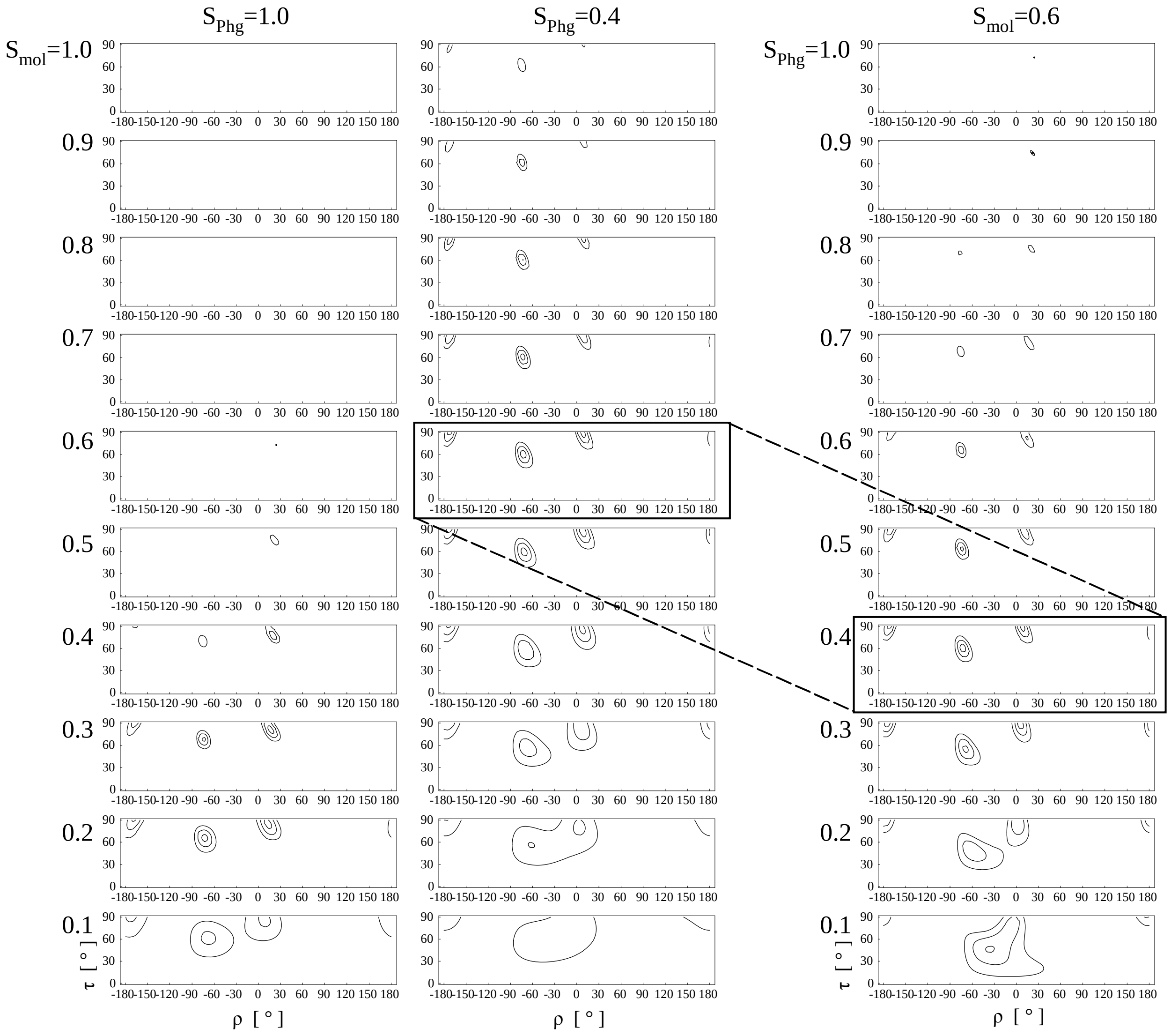

Figure 6.4: Series of (ρ,τ)-plots of *rmsd* in fits of an α-helix model to the data acquired on the core of the N-terminal segment of B18. One order parameter is held fixed, while the other is varied from 1.0 (top) to 0.1 (bottom). Fixed values of (left) S_{Phg}=1.0, (middle) S_{Phg}=0.4, (right) S_{mol}=1.0. Contours are shown at rmsd=1,2,3 ppm, and boxes denote identical plots.

In the left column of figure 6.4 a series of *rmsd*-profiles is presented, which are calculated for a fixed value S_{Phg}=1.0 of the side chain order parameter, i.e. the naive assumption of a perfectly fixed torsion. The molecular order parameter is varied from S_{mol}=1.0 (top) to S_{mol}=0.1 (bottom), contours are shown at *rmsd*=1,2,3. In the *rmsd*-plots of the first column, two minima of *rmsd* are visible, one at (ρ,τ)=(-74°,67°) and one at (ρ,τ)=(15°,83°), with exact value of molecular order parameter of S_{mol}=0.25 in both cases. Both minima are obviously below *rmsd*=1 ppm, meaning that both already give acceptable fits of the data. In a subsequent step, both S_{mol} and S_{Phg} are treated as variables. This allows to characterize each individual minimum more closely by searching for an even better fit in four dimensions.

When applied to the first solution, the procedure yields a refined fit of *rmsd* = 0.01 at (ρ,τ) = (-72.6°,60.2°) with order parameters of S_{mol} =0.6 and S_{Phg}=0.4. The procedure obviously needs to be carried out for the second minimum as well. However, an illustration of the procedure is intended here, so the first minimum (which is later proven to represent B18 in the bilayer) is used to investigate the influence of both order parameters on the fit. All best-fit values found in four dimensions are given in table 6.3 below.

The two remaining columns of figure 6.4 show series where one order parameter is varied while the second one is fixed at its optimum value. The middle column has the rotational order parameter fixed at its optimum value S_{Phg}=0.4, while the right column has the molecular order parameter fixed at its optimum value S_{mol}=0.6. Consequently, the optimum *rmsd*-plot at S_{Phg}=0.4 and S_{mol}=0.6 is shown twice, as indicated by boxes in figure 6.4. All plots show a remarkable qualitative similarity. The *rmsd* function retains its overall shape showing two minima in almost all plots. The positions of the minima are virtually constant, the minima only become more shallow when the order parameters reach extreme values. The reason for the surprising similarity of all these plots is rationalized by the effect of the different modes of mobility on the ^{19}F CSA tensor. Although S_{mol} and S_{Phg} describe quite different modes of mobility, they still have a very similar effect on the ^{19}F CSA tensor. Since the tensor is characterized by an asymmetry of η≈1, the intermediate component σ_{22} is very close to the isotropic position. Thus, both order parameters act mostly on σ_{11} and σ_{33} and leave σ_{22} more or less unaffected.

As a result of their highly similar effect on the rmsd-contours, the presented determination of S_{mol} and S_{Phg} is not very reliable. At the same time, the plots show that even large errors in the description of molecular mobility do not hamper the determination of ρ and τ. The detailed study of global and local molecular mobility may be a rewarding field for further studies, especially when considering that the 4F-Phg side chain represents a long lever, which may amplify the motion of the side chain tip to far higher amplitudes than found on the rather rigid backbone.

As a concluding remark, we note that the assumption of a freely rotating phenyl ring does not yield a reliable fit of the data. Figure 6.5 gives the example of the best-fit *rmsd*-profile calculated for the N-terminal segment ^{105}LLL^{107}, calculated for the case of a freely rotating side chain. It differs considerably from the ones attained for the motionally restricted side chain underlying the fits of figure 6.4 above. Figure 6.5 may be regarded as an extension to the right column of figure 6.4, to which it also bears a slight qualitative resemblance. Still, it is clearly qualitatively different from the plots of figure 6.4, since it lacks one of the two minima found there. In addition, the plot shows an additional minimum at (ρ,τ)=(46°,12°), which is conspicuous not so much for its ambivalent *rmsd*=0.98, but for the extreme value of the molecular order parameter, S_{mol}=1.0. (Raising S_{mol} above this allowed limit actually further decreases the *rmsd*.) This unrealistically high molecular order parameter is a direct consequence of the unrealistically low order assumed for the side chain. The solution present in both figures is now found at (ρ,τ)=(-30°,62°), and again at an unrealistic S_{mol}=1.0. Although this orientation is surprisingly close to the one found by the more realistic model above, it must be seen as coincidence that the persisting minimum is later found to be the 'good' one.

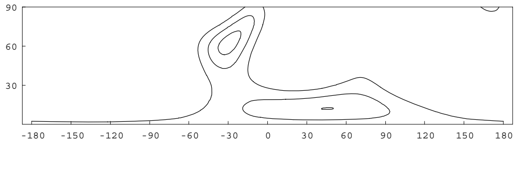

Figure 6.5: Rmsd-profile giving best fit for the core of the N-terminal segment assuming freely rotating phenyl side chains (i.e. S_{Phg}=0.0), with contours shown at *rmsd*=1, 2, and 3 ppm.

Inclusion of peripheral and hinge labels rules out 'false' solutions

In the analysis of the three positions labeled in the core of the N-terminal segment of B18, the preceding section found multiple solutions that were equally consistent with the experimentally observed resonances. The corresponding best-fit *rmsd* plot was highlighted by a box in figure 6.4, and is repeated in the upper left panel of figure 6.6. Here, the plot is presented in a slightly different fashion with a finer choice of contours (rmsd=0.2, 0.4, 0.6, 0.8, 1.0, 1.2) to now emphasize the plot's minima rather than its overall shape. In addition, the upper right panel of figure 6.6 gives the analogous plot found for the three core labels of the C-terminal helix. The situation found for the C-terminal segment is almost identical to the one found for the N-terminal one, namely having two solutions, both of which fully reproduce the experimental data.

To resolve the problem of multiple solutions, the analysis was extended to include additional labels. The B18 analogue labeled in the terminal position 103 as well as the one labeled in position 110 in the central loop of the B18 molecule were now included into the analysis of the N-terminal segment. The left hand side of figure 6.6 shows the respective rmsd plots found. Both extensions lack the minimum at τ = 84°, while the second minimum at (ρ,τ) = (-73°,60°) is retained for both cases at *rmsd* < 1, i.e. still giving perfectly acceptable fits. For the C-terminal segment the inclusion of the C-terminal label in position 120 retains only the minimum at (ρ,τ)=(-23°,89°). Obviously, these findings suggest that a 'good' fit has been identified, given that the additional labels are indeed forming part of the α-helical structural element. The assumption that both termini of B18 are well-structured in the membrane-bound state rather than showing 'frayed ends' is very reasonable in itself, considering the high stability of common secondary structure motifs, and is further supported by the H_α chemical shifts of wild-type B18 found in the high-resolution ^{1}H-NMR study of Glaser *et al.*[6] The confirmed α-helix solutions are given in bold typeface in table 6.3, while solutions ruled out by the inclusion of additional labels are given in parenthesis.

Interestingly, the attempt to include residue L110 as a hypothetical part of the C-terminal helix did not yield an acceptable *rmsd*, as shown by the blank panel in the lower right of figure 6.6. Consequently, the α-helical conformation must be disrupted between L110 and L116. This finding contradicts previous speculations that fusogenic peptides form extended α-helices in membranes. [5;26-28]

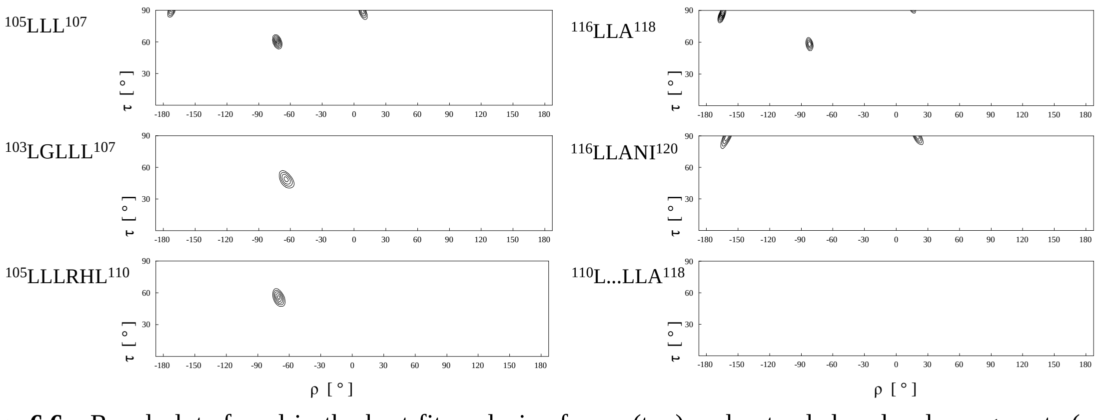

Figure 6.6: Rmsd plots found in the best-fit analysis of core (top) and extended molecular segments (middle and bottom, analyzed sequence stretches as indicated) for the N-terminal (left) and C-terminal (right) segments of B18 analyzed with an ideal α-helical model.

Only the α-helical model is compatible with the B18 resonances

Like many other fusogenic peptides, B18 exhibits a pronounced conformational plasticity. Depending on the experimental conditions (concentration, solvent composition, pH, presence of divalent cations, detergent micelles, type of lipid, etc.), the peptide changes its aggregation state (monomer, or self-assembled amyloid fibril) and conformation (random coil, α-helix or β-sheet).[4;6;29;30] It is not known which conformation and aggregation state represents the biologically active situation. Consequently, all these possible structures had to be considered in the present data analysis. As alternative to the α-helical fits presented above, also idealized β-sheet and 3_{10}-helical structural elements were used in an attempt to fit the data. This was done in the same manner presented above, i.e. including two order parameters, S_{mol} and S_{Phg}, and initially fitting only the core region of each molecular segment before including the loop and termini.

Table 6.3: Calculated structural and dynamic parameters for the N- and C-terminal peptide segments containing three, four, or five labeled sites, when modeled with different secondary structures (α-helix, β-sheet, 3_{10}-helix).

Sequence stretch	rmsd	ρ [°]	τ [°]	S_{mol}	S_{Phg}
N-terminal segment					
	α-Helix				
	(0.04)	(13.7)	(83.5)	(0.3)	(0.8)
^{105}LLL^{107}	**0.01**	**-72.6**	**60.2**	**0.6**	**0.4**
^{103}LGLLL^{107}	**0.48**	**-64.2**	**48.6**	**0.9**	**0.2**
^{105}LLLRHL^{110}	**0.08**	**-69.1**	**53.0**	**0.9**	**0.3**
^{103}LGLLLRHL^{110}	**0.99**	**-66.9**	**53.5**	**0.8**	**0.2**
	β-Sheet				
^{105}LLL^{107}	2.50	-	-	-	-
^{103}LGLLL^{107}	2.97	-	-	-	-
^{105}LLLRHL^{110}	4.07	-	-	-	-
	3_{10}-Helix				
^{105}LLL^{107}	0.05	80.6	35.9	0.7	0.1
^{103}LGLLL^{107}	1.49	193.1	42.6	0.2	0.8
^{105}LLLRHL^{110}	1.77	130.1	46.3	0.4	0.4
C-terminal segment					
	α-Helix				
	(0.02)	(95.0)	(112.5)	(0.8)	(0.35)
^{116}LLA^{118}	**0.03**	**22.6**	**89.2**	**0.8**	**0.35**
^{116}LLANI^{120}	**0.14**	**19.3**	**91.3**	**0.5**	**0.6**
^{110}LRHHSNLLA^{118}	1.42	100.0	118.2	1.0	0.4
	β-Sheet				
^{116}LLA^{118}	2.40	-	-	-	-
^{110}LRHHSNLLA^{118}	15.22	-	-	-	-
^{116}LLANI^{120}	5.07	-	-	-	-
	3_{10}-Helix				
^{116}LLA^{118}	0.02	50.4	42.8	0.5	0.35
^{110}LRHHSNLLA^{118}	3.04	-	-	-	-
^{116}LLANI^{120}	4.66	-	-	-	-

All best-fit results are summarized in table 6.3, where values for the fitted angles and order parameters are only given when acceptable fits were reached. Clearly, only the helix and no other model is able to convincingly explain the observed NMR data. A β-sheet model would be of special interest, but there is positively no acceptable fit accessible with such model. It is actually possible to infer the absence of β-sheet structure directly from the raw ^{19}F-NMR data, since adjacent residues in a β-sheet are aligned in almost the same direction and should therefore give rise to very similar resonance frequencies. This is not observed in neither the N- nor C-terminus, not even when considering only the core tripeptide segments.

A 3_{10}-helical conformation can be ruled out as the rmsd values observed for this model are worse than for an α-helix. Moreover, the fit cannot be extended to include the terminal labels. Considering that the 3_{10}-helical H-bonding pattern is generally less favorable, especially in a hydrophobic membrane environment, we conclude that it is far less convincing than the α-helical model.

Of special interest was an extension of the idealized α-helical model to include a wider range of (still perfectly symmetric) structures by systematically varying the Ramachandran angles φ and ψ by ±10°. Sets of Euler angles α and β were determined for each of these non-ideal α-helices and used for best-fit analysis. This extended analysis influenced the results for ρ and τ by only ±10°, while giving equally good fits. Moreover, allowing a change in χ_1 of 20° translates into an error in ρ and τ of below ±10°. Therefore, the results are not listed in table 6.3, but allow for an estimate of ±10° for the error in the presented best-fit values for ρ and τ.

In summary, we find that the structure of the membrane-associated peptide B18 shows two α-helical segments that extend to include both termini, i.e. the peptide's termini are well-folded rather than having frayed ends. The overall structure of the entire molecule consists of two distinct α-helical stretches (L105 to L110, and L116 to L120) that are connected by a loop region (between R111 and N115) which does not participate in α-helix formation. All findings are in good agreement with the ^{1}H-NMR study in solution.[6] The helix-break-helix motif will be discussed in terms of biological relevance and implications in the following section.

Discussion: B18 assumes a 'boomerang'-structure when membrane-bound

The resulting picture of B18 in the lipid bilayer is illustrated in figure 6.7, where both structural elements of the peptide are shown connected by a speculative loop conformation. The N-terminal segment is inserted into the lipid bilayer with a tilt angle of $\tau \approx 54° \pm 10°$ (angle between helical axis and the membrane normal), whereas the C-terminal helix is aligned almost parallel to the membrane surface at $\tau \approx 91° \pm 10°$. The helix-break-helix motif is evident, and is quite reminiscent of a boomerang. The angle between the two helical molecular segments is about 143°, although it is not possible to deduce the relative depths of immersion for the two segments.

The azimuthal rotation $\rho \approx -67° \pm 10°$ of the N-terminus and $\rho \approx 19° \pm 10°$ of the C-terminus are consistent with the amphiphilic profile of the peptide, i.e. hydrophilic residues are

pointing into the direction of the hydrophilic headgroup region while hydrophobic residues are pointing toward the hydrophobic acyl chain region of the lipid bilayer. Note that the N-terminal helix is considerably more hydrophobic, especially over the first few residues. This property suggests that the N-terminal segment is almost fully immersed into the hydrophobic core of the lipid bilayer, consistent with the oblique penetration of the peptide into the hydrophobic core suggested by ATR-IR spectroscopy[29]. The tilted N-terminal helix can thus lead to considerable perturbation of the lipid acyl chains, which lowers the energy barrier for merging the outer monolayers during fusion.[5] The hydrophilic residues found on top of the N-terminal segment and in the presumably unstructured hinge region do not contradict the proposed depth of immersion, since arginine as well as histidine bear their charges at the end of long side chains, and may thus be able to 'snorkel' to the bilayer surface even from a deeper point of immersion.[31]

The horizontal orientation found for the amphiphilic C-terminal segment suggests binding at the bilayer surface, as B18 has been shown to replace water molecules from the lipid headgroups.[29] Thereby, the hydration repulsion between apposing membranes is decreased, which favors vesicle aggregation and fusion.

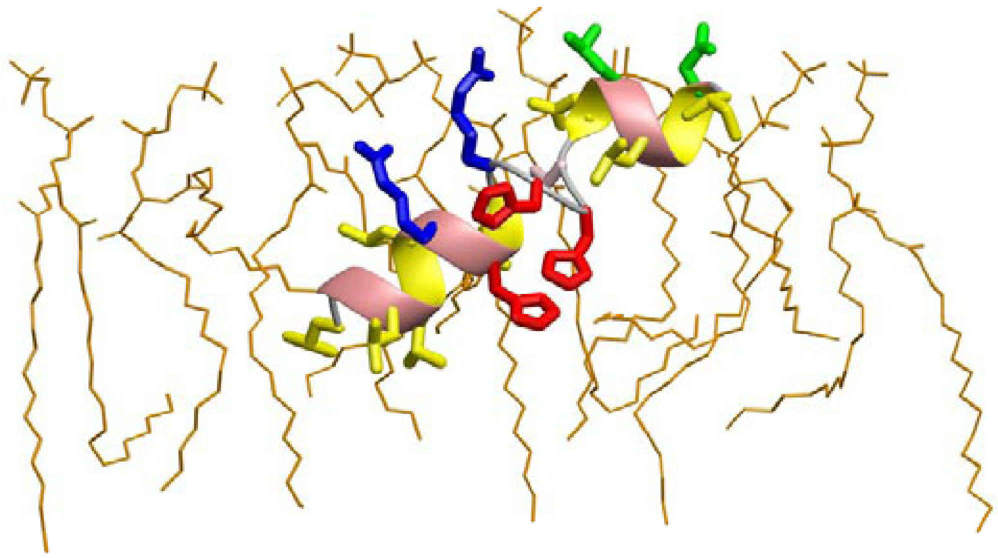

Figure 6.7: Structural model of the fusogenic B18 peptide in a flat lipid bilayer in liquid-crystalline state. The molecular representation as a ribbon diagram shows hydrophobic amino acids in yellow.

In summary, the unusual 'boomerang'-like membrane association of B18 offers an explanation how the peptide may disturb the hydrophobic core of the lipid bilayer while at the same time dehydrating the lipid headgroup region. Both of these two effects are believed to be necessary to induce membrane fusion.

Previous studies of various fusion peptides have shown that they often assume an α-helical conformation upon interacting with lipid bilayers.[4;32] Theoretical analysis of their amphiphilic surfaces suggested that they might insert as a continuous helix into the membrane under an oblique angle.[5;26-28] More recently, the fusion peptide derived from the influenza virus hemagglutinin A was found to exhibit a pronounced kink in its ^{1}H-NMR structure in detergent micelles.[33;34] Under the assumption that this helix-break-helix structure would maintain its angular shape, it was docked onto a lipid bilayer and shown to be consistent with

the behavior of several ESR labels placed along the peptide sequence.[33] By indirectly measuring the tilt angle via the depth of side chain penetration into the bilayer, this ESR study suggested for the first time a 'boomerang'-like mode of insertion for the influenza fusion peptide. These findings were only very recently confirmed in a molecular dynamics simulation.[35]

Our ^{19}F-NMR study of a different fusogenic peptide has now confirmed the same helix-break-helix motif by directly measuring orientational constraints in a flat lipid bilayer, revealing a similar mode of insertion. Comparing these very similar structural models found by complementary experimental techniques on two unrelated peptides, it is tempting to speculate that 'boomerang'-like membrane insertion could be a common functional motif for other fusogenic peptides as well.

Reference List

(1) Afonin, S.; Dürr, U. H. N.; Glaser, R. W.; Ulrich, A. S. *Magn.Reson.Chem.* **2004**, *42*, 195-203.

(2) Hofmann, A.; Glabe, C. G. *Semin.Dev.Biol.* **1994**, *5*, 233-242.

(3) Vacquier, V. D.; Swanson, W. J.; Hellberg, M. E. *Dev.Growth Differ.* **1995**, *73*, 1.

(4) Ulrich, A. S.; Otter, M.; Glabe, C. G.; Hoekstra, D. *J.Biol.Chem.* **1998**, *273*, 16748-16755.

(5) Pécheur, E. I.; Sainte-Marie, J.; Bienvenüe, A.; Hoekstra, D. *J.Membrane Biol.* **1999**, *167*, 1-17.

(6) Glaser, R. W.; Grüne, M.; Wandelt, C.; Ulrich, A. S. *Biochemistry* **1999**, *38*, 2560-2569.

(7) Afonin, S.; Glaser, R. W.; Berditchevskaia, M.; Wadhwani, P.; Gührs, K.-H.; Möllmann, U.; Perner, A.; Ulrich, A. S. *Chembiochem* **2003**, *4*, 1151-1163.

(8) Glaser, R. W.; Ulrich, A. S. *J.Magn.Reson.* **2003**, *164*, 104-114.

(9) Massiot, D.; Fayon, F.; Capron, M.; King, I.; Le Calvé, S.; Alonso, B.; Durand, J.-O.; Bujoli, B.; Gan, Z.; Hoatson, G. *Magn.Reson.Chem.* **2002**, *40*, 70-76.

(10) Freeman, R.; Kempsell, S. P.; Levitt, M. H. *J.Magn.Reson.* **1980**, *38*, 453-479.

(11) Levitt, M. H.; Freeman, R. *J.Magn.Reson.* **1979**, *33*, 473-476.

(12) Griffin, R. G.; Yeung, H.-N.; LaPrade, M. D.; Waugh, J. S. *J.Chem.Phys.* **1973**, *59*, 777-783.

(13) Hiyama, Y.; Silverton, J. V.; Torchia, D. A.; Gerig, J. T.; Hammond, S. J. *J.Am.Chem.Soc.* **1986**, *108*, 2715-2723.

(14) Mehring, M. *High Resolution NMR of Solids*; Springer: Berlin, 1976.

(15) Nehring, J.; Saupe, A. *J.Chem.Phys.* **1970**, *52*, 1307-1310.

(16) Salgado, J.; Grage, S. L.; Kondejewski, L. H.; Hodges, R. S.; McElhaney, R. N.; Ulrich, A. S. *J.Biomol.NMR* **2001**, *21*, 191-208.

(17) Siminovitch, D. J.; Raleigh, D. P.; Olejniczak, E. T.; Griffin, R. G. *J.Chem.Phys.* **1986**, *84*, 2556-2565.

(18) Derome, A. E. *Modern NMR techniques for chemistry research*; Pergamon Press: Oxford, 1987.

(19) Afonin, S. Structural studies on membrane-active peptides in lipid bilayers by solid state ^{19}F-NMR. 2003. Friedrich-Schiller-Universität Jena.
Ref Type: Thesis/Dissertation

(20) Ulrich, R.; Glaser, R. W.; Ulrich, A. S. *J.Magn.Reson.* **2003**, *164*, 115-127.

(21) Khare, R.; Paulaitis, M. E. *Macromolecules* **1995**, *28*, 4495-4504.

(22) IUPAC-IUB commision on biochemical nomenclature *Biochemistry* **1970**, *18*, 3471-3479.

(23) Ramachandran, G. N.; Ramakrishnan, C.; Sasisekharan, V. *J.Mol.Biol.* **1963**, *7*, 95-99.

(24) Kovacs, F. A.; Denny, J. K.; Song, Z.; Quine, J. R.; Cross, T. A. *J.Mol.Biol.* **2000**, *295*, 117-125.

(25) van der Wel, P. C. A.; Strandberg, E.; Killian, J. A.; Koeppe II, R. E. *Biophys.J.* **2002**, *83*, 1479-1488.

(26) Lins, L.; Charloteaux, B.; Thomas, A.; Brasseur, R. *Proteins* **2001**, *44*, 435-447.

(27) Brasseur, R. *Mol.Membr.Biol.* **2000**, *17*, 31-40.

(28) Bradshaw, J. P.; Darkes, M. J. M.; Harroun, T. A.; Katsaras, J.; Epand, R. F. *Biochemistry* **2000**, *39*, 6581-6585.

(29) Binder, H.; Arnold, K.; Ulrich, A. S.; Zschörnig, O. *Biochim.Biophys.Acta* **2000**, *1468*, 345-358.

(30) Ulrich, A. S.; Tichelaar, W.; Förster, G.; Zschörnig, O.; Weinkauf, S.; Meyer, H. W. *Biophys.J.* **1999**, *77*, 829-841.

(31) Killian, J. A.; von Heijne, G. *Trends Biochem.Sci.* **2000**, *25*, 429-434.

(32) Peuvot, J.; Schanck, A.; Lins, L.; Brasseur, R. *J.theor.Biol.* **1999**, *198*, 173-181.

(33) Han, X.; Bushweller, J. H.; Cafiso, D. S.; Tamm, L. K. *Nat.Struct.Biol.* **2001**, *8*, 715-720.

(34) Hsu, C.-H.; Wu, S.-H.; Chang, D.-K.; Chen, C. *J.Biol.Chem.* **2002**, *277*, 22725-22733.

(35) Huang, Q.; Chen, C.-L.; Herrmann, A. *Biophys.J.* **2004**, *87*, 14-22.

VI. B18 fusogenic peptide

VII. Gramicidin S: β-Sheet antimicrobial peptide

Fluorine NMR resonances indicate a flat alignment when ^{19}F-labeled gramicidin S associates with DMPC bilayers.[1] Additional resonances are observed under certain concentration and temperature conditions, characterized in detail by Afonin[2], which indicates that the peptide can change its orientation in the membrane. This chapter gives a structural analysis of the re-alignment effect, utilizing additional information gathered from molecular dynamics simulations and ^{15}N-NMR experiments. The novel orientation found can be functionally interpreted in terms of the peptide's mechanism. The presented results were submitted for publication in *Journal of the American Chemical Society.*

Introduction

Gramicidin S (gS) is a cationic decapeptide which is synthesized non-ribosomally in the periplasmatic space of *Bacillus brevis*.[3] It has the symmetric sequence *cyclo*-(Val-Orn-Leu-D-Phe-Pro)$_2$, where D-Phe indicates the D-enantiomer of phenylalanine. Orn denotes the unusual amino acid ornithine, which is an intermediate in the urea cycle, but is not genetically encoded for. Gramicidin S exhibits antimicrobial activity against a broad spectrum of Gram-negative and Gram-positive bacteria and several fungi, and it also possesses some hemolytic activity[4-6]. The structure of gS is known from X-ray crystallography of a gS-urea complex[7] as well as from ^{1}H-NMR studies in a number of different solvents[8;9]. Its antiparallel β-sheet conformation possesses a twofold symmetry, in which two equivalent short strands are connected by β-turns (of type II'[10]) consisting of the D-Phe and Pro residues. The molecule has a pronounced amphiphilic character, since the positively charged ornithine side chains are located on one face of the cyclic β-sheet, while the hydrophobic side chains of Val and Leu point towards the opposite side[7;9;11]. Just as in the case of other amphiphilic peptide antibiotics[12;13], it is generally accepted that the site of action of gS is the plasma membrane of the target cell[14;15]. Gramicidin S shows a high affinity for a wide variety of natural and synthetic lipid bilayers with different head groups and different viscous properties[14-16]. Binding of the peptide leads to moderate shifts and a considerable broadening of the main lipid phase transition[14;15], and it increases the membrane permeability for ions and small metabolites in a concentration-dependent manner[17]. Membrane permeability is induced in discrete, step-like conductance events in electrophysiological experiments[17], suggesting the formation of stable pore structures.

The left panel of figure 7.1 shows the cyclic backbone of gS. In this representation, the C_2 symmetry of the molecule becomes evident. Also shown are the four intramolecular hydrogen

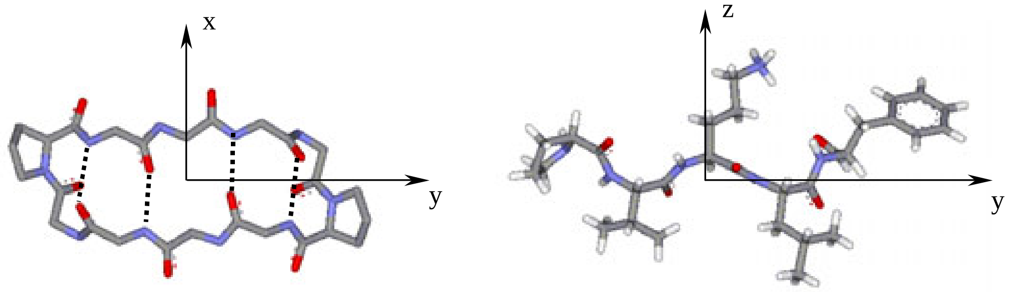

Figure 7.1: Wild-type gramicidin S with definition of the molecular coordinate system. View along the symmetry axis (left) showing backbone heavy atoms only, and indicating the four intramolecular hydrogen bonds, (right) side view including hydrogen atoms.

bonds, which give the structure of a two-stranded antiparallel β-sheet to the molecule. The highly rigid backbone structure effected by the β-sheet motif makes gS also interesting as a model for testing ^{19}F- labeling in a system of well-known and stable conformation. In the right panel of figure 7.1 a side view of the whole molecule is given. For reasons of clarity, only the proximal one of the two identical β-strands is shown. This view emphasizes the amphiphilic character given to the molecule by the polar ornithine side chains.

In an earlier study, Salgado *et al.*[1] investigated a ^{19}F-labeled gramicidin S analogue in DMPC bilayers, giving a first application of solid-state ^{19}F-NMR to biomembranes. In that analogue both symmetry-related Leu side chains in positions 3 and 3' of the peptide were replaced by 4F-Phg. The analogue shall here be termed gS-3/3', a molecular model is shown in the right panel of figure 7.2. From the ^{19}F-NMR spectra of gS-3/3' a peripheral alignment of the peptide in liquid crystalline DMPC bilayers was inferred. The peptide's β–sheet is aligned flat on the lipid bilayer, which allows the Val and Leu side chains to insert into the hydrophobic lipid core of the bilayer, and the hydrophilic ornithine side chains to interact favorably with the lipid headgroup region. A molecular order parameter of $S_{mol} = 0.34$ was found. This surface-bound state will be referred to as the 'S-state' of gramicidin S, in accordance with the common terminology of the two-state model of antimicrobial peptides.[18]

Additional ^{19}F-NMR resonances are found when measuring at temperatures close to or within the lipid main phase transition. These novel resonances are directly indicative of a changed peptide orientation. It may be expected that re-orientation should be connected to the change of the peptide into its active I-state[18]. We will term the new alignment and the resulting additional NMR resonances as ‘I-state’, irrespective of the slightly speculative nature of that attribution. Afonin[2] carried out a comprehensive phenomenological study of the effect, studying the influence of peptide concentration, lipid composition, temperature, and pH onto the I-state resonance. He found the I-state to occur preferentially in the short-chain lipid DLPC, but to also be present in DMPC and DPPC bilayers in a certain temperature range around the lipid phase transition.

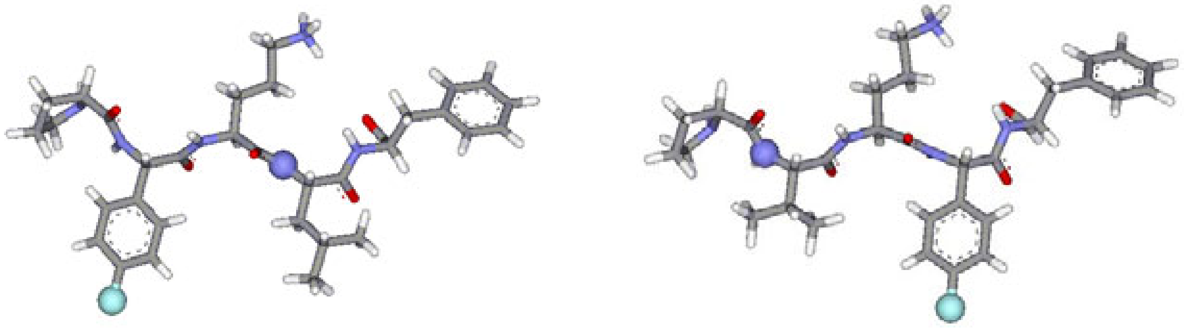

Figure 7.2: Side views of the two 4F-Phg-labeled analogues of gramicidin S used in this study, gS-1/1' (left) and gS-3/3' (right). Shown as spheres are the ^{19}F (light blue) and ^{15}N (dark blue) isotope labels. Only the proximal strand of each peptide is shown.

To help with the ambiguous structural interpretation of the new resonances, the labeling scheme was extended to include three additional orientational parameters. First, another fluorine labeled species was prepared by substituting 4F-Phg for both valine residues in positions 1 and 1’. This molecule is denoted gS-1/1’, the left panel of figure 7.2 gives its structure. The I-state of the gS-1/1’ analogue forms somewhat less readily than in gS-3/3’. Actually, Afonin[2] observes the I-state only in the phase transition regime of short-chain

DLPC, but not in DMPC or DPPC. As a second labeling strategy, both analogues gS-1/1' and gS-3/3' were also synthesized with a backbone nitrogen replaced by its NMR active isotope, ^{15}N. In the case of gS-1/1', the nitrogen of Leu 3 and 3' was chosen, for gS-3/3' residues Val 1 and 1' were synthesized using ^{15}N-Val. The labeling sites are indicated by spheres colored in dark blue in figure 7.2. Since ^{15}N isotope labeling is not disturbing the chemical properties of peptides, no further distinction is made between ^{15}N-labeled and unlabeled species. Both analogues were indeed synthesized with and without ^{15}N-label in order to economize the costly ^{15}N isotope label. This chapter integrates data obtained on both analogues from fluorine as well as nitrogen labels to yield a comprehensive structural picture explaining the novel alignment.

Materials and Methods

Peptide synthesis and sample preparation

The ^{19}F- and ^{15}N-labeled analogues of gramicidin S were synthesized and purified by Parvesh Wadhwani and Sergii Afonin as published[19]. In the same publication, evidence from CD spectroscopy and antimicrobial testing confirmed that the fluorine-labeled analogues possess the same structural and functional properties as the wild type.

The lipid system and peptide concentration were chosen according to Afonin's phenomenological studies[2], with the aim of stabilizing and maximizing the new spectral components that are of interest here. For gS-3/3', the I-state was found in a number of different lipids of different chain length. We decided to use DMPC, since its phase transition is close to room temperature, which greatly eases experimental effort. DLPC had to be chosen as the lipid system for gS-1/1', since it is the only lipid in which an I-state is found. For fluorine measurements, a peptide:lipid ratio of 1:40 was used, while the lower sensitivity of ^{15}N-NMR necessitated a somewhat higher peptide:lipid ratio of 1:20. Peptide and lipid were co-dissolved in a 80:20 mixture of chloroform and methanol, oriented samples were prepared in the same manner described for B18 in chapter VI.

^{19}F-NMR spectroscopy

Instrumentation and spectroscopic parameters were identical to the ones used on B18 samples. The temperatures were chosen to optimally observe the two distinct orientational states of gramicidin S. For observing the S-state, temperatures were chosen well above the respective lipid's main phase transition, at 25°C for gS-1/1' in DLPC, and at 35°C for gS-3/3' in DMPC. The I-state is observed only in the vicinity of the main lipid phase transition, so temperatures were chosen to match the phase transitions of DLPC and DMPC at –10°C and 25°C, respectively.

Molecular modeling

In contrast to the B18 fusion peptide, for gramicidin S a number of experimental structures have been determined and it is a well established fact that the gS backbone has a rigid cyclic geometry without structural plasticity. This situation allows us to base data analysis on a single experimental structure instead of a large number of hypothetical ones. Afonin[2] gives a review of the slightly different structures reported for gS in different environments and, by use of a CPMG distance determination, finds the one determined by Xu *et al.*[9] to best represent gramicidin S in a lipid bilayer environment. It was recorded at 5 mM concentration in DMSO using sophisticated analysis of a standard NOESY solution-state NMR experiment. It has to be noted that Xu *et al*. do not provide a structure in pdb-format, since gramicidin S is too small a molecule to be deposited in the Brookhaven data bank. In their study, they only report a set of Ramachandran angles[20] (φ,ψ) for the backbone, along with dihedrals for the side chains. Therefore, a structural model in pdb-format had to be created from these dihedrals. It turned out that the created structure did not perfectly close back up onto itself.

However, the gap in ring-closure could be bridged in InsightII and was small enough not to hamper use of the structure for data analysis.

Starting from this 'Xu-structure', the appropriate molecular models were created by replacing the respective Val-1/1' and Leu-3/3' side chains by 4F-Phg. (Figure 7.2 above was already created from these 'mutated' structures.) The molecular coordinate system MOL of the model structures was chosen to line up with the moments of inertia of the molecule. This procedure will automatically make MOL orthonormal and can be carried out easily in most molecular modeling programs. The molecule's moments of inertia will reflect the C_2 symmetry, with one moment of inertia being parallel to the symmetry axis. The z^{MOL}-axis was chosen to be along the symmetry axis, with the positive direction pointing towards the ornithine side chains. For gS, the approach of evaluating the moments of inertia makes the x^{MOL}- and y^{MOL}-axes line up with the general shape of the molecule, as intuition would suggest. We chose y^{MOL} to coincide with the molecule's long axis parallel to its β-strands. This choice will make $(\rho,\tau) = (90°,90°)$ describe a fully inserted molecule where y^{MOL} lines up with the membrane normal. The described choice of MOL is indicated in figure 7.1. The model structures generated in pdb-format were then used to extract atom positions as input for the second-generation analysis program described in chapter II, which is in turn used to calculate the χ^2 error function according to equation (2.2).

In addition to the backbone structure, the torsion angle of the fluoro-phenyl side chain needs to be known for structural analysis. It is described by the angle χ_1, defined as the dihedral angle between the N-C_α-C_β-C_γ atoms in 4F-Phg (*cf.* chapter VI, esp. figure 6.3). There is clear spectroscopic evidence that in the I-state of gramicidin S this angle is restricted to a narrow range of values. Using the method of energy profiles, Salgado *et al.*[1] and Afonin[2] determined energetically favored ranges of χ_1 in β–sheet structures, and table 7.1 gives an overview of their results. They observe that minima in the conformational energy profiles of a β-sheet structure are far less pronounced than in helical structures. Since their results also show considerable deviation between gS and idealized β–sheet structures, the present study pays additional attention to the determination of 4F-Phg side chain torsion. In a first approach, the data analysis was extended to include any arbitrary χ_1, i.e. to cover *any* torsion angle. In addition, MD simulations were performed to get a better idea of the *most favorable* torsion angle.

Table 7.1: Energetically favored values χ_1^{opt} for the torsion angle χ_1 as previously found for different backbone situations, with limits of the energetically accessible range $[\chi_1^{min} \ldots \chi_1^{max}]$

publication	system	χ_1^{min}	χ_1^{opt}	χ_1^{max}
Salgado et al.[1]	N-acetyl-N'-methylamide-4F-Phg (β-sheet Ramachandran angles)	50°	60°	70°
	N-acetyl-N'-methylamide-4F-Phg (Xu Ramachandran angles)	35°	55°	60°
Afonin[2;21;21;21]	AAAA-FPhg-AAAA (β-sheet Ramachandran angles)	not reported	65°	not reported
	gS-3/3' (Xu backbone)	-30°	-3°	20°
	gS-1/1' (Xu backbone)	-45°	-13°	10°

Molecular dynamics simulation

Molecular dynamics trajectories of both gS analogues were generated *in vacuo* using the COSMOS force field[22;23] as implemented in the program COSMOS (COSMOS GbR, Jena, Germany, www.cosmos-software.de). 20 million time steps of 0.5 fs each were calculated, giving a total simulation time of 10 ns. Values for the trajectories of the dihedral angles χ_1 and the F-F-distance were extracted from the molecular coordinates every 500 time steps.

The starting structure here is as determined by Doi et al.[24] For this structure, an original pdb-file was available (at http://www.oups.ac.jp/unsupported/bukka1/research/xray_structure/tcgs/index.html). Using this structure had the additional advantage of not biasing the results by starting from our favored structure. Val-1/1' or Leu-3/3' were replaced by idealized 4F-Phg side chains to give models of the fluorinated analogues as described above. MD calculations were performed at temperatures of 293 K and 593 K. The high temperature runs were intended to find *all* favorable conformation, since multiple local minima may be separated from each other by high energy barriers.

^{15}N-NMR spectroscopy

The ^{15}N-labeled analogues of gramicidin S were used to set up ^{15}N-NMR spectroscopy of macroscopically oriented lipid bilayers in our laboratory for the first time. To account for this situation, the procedures shall be presented in some detail.

The spectrometer used was a Bruker Avance 500 MHz instrument with a wide-bore magnet (Bruker Biospin GmbH, Rheinstetten, Germany). Two flatcoil probes were used, one double-tunable to proton and nitrogen (50.7 MHz) frequencies, the other one triple-tunable to proton, fluorine, and nitrogen frequencies and equipped with a goniometer. The simpler design of the former made it reach about twice the signal-to-noise ratio of the latter. Thus, the goniometer probe was only chosen when spectra at various sample tilt angles had to be recorded.

Due to the long T_1 relaxation time and low sensitivity of the ^{15}N nucleus, direct polarization of nitrogen using single-pulse or echo experiments is not feasible in biologically relevant concentration regimes. Instead, the cross-polarization[25;26] (CP) pulse sequence is commonly used. This sequence applies a 90° pulse at the proton frequency and subsequently transfers the polarization from protons to nitrogen by simultaneous irradiation at both frequencies under Hartmann-Hahn matching conditions. Thus, it is possible to choose the recycle delay time according to proton T_1 relaxation, which is considerably shorter. In our experiments, a ramped CP sequence[27] was used, which was shown to give best intensity on oriented lipid samples.[28] A recycle delay time of 2.0 s was chosen, giving measurement times between 6 and 24 hours when acquiring between 10000 and 40000 scans. During the FID, 1024 points were recorded in the time domain, with a dwell time of 5 µs, resulting in 5.17 ms acquisition time and 100 kHz spectral width. During acquisition, the TPPM20 decoupling scheme[29] was used for proton decoupling at approx. 30 kHz field strength.

Hartmann-Hahn match was optimized at a field strength of approx. 30 kHz. This was limited by the probe's power handling capacities, which was initially far worse, and could not be further improved in several attempts by the manufacturer. When trying to optimize CP contact times, considerable influence of contact time on the spectral lineshape was observed. This became especially obvious when trying to record the CSA powder spectrum of

lyophilized gS-3/3' peptide. The longer the contact time, the closer the resemblance between the observed spectrum and the theoretically expected powder lineshape became. A spectrum recorded at 2.5 ms contact time is presented in the right panel of figure 7.3. Although it still shows noticeable deviations from an ideal tensor lineshape, a contact time of 2.5 ms was chosen for our experiment in order not to damage the probes.

A number of substances have been used for defining the nitrogen frequency scale in biological ^{15}N-NMR (and even more in non-biological ^{15}N-NMR). Among others, $^{15}NH_3$, $^{15}NH_4Cl$, $^{15}NH_4NO_3$, or ^{15}N-urea can be used to define the 0 ppm frequency of a nitrogen scale. Most common are the two substances mentioned first, i.e. $^{15}NH_3$ (in liquid form, which ammonia will retain at room temperature when sealed in a glass vial at low temperature), and $^{15}NH_4NO_3$ (as saturated solution in H_2O). Table 7.2 summarizes these two scales, along with values on $^{15}NH_4Cl$, which was available in our laboratory and used in all experiments.

Table 7.2: Relevant chemical shift values for ^{15}N-referencing[30;31]

substance	conditions	on liq. $^{15}NH_3$ scale	on $^{15}NH_4NO_3$ scale
$^{15}NH_3$	liquid, 25°C	0.0ppm	-20.7ppm
$^{15}NH_4NO_3$	saturated solution, 25°C	20.7ppm	0.0ppm
$^{15}NH_4Cl$	saturated solution, 25°C	27.3ppm	6.6ppm
$^{15}NH_4Cl$	polycrystalline salt, 25°C	38.7ppm[a]	18.0ppm

[a] Bechinger[32;33] uses 41.5 ppm

These substances are used as external standards—in contrast to ^{1}H-NMR, where internal standards are common, and ^{13}C-NMR, where both types are used. External standards offer the advantages of insensitivity to pH, lack of biomolecular interactions, and absence of solubility or stability problems. As disadvantages, they are inconvenient in handling and sensitive to bulk susceptibility effects—as described in various studies.[34-36] In our setup, we found the absolute frequencies measured on a polycrystalline sample at 0° and 90° goniometer settings to be shifted by 250 Hz due to shape-dependent magnetic susceptibility.

A study by Wishart *et al.*[37] aims at unifying referencing standards in biomolecular NMR, thereby making isotropic chemical shifts exploitable as a source of structural information.[38] They describe the current situation as unsatisfactory and recommend referencing all nuclei with respect to ^{1}H. As an especially striking example of unreliable referencing, they discourage use of chemical shifts measured on non-superconducting magnets, where the magnetic field is usually aligned in horizontal direction. Thus, the influence of magnetic susceptibility is very different from that on superconducting magnets (where the field is usually vertical, i.e. parallel to the long axis of the sample), making comparison of data acquired before and after 1970 problematic.

For the present study, the following method of referencing was applied. As described by Hori *et al.*[39], ^{15}N chemical shifts were referenced to $^{15}NH_4NO_3$ by setting the signal of poly-crystalline $^{15}NH_4Cl$ salt to 18.0 ppm. This procedure allows simultaneous optimization of the Hartmann-Hahn condition using the same sample. A solution sample does not allow this procedure, since the dipolar couplings mediating CP polarization transfer are averaged to zero in solution. Using the equipment described above, a saturated solution of $^{15}NH_4NO_3$ sealed in a polyethylene bag gave a line around 60 Hz = 1 ppm wide. The sample of $^{15}NH_4Cl$ salt

employed in referencing our spectra gave a broader resonance of approx. 350 Hz (= 7 ppm) linewidth. Although the difference in linewidth seems considerable, it needs to be seen in relation to the width of the peptide resonances to be observed. The comparatively sharp resonance of oriented S-state gS-3/3' at 35°C has a width around 500 Hz (= 10 ppm). Therefore, the error introduced by using salt instead of solution for referencing is far smaller than the intrinsic error in linewidth.

As background information for orientational analysis of NMR resonances observed in macroscopically oriented lipid bilayers, the principal values of the rigid ^{15}N CSA tensor and its situation within the molecular geometry need to be known. Their determination has found some interest in past and present studies. Pioneering studies were carried out on di- or tri-peptides[40-44], and more recently numerous values within functional peptides[45-47] as well as uniformly labeled proteins[48] were reported. Straus *et al.*[49] offer a thorough overview of the literature situation as supplementary material to their publication. Most important to note is that values reported for glycine as well as for proline nitrogens are quite different from the remaining amino acids, which among each other show very similar values.

The left panel of figure 7.3 shows the reported geometrical situation of the nitrogen CSA tensor within the molecular geometry of the peptide bond. The atoms of the peptide plane are shown as spheres, with the nitrogen atom in the center, its hydrogen pointing up, the C_α carbon atom to the right, and the carbonyl group to the left with its oxygen pointing down. The rigid peptide plane is additionally indicated by thin lines. The peptide plane is shown within the coordinate system PPL that is used for describing local geometry and that was introduced in chapter II. Its z-axis is defined to lie along the N-H bond, pointing from nitrogen to hydrogen. The PPL x-axis was chosen to lie within the peptide plane, positive direction pointing towards C_α, and to be parallel to the z-axis. The y-axis is then fixed by the requirement to be perpendicular to both x- and z-axis and to form a right-handed coordinate system. The σ_{33} (within peptide plane), σ_{22}, and σ_{11} components of the CSA tensor are shown in black, green, and red color, respectively. It can be seen that the least shielded component σ_{11} of the CSA tensor is aligned almost perfectly along the NH-bond. Straus *et al.*[49] state that the reported angles between z^{PPL} (i.e. NH-bond direction) and z^{PAS} average to θ = 16.7°. Moreover, the σ_{11} component is found to have large values around 200 ppm, while both σ_{22}

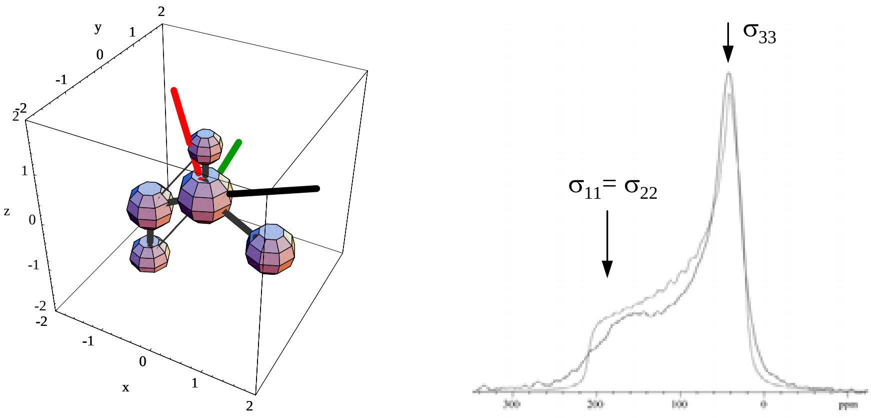

Figure 7.3: (Left) Geometrical situation of the nitrogen CSA tensor within a peptide plane, shown within the coordinate system PPL. See text for detailed explanations. (Right) ^{15}N-CSA powder spectrum of lyophilized gS-3/3' (black), along with SIMPSON best-fit spectrum (gray).

and σ_{33} have small and very similar values around 50 ppm. For this reason, ^{15}N-NMR is most sensitive to the angle between NH-bond and external magnetic field. The reader may find the panel somewhat primitive. But one needs to hold in favor that it is generated from within the program *Mathematica* using the data and transformations actually used in analysis. For this reason it is shown here without any PowerPoint-fudging.

In contrast to the educated guess of angle θ, the principal components of the ^{15}N CSA tensor could be experimentally determined on the peptide of interest, gS-3/3'. A best-fit analysis using SIMPSON yielded values of 22.3 ppm, 41.3 ppm, and 210.6 ppm, corresponding to an isotropic shift of 91.4 ppm, an anisotropy parameter of $\delta = 119.2$ ppm, and an asymmetry of η of 0.16, in good correspondence with literature values. Experimental and simulated spectrum are shown in the right panel of figure 7.3, with σ_{11}, σ_{22}, and σ_{33} indicated. Besides the CP excitation problems mentioned above, there seem to be shoulders in the powder lineshape, hinting at heterogeneity within the lyophilized peptide sample. An attempt at measuring the peptide’s ^{15}N CSA tensor in a lipid dispersion, i.e. in a membrane environment, did not give sufficient intensity. This is probably because increased molecular mobility hampers CP transfer, which would have furthermore misrepresented the CSA tensor due to partial averaging.

The observed lack in intensity seems to be related to other reported problems in obtaining cross-polarized ^{15}N spectra from lipid/peptide systems. Balla *et al.*[50] reason that "a combination of [peptide] mobility and alignment at the magic angle would explain the difficulty in obtaining CP spectra from the aligned maculation samples". The situation of a N-H dipolar coupling vector incidentally aligned at the magic angle in the macroscopically oriented lipid sample may well apply in the case of re-oriented gramicidin S. Hallock *et al.*[51] also report drastically reduced signal intensity in certain aligned samples and argue that "coupled motions between the lipids and the peptide" may make CP ineffective.

Results

^{19}F-NMR analysis

Gramicidin S at low concentrations binds peripherally to liquid crystalline DMPC bilayers. The corresponding resonances observed on the fluorine-labeled analogues gS-1/1' and gS-3/3' are given in table 7.3, where they are denoted as the surface-bound 'S-state'. The value measured for gS-3/3' reproduces the one reported by Salgado *et al.*[1], the value measured on gS-1/1' is almost identical. This is a direct consequence of the almost parallel arrangement of the (i)- and (i+2)-side chains in a β-strand, thus confirming the result of Salgado *et al.*

When an aligned sample of peptide:lipid ratio ≥1:40 is brought to temperatures around the lipid phase transition, additional resonances gradually appear in the ^{19}F-NMR spectra. The ^{19}F-NMR spectrum of 1:40 gS-3/3' in DMPC at 35°C is shown together with table 7.3, the two new resonances being marked by arrows. The third resonance represents the S-state which is also observed at this concentration, but is no longer present at the higher concentration of 1:20, indicating that formation of the new resonances is a cooperative process. Both new resonances in the gS-3/3' spectra were always observed to have equal intensities. This observation makes it extremely unlikely that the two resonances are related to two different states of gS giving one resonance each. Also, the hypothesis of two (most likely χ_1-) conformers of the same state can be ruled out, since identical population of both conformers is equally unlikely. Therefore, the two resonances were interpreted as arising from the two labels of a single gS-3/3' molecule. For gS-1/1' only a single novel resonance was observed. In no case did the rotational diffusion of gS around the lipid bilayer normal cease, as evidenced by identical but scaled spectra when observing oriented samples tilted perpendicular with respect to the external magnetic field.

In this chapter a structural interpretation is given for the new resonances shown shaded in table 7.3. They are directly indicative of a changed peptide orientation, most likely into its second, active state.[18] Therefore, the novel alignment and the resulting additional NMR resonances are termed 'inserted' or 'I-state', irrespective of the slightly speculative nature of that attribution.

Table 7.3: Resonances observed in ^{19}F-NMR of macroscopically aligned samples of gramicidin S analogues. (Left) Prototypical spectrum measured on gS-3/3' at 23°C and at a peptide:lipid ratio of 1:40. (Right) Overview of resonance positions observed on both analogues within and above the lipid phase transition.

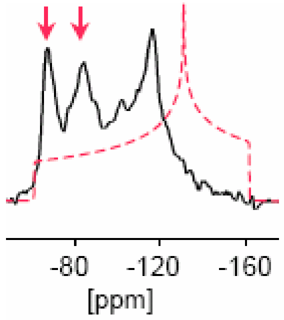

	gS-1/1' in DLPC		gS-3/3' in DMPC	
resonance	T	σ	T	σ
S-state	25°C	-118.0 ppm	35°C	-118.0 ppm[a]
	-10°C	not present	23°C	-120.0 ppm
I-state	-10°C	-86.0 ppm	23°C	-65.0 ppm -77.5 ppm

[a]as reported by Salgado *et al.*[1]

A dashed line in the ^{19}F-NMR spectrum accompanying table 7.3 indicates the corresponding powder pattern lineshape, which was modeled according to a measurement by Salgado *et al.*[1] for gS-3/3' in a gel-state DMPC dispersion. They report tensor principal values of –65.5 ppm, –126.5 ppm, and –153.0 ppm, corresponding to an isotropic chemical shift of –115.0 ppm. Remarkably, one of the I-state resonances of gS-3/3' is situated on the very edge of the tensor, being identical to the least shielded value of σ_{11} = -65.5 ppm. This is a direct proof that gS-3/3' in the I-state is almost completely immobilized, showing neither overall wobble nor mobility in side chain torsion. Diffusional rotation around the membrane normal, however, is still present but is neither influencing our spectra nor reflected in S_{mol}. Compared to the situation found for fluoro-phenyl side chains in B18, for which the preceding chapter reported restricted mobility, the fluoro-phenyl side chain in gS is even more restricted in its mobility as it does not show any oscillatory fluctuation around its equilibrium torsion, i.e. S_{Phg} = 1.0. Also, chemical exchange between different conformers of side chain torsion can be ruled out, since it would lead to an averaging of tensor components. The drastically reduced mobility of gS is rather surprising, since the analysis of Salgado *et al.*[1] found the S-state to be highly mobile, with an order parameter of only S_{mol} = 0.34. Also, a completely rigid situation of the side chain torsion is not expected from the rather shallow energy profiles found for χ_1 in β-sheet structures.

The complete immobilization of gS in its I-state is crucial for the following best-fit analysis, since it reduces the number of free parameters to a tractable number. Because of immobilization, we are able to set the corresponding order parameters to their fully rigid value, S_{mol} = 1.0 and S_{Phg} = 1.0, leaving us with only ρ and τ to be fitted to experimental data. In addition there is the side chain torsion angle χ_1 for which no fully reliable value can be given, and which needs to be seen as a 'semi-free' parameter.

Model structures for gS-1/1' and gS-3/3' were generated starting from the wild-type gS structure determined by Xu *et al.*[9] The side chain torsion χ_1 in 4F-Phg was initially handled as a free parameter, in order to assess its influence on the fits and to test whether it may be extracted from the data. Model structures with χ_1 varied in steps of 20° were used to fit the data, with χ_1 ranging from –80° to 100°. Note that these extreme values are equivalent, so the generated plots 'close up onto themselves'. The experimental error was conservatively estimated to be Δσ = 1 ppm for each data point. The resulting ρ-τ-plots for χ^2 are shown in figure 7.4 with contours corresponding to values of χ^2 = 1, 2, 5, 10, and 20. The necessary plot ranges should be reduced by the C_2-symmetry of the gS molecule to a ρ-range of [-90°,90°] (center chosen at 0° for beauty of presentation) and a τ-range of [0°, 90°]. The actual ρ-τ-plots do not exactly show the expected symmetric situation for τ≥90°, but show circular patterns which are symmetric around a line slightly tilted with respect to the line τ = 90°. This situation is caused by choosing two of the molecular moments of inertia as the z^{MOL}- and y^{MOL}-axes. This handy definition of axes is not absolutely exact and does not perfectly line up with the C_2 symmetry axis and the intuitive 'long axis' of the molecule given by the β-strands. To account for the slightly rotated χ^2-functions, figure 7.4 presents τ in a range of $45° \leq \tau < 135°$, i.e. its full range reduced by regions of small and large τ where χ^2 has unreasonable values ≥20.

For gS-1/1', the χ^2-plots of figure 7.4 show perfect χ^2-minima for all values of torsion angle χ_1. They are reminiscent of the ring-area plots typical for single labels (*cf.* ^{15}N-NMR analysis presented below), but actually two or three distinct minima are found within each ring. The peculiar shape of the χ^2-functions can be attributed to the coinciding resonances of both labels in gS-1/1'. The observed χ^2-minima are compiled in table 7.4

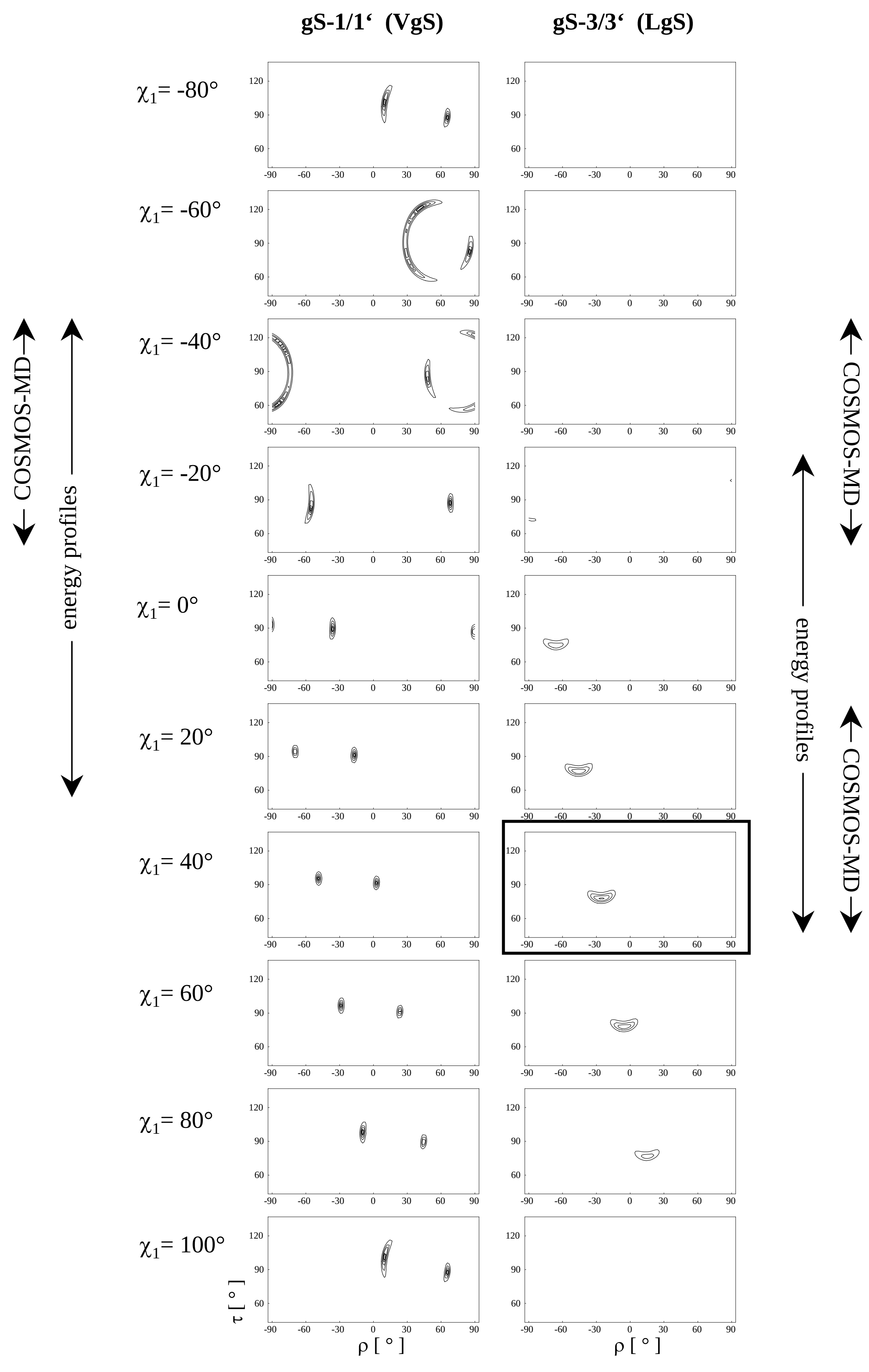

Figure 7.4: ρ-τ-Plots of χ^2 in gS-1/1' (left) and gS-3/3' (right) for given values of phenyl torsion χ_1. A box marks the unique best-fit solution found for gS-3/3'. Arrows indicate the 'allowed' χ_1-ranges expected from energy profiles and COSMOS molecular dynamics simulations.

Table 7.4: Minima of χ^2-functions for a given value of phenyl torsion, χ_1, and completely immobilized molecule (S_{mol}=S_{Phg}=1.0).

	gS-1/1'						gS-3/3'		
χ_1	ρ	τ	χ^2	ρ	τ	χ^2	ρ	τ	χ^2
-80°	10°	102°	0	66°	88°	0	37°	75°	21
-60°	41°	121°	0	86°	83°	0	61°	76°	53
	31°	76°	2.47						
-40°	48°	86°	0	-79°	111°	1.64	-111°	71°	47
				-85°	61°	0			
-20°	68°	87°	0	-55°	84°	0	-88°	72°	19
0°	89°	87°	0	-36°	89°	0	-66°	74°	6.2
20°	-70°	94°	0	-17°	91°	0	-46°	77°	2.4
40°	-49°	96°	0	3°	92°	0	-25°	78°	1.73
60°	-29°	97°	0	23°	91°	0	-5°	78°	2.7
80°	-10°	98°	0	45°	90°	0	16°	77°	7.3
100°	10°	102°	0	66°	88°	0	37°	75°	22

In the case of gS-3/3', qualitatively different χ^2 functions are found which do not show uniformly good fits for all χ_1-values. Rather, χ_1 needs to be restricted to a range between 20° and 60° to give acceptable fits of the ^{19}F-NMR data. A unique minimum of χ^2 = 1.722 is found for χ_1 = 38°, marked by a a box in figure 7.4, and corresponding to an overall orientation of (ρ,τ) = (-27°,78°). All χ^2-minima found are reported in table 7.4, with the unique best-fit solution highlighted by a shaded box. The range of χ_1 found to be consistent with our data is in good agreement with the 'allowed' ranges found by the method of energy profiles (*cf.* table 7.1 and arrows in figure 7.4).

Both analogues show a reasonably narrow range of solutions in τ, which proves that the molecule is tilted with its C_2 symmetry axis and the membrane normal forming an angle of τ = 70°-90°. This upright orientation exposes *both* the hydrophobic face and the hydrophilic ornithine side chains *laterally*, which cannot easily be understood in the bilayer environment with its horizontally extended hydrophobic and hydrophilic 'planes'. It should be noted that the upright orientation may be directly inferred from the peculiar resonance coinciding with σ_{11} of the ^{19}F CSA tensor in 4F-Phg (*cf.* figure 6.3). For the fluoro-phenyl group to align its least shielded principal CSA value with B_0, its symmetry axis needs to be perpendicular to the external magnetic field, as shown in the leftmost resonance of figure 1.8. The C_2 symmetry axis of gS has to take the same orientation, since it is roughly parallel to the fluoro-phenyl symmetry axes. But since the exact torsion angle χ_1 is not known, no conclusion about the global azimuthal rotation ρ can be drawn from a local phenyl orientation.

The uncertainty in the determination of ρ is evident from the broad ranges of ρ covered in the ρ-τ-plots of figure 7.4. This is most striking in the case of gS-1/1', where all possible values of ρ are compatible with the NMR data. Due to the nearly parallel alignment of the fluoro-phenyl and peptide symmetry axes, the assumed value of χ_1 and the solution found for ρ even show a linear dependency. Indicated alongside the ρ-τ-maps of χ^2 are the ranges of χ_1 that are predicted to be favorable by energy profiles. They narrow down the allowed ranges of ρ considerably. Still, they do not allow a satisfactorily good determination of ρ, and may not be perfectly reliable since they are determined on a rigid molecular model *in vacuo*.

In conclusion, it has to be stated that the additionally synthesized peptide gS-1/1' does not add as much information as was hoped for. This is a direct consequence of the nearly parallel

arrangement of the (i)- and (i+2)-side chains in a β-strand situation. Since all 4F-Phg labels are also nearly parallel to the molecular z-axis, our labeling strategy—in the special case of gramicidin S—does not allow a reliable determination of the molecular azimuthal rotation, ρ. This is especially disappointing in the present situation, as the τ-value of the I-state is contradicting biophysical intuition, and additional information is needed to give a convincing interpretation. To overcome the problem, additional information on the torsion angle χ_1 was sought for in a MD simulation. Moreover, ^{15}N-labels introduced into the gS backbone were used to gather additional spectroscopic information and orientational constraints.

Molecular dynamics simulations of side chain torsion angle

In an attempt to improve our knowledge of side chain torsion, a molecular dynamics (MD) study of gramicidin S *in vacuo* was performed. This was meant to complement the analysis presented above, which was carried out to include *any* torsion angle. Now, a better idea of the *actual* torsion angle was sought for.

Three COSMOS MD trajectories of 10 ns duration were run for each of the two gS analogues, gS-1/1' and gS-3/3'. One out of three MD runs was performed at a high temperature of 593 K in order to fully explore conformational space and find all allowed values of side chain torsion. Figure 7.5 shows the resulting trajectories of fluoro-phenyl torsion χ_1, and table 7.5 compiles the average χ_1 values found after equilibration. These values were also used to mark the 'allowed panels' in figure 7.4. Note that figure 7.5 shows twice the necessary angular range for reason of clarity, while table 7.5 reduces the range to the essential $-90° < \chi_1 \le 90°$. As each molecule carries two 4F-Phg side chains, each MD run produced two χ_1-trajectories and two average values.

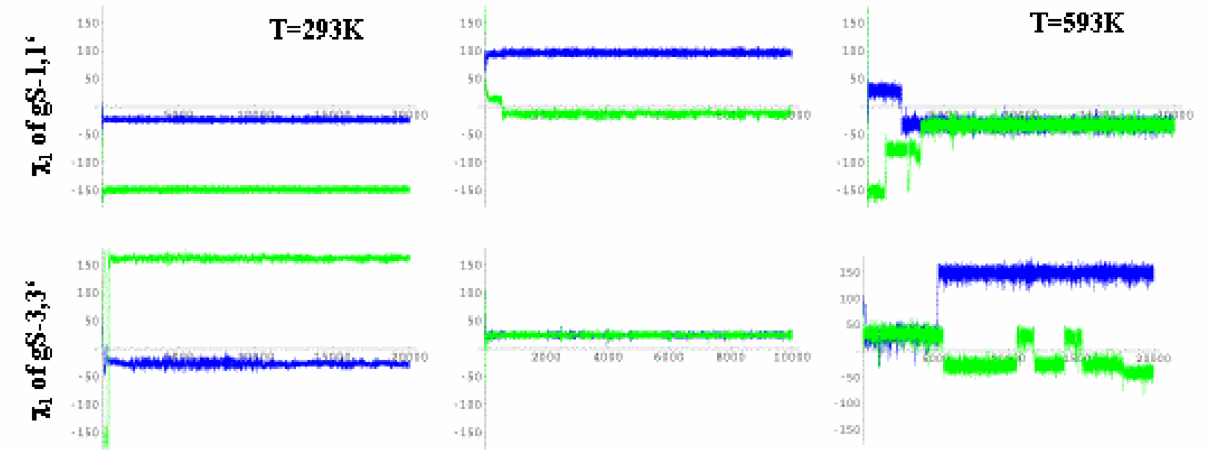

Figure 7.5: COSMOS-MD-trajectories of 4F-Phg side chain torsion angle χ_1 observed on gS-1/1' (top) and gS-3/3' (bottom). For each analogue two MD runs were performed at 293 K (left and middle), and one at 593 K (right).

Table 7.5: Average equilibrium χ_1 values in COSMOS MD simulations

molecule	run	temperature	χ_1	χ_1
gS-1/1'	1	293 K	-23°	31°
	2	293 K	-84°	-13°
	3	593 K	-33°	-33°
gS-3/3'	1	293 K	-27°	-19°
	2	293 K	24°	24°
	3	593 K	-32°	-33°

The high-temperature trajectories reach equilibrium values after approximately 3 ns. During equilibration they cover the whole range of possible angles, thereby ensuring that no favorable conformation is overlooked. The equilibrium state for gS-3/3’ may not be fully stable, since one of the phenyl side chains flips to another value of χ_1 twice. In both analogues a torsion of χ_1 = -33° is found, which is near the edge of the range found to be 'allowed' in energy profiles (*cf.* table 7.1). The observed standard deviation of only 7° seems to contradict the energy profiles where very flat minima are found for a β-sheet situation. This may be caused by the coupling to the surrounding heat bath. Too short a value of the coupling's time constant may suppress the temperature fluctuations that are thermodynamically meaningful at the molecular scale level.

The room temperature trajectories equilibrate much faster. They converge to very narrow χ_1 ranges with a standard deviation of only 4°, but they do not reach unique conformations. The first run on gS-1/1’ again found χ_1 on the border of the 'allowed' range, while the second run produced an outlier at χ_1 = -84°, which is clearly not 'allowed' according to the energy profiles. Both runs on gS-3/3’ produced χ_1 values consistent with the energy profiles. Both values in the first run were found on the negative 'allowed' edge around –20°, and both values in the second run on the positive end of the 'allowed' range, around 25°.

In contrast to the analysis in terms of energy profiles, no unique answer for the torsion angle χ_1 is found in the COSMOS MD simulations. MD yields χ_1 values on the very edge of the sterically permitted range, with surprisingly low standard deviations. An explanation would be a correlation between the χ_1 values in one molecule, i.e. that by steric repulsion both fluoro-phenyl side chains force each other into the extremes of the energetically allowed ranges. Such correlation would be a pure *in vacuo*-effect, since a realistic simulation would include solvent molecules and lipid acyl chains, which will in turn readily cover up the weak long-distance interactions between the two fluoro-phenyl rings.

We conclude that MD, although being methodologically far superior to primitive energy potentials, does not give a reliable idea of χ_1 in the present case. The core of the problem is found in the restrictions put onto the structure. For the *in vacuo* MD simulations, only the inclusion of hydrogen bonds restricts the molecular structure, warranting the experimentally observed β-sheet conformation. Other than backbone conformation, no experimental evidence enters the MD calculation. In the method of energy profiles, on the other hand, the molecule is constrained to the experimentally observed conformation. This conformation is assumed to be perfectly rigid, and no structural adaptation or relaxation is allowed for. In comparison, the method of energy profiles imposes too strong a restriction, while *in vacuo* MD provides too little restriction. The ambiguities and instabilities found in the COSMOS trajectories indicate that too little restriction implies more problems in the present case.

Therefore, the present analysis sticks to the crude method of energy profiles while being fully aware of the need to refine methodology in future applications.

An additional result was obtained concerning the distance between the two fluorine labels. In the second run at 293 K, values for fluorine-fluorine distance were collected. They average to 9.7 Å for gS-1/1’ and 7.5 Å in gS-3/3’, with a standard deviation of 0.1 Å. The distances derived from the NMR structure of Xu *et al.*[9] are almost identical, 9.5 Å and 7.0 Å, respectively. This is another indication that Xu *et al.*'s structure gives an excellent model for gS (though not necessarily in a membrane environment), especially since a different structure (determined by Doi *et al.*[24]) was used as starting point for the present MD runs. During the run, it quickly converged to a structure similar to Xu *et al.*'s, proving its favorable energetical properties.

^{15}N-NMR analysis

To overcome the problem of the still ambiguous 4F-Phg torsion angle χ_1, both gramicidin analogues gS-1/1' and gS-3/3' were also synthesized with backbone ^{15}N labels, namely ^{15}N-Leu$^{3,3'}$ and ^{15}N-Val$^{1,1'}$, respectively. These labels were expected to ideally complement the fluorine labels discussed above, because the unique component of the almost rotationally symmetric ^{15}N CSA tensor (which is almost parallel to the N-H bond, cf. figure 7.3) is orthogonal to the C_ζ-F bond that was found to be problematic in the ^{19}F analysis. ^{15}N-NMR measurements were carried out on oriented bilayer samples, and again additional resonances were found under the relevant conditions. Along with table 7.6 the ^{15}N-NMR spectrum of gS-3/3’ in DMPC at 25°C is shown. The new resonance is marked by an arrow, while the unmarked resonance corresponds to the S-state that is also observed at temperatures above the lipid phase transition. The lyophilate powder lineshape is indicated schematically by a dashed line, the underlying experimental spectrum was shown as figure 7.3. Table 7.6 gives a compilation of all observed resonance positions.

In some samples of gS-3/3’ in DMPC, the S-state resonance at the lipid phase transition temperature did not change its position upon changing the sample's tilt with respect to B_0. This finding indicates that in these samples the S-state had lost its orientation and mobility, in contradiction to the fluorine results. At the same time, the I-state was found unchanged, indicating its high structural stability. It should be noted that sample stability was an important issue in nitrogen CP measurements. These experiments require long measurement times (several days, as compared to few hours in ^{19}F-NMR of gS) and introduce higher r.f. powers into the sample. Sample stability was confirmed by ^{31}P-NMR measurements before and after every ^{15}N-NMR experiment.

Table 7.6: Resonances observed in ^{15}N-NMR of gS-1/1’ and gS-3/3’, and spectrum observed on gS-3/3’ at a 1:40 lipid to peptide ratio in DMPC at 25°C.

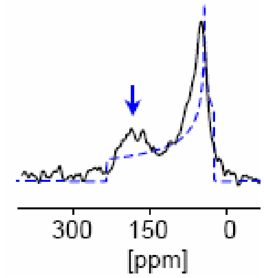

	gS-1,1'		gS-3,3'	
resonance	T	σ	T	σ
S-state	25°C	89 ppm	35°C	61 ppm
	-10°C	60 ppm	25°C	51 ppm
I-state	-10°C	157 ppm	25°C	185 ppm

For both analogues, the ^{15}N-NMR resonances characteristic of the I-state were found to be extremely broad, with a FWHM around 80 ppm. From ^{31}P- and ^{19}F-NMR spectra an increase in mosaic spread can be ruled out. Therefore, the extreme spectral width is most likely caused by an overlap of two individual lines originating from the two ^{15}N labels of each analogue. Since the two lines are not resolved, their individual frequencies could not be exactly determined. To take this uncertainty in resonance frequencies into account, analysis was carried out not only for the spectral maxima highlighted by shaded boxes in table 7.6, but also assuming two differing resonances. Their frequencies, σ_1 and σ_2, were assumed to be centered at the observed maximum, and to differ by $\Delta\sigma$ = 20 or 40 ppm (for concrete values see table 7.7).

The resulting ρ-τ-plots of the χ^2-analysis are shown in figure 7.6. The experimental error was estimated to have a standard deviation of 10 ppm, contours are shown at χ^2 = 2, 4, and 6. As in the case of ^{19}F-NMR, the fact that molecular mobility had ceased (S_{mol} = S_{Phg} = 1.0) was a vital prerogative for the analysis. In each case, acceptable fits of experimental data are found. The best-fit profiles found for both analogues show qualitative similarity, which is again effected by the similarity of the (i)- and (i+2)-residues in a β-strand situation.

For reasons of completeness, table 7.7 presents the minima of χ^2 that are found, although they bear far less significance than the areas encircled by the χ^2 = 2 contours (*cf.* chapter II). For both analogues a perpendicular tilt of τ = 90° is found when coinciding resonances are assumed, which is the expected result for symmetry reasons. With increasing $\Delta\sigma$, an increasingly tilted molecule needs to be assumed to fit the experimental data, up to $\tau \approx 70°$, in good agreement with the fluorine results. In the case of gS-1/1', as well as for gS-3/3' with $\Delta\sigma$ = 0, two best-fit orientations are found. For gS-3/3' under the assumption of differing resonances, a unique solution is found, which is not giving a perfect fit anymore at $\Delta\sigma$ = 40 ppm. In the following section, an unambiguous solution is identified by comparison with the fluorine data.

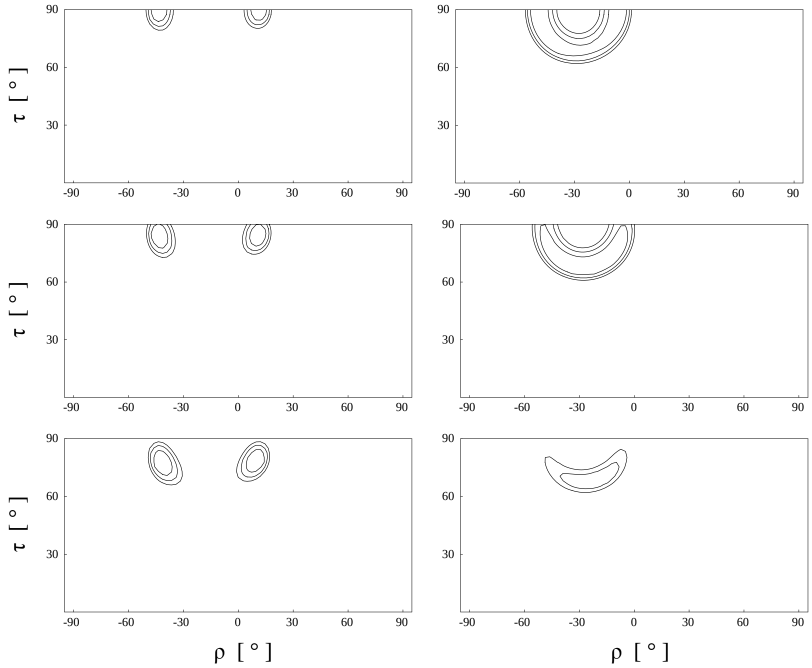

Figure 7.6: Least-squares fits to gS-1/1' (left) and gS-3/3' (right), carried out for a series of different nitrogen resonance frequencies: (top) coinciding resonances, 20 ppm (middle) and 40 ppm (bottom) difference between the two resonances (*cf.* table 7.7)

Table 7.7: Minima in χ^2 functions calculated from ^{15}N-NMR data of both gS analogues, assuming thattwo different line positions σ_1 and σ_2 underlie the observed broad resonance.

	gS-1/1'					gS-3/3'				
$\Delta\sigma$ [ppm]	σ_1 [ppm]	σ_2 [ppm]	ρ [°]	τ [°]	χ^2	σ_1 [ppm]	σ_2 [ppm]	ρ [°]	τ [°]	χ^2
0	157	157	-43	90	0	185	185	-50	90	0
			10	90	0			-6	90	0
20	147	167	-42	84	0	175	195	-22	69	0
			10	84	0					
40	137	177	-41	78	0	165	205	-22	68	2.5
			9	78	0					

Consensus orientation

Given the situation of an ambiguous χ_1 in ^{19}F- and insufficient resolution in ^{15}N-analysis, a summary representation showing the unique 'consensus regions' was generated from overlays of the ρ-τ-plots presented above. The outermost points reached by each contour were used to generate a 'summary contour' for the corresponding χ^2 value. For ^{19}F analysis, only panels for energetically allowed χ_1 values were used, while in the case of ^{15}N all χ_1 profiles presented above entered the summary analysis. The left panel of figure 7.7 shows the resulting ρ-τ-plots for both labels of each analogue. A unique region of overlap can immediately be identified when comparing the four plots. It is marked by circles and is centered around Euler angle values of ρ = -45°±10° and τ = 80°±10°. This 'consensus orientation' of gS is shown in the right panel of figure 7.7, where z^{LAB} is within the paper plane and points upwards, and the viewer is looking down the positive z^{MOL}-axis. From the width of the overlap the error in the resulting peptide orientation is estimated to be ±10°.

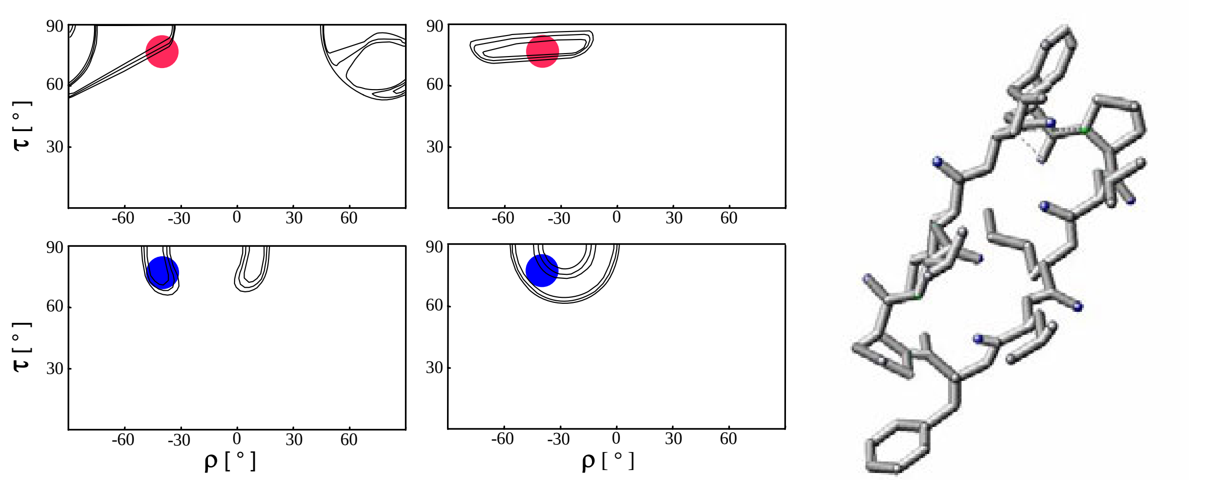

Figure 7.7: (Left) Summary representation of χ^2-profiles generated from ^{19}F- (top) and ^{15}N-NMR data for gS-1/1' (left) and gS-3/3' (right), which show a unique overlap at $\tau\approx80°$ and $\rho\approx-45°$, as indicated by the circles. (Right) Corresponding orientation of the gS molecule, viewed from its hydrophobic side.

In conclusion, a unique orientation consistently explaining the additional I-state resonances is found. A convoluted analysis process was necessary which had to integrate input from various sources. Data from ^{15}N- and ^{19}F-NMR as well as from molecular modeling and high-resolution NMR structure determination was included. We note that we see the future in a combined analysis, where NMR data is introduced into a molecular dynamics program (e.g. COSMOS) in the form of 'constraints', as is common practice in solution-state NMR spectroscopy. ^{15}N- and ^{19}F-NMR were found to ideally complement each other in the case of gS, since their most sensitive tensor components are found to be virtually orthogonal in the β-strand structure. For the same reason, the inclusion of an additional label of the same nucleus was found to be less helpful, since here the sensitive directions are found to be almost parallel. As a final step, the new orientation found for gS in lipid bilayers needs to be interpreted in biophysical and functional terms.

Discussion: Functional pore-model

The new 'upright' orientation found for gramicidin S by ^{19}F- and ^{15}N-NMR data is puzzling from a biophysical point of view. It exposes the hydrophilic ornithine side chains laterally, which seems energetically unfavorable in a membrane environment. But considering the special value of ρ found in our analysis and the lack of wobbling motions, an oligomeric model seems to be convincing. Two or more gS molecules can associate via hydrogen bonding reminiscent of an extended β-sheet. The special slant observed for the β-strands is ideally predisposed to allow two hydrogen bridges to be formed between two gS monomers (Orn2NH→Pro5'CO, and Orn2'NH→Pro5CO). If this bonding pattern would continue over several oligomers, the resulting structure would curl up and close up onto itself, while remaining within the dimensions of a single lipid bilayer. Closure of the structure is made possible by the tendency for twisting that is intrinsic to an extended β-sheet[52]. The resulting

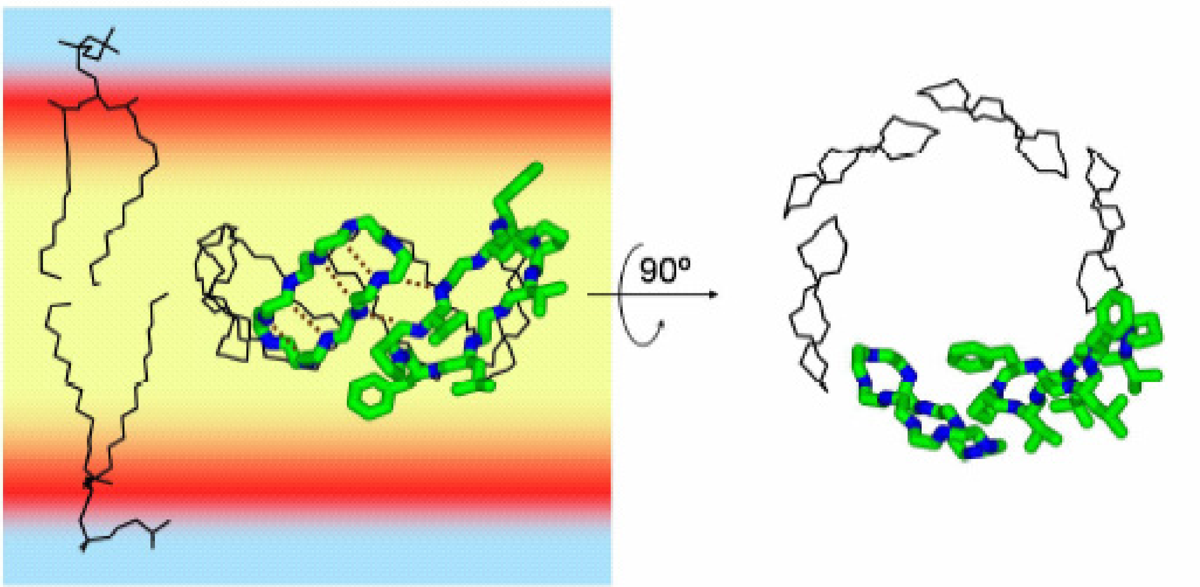

Figure 7.8: Proposed model for oligomeric gramicidin S oligomer in a DMPC membrane, satisfying the orientational constraints obtained from ^{19}F- and ^{15}N-NMR. (Left) The oligomer is depicted from within the lipid bilayer interior (showing only backbone atoms for clarity, but with hydrophobic side chains added to one monomer). Dotted lines indicate the H-bonds stabilizing the β-barrel. Two DMPC molecules give the dimensions of the lipid bilayer, with background colors highlighting regions of differing hydrophobicity. (Right) Top view.

structural motif is called a 'β-barrel' and is very common in proteins found in the outer membrane of bacteria, in mitochondria, as well as in some water-soluble proteins[53]. Actually, β-barrel membrane proteins form a large class of membrane proteins[54;55], in parallel to the typical α-helical motifs of single- and seven-helix receptor proteins. A well-researched example are porins[56], which form pores through the monomers of a trimeric assembly.

In analogy to the present situation, Wimley *et al.*[57] find membrane-binding, β-sheet formation and aggregation in a very simple model hexapeptide, Ac-Trp-Leu_5. They also speculate on a structure resembling a β-barrel, but rule it out on the basis of a PATIR-FTIR measurement. (It seems tempting to introduce an isotope label into their system and determine the orientational behavior present.)

For the reported gS orientation, a closed β-barrel structure was found sterically feasible by docking assays using COSMOS. A possible hexameric structure is presented in side and top views in figure 7.8, along with phospholipid molecules for dimensional reference. Only recently, a X-ray crystallographic study by Grotenbreg *et al.*[58] reported a very similar hexameric assembly for an asymmetric furanoid-sugar-containing analogue of gS. In our case, the number of monomers is speculative, but cannot be very high since the assembly shows rotational diffusion around the membrane normal. Nor can it be very small (such as a dimer) because the entire assembly does not wobble in the lipid bilayer. It has to be noted that the feasibility of the suggested β-barrel structure is highly dependent on the particular value found for ρ. A slightly different value would prohibit hydrogen bonding (although a value differing by approx. ±15° would allow similar structures with one or three hydrogen bridges, respectively). A positive value of ρ would prohibit the suggested structure altogether, since here the intrinsic β-sheet twist would not allow the structure to close back onto itself but form a helical ribbon (cross-β-sheet fibril) instead.

The proposed oligomeric structure explains the observed loss of molecular mobility. It also solves the problem of laterally exposed hydrophobic ornithine side chains. Those are now projecting towards the middle of the assembly, making the outside completely hydrophobic. The hydrophobic outside suggests a location of the assembly in the hydrophobic core of the lipid bilayer, which is indicated as yellow background coloring in figure 7.8 and demonstrates that the dimensions of the assembly are compatible with the bilayer dimensions.

The dissociation constant reported for the terminal NH_3^+ group of free ornithine is pK = 10.52, which is almost identical to that of lysine, pK = 10.67.[59] These values indicate that the ornithine side chains of gramicidin S are probably in their protonated form, i.e. carrying a positive charge. As a result, a very high positive charge density would be found in the center of the proposed gS oligomer, making the whole assembly energetically unfavorable. To counter this objection, it can be speculated that the terminal NH_3^+ groups of two or more ornithines form a correlated cooperative network with multiple pK values, making the pK value of the free amino acid meaningless. Thus, such a system may distribute the charge of a single proton over several NH_2 groups at physiological pH. Another mechanism reducing charge density in the middle of the assembly could be complexation of an ion such as Na^+, i.e. replacing several protons by a single ion which may be complexed by multiple ornithine residues.

All details reported so far on the proposed model structure strongly suggest a molecular mechanism for the antimicrobial function of gS. Being immersed in the hydrophobic core of the lipid bilayer and possessing a highly hydrophilic center, the assembly may act as a pore,

allowing solutes and ions to pass the membrane and thus killing microbes by permeabilizing their membranes. In the standard for antimicrobial function,[18] the observed re-orientation of gS would indeed represent a structural flip of the peptide into its active I-state, thereby killing microbes by a barrel-stave mechanism (*cf.* chapter I). Step-like conductance events indicative of opening and closing (or assembly and disassembly) of pores are actually characteristic of gS in electrophysiological experiments.[17] In addition, our model explains why an artificially decreased hydrophilic vs. hydrophobic 'sidedness' in specifically designed analogues results in loss of antimicrobial function[11], since sidedness of the gS molecule would be a central prerequisite for pore formation.

Formation of a pore would be strikingly similar to the action of pore-forming toxins. These large cytotoxic proteins are known to form oligomers, where each monomer inserts one or two β-hairpins into bacterial membranes. The inserted β-hairpins form β-barrels upon oligomerization, opening a lethal pore in the target membrane. Examples of pore-forming toxins are α-hemolysin from *Staphylococcus aureus*[60] and perfringolysin O from *Clostridium perfringens*[61].

Oligomerization was also observed in other β-sheet antimicrobial peptides. PG-1 is a β-sheet antibiotic peptide found in porcine leukocytes, and is found to form dimers.[62] Wimley *et al.*[63] report the dimerization of HNP-2, a human defensin. In addition, they find evidence for pore formation in vesicle leakage experiments. They suggest a pore model of a hexamer of dimers, but do not provide any structural evidence. We note that in our docking assays dimers of gS making contact on their hydrophilic face were found to be very stable, but do not offer an explanation for the observed orientation.

In conclusion, we propose the model of an oligomeric pore to structurally explain the antimicrobial action of gramicidin S. Our model is based on an unambiguous orientation determination of gS in its I-state, determined from multiple solid-state NMR constraints on macroscopically aligned bilayer samples.

Reference List

(1) Salgado, J.; Grage, S. L.; Kondejewski, L. H.; Hodges, R. S.; McElhaney, R. N.; Ulrich, A. S. *J.Biomol.NMR* **2001**, *21*, 191-208.

(2) Afonin, S. Structural studies on membrane-active peptides in lipid bilayers by solid state ^{19}F-NMR. Ph.D. thesis, Friedrich-Schiller-Universität Jena, 2003.

(3) Gause, G. F.; Brazhnikova, M. G. *Nature* **1944**, *154*, 703.

(4) McInnes, C.; Kondejewski, L. H.; Hodges, R. S.; Sykes, B. D. *J.Biol.Chem.* **2000**, *275*, 14287-14294.

(5) Kondejewski, L. H.; Farmer, S. W.; Wishart, D. S.; Kay, C. M.; Hancock, R. E. W.; Hodges, R. S. *J.Biol.Chem.* **1996**, *271*, 25261-25268.

(6) Kondejewski, L. H.; Farmer, S. W.; Wishart, D. S.; Hancock, R. E. W.; Hodges, R. S. *Int.J.Pept.Protein Res.* **1996**, *47*, 460-466.

(7) Hull, S. E.; Karlsson, R.; Main, P.; Woolfson, M. M.; Dodson, E. J. *Nature* **1987**, *275*, 206-207.

(8) Gibbs, A. C.; Kondejewski, L. H.; Gronwald, W.; Nip, A. M.; Hodges, R. S.; Sykes, B. D.; Wishart, D. S. *Nat.Struct.Biol.* **1998**, *5*, 284-288.

(9) Xu, Y.; Sugár, I. P.; Krishna, N. R. *J.Biomol.NMR* **1995**, *5*, 37-48.

(10) Richardson, J. S. *Adv.Prot.Chem.* **1981**, *34*, 167-339.

(11) Kato, T.; Izuyima, N. *Biochim.Biophys.Acta* **1977**, *493*, 235-238.

(12) Bechinger, B. *Biochim.Biophys.Acta* **1999**, *1462*, 157-183.

(13) Sitaram, N.; Nagaraj, R. *Biochim.Biophys.Acta* **1999**, *1462*, 29-54.

(14) Prenner, E. J.; Lewis, R. N. A. H.; McElhaney, R. N. *Biochim.Biophys.Acta* **1999**, *1462*, 201-221.

(15) Prenner, E. J.; Lewis, R. N. A. H.; Kondejewski, L. H.; Hodges, R. S.; McElhaney, R. N. *Biochim.Biophys.Acta* **1999**, *1417*, 211-223.

(16) Prenner, E. J.; Lewis, R. N. A. H.; Neuman, K. C.; Gruner, S. M.; Kondejewski, L. H.; Hodges, R. S.; McElhaney, R. N. *Biochemistry* **1997**, *36*, 7906-7916.

(17) Wu, M.; Maier, E.; Benz, R.; Hancock, R. E. W. *Biochemistry* **1999**, *38*, 7235-7242.

(18) Huang, H. W. *Biochemistry* **2000**, *39*, 8347-8352.

(19) Afonin, S.; Glaser, R. W.; Berditchevskaia, M.; Wadhwani, P.; Gührs, K.-H.; Möllmann, U.; Perner, A.; Ulrich, A. S. *Chembiochem* **2003**, *4*, 1151-1163.

(20) Ramachandran, G. N.; Ramakrishnan, C.; Sasisekharan, V. *J.Mol.Biol.* **1963**, *7*, 95-99.

(21) Afonin, S.; Dürr, U. H. N.; Glaser, R. W.; Ulrich, A. S. *Magn.Reson.Chem.* **2004**, *42*, 195-203.

(22) Sternberg, U.; Koch, F.-T.; Bräuer, M.; Kunert, M.; Anders, E. *J.Mol.Model.* **2001** , *7*, 54-64.

(23) Möllhoff, M.; Sternberg, U. *J.Mol.Model.* **2001**, *7*, 90-102.

(24) Doi, M.; Fujita, S.; Katsuya, Y.; Sasaki, M.; Taniguchi, T.; Hasegawa, H. *Arch.Biochem.Biophys.* **2001**, *395*, 85-93.

(25) Pines, A.; Gibby, M. G.; Waugh, J. S. *J.Chem.Phys.* **1973**, *59*, 569-590.

(26) Levitt, M. H.; Suter, D.; Ernst, R. R. *J.Chem.Phys.* **1986**, *84*, 4243-4255.

(27) Metz, G.; Wu, X.; Smith, S. O. *J.Magn.Reson.A* **1994**, *110*, 219-227.

(28) Kim, H.; Cross, T. A.; Fu, R. *J.Magn.Reson.* **2004**, *168*, 147-152.

(29) Bennett, A. E.; Rienstra, C. M.; Auger, M.; Lakshmi, K. V.; Griffin, R. G. *J.Chem.Phys.* **1995**, *103*, 6951-6958.

(30) Berger, S.; Braun, S.; Kalinowski, H.-O. *NMR-Spektroskopie von Nichtmetallen; Band 2: ^{15}N-NMR-Spektroskopie*; Georg Thieme Verlag: Stuttgart, 1992.

(31) Levy, L. G.; Lichter, R. L. *Nitrogen-15 nuclear magnetic resonance spectroscopy*; John Wiley and Sons Inc.: New York, USA, 1979.

(32) Aisenbrey, C.; Bechinger, B. *Biochemistry* **2004**, *43*, 10502-10512.

(33) Bechinger, B. *Biophys.J.* **2001**, *81*, 2251-2256.

(34) Glaser, R. W.; Ulrich, A. S. *J.Magn.Reson.* **2003**, *164*, 104-114.

(35) Soubias, O.; Saurel, O.; Réat, V.; Milon, A. *J.Biomol.NMR* **2002**, *24*, 15-30.

(36) Ulrich, R.; Glaser, R. W.; Ulrich, A. S. *J.Magn.Reson.* **2003**, *164*, 115-127.

(37) Wishart, D. S.; Bigam, C. G.; Yao, J.; Abildgaard, F.; Dyson, H. J.; Oldfield, E.; Markley, J. L.; Sykes, B. D. *J.Biomol.NMR* **1995**, *6*, 135-140.

(38) Wishart, D. S.; Sykes, B. D. *Methods Enzymol.* **1994**, *239*, 363-392.

(39) Hori, Y.; Demura, M.; Iwadate, M.; Ulrich, A. S.; Niidome, T.; Aoyagi, H.; Asakura, T. *Eur.J.Biochem.* **2001**, *268*, 302-309.

(40) Harbison, G. S.; Jelinski, L. W.; Stark, R. E.; Torchia, D. A.; Herzfeld, J.; Griffin, R. G. *J.Magn.Reson.* **1984**, *60*, 79-82.

(41) Hartzell, C. J.; Whitfield, M.; Oas, T. G.; Drobny, G. P. *J.Am.Chem.Soc.* **1987**, *109*, 5966-5969.

(42) Hartzell, C. J.; Pratum, T. K.; Drobny, G. *J.Chem.Phys.* **1987**, *87*, 4324-4331.

(43) Oas, T. G.; Hartzell, C. J.; Dahlquist, F. W.; Drobny, G. P. *J.Am.Chem.Soc.* **1987**, *109*, 5962-5966.

(44) Wu, C. H.; Ramamoorthy, A.; Gierasch, L. M.; Opella, S. J. *J.Am.Chem.Soc.* **1995**, *117*, 6148-6149.

(45) Henzler Wildman, K. A.; Lee, D.-K.; Ramamoorthy, A. *Biochemistry* **2003**, *42*, 6558.

(46) Teng, Q.; Cross, T. A. *J.Magn.Reson.* **1989**, *85*, 439-447.

(47) Nevzorov, A. A.; Mesleh, M. F.; Opella, S. J. *Magn.Reson.Chem.* **2004**, *42*, 162-171.

(48) Fushman, D.; Cowburn, D. *Methods Enzymol.* **2001**, *339*, 109-126.

(49) Straus, S. K.; Scott, W. R. P.; Watts, A. *J.Biomol.NMR* **2003**, *26*, 283-295.

(50) Balla, M. S.; Bowie, J. H.; Separovic, F. *Eur.Biophys.J.* **2004**, *33*, 109-116.

(51) Hallock, K. J.; Lee, D.-K.; Omnaas, J.; Mosberg, H. I.; Ramamoorthy, A. *Biophys.J.* **2002**, *83*, 1004-1013.

(52) Marassi, F. M. *Biophys.J.* **2001**, *80*, 994-1003.

(53) Tsien, R. Y. *Annu.Rev.Biochem.* **1998**, *67*, 509-544.

(54) Wimley, W. C. *Curr.Opin.Struct.Biol.* **2003**, *13*, 404-411.

(55) Tamm, L. K.; Arora, A.; Kleinschmidt, J. H. *J.Biol.Chem.* **2001**, *276*, 32399-32402.

(56) Seshadri, K.; Garemyr, R.; Wallin, E.; von Heijne, G.; Elofsson, A. *Protein Sci.* **1998**, *7*, 2026-2032.

(57) Wimley, W. C.; Hristova, K.; Ladokhin, A. S.; Silvestro, L.; Axelsen, P. H.; White, S. H. *J.Mol.Biol.* **2004**, *277*, 1091-1110.

(58) Grotenbreg, G. M.; Timmer, M. S. M.; Llamas-Saiz, A. L.; Verdoes, M.; van der Marel, G. A.; van Raaij, M. J.; Overkleeft, H. S.; Overhand, M. *J.Am.Chem.Soc.* **2004**, *126*, 3444-3446.

(59) *CRC handbook of chemistry and physics*; CRC Press: Boca Raton, FL, 2003.

(60) Montoya, M.; Gouaux, E. *Biochim.Biophys.Acta* **2003**, *1609*, 19-27.

(61) Ramachandran, R.; Heuck, A. P.; Tweten, R. K.; Johnson, A. E. *Nat.Struct.Biol.* **2002** , *9*, 823-827.

(62) Fahrner, R. L.; Dieckmann, T.; Harwig, S. S.; Lehrer, R. I.; Eisenberg, D.; Feigon, J. *Chem.Biol.* **1996**, *3*, 543-550.

(63) Wimley, W. C.; Selsted, M. E.; White, S. H. *Protein Sci.* **1994**, *3*, 1362-1373.

VIII. PGLa: α-Helical antimicrobial peptide

The antimicrobial peptide PGLa forms an amphiphilic α-helix when bound to a membrane. We find that the helix axis assumes two distinct molecular orientations when observed at different concentrations in DMPC bilayers. NMR spectroscopy of CF_3-Phg (fluorine-) and Ala-d_3 (deuterium-) labeled PGLa analogues allows quantitative description of re-orientation. Here, a structural analysis of the spectroscopic observations is performed. An additional ^{15}N-labeled peptide had to be included in the analysis to distinguish between multiple best-fit solutions for the ^{19}F- as well as ^{2}H-NMR data. Results from the different labeling schemes convincingly agree. Detailed analysis including various molecular models allows for an assessment of error margins. The results are published in *Journal of Magnetic Resonance*[1] and in *Biophysical Journal*[2] (publications attached as appendix D and E), and are being prepared for a third publication.

Introduction

PGLa (peptidyl-glycylleucine-carboxyamide) is an antimicrobial peptide found in the skin of the African clawed frog *Xenopus laevis*.[4;5] It has the amino acid sequence

H_2N-^{1}GMASKAG**AI**^{10}**A**GK**IA**KVALK^{20}AL-$CONH_2$.
** * **

As a member of the magainin family of water-soluble peptides, it assumes an α-helical secondary structure upon membrane binding.[6] The binding is selective to the negatively charged bacterial and fungal membranes, which are permeabilized by the peptide. A specific protein receptor is not involved in this antimicrobial action,[7] making it very unlikely that any resistance would develop against this class of peptides. A better understanding of the detailed mechanism of action would help to improve their therapeutic properties, in particular the differentiation between bacterial and eukaryotic membranes.

In previous solid-state NMR studies on a series of selectively ^{15}N-labeled samples, the helix axis of PGLa was found to align roughly parallel to the membrane surface (τ=90°±30°), as expected from the peptide's amphiphilic character. Figure 8.1 gives a helical wheel projection of PGLa where PGLa's striking amphiphilic profile is made visible, with all hydrophilic residues (4 lysines, 1 serine, N-terminal glycine) pointing into a narrow sector of the α-helix. This distribution of cationic and hydrophobic side chains allows a straightforward prediction of how the peptide should be rotationally positioned within the lipid bilayer, although this alignment was not accessible from the ^{15}N-NMR data.

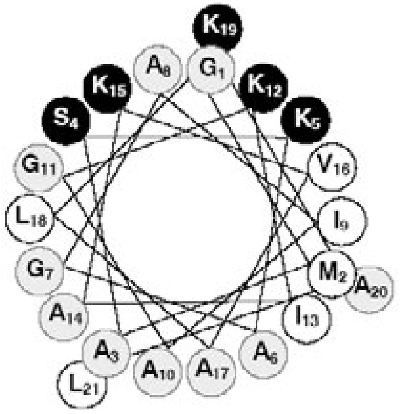

Figure 8.1: Helical wheel representation of the antimicrobial peptide PGLa with hydrophilic residues in black and hydrophobic residues in white.

Our laboratory has incorporated different types of isotope labels into the PGLa sequence, with the aim to confirm

previous results regarding PGLa's orientation in lipid bilayers, and to determine its orientation more accurately. In addition, a comparison of different isotope labeling strategies was intended.

Glaser *et al.*[8] prepared a 4F-Phg labeled analog of PGLa. In oriented DMPC bilayer samples this analog showed a qualitative change in fluorine resonance frequencies in different concentration regimes, indicative of different orientational states.

To extend the fluorine labeling scheme used in chapters VI and VIII to CF_3-groups, a series of five PGLa analogues carrying one CF_3-Phg label each were synthesized by Sachse.[9] In each analogue, a single Ala or Ile side chain was replaced by CF_3-Phg, as marked by asterisks in the sequence above. Four out of of five analogs were shown to be structurally and functionally intact, and hence meaningful for structural analysis.[1] PGLa-Ala8(CF_3-Phg) had to be excluded from the study since it showed a reduced α-helix content in CD spectroscopy and a considerably reduced activity in antimicrobial assays. The behavior of the intact CF_3-Phg labeled PGLa analogues was then studied in different types of model membranes. Unexpectedly, two distinct orientational states were detected, and could be comprehensively characterized at peptide to lipid ratios of 1:200 and 1:50, respectively. In these studies by Glaser *et al.*[8] and of Sachse[9], the advantages of ^{19}F-NMR became directly obvious: The exquisitely high sensitivity of the fluorine nucleus made it possible to scan large temperature and concentration regimes in short times. Additionally, and most significantly, the use of a CF_3-label eliminates the need to know the Phg side chain torsion angle χ_1, which had complicated the structure analysis of B18 and gramicidin S (see chapters VI and VII).

For comparison to more common but far less sensitive deuterium NMR, a parallel series of five CD_3-labeled analogues was prepared by Tremouilhac.[10] The five positions used for CF_3-labeling were substituted by Ala-d_3, as this side chain also provides a defined rigid connection of the label to the peptide backbone. Please note that in two cases the deuterium labeling potentially introduces some distortion, since Ile was replaced by Ala-d_3. In macroscopically aligned DMPC bilayers, the deuterated species of PGLa changed their spectral properties, thereby indicating re-orientation, as did the fluorinated analogs.

In addition, a single PGLa analogue carrying a ^{15}N label in position Gly^{11} was synthesized to complement fluorine and deuterium data.

In the following, a structural interpretation for the changing spectral properties of PGLa is given. It is based on a best-fit analysis of the respective data using molecular models as described in chapter II. Special attention was paid to quantify the influence that the choice of conformational model takes on the results. Idealized model structures were systematically varied, and a more realistic model was generated which takes into account the influence of the bulky CF_3-Phg side chain on an ideal α-helix.

Materials and methods

Synthesis and sample preparation

Five CF_3-Phg labeled analogues of PGLa were synthesized and purified by Parvesh Wadhwani and Carsten Sachse, and their structural and functional integrity was checked by CD spectroscopy and antimicrobial assays.[1;9] Peptide:lipid ratios of 1:200 and 1:50 PGLa in DMPC were chosen for the preparation of macroscopically aligned bilayer samples. The peptide (typically 0.25 mg) was dissolved in water, and DMPC was dissolved in methanol. Both components were mixed to give a 70% methanol solution, which was then spread onto glass slides and further treated to give oriented samples as described for B18.

Five Ala-d_3 and one ^{15}N-Gly[11] labeled analogues of PGLa were synthesized and purified by Parvesh Wadhwani and Pierre Tremouilhac.[10] ^{2}H-NMR spectra were measured in dispersions of multilamellar vesicles (MLVs) of DMPC, in order to enhance the signal-to-noise ratio by increasing the total amount of peptide that can be accumulated within the NMR coil. Earlier studies on deuterated model peptides found splittings measured in MLVs to give almost identical results as in oriented samples.[11;12] For making MLVs, peptide and DMPC were co-dissolved in a minimum amount of chloroform at 1:200 and 1:50 peptide:lipid ratio, then air dried to form a film on the walls of a glass vessel. This film was vacuum-dried and re-hydrated by adding the equivalent weight of deuterium depleted water. The resulting MLV dispersion was packed into a flat polyethylene bag for NMR spectroscopy.

For ^{15}N-NMR spectroscopy, oriented samples from ^{15}N labeled peptides were prepared as described above.

NMR spectroscopy

All data were acquired at 35°C. Instrumentation and spectroscopic parameters for ^{19}F solid-state NMR experiments were identical to the ones used on B18 samples. The spectra were acquired with single-pulse experiments (as discussed in chapter IV), in contrast to the Hahn echo experiments used for monofluorinated B18 and gS samples. Typically, several 1000 scans were collected in 2-4 hours.

^{2}H-NMR experiments were performed at 76.78 MHz on a Bruker Avance 500 MHz NMR spectrometer, using a quadrupolar echo sequence with 4.0 μs 90°-pulses, 30 μs echo delay time, 80 ms recycle delay, and 250 kHz spectral width. 300,000 to 2,000,000 scans were collected.

^{15}N-NMR experiments were performed at 50.68 MHz on a Bruker Avance 500 MHz NMR spectrometer, using a ramped cross polarization sequence with a CP power of 40 kHz, 2.5 s relaxation delay time, 100 kHz spectral width, 2048 data points, and TPPM20 proton decoupling. In hydrated samples the contact time was 1 ms, and 2 ms in dry peptide powder. 30,000 and 200,000 scans were collected, respectively. Spectra were referenced to $^{15}NH_4NO_3$ by setting the signal of solid $^{15}NH_4Cl$ to 18.0 ppm.

The quality of orientation of the lipid bilayers was determined by ^{31}P-NMR, and typically 80 to 90% of the lipid was well aligned between the glass plates.

Molecular modeling

No experimentally determined structure is available for the PGLa peptide, contrary to the gramicidin S peptide presented in the previous chapter. Model building therefore had to again resort to idealized secondary structure elements, as was done for the fusogenic peptide B18 in chapter VI. Since the α-helical conformation of membrane-associated PGLa is a well-established fact[6], the analysis concentrates on α-helices. Nevertheless, attempts were made to fit the data with idealized models for 3_{10}-helix (modeled with Ramachandran angles of φ = -50°, ψ=-28°), π-helix (φ=-57°, ψ=-71°) and β-sheet (φ=-139°, ψ=135°).

The main focus was put on α-helical structures, for which a poly-Ala sequence was generated as starting model. The molecular modeling package SYBYL offers a comprehensive library of amino acid side chains together with typical Ramachandran angle values based on statistical analysis of elucidated structures. The poly-Ala α–helix was chosen because the small uncharged side chain Ala causes least distortion in the α-helical conformation. It showed Ramachandran angles of φ=-58° and ψ=-47°, and shall be referred to as the 'standard' α-helix. The standard α-helix was found to give values of α=53.2° and β=121.1° for the Euler angles describing the transformation from PPL to MOL coordinate systems (cf. chapter II, esp. equation 2.6). The helix pitch angle ω, describing the angle between two adjacent residues (as introduced in equation 2.10), was found to be ω=99.8°.

Apart from the standard α-helix, two different types of variation from ideal α–helical structure were considered. In a first set of model structures, the Euler angle β as well as the pitch angle ω were systematically varied to quantify the influence of structural deviations on the best-fit results. The side chain Euler angle α was not varied in this series, since a change in α automatically leads to a change of -ρ by the same amount without affecting the quality of the fit. Note that all of these models show perfect helical symmetry. They will be referred to as 'regular' α-helices in the following. Orientational fits were calculated for a large number of regular α-helical structures with ω between 95 and 102°, and β between 105 and 120°. Steps were small enough (1-5°) to see a smooth shift in the results of the respective best-fits.

As a second modification of α-helical structure from its standard conformation, we tried to model the distortion that the bulky CF_3-side chain is likely to afflict on the α-helical peptide backbone. Starting from the standard α-helix structure, four pdb-structures for the four CF_3-Phg labeled analogs were generated in SYBYL by 'mutations' from a poly-Ala helix. These structures were then subjected to 500 steps of energy minimization in order to relax the respective local structure and accommodate the CF_3-Phg side chains. The small number of steps restricts the adaptation of the helix to the mutation to the close vicinity of the CF_3-Phg label. Therefore, the average pitch angle ω between residues is not changed, and only local effects are visible. A more global energy minimization would not make the model more realistic, since it cannot account for the lipid environment, which is the most relevant determinant of global structural deviations. Each PGLa-CF_3 structure was energy-minimized individually and then fitted back onto the wildtype structure given the MOL coordinate system. (Done in MOLMOL[13], commands: SelectAtom ':3-19@CA', Fit to_first). This overlay of the four analogs onto the wildtype allowed to collect the relevant coordinates of C_ε and C_ζ of each individual label in the common molecular coordinate system MOL. The energy-minimized structures showed a reduced side chain angle β in CF_3-Phg when compared to a poly-Ala helix, and rather variable values for the pitch angle ω between two adjacent residues.

All model structures were generated in pdb-format using SYBYL, where also energy-minimization was performed. In all helical structures the molecular coordinate system MOL was defined to have the z^{MOL}-axis along the helix axis of the peptide and the C_α atom of Lys^{12} positioned radially on the y^{MOL}-axis. This is analogous to the definitions used for B18 illustrated in figure 6.2.

Orientational analysis

The ^{19}F-NMR structure analysis of orientation-dependent dipolar couplings is considerably simpler than the analysis of anisotropic chemical shift values that was performed in chapters VI and VII of the present thesis. As given in equation (1.9), the orientation dependence of dipolar interaction is governed by the orientation of the internuclear connection *vector*. All necessary calculations are *vectorial* in nature and, therefore, easier to carry out and far easier to visualize and interpret than for a CSA tensor. Since the effective dipolar coupling in CF_3-Phg is perfectly aligned with the C_ε-C_ζ connecting vector, there is no necessity to define PAS and PPL coordinate systems here. Also, the ambiguous phenyl torsion angle χ_1 does not need to be considered, since it does not influence the direction of the C_ε-C_ζ axis onto which all dipolar couplings are averaged by the fast rotation of the CF_3-group around that axis.

The C_ε-C_ζ connecting vectors were extracted from the pdb files of the four labeled peptide analogues and used as input for the *Mathematica* programs described in chapter II. The programs transformed the input vectors into LAB coordinates for all possible values of ρ and τ following equations (2.3a) and (2.5). The expected dipolar splittings were then calculated from equation (1.10), using a maximum splitting value of $D_{ij}^{0} = -15.8\,\text{kHz}$, which in turn was calculated using equation (1.11). There, a fluorine-fluorine distance of 2.159(24)Å was employed, which is the value expected from a CF-bond length of 1.322(15)Å[14] in ideal tetrahedral geometry (see chapter V).

A perfectly analogous procedure was followed in the ^{2}H-NMR analysis of the Ala-d_3 labeled peptides. The mathematical equivalence of the quadrupolar splitting given by equation (1.12) and the dipolar splitting in equation (1.10) was already pointed out in chapter I. A value of 167 kHz is reported for the quadrupolar coupling constant of a rigid aliphatic deuteron. The maximum splitting in a powder spectrum, $\Delta\nu_0$, is then 250 kHz.[15] In the present case, this value needs to be scaled down by a factor of –1/3 to account for rotation of the CD_3-group around its symmetry axis (*cf*. equation 2.13), i.e. this study uses a value of $\Delta\nu_0 = 84.0\,\text{kHz}$ to predict quadrupolar couplings following equation (1.12).

For ^{15}N-NMR analysis, the same procedure was used as described in the preceding chapter for ^{15}N-labeled gramicidin S. The ^{15}N CSA tensor was determined on lyophilized PGLa-^{15}N-Gly^{11}, showing principal values of σ_{11}=14.5 ppm, σ_{22}=32.3 ppm, and σ_{33}=196.2 ppm. These values correspond to an isotropic position of σ_{iso}=83.9 ppm, an anisotropy of δ=115.2 ppm, and an asymmetry parameter of η=0.16 and were used to predict anisotropic ^{15}N chemical shift frequencies according to equation (1.3).

Since the NMR-data obtained on different nuclei is to be compared, data analysis using a χ^2 error function according to equation (2.2) was performed as outlined in chapter II. The *Mathematica* code used in the calculations is available on our website http://www-ifia.fzk.de/IFIA_Webseiten/Webseiten_ Ulrich/index.html .

Results

^{19}F-NMR spectroscopy

For all PGLa-CF_3 analogs, Sachse[9] prepared macroscopically aligned DMPC bilayer samples to record ^{19}F-NMR spectra. Representative spectra of PGLa-Ile13(CF_3-Phg) at different concentrations are shown in the panel of table 8.1. The presented spectra were recorded with single-pulse NMR experiments, where acquisition directly followed a 90°-pulse in the ^{19}F-observe channel. Continuous wave ^{1}H-decoupling was applied during acquisition. The gap between the 90°-pulse and the onset of acquisition was compensated by first order phase correction or backward linear prediction. The single-pulse experiment was slightly more sensitive than any echo experiment, which gave nearly identical spectra (data not shown). This finding confirms the conclusion of chapter IV that modern spectrometers give sufficient time resolution to record solid-state NMR spectra in a single-pulse experiment, thus avoiding the spectral distortions found in echo-spectra of substances showing both dipolar and CSA interaction.

Each ^{19}F-NMR spectrum of a CF_3-group at a single fixed orientation is epected to reveal a triplet (three narrow signals showing a ratio of 1:2:1 between their peak intensities), according to textbook knowledge. This simple spectral lineshape was the basis for the simulation of CF_3-powder patterns presented in chapter III, and was earlier observed for small and highly mobile organic molecules in oriented membranes.[16] However, the experimentally observed spectra of table 8.1 are heavily and—even more surprising—inhomogenously broadened. The asymmetry of the triplet was observed in all PGLa-CF_3 analogs, and always showed a narrow intense peak near the isotropic chemical shift, and the broadest peak at furthest distance from the isotropic value.

We attribute the triplet asymmetry to different transverse relaxation rates (T_2) in the three signal components, which are caused by the reduced mobility of the peptide. The transverse relaxation rate, which is inversely proportional to linewidth, is governed by two factors: The first is the spectral density of the thermal fluctuations of the angle θ between the CF_3-axis and the static magnetic field on the time-scale of the experiment. In PGLa-CF_3, it obviously is identical for all three spectral components, and falls into a range that allows for efficient relaxation of nuclear magnetization.

The second relevant factor influencing transverse relaxation is the effective frequency range that reflects the spectral changes caused by the fluctuations of θ. If a larger spectral range is covered, the influence of motional properties on nuclear magnetization will be stronger and more diverse, and consequently bulk magnetization will dephase faster, i.e. mobility will make spin-spin-relaxation stronger. In PGLa-CF_3, the spectral range covered by each component of the observed triplet has a remarkably different width. In the rotating CF_3-group, anisotropic chemical shift and homonuclear dipolar coupling are both proportional to $3\cos^2\theta-1$, and at a magnetic field of 11.7 T they have approximately the same magnitude (see chapter IV). In one of the three spectral components these two orientation-dependent effects have opposite signs and partially compensate one another. Therefore, in any orientation the resonance frequency of this component does not shift much from the isotropic chemical shift value. The central component of the triplet is observed at the pure anisotropic chemical shift, since here the dipolar contribution is zero. In the third component both orientation-dependent effects add up, hence the resonance frequency of this component shows by far the strongest dependence on the instantaneous CF_3-axis orientation. Since it covers the largest frequency

range, it is expected to relax most effectively and, therefore, to have the broadest T_2 linewidth. On the other hand, the spectral component closest to the isotropic chemical shift position is expected to relax slowest due to the small spectral changes connected to its thermal mobility. Consequently, it should show the narrowest line, which is exactly what is observed in the spectra of table 8.1.

The observed effect is termed 'differential relaxation'[17] or 'relaxation interference'[18] or 'cross-correlated relaxation'[19] in the literature. Goldman[18] states in 1984 that it "has been known for almost 30 years and repeatedly rediscovered". Upon closer examination, the spectra of highly mobile organic molecules in oriented membranes recorded by Grage *et al.*[16] also show a slight inhomogeneity in linebroadening, that easily escapes the eye but is definitely present. In the PGLa-CF_3 experiments presented here, we could not make constructive use of the effect as we were interested only in the orientation-dependence of the signal. For future analysis of the interaction of CF_3-groups with other nuclei, however, it may be worthwhile considering the development of TROSY experiments[20], which suppress the two broadened components to leave only the narrow component for eased observation.[19] Moreover, it may prove possible to directly determine the molecular order parameter S_{mol} from the observed strength of differential relaxation. In the present study, S_{mol} had to be extracted along with the structural parameters (τ and ρ) from very restricted sets of tediously generated data points. An independent determination would well justify the effort of calculating explicit relationships between molecular mobility and linewidth. Tjandra *et al.*[21] already demonstrated how S_{mol} can be inferred from differential relaxation in the case of an amide nitrogen.

The presence of CSA interactions in addition to the dipolar couplings in the CF_3-group has another important impact on spectral lineshape. As can be seen in the panel of table 8.1, the presence of the CSA interaction gives the central component of the triplet a distinct positive or negative sign (downfield or upfield with respect to σ_{iso}). This effect allows for a determination of the sign of dipolar coupling.

When the CF_3-label is aligned parallel with respect to the membrane normal (θ=0°), the observed triplet shows maximum dipolar splitting.[16] As θ approaches the magic angle, the splitting decreases to zero, and for θ>54.7° it increases again but with a negative sign.

Table 8.1: Dipolar splitting values observed in four different CF_3-Phg labelled PGLa-CF_3 and representative ^{19}F-NMR spectra showing concentration-dependent re-orientation for PGLa-Ile^{13}(CF_3-Phg) in DMPC.

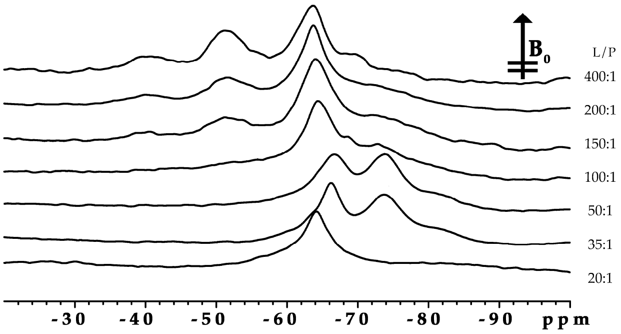

	peptide to lipid ratio	
position	1:200	1:50
Ile 9	0.0 kHz	-4.7 kHz
Ala 10	0.0 kHz	-3.1 kHz
Ile 13	+5.6 kHz	-3.3 kHz
Ala 14	-5.4 kHz	-5.3 kHz

Thus, any observed dipolar splitting $\left|D_{ij}\right| \leq \frac{1}{2} \cdot S_{mol} \cdot D_{ij}^{0}$ will give two solutions for the angle θ, one corresponding to positive and one to negative dipolar coupling. The sign of dipolar coupling cannot be measured from a splitting alone.[22] Fortunately, in the present case it can be deduced from the anisotropic chemical shift of the oriented sample. Due to the rotation of the three equivalent fluorine atoms, the ^{19}F CSA tensor is axially symmetric, and the anisotropic chemical shift has the same functional dependence of $cos^2\theta$ as the dipolar coupling, with an identical definition of θ. Therefore, the anisotropic chemical shift contains the same information as dipolar coupling and would by itself allow for a determination of θ. However, this procedure is more problematic in view of the need for chemical shift referencing and bulk magnetic susceptibility effects.[8;23] Consequently, we recommend to determine θ accurately from the dipolar splitting, and to use the chemical shift of the triplet signal only to resolve the degeneracy between tilt angles θ above and below the magic angle.

The principal axis values of the CSA tensor of a rotating CF_3-group are not yet (but see chapter IV) available from the literature but can be estimated from our samples. We found that the most deshielded value lies along the rotational axis. This was concluded from the ^{19}F-NMR spectra of the PGLa-10(D-CF_3-Phg) analog in oriented samples, which showed a dipolar splitting of about 11 kHz with a chemical shift of –38 ppm for the central peak of the CF_3-triplet, while the isotropic chemical shift was at –63 ppm. According to equation (1.9), any splitting above 8 kHz can only arise from orientations $0° \leq \theta \leq 35.3°$. Therefore, anisotropic chemical shifts downfield of the isotropic value correspond to $0° \leq \theta \leq 54.7°$, and upfield shifts correspond to $54.7° \leq \theta \leq 90°$. We thus define the signed dipolar splitting D_{ij}^{0} to be positive for downfield and negative for upfield chemical shifts. The resulting sign of D_{ij}^{0} is the true sign of the dipolar coupling, as the negative sign of the dipolar coupling constant and the negative sign of the rotational order parameter S_{rot} compensate each other.[24] The determination of sign in the dipolar coupling of CF_3-groups represents very valuable additional information, removing the degeneracy in angle determination.

Using the dipolar sign convention, it is now possible to read a signed value of dipolar coupling from the heavily broadened spectra. The splitting values thus determined at two different lipid to peptide ratios in the experiments of Sachse[9] are compiled in table 8.1. Within each concentration regime, splittings observed in different labeled positions show different values among each other. This finding indicates that there is no long-axial rotation of the peptide around its helix axis, since this mode of mobility would average all splittings onto a single value identical in all labeled positions due to the cylindrical symmetry of the α-helix. At low and high concentrations of PGLa in DMPC bilayers, completely different values of signed dipolar splitting are observed in all analogs. The effect is clearly visible in the spectra of PGLa-Ile^{13}(CF_3-Phg) in DMPC presented in the panel of table 8.1. This change in spectral properties is indicative of change in the orientation of the PGLa helix in the lipid bilayer. The remainder of this chapter will give a structural picture of both low- and high-concentration state of the peptide, along with an estimate of the uncertainties in the analysis.

^{19}F-NMR analysis of PGLa at low concentration

The ^{19}F-NMR dipolar splitting values compiled in table 8.1 were analyzed by fitting different α-helical model structures to the data as described in materials and methods. Figure 8.2 shows two selected χ^2 error functions obtained on two different α-helical models. Note that the figure gives 'projective' ρ-τ-plots, as opposed to the cross-sectional ρ-τ-plots presented in all previous chapters. There, a ρ-τ-plane corresponding to a cross-section through the three-dimensional ρ-τ-S_{mol} parameter space was taken at one constant value of S_{mol}. Now, the minimum of χ^2 in the complete range of feasible order parameters $0.4<S_{mol}<1.0$ was determined for every pair of angles (ρ,τ) and displayed as a contour plot. In this fashion the χ^2 function can be characterized in its complete three-dimensional ρ-τ-S_{mol} parameter space in a single two-dimensional map, making sure that no minimum is overlooked because the chosen cross-section does not contain it.

Initially, a standard α-helix (φ=-58°, ψ=-47°) was fit to the data, and the left panel of figure 8.2 shows the χ^2 function. A global minimum is found with χ^2=0.39, which is a very acceptable fit (*cf.* chapter II). The corresponding peptide tilt angle of τ=89° is in good agreement with a previous ^{15}N-NMR analysis of PGLa,[6] and the azimuthal rotation angle ρ=106° agrees well with the expected alignment of the amphiphilic helix (*cf.* figure 8.1). The order parameter of S_{mol}=0.6 indicates that the peptide is reasonably mobile in the liquid crystalline lipid bilayer at the low peptide:lipid ratio 1:200, as seen before for other comparable systems.[25;26] There is only one further local minimum observed (ρ=121°, τ=14°, S_{mol}=1.0), which has a much higher χ^2 deviation of 15.7 and can be safely ignored.

In addition, the data was also fitted with the energy-minimized model of PGLa described in materials and methods, where the four analogues were constructed with individual CF_3-Phg labels and subjected to 500 steps of energy-minimization to account for the structural distortion effected by the bulky label. The resulting χ^2 function is shown in the right panel of figure 8.2 for comparison to the fit of a regular α-helix. It shows noticeable distortions and only qualitative similarity remains between the two χ^2 error functions. To our surprise, the fit

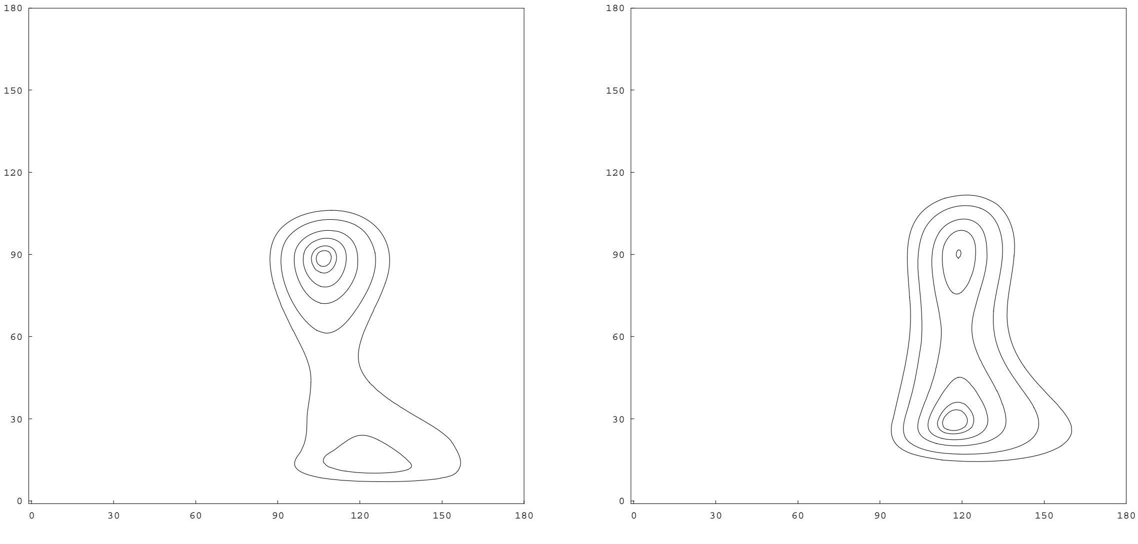

Figure 8.2: Projective (ρ,τ)-plots of χ^2-function resulting from best-fit of standard (left) and energy-minimized (right) α-helical model to ^{19}F-NMR splittings observed on PGLa-CF_3 analogues at 1:200 peptide:lipid ratio in DMPC. Contours are shown at χ^2 values of 1, 2, 5, 10, 20 and 30.

of the energy-minimized model gave a second very good fit for a tilted transmembrane orientation of the helix, while the solution previously found is present only with a rather high, yet still acceptable error of χ^2=1.94.

Apparently, use of two different model structures does not severely change the qualitative shape of the χ^2 profile, but may strongly raise or lower the minimum values found in the error function. Since this value decides about the acceptability of a minimum, a shift may completely change the interpretation. This is obvious in the χ^2 profiles of figure 8.2, where a different minimum would be picked in each case if the analysis relied on only one of the two plots and their corresponding conformational models.

In order to further quantify the effect of deviating α-helical geometry on the fits, we also calculated the orientational fits for a large number of regular α-helical structures with ω incremented between 95 and 102°, and β between 105 and 120°. Steps were small enough (1-5°) to see a smooth shift in the results of the fit. Best-fit results for the 'standard', the 'energy-minimized' and two representative 'regular' α-helices are compiled in table 8.2, along with respective values of the Euler angles α and β that parameterize the transformation between PPL and MOL coordinate systems, *cf.* equation (2.10).

All α-helical structures, both regular and energy-minimized ones, had a local minimum in the range of ρ=100-120°, and τ=88-99°. Consequently, the uncertainty in the molecular orientation can be estimated to be about 10-20° resulting from small variations in the helix conformation. This confirms that the most severe effect of variations in the model structures is their influence on the absolute values of χ^2 minima. Extreme caution needs to be taken not

Table 8.2: Best-fit orientations reached on various model structures for 1:200 concentration data of PGLa

Structure				Orientation[d]			
	ω [°]	α [°]	β [°]	χ^2	ρ [°]	τ [°]	S_{mol}
α-Helix, standard[a]	99.8	53.2	121.1	**0.39**	**106**	**89**	**0.63**
α-Helix, energy-minimized[b]	91.7-98.4	43.6-51.9	109.8 -111.6	0.10	117	29	0.85
				1.94	**119**	**90**	**0.57**
α-Helix, adapted[c]	100	47	110	0.51	113	29	0.99
				0.97	**112**	**98**	**0.60**
α-Helix, adapted[c]	96	47	110	**0.08**	**103**	**99**	**0.80**
				5.00	108	29	1.00
3_{10}-Helix[a]	119	53.5	111.2	13.90	148	43	1.00
π-Helix[a]	85.3	52.5	131.1	10.40	164	82	0.84
β-Sheet[a]	178.9	28.3	98.2	53.40	40	142	1.00

The peptide is calculated for structural models with the following side chain arrangements: [a]Secondary structure of poly-Ala chains as constructed in SYBYL with φ=-58°/ψ=-47° (α-helix); φ=-50°/ψ=-28° (3_{10}-helix); φ=-57°/ψ=-71° (π-helix); and φ=-139°/ψ=135° (β-sheet). [b]α-helix after 500 steps of energy-minimization. [c]Regular α-helices with slightly modified structure (see text). [d]The global minimum of χ^2 and all local minima with χ^2 < 10 are shown.

to overlook 'good' minima on account of artifactual minima with a better χ^2 value. The uncertainty due to experimental inaccuracy (about ±0.5kHz) was considerably smaller. Model structures other than α-helical did not yield any acceptable fits according to the results included in table 8.2.

In summary, the analysis of ^{19}F-data confirms the flat alignment of PGLa at the surface of DMPC bilayers at a peptide to lipid ratio of 1:200, with the helix axis perpendicular to the membrane normal. For the first time the rotation angle was determined to be ρ=106°, in good consistency with the amphiphilic profile of PGLa. This flat orientation will be referred to as the surface-bound 'S-state' (*cf*. chapter I). There is an additional (artifactual) solution present for the energy-minimized as well as for some of the regular α-helices. It was possible to rule out the additional solution on the basis of ^{19}F-NMR measurements on D-epimeric peptides, which are by-products in the incorporations of 4F- as well as CF_3-Phg via solid-phase peptide synthesis. These studies are presented in detail in our first publication on PGLa[1], but are not shown here since the author did not take substantial part in them. In the context of this thesis, a decision between the concurring minima will be found by use of ^{15}N-NMR measurements, see below.

^{19}F-NMR analysis of PGLa-CF_3 at high concentration

As is evident in table 8.1, all PGLa-CF_3 analogs show markedly different dipolar splittings in ^{19}F-NMR when the peptide:lipid ratio is increased to above ca. 1:150. To have data well representative of the switched high-concentration state, a peptide:lipid ratio of 1:50 was chosen to record spectra of the high-concentration state.

Least-squares analysis of the high-concentration data was performed analogously to the analysis presented for 1:200 peptide:lipid results in the preceding section. The χ^2 functions calculated for the standard and the energy-minimized α-helix models are presented in figure 8.3. The projective χ^2 plot for the standard α-helix shows a single distinct fit to the data at (ρ,τ)=(85°, 123°) giving an error of χ^2=0.16. This solution corresponds to the peptide being

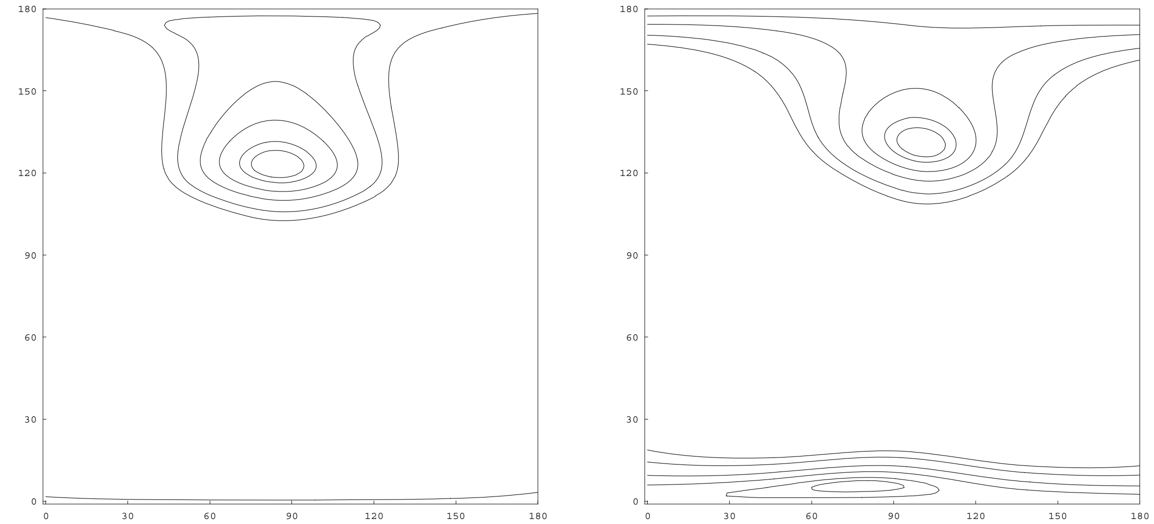

Figure 8.3: Projective (ρ,τ)-plots of χ^2-function resulting from best-fit of idealized (left) and energy-minimized (right) α-helical model to ^{19}F-NMR splittings observed on PGLa-CF_3 analogues at 1:50 peptide:lipid ratio in DMPC. Contours are shown at χ^2 values of 1, 2, 5, 10, 20 and 30.

tilted away from the flat surface orientation by about 30°. It is present also in the fit of the energy-minimized α-helical model to the data, listed in the right panel of figure 8.3. As was the case in the low-concentration regime, the energy-minimized model yields an additional perfectly acceptable fit at (ρ,τ)=(100°, 131°). The second minimum is not present for all model structures, while the first one was found in all investigated model structures (i.e. here the danger of missing a minimum due to a large χ^2 value appears to be less pronounced than in the low-concentration case). Table 8.3 collects all minima with $\chi^2 < 2$ that were found for the standard and energy-minimized as well as for a selection of regular α-helices with their respective best-fit parameter values.

In summary, ^{19}F-NMR analysis of PGLa at high-concentration shows the peptide to be tilted to a different orientation, where the helix is no longer flat on the lipid bilayer (τ=90°) but encloses an angle of 57° with the bilayer normal. Measurements on D-epimers were again useful to confirm the obliquely tilted orientation of PGLa at high concentration in the membrane, and clearly excluded the possibility of a transmembrane orientation of the PGLa helix.[2] Once again, these results shall not be presented in the current context, where a reliable confirmation of the oblique orientation is found by ^{2}H- and ^{15}N-NMR.

Table 8.3: Best-fit orientations reached on various model structures for PGLa at a 1:50 peptide-to-lipid ratio

Structure				Orientation[c]			
	ω [°]	α [°]	β [°]	χ^2	ρ [°]	τ [°]	S_{mol}
α-Helix, standard[a]	99.8	53.2	121.1	**0.16**	**84.6**	**122.5**	**0.63**
α-Helix, energy-minimized[b]	91.7-98.4	43.6-51.9	109.8-111.6	**0.18**	**100.3**	**130.6**	**0.64**
				1.22	69.7	4.0	0.9
regular α-helix	100	47	110	**0.17**	**90.8**	**133.4**	**0.63**
				1.54	100.5	5.2	0.9
regular α-helix	96	47	110	**0.19**	**91.6**	**129.8**	**0.67**
regular α-helix	102	47	110	**0.11**	**90.6**	**135.0**	**0.64**
				1.16	101.6	5.4	0.9
regular α-helix	100	47	105	**0.19**	**91.8**	**139.5**	**0.63**
				0.15	96.4	12.0	0.9
regular α-helix	100	47	115	**0.16**	**90.9**	**128.9**	**0.63**

[a]secondary structure of poly-Ala chains as constructed in SYBYL with φ=-58°/ψ=-47° [b]α-helix after 500 steps of energy-minimization. [c]All local minima with $\chi^2 < 2$ are shown.

^{2}H-NMR of PGLa-Ala-d_3

To confirm the results obtained by ^{19}F-labeling, and to comparie both labeling schemes, a second set of peptides with Ala-d_3 labels in the same individual positions 9, 10, 13, 14 was synthesized by P. Tremouilhac.[10] Quadrupolar splittings found in ^{2}H-NMR of multilamellar DMPC vesicles are compiled in table 8.4. Shown along with the observed deuterium splittings is the ratio they make with the corresponding fluorine dipolar splittings that were reported in table 8.1. This ratio is expected from the static coupling constants $D_{ij}^0 / \Delta \nu_0 = 15.8 \text{kHz} / 42.0 \,\text{kHz} = 0.38$. Three out of four experimental ratios in the low-concentration data are found to be almost identical to the expected value, the fourth one could not reliably determined since both fluorine and deuterium splittings are very small. In the high-concentration regime, the experimental ratios do not agree well, as almost each one shows a deviation from the expected value, with no one being especially bad. The fact that both labeling schemes show deviations to a different extent in the two concentration conditions indicates that distortions introduced by any labeling scheme are not a static phenomenon but may reach different degrees in different circumstances.

Table 8.4: Observed quadrupolar splittings in PGLa-Ala-d_3 analogues

	1:200 lipid-to-peptide ratio			1:50 lipid-to-peptide ratio		
labeled position	splitting	sign [a]	D:F-ratio	splitting	sign	D:F-ratio
Ile 9	2.6 kHz	?	0.00	10.6 kHz	-	0.48
Ala 10	7.5 kHz	?	0. 40 [b]	11.1 kHz	-	0.28
Ile 13	13.2 kHz	+	0.42	9.0 kHz	-	0.38
Ala 14	13.3 kHz	-	0.41	9.8 kHz	-	0.53

[a]Positions where the triplet is not resolved and therefore sign determinations is not reliable are marked by '?'.
[b]Fluorine splitting was reported as 0.0 kHz in table 8.1 and in our first publication on PGLa, Glaser *et al.*[1] This value was chosen because the triplet is not resolved. Still, it is clearly on the 'positive' side of the isotropic position, and may roughly be estimated as +3.0 kHz

The data reported in table 8.4 were subjected to a best-fit analysis using only the standard α-helical model of the ^{19}F-analysis above. Resulting χ^2 plots for both low and high concentration regimes are shown in the top row of figure 8.4. These plots show a markedly increased number of minima when compared to the corresponding plots in the ^{19}F analysis. This degeneracy in determining the angle θ is due to the fact that no *signed* values can be determined for ^{2}H quadrupolar splittings. A detailed explanation was given above for the ^{19}F case, where degeneracy could be resolved by considering the anisotropic chemical shift. This is not possible in case of ^{2}H data, where no noticeable CSA is present. Yet in the present case, a somewhat dubious source of the sign information may be considered: Transfer of the signs determined in ^{19}F-NMR onto the ^{2}H data. This was done for test purposes using transferred signs as given in table 8.4 for the ^{2}H splittings of residues 13 and 14. The resulting χ^2 plots are given in the lower panels of figure 8.4, and now show only half the number of minima found in the 'un-signed' χ^2 functions. These minima are compiled in table 8.5 and labeled with arrows and the respective value of $S_{mo}l$ in the lower panels of figure 8.4.

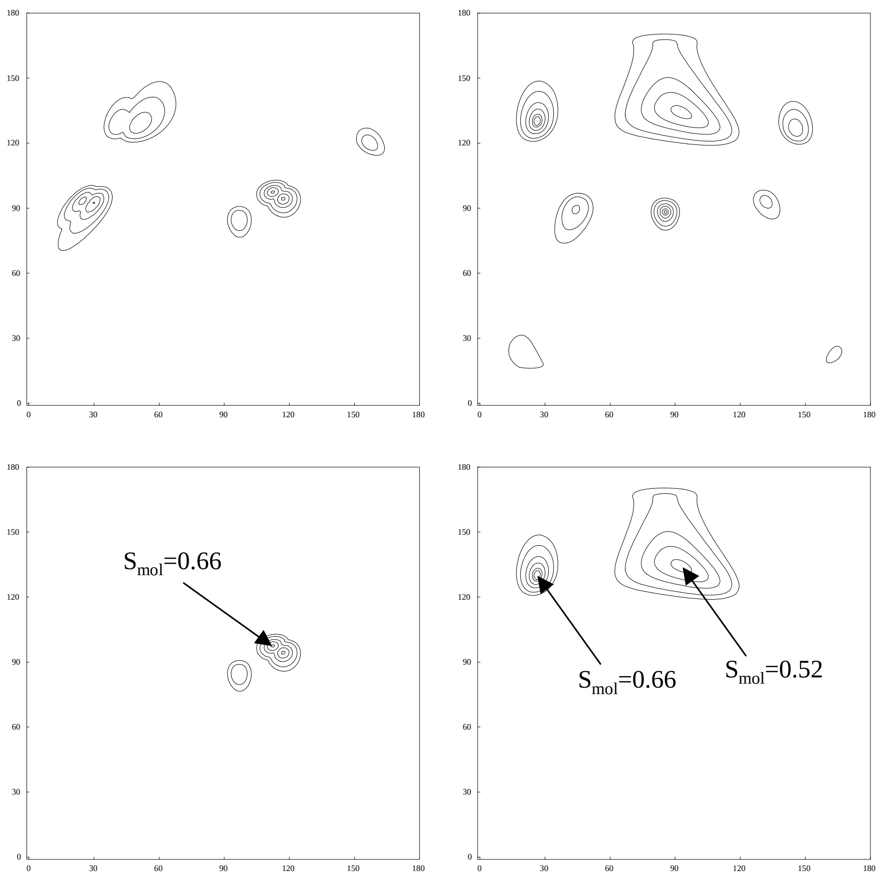

Figure 8.4: Projective (ρ,τ)-plots of χ^2 for ^{2}H-NMR data acquired on PGLa-Ala-d_3 labeled in positions 9, 10, 13, and 14 (that were CF_3-Phg labeled earlier), at 1:200 (left) and 1:50 (right) peptide to lipid in DMPC. Plots were either calculated without sign of dipolar coupling (top), or adopting the sign observed in CF_3-Phg labels in positions 13 and 14 (bottom). Contours are shown at χ^2 of 1, 2, 5, 10, 20, 30.

Table 8.5: Best-fit orientational results on ^{2}H-NMR data of PGLa at 1:200 as well as 1:50 peptide-to-lipid ratio using a standard α-helical model.

Structure				Orientation[b]			
	ω [°]	α [°]	β [°]	χ^2	ρ [°]	τ [°]	S_{mol}
1:200 P:L data							
α-Helix, standard[a]	99.8	53.2	121.1	**1.19**	**117**	**94**	**0.66**
				2.16	**112**	**97**	**0.72**
1:50 P:L data							
α-Helix, standard[a]	99.8	53.2	121.1	**1.50**	**93**	**134**	**0.52**
				0.22	**26**	**130**	**0.66**
				0.63	85	88	0.67

[a]secondary structure of poly-Ala chains as constructed in SYBYL with φ=-58°/ψ=-47°.
[b]All local minima with χ^2 < 5 are shown.

^{15}N-NMR analysis of PGLa-^{15}N-Gly^{11} supports findings

To complement the ^{19}F- and ^{2}H-NMR data presented above, to resolve ambiguous multiple solutions, and to decide whether the observed spectral changes are genuinely due to a re-alignment of PGLa, a peptide labeled with ^{15}N at Gly^{11} was studied. ^{15}N-NMR experiments have a much lower sensitivity compared to ^{19}F,[27] but ensure that the label does not disturb the local peptide conformation nor its interaction with other molecules. Oriented samples were prepared with the same concentrations discussed above, and the spectra recorded on these samples are presented in figure 8.5. At low peptide concentration (P:L = 1:200) the ^{15}N signal of the oriented sample appears at 40 ppm, while at high concentration (1:50) it moves to 68 ppm. At the same time the width of the observed line increases from about 10 ppm to above 40 ppm. These findings again confirm the presence of a qualitative change in the peptide's orientation.

To find out which alignments of the peptide helix are compatible with these data, the principal axis values of the ^{15}N CSA tensor need to be known. As glycine differs slightly from other amino acids,[28] the values were determined from the lyophilized peptide powder, which is shown superimposed over the oriented spectra. To account for the mobility of the peptide in lipid membranes with an order parameter of $S_{mol}\approx0.6$, the static powder spectrum is scaled by a factor 0.7 in this display. A slightly higher factor was chosen for the ^{15}N-label in the backbone to compensate for any extra wobble of the CF_3-Phg side chain and any motion in the lyophilized peptide.

Orientational analysis of the ^{15}N data yielded the χ^2 plots shown in figure 8.6. The information from only a single label does not allow to determine a distinct orientation, consequently the χ^2 plots show only *ranges* of allowed orientations. For the tilt angle τ the value of 90° for a P:L of 1:200 confirms the S-state, as expected (left panel of figure 8.6). At high peptide concentration of 1:50 a helix tilt of about $\tau\approx65°$ or 115° (=180°-65°) was determined, which is also in full agreement with the ^{19}F-NMR analysis (right panel). In fact, for any reasonable choice of $0.5<S_{mol}<1.0$ only an oblique helix tilt can explain the ^{15}N data at P:L=1:50. Note that although the signal lies close to (but not at) the isotropic position of ^{15}N, free tumbling or micellarization of the sample by action of the peptide can be excluded in view of the ^{19}F- and ^{31}P-NMR data on essentially equivalent samples. The evaluation of an oblique helix tilt angle thus unequivocally confirms the picture derived above by ^{19}F-NMR.

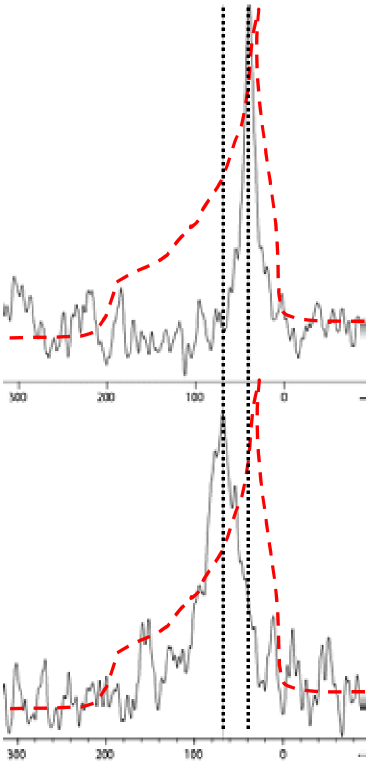

Figure 8.5: ^{15}N-NMR spectra observed on ^{15}N-Gly$_{11}$-PGLa in DMPC at 1:200 (top) and 1:50 (bottom) peptide:lipid ratios with schematic representation of ^{15}N-CSA tensor (dashed lines).

In addition to the orientation ranges consistent with the ^{15}N resonance frequencies in both concentration regimes, figure 8.6 shows the minima found in the χ^2-maps of figure 8.2, 8.3 and 8.4 as colored circles. Thus, figure 8.6 serves as a summary of all orientational results found in the present chapter, which are to be discussed in the remainder of the chapter.

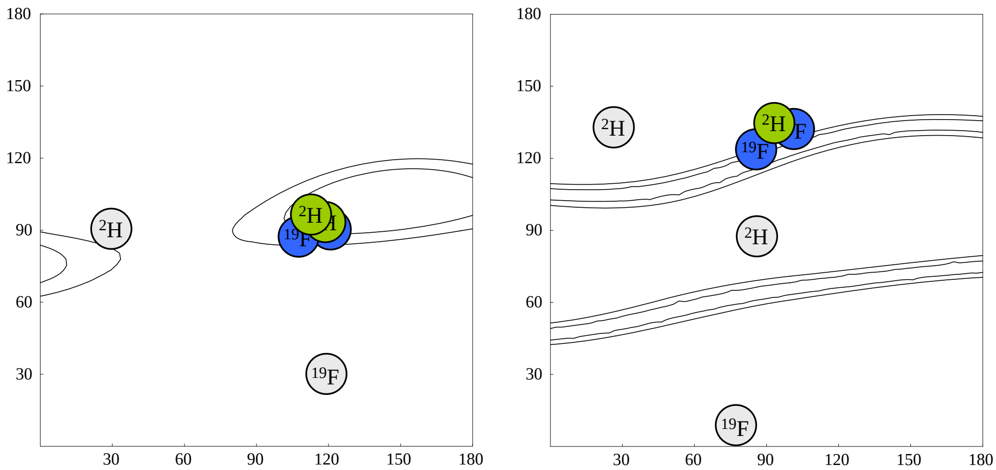

Figure 8.6: (ρ,τ)-Regions consistent with observed ^{15}N resonance at P:L 1:200 (left) and 1:50 (right), with contours shown at 4 and 8 ppm rmsd. Note that in the 1:50 case the allowed solutions are in the narrow regions within each of the two 'bands', while for 1:200 there is only one (large) allowed region encircled by the central oval shape. The order parameter is estimated to be S=0.65 from the $^{19}F/^{2}H$ results reported above, and these results are included as colored circles when consistent with the ^{15}N data, or as gray circles where non-consistent.

Summary and discussion

^{19}F-NMR ideally complements the more common labeling schemes

Each of the three nuclei used as a silective isotope label in PGLa allowed to determine valuable information on the peptide's orientation within lipid bilayers. The results from all three labeling schemes are summarized schematically in figure 8.6. There, it is evident that full quantitative agreement is reached between the three labeling schemes in both concentration conditions studied. At a peptide to lipid ratio of 1:200, two of the three minima found from ^{2}H data are almost identical and are also in very good agreement with one of the two solutions found in ^{19}F-NMR, namely the one at $(\rho,\tau)=(106°, 89°)$, $S_{mol}=0.63$. This good agreement is not surprising, but is a direct consequence of the deuterium:fluorine splitting ratios of table 8.4 being very close to the values expected in non-perturbed structures, making all ^{19}F-reasoning directly applicable to the ^{2}H-NMR data. The coinciding fluorine and deuterium minima are further consistent with the ^{15}N-allowed regions and are thus shown to be the single best-fit orientation for the low-concentration of PGLa.

At 1:50 peptide-to-lipid ratio, the consistency between the fluorine and deuterium splittings is not as good as at low peptide concentration. Still, a coinciding best-fit orientation is found at $(\rho,\tau)\approx(95°, 135°)$, $S_{mol}\approx0.5$. For this 'consensus orientation', the best-fit orientations found from fluorine and deuterium data are sufficiently close to be considered in good agreement. This is visible in the right panel of figure 8.6, where the deviation between the two fluorine solutions derived from two different models (blue circles) is far stronger than the deviation between each fluorine solution and the deuterium solution (green circle). This fact indicates that a deviation (or in the present case rather a deviation between analogues of different labeling schemes) of the dipolar or quadrupolar splitting has a far less pronounced effect on the resultant best-fit orientation than the model structure employed, as will be further discussed below. The ^{15}N-data additionally confirms the consensus orientation and rules out all other orientations that were found to be consistent with either the ^{19}F- or ^{2}H-data. All solutions thus ruled out are shown as gray-colored circles in figure 8.6. Note that earlier in this chapter a number of deuterium solutions were ruled out by their inconsistency with the sign of fluorine dipolar splittings. These can now be ruled out by their inconsistency with ^{15}N-allowed regions, which is a far more satisfactory line of reasoning.

On the whole, the present study demonstrates how ^{19}F-NMR ideally complements more common labeling schemes. In the present case the information obtained from both CF_3- and CD_3-groups reflects the orientation of the C_α-C_β-bond (which is parallel to the axis of symmetry of the respective group). Therefore, ^{19}F-labeling strongly enhances the power of the common ^{2}H-labeling methodology, since it probes the same geometrical direction at highly increased sensitivity. Note that the investigation of the concentration-dependent behavior of PGLa was only possible since ^{19}F-labeling provided the sensitivity necessary to scan a large range of concentration conditions to detect the re-orientation effect.[1;8;9] Also, the sign of dipolar splitting, which is available only in ^{19}F-NMR, noticeably increases the amount of information gathered from a limited number of data points. Once the representative conditions for any system at hand are found by ^{19}F-NMR, further experiments may return to non-disturbing deuterium labeling as a means of precision measurements.

Note that also deuterium labeling may introduce distortions into a molecule. In the present case, Ile residues were replaced twice by the much smaller Ala-d_3 in view of the limited

number of eligible labeling sites. Consequently, deuterium labeling may have disturbed the PGLa molecule. This distortion is comparable in magnitude and opposite in quality as replacing a small Ala by the more bulky CF_3-Phg side chain. Therefore, it cannot be decided whether fluorine or deuterium data are more reliable, since both substitutions were done in a potentially disturbing manner.

Labeling backbone amide sites with ^{15}N is another commonly employed isotope labeling scheme in biomolecular NMR. Due to the properties of the ^{15}N CSA tensor, nitrogen labeling probes essentially the direction between nitrogen and its covalently bonded hydrogen (cf. figure 7.3 and explanations thereto). The ^{15}N-^{1}H orientation is roughly orthogonal to the C_α-C_β-direction probed by CD_3- and CF_3-groups. As a result, nitrogen labeling supplies data of almost no redundancy when applied in addition to deuterium or fluorine labeling. This is most easily understood in the case of an α-helix, where all C_α-C_β-bonds are pointing radially away from the helix axis, while the ^{15}N-^{1}H-bond lies parallel to the helix axis. Geometrical orthogonality between different molecular axes is often employed in other types of experiments, e.g. in a recent relaxation study[30] where the orthogonality of ^{15}N-^{1}H and $^{13}C_\alpha$-^{13}CO bonds in the peptide plane was utilized to measure different relaxation rates connected to the respective NMR interactions. The determination of mobility enabled the authors to question the usually assumed 'crank-shaft' motion of the peptide plane.

The simple fact of orthogonality between ^{15}N-^{1}H- and C_α-C_β-directions makes Aisenbrey and Bechinger[29] claim to measure the membrane-bound orientation of an α-helical peptide from only two labels, namely a pair of orthogonal ^{15}N- and Ala-d_3-labels, to give τ and ρ. Considering the ambiguities found in the analysis of PGLa data and the need to account for mobility in terms of S_{mol}, this claim may seem somewhat too ambitious. Nonetheless, the present study found data from only a single ^{15}N-label to be extremely helpful in ruling out numerous false minima consistent with ^{19}F- and ^{2}H-data.

Assessment of error margins in best-fit analysis

Before the discussion moves on to the description and interpretation of the best-fit results, our use of model theory should be critically examined and an estimation of the error margins needs to be given.

First, the implicit assumptions made in fitting any idealized model shall be scrutinized. Obviously, the decision for any distinct conformational model (here: α-helix) is the strongest assumption made, and needs to have strong experimental support (here: Bechinger's solution-state study[6] and CD data gathered in our lab[1]). The second assumption made is that of applicability of this *wildtype* structure element to the situation of the multitude of labeled peptides, i.e. we need to be sure that the labels introduce only minor distortions to the wildtype structure. Again, this assumption cannot be made *per se*, but needs experimental support, which was found in CD spectroscopy and antimicrobial assays in the present case.[1] The third assumption involved regards molecular mobility: It needs to be assumed that fast molecular motions of the peptide (i.e. its deviations from the a single static orientation) are not only isotropic, but also that they are identical at all labeled sites. This is most likely not the case, neither for the motion of the whole molecule in the membrane, nor for the internal motion of the respective side chain within the molecule.

The limitations of these model assumptions are the major source of uncertainty, compared to which the experimental errors in measuring dipolar couplings are found to be less critical for an accurate determination of the molecular orientation. The influence of deviations in the any idealized structural element to be fitted to the PGLa data was assessed by fitting numerous regular α-helices, and the resulting error was found to be around ±15°. The distortions introduced into the molecule by the CF_3-Phg labeling scheme were assessed by creating an energy-minimized model structure. This structure did not yield best-fit parameters outside the range found in the multitude of regular α-helices. The last model assumption—that molecular mobility is amply reflected in only a single molecular order parameter S_{mol} –cannot be tested by changing the model, since changing the model here means introducing additional order parameters (as was done in chapter VI for 4F-Phg side chain torsion). Eventually, this approach would lead to one (or two) individual order parameters for each label, which obviously will not allow to extract meaningful information from the data. Therefore, differing mobility at each labeled position may be a major source of error. In the present case, the degree of differential relaxation is found to be equally strong in all observed triplets, indicating that in the case of PGLa motional properties are *not* grossly different.

In the best-fit analyses at hand, the dipolar input was systematically varied to assess the resulting error margins. An experimental inaccuracy in the dipolar splitting of ± 0.5 kHz was found to translate into an intrinsic error in τ and ρ of less than ± 10°. Nevertheless, this margin includes the ambiguity of choosing one or another α-helical conformation for the data analysis, as demonstrated by the presented systematic analysis of different conformational models. Since the L-CF_3-Phg labels used to replace Ile or Ala may induce slight distortions in the peptide backbone, the error margins should be considered more generously, say ± 20°. Especially in the tilted state, which appears to involve specific peptide-peptide interactions, the stiff CF_3-Phg labels might be more problematic than in the monomeric S-state. The information from a single non-perturbing ^{15}N-label is not very accurate either (about ± 20° in τ, and ρ is generally not accessible by ^{15}N CSA analysis of single labels). Nonetheless, the distinct changes in the ^{19}F dipolar couplings and in the ^{15}N chemical shift unequivocally show that PGLa undergoes a concentration-dependent re-alignment.

With a small number of orientational constraints we can only test whether a certain helix conformation and orientation is compatible with the NMR data. In fact, the four constraints from the L-CF_3-Phg labels alone would also be compatible with a distorted helix that is slightly tilted away from a transmembrane orientation. However, the independent additional constraints (one ^{15}N-Gly^{11} label as described above, and four D-CF_3-Phg epimers[1;2]) support the oblique tilt of the central helical segment of PGLa and make any alternative interpretation of the data very unlikely.

Membrane-bound PGLa shows a distinct switch in orientation

The orientations determined for PGLa at 1:200 and 1:50 peptide to lipid ratio are clearly different, as was expected from the markedly different spectra found for all three isotope labels in each concentration condition. At low peptide concentration the results from the three labeling schemes conclusively show the peptide to be perpendicular to the membrane normal (τ=90°) and the azimuthal rotation ρ to be consistent with the amphiphilic profile of the molecule.

When the peptide to lipid ratio is increased to 1:50, the helix axis tilts to an oblique angle of $\tau \approx 55°$. We shall refer to this orientational state as the tilted 'T-state', extending the nomenclature of Huang's two-state model.[31] Figure 8.7 gives a representation of both S- and T-state within a lipid bilayer environment. In the T-state, the C-terminus of PGLa is more deeply inserted into the lipid bilayer than the N-terminus. The C-terminal insertion of the peptide into the more hydrophobic regions of the lipid bilayer is aided by PGLa's C-terminal amidation.

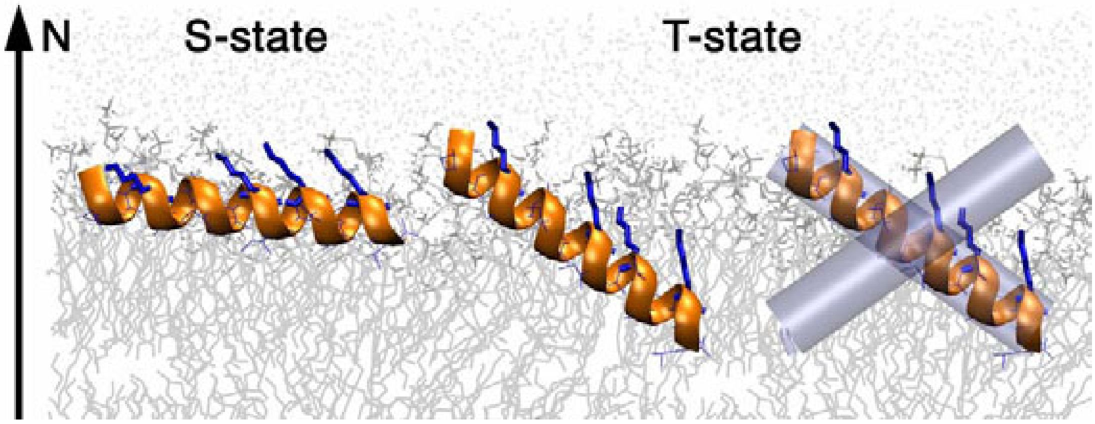

Figure 8.7: Illustration of the observed re-alignment of PGLa in a DMPC membrane. At low peptide concentration the amphiphilic helix lies flat on the surface in the S-state. With increasing concentration, it assumes a tilted T-state, whose stability may be explained by the formation of antiparallel peptide dimers.

At first glance, the peptide to lipid ratio of 1:50 may seem exceedingly high, suggesting that the observed re-orientation represents nothing but an artifact, caused by the unnatural situation of over-concentrated peptides in artificially oriented lipid bilayer stacks. However, strong support is found in the literature that actual biological concentrations of antimicrobial peptides on microbial membranes are of comparable magnitude. A study of Blazyk *et al.*[32] gives 1:100 as a conservative estimate for the peptide to lipid ratio corresponding to their lowest observed minimal inhibitory concentration (MIC) of their model peptide. In another[32] study by Steiner *et al.*[33], a biologically active peptide to lipid ratio of 1:10 or even more could be inferred (assuming an average area of 70Å^2 for a single lipid headgroup[34]). This study explicitly states that dense carpets of peptide may even cover the whole surface of the investigated micro-organisms. Thus, the switch in PGLa's orientation at high concentration—although only minor in magnitude—is very likely to be physiologically relevant. Its possible implications for biological function will be discussed in the next section.

Possible implications for the antimicrobial function of PGLa

Notably, the concentration-dependent series of NMR experiments[9] never showed a gradual shift of the signals (*cf.* table 8.1). This is taken as evidence for the presence of two distinct populations of peptides in different orientational states, which are in fast exchange at intermediate peptide concentration. There is, however, no reason why a single PGLa molecule should be stable on its own in a tilted alignment at high concentration. The formation of large peptide aggregates can be excluded in view of the long-axial rotation of PGLa about the membrane normal, which is maintained at high concentration. Therefore, the most probable explanation for the occurrence of the T-state is the formation of peptide dimers, although there is no direct experimental evidence from our NMR data. Indeed, PGLa is known to form dimers in a lipid monolayer at the air-water interface.[35] Dimerization in the membrane has also been described for related antimicrobial peptides: REDOR distance measurements on the model peptide K3 showed parallel dimers[36;37], transferred NOE of a magainin analogue indicated antiparallel dimers[38], and PGLa was found to associate with magainin as antiparallel heterodimers[39]. Up to now, the tilt angle of such peptide dimers in the membrane has not been accessible, as these previous experiments provided distance constraints but no orientational information. In our case of PGLa, the homodimers in DMPC must be rotationally symmetric with respect to the membrane normal, since we observe only a single set of NMR signals. The fact that both states are observed with the same molecular order parameter $S_{mol} \approx 0.6$ is consistent with dimer formation, since association of only two monomers does not sufficiently increase the moment of inertia to noticeably reduce wobbling. Self-assembly of PGLa into antiparallel dimers may thus account for the stability of the tilted T-state, as schematically illustrated in figure 8.7.

The idea of dimer formation is further supported by structural properties of the PGLa peptide. Dimer formation in membrane proteins has been extensively studied on the transmembrane domain of glycophorin A, a membrane protein that forms dimers in human red blood cells.[40] Here, as well as in a number of other oligomerizing transmembrane helices, a shallow 'patch' of two adjacent glycine residues was found to be vital for dimer formation.[41;42] And indeed, in the PGLa sequence two glycine residues are present in close spatial proximity in positions 7 and 11, as can be seen from the helical wheel representation of figure 8.1. Thus, these two residues may form an analogous patch that exposes the α-helix backbone and that may act as the interface between two monomers. In addition, β-branched amino-acids that form a 'ridge' beside the shallow Gly-patch[43] are speculated to aid dimer formation in glycophorin A due to their intrinsically low side chain entropy, which minimizes entropy loss upon dimer formation.[44] And again, the PGLa sequence has the β-branched side chains Ile^9, Ile^{13} and Val^{16} forming a ridge along the α-helix, cf. figure 8.1. This ridge is not directly adjacent to the Gly-patch, as in the case in glycophorin A, but is separated from the glycines by the residues Ala^6, Ala^{10}, and Ala^{14}. Still, the structural similarity seems striking enough to be borne in mind for future consideration.

The tilted T-state of PGLa exhibits quite unexpected properties that do not fit well into the currently discussed structural models of antimicrobial action.[31;45-47] It is clearly not compatible with a barrel-stave pore, and the rotational diffusion of the peptide around the membrane normal does not support the carpet model either. The oblique tilt with an order parameter nearly identical to that of the S-state is also not compatible with a toroidal wormhole. Although the high peptide concentration of the T-state may appear to correlate with the threshold for pore formation[48], there is no evidence from our experiments that this state should be directly responsible for the destruction of the membrane barrier. Dimerization of PGLa at the membrane surface is a plausible explanation of our data in the light of

observations from similar amphiphilic helical membrane peptides from the same family. The T-state may thus be an intermediate in the formation of pores on the way from the monomeric S-state towards a cooperative I-state.

Reference List

(1) Glaser, R. W.; Sachse, C.; Dürr, U. H. N.; Wadhwani, P.; Ulrich, A. S. *J.Magn.Reson.* **2004**, *168*, 153-163.

(2) Glaser, R. W.; Sachse, C.; Dürr, U. H. N.; Wadhwani, P.; Strandberg, E.; Ulrich, A. S. *Biophys.J.* **2005**, *submitted*.

(3) Strandberg, E.; Wadhwani, P.; Tremouilhac, P. P. Y.; Dürr, U. H. N.; Ulrich, A. S. *in preparation* **2004**.

(4) Hoffmann, W.; Richter, K.; Kreil, G. *EMBO J.* **1983**, *2*, 711-714.

(5) Latal, A.; Degovics, G.; Epand, R. F.; Epand, R. M.; Lohner, K. *Eur.J.Biochem.* **1997**, *248*, 938-946.

(6) Bechinger, B.; Zasloff, M.; Opella, S. J. *Biophys.J.* **1998**, *74*, 981-987.

(7) Wade, D.; Boman, A.; Wåhlin, B.; Drain, C. M.; Andreu, D.; Boman, H. G.; Merrifield, R. B. *Proc.Natl.Acad.Sci.U.S.A.* **1990**, *87*, 4761-4765.

(8) Glaser, R. W.; Ulrich, A. S. *J.Magn.Reson.* **2003**, *164*, 104-114.

(9) Sachse, C. ^{19}F-Festkörper-NMR-Untersuchungen zur Orientierung und Dynamik des antimikrobiellen Peptids PGLa in Lipidmembranen. 2003. Friedrich-Schiller-Universität Jena.
Ref Type: Thesis/Dissertation

(10) Tremouilhac, P. P. Y. Chemical synthesis of deuterium labeled peptides and investigation of their orientation in lipid membrane by ^{2}H-solid state NMR. 2004. Ecole National Supérieure de Chimie de Lille.
Ref Type: Thesis/Dissertation

(11) Strandberg, E.; Özdirekcan, S.; Rijkers, D. T. S.; van der Wel, P. C. A.; Koeppe II, R. E.; Liskamp, R. M. J.; Killian, J. A. *Biophys.J.* **2004**, *86*, 3709-3721.

(12) van der Wel, P. C. A.; Strandberg, E.; Killian, J. A.; Koeppe II, R. E. *Biophys.J.* **2002**, *83*, 1479-1488.

(13) Koradi, R.; Billeter, M.; Wüthrich, K. *J.Mol.Graphics* **1996**, *14*, 51-55.

(14) *Landolt-Börnstein numerical data and functional relationships in science and technology*; Springer: Berlin, 1997.

(15) Davis, J. H. *Biochim.Biophys.Acta* **1983**, *737*, 117-171.

(16) Grage, S. L.; Ulrich, A. S. *J.Magn.Reson.* **2000**, *146*, 81-88.

(17) Farrar, T. C.; Stringfellow, T. C. Relaxation of transverse magnetization for coupled spins; In *Encyclopedia of NMR*; Grant, D. M., Harris, R. K., eds. Wiley: New York, 1996; pp 4101-4107.

(18) Goldman, M. *J.Magn.Reson.* **1984**, *60*, 437-452.

(19) Riek, R.; Wider, G.; Pervushin, K.; Wüthrich, K. *Proc.Natl.Acad.Sci.U.S.A.* **1999**, *96*, 4918-4923.

(20) Pervushin, K.; Riek, R.; Wider, G.; Wüthrich, K. *Proc.Natl.Acad.Sci.U.S.A.* **1997**, *94*, 12366-12371.

(21) Tjandra, N.; Szabo, A.; Bax, A. *J.Am.Chem.Soc.* **1996**, *118*, 6986-6991.

(22) Ulrich, A. S.; Grage, S. L. Solid state ^{2}H-NMR; In *Solid state NMR of polymers*; Ando, I., Asakura, T., eds. Elsevier: Amsterdam, 1998; pp 190-211.

(23) Ulrich, R.; Glaser, R. W.; Ulrich, A. S. *J.Magn.Reson.* **2003**, *164*, 115-127.

(24) Levitt, M. H. *J.Magn.Reson.* **1997**, *126*, 164-182.

(25) Afonin, S.; Dürr, U. H. N.; Glaser, R. W.; Ulrich, A. S. *Magn.Reson.Chem.* **2004**, *42*, 195-203.

(26) Salgado, J.; Grage, S. L.; Kondejewski, L. H.; Hodges, R. S.; McElhaney, R. N.; Ulrich, A. S. *J.Biomol.NMR* **2001**, *21*, 191-208.

(27) Afonin, S.; Glaser, R. W.; Berditchevskaia, M.; Wadhwani, P.; Gührs, K.-H.; Möllmann, U.; Perner, A.; Ulrich, A. S. *Chembiochem* **2003**, *4*, 1151-1163.

(28) Sternberg, U.; Witter, R.; Ulrich, A. S. *Annu.Rep.NMR Spectr.* **2004**, *52*, 53-104.

(29) Aisenbrey, C.; Bechinger, B. *Biochemistry* **2004**, *43*, 10502-10512.

(30) Wang, T.; Cai, S.; Zuiderweg, E. R. P. *J.Am.Chem.Soc.* **2003**, *125*, 8639-8643.

(31) Huang, H. W. *Biochemistry* **2000**, *39*, 8347-8352.

(32) Blazyk, J.; Wiegand, R.; Klein, J.; Hammer, J.; Epand, R. M.; Epand, R. F.; Maloy, W. L.; Kari, U. P. *J.Biol.Chem.* **2001**, *276*, 27899-27906.

(33) Steiner, H.; Andreu, D.; Merrifield, R. B. *Biochim.Biophys.Acta* **1988**, *939*, 260-266.

(34) Nagle, J. F.; Tristram-Nagle, S. *Biochim.Biophys.Acta* **2000**, *1469*, 159-195.

(35) Konovalev, O.; Myagkov, I.; Struth, B.; Lohner, K. *Eur.Biophys.J.* **2002**, *31*, 428-437.

(36) Toke, O.; O'Connor, R. D.; Weldeghiorhis, T. K.; Maloy, W. L.; Glaser, R. W.; Ulrich, A. S.; Schaefer, J. *Biophys.J.* **2004**, *87*, 675-687.

(37) Toke, O.; Maloy, W. L.; Kim, S. J.; Blazyk, J.; Schaefer, J. *Biophys.J.* **2004**, *87*, 662-674.

(38) Wakamatsu, K.; Takeda, A.; Tachi, T.; Matsuzaki, K. *Biopolymers* **2002**, *64*, 314-327.

(39) Hara, T.; Mitani, Y.; Tanaka, K.; Uematsu, N.; Takakura, A.; Tachi, T.; Kodama, H.; Kondo, M.; Mori, H.; Otaka, A.; Nobutaka, F.; Matsuzaki, K. *Biochemistry* **2001**, *40*, 12395-12399.

(40) MacKenzie, K. R.; Prestegard, J. H.; Engelman, D. M. *Science* **1997**, *276*, 131-133.

(41) Javadpour, M. M.; Eilers, M.; Groesbeek, M.; Smith, S. O. *Biophys.J.* **1999**, *77*, 1609-1618.

(42) Eilers, M.; Shekar, S. C.; Shieh, T.; Smith, S. O.; Fleming, P. J. *Proc.Natl.Acad.Sci.U.S.A.* **2000**, *97*, 5796-5801.

(43) Smith, S. O.; Song, D.; Shekar, S.; Groesbeek, M.; Ziliox, M.; Aimoto, S. *Biochemistry* **2001**, *40*, 6553-6558.

(44) Liu, W.; Crocker, E.; Siminovitch, D. J.; Smith, S. O. *Biophys.J.* **2003**, *84*, 1263-1271.

(45) Shai, Y. *Biochim.Biophys.Acta* **1999**, *1462*, 55-70.

(46) Strandberg, E.; Ulrich, A. S. *Concepts Magn.Res.* **2004**, *23A*, 89-120.

(47) Zasloff, M. *Nature* **2002**, *415*, 389-395.

(48) Wieprecht, T.; Apostolov, O.; Beyermann, M.; Seelig, J. *Biochemistry* **2000**, *39*, 442-452.

IX. Summary

Membrane-associated proteins and peptides constitute one of the major challenges to structural biology today. Compared to their importance, methodology for their structural analysis is only poorly developed. Solid-state NMR spectroscopy is currently one of the most promising approaches to study these systems. Labeling membrane-associated proteins or peptides with fluorine as non-natural reporter nucleus offers a novel and highly sensitive alternative to the more common, non-disturbing isotope labeling schemes established so far.

The work presented here deals with the development of ^{19}F-NMR methodology as well as data analysis schemes to extract the wealth of structural and motional information present in solid-state ^{19}F-NMR spectra.

To create a database of fundamental ^{19}F parameters for use as background information in future NMR studies, a substantial number of ^{19}F-labeled aromatic and aliphatic amino acids was characterized. In most of the commercially available substances a pronounced crystallographic polymorphism was found. MAS experiments at 600 MHz allowed to separate all different contributions and to determine the principal values of their CSA tensors. In addition, T_1 and T_2 relaxation times were determined over a wide temperature range. T_1 relaxation times were found to vary over two orders of magnitude in between the substances, reaching values of several 100 seconds when fluorine was substituted at an aromatic ring or ring system. Also, a notable variation with temperature was found. T_2 values, on the contrary, did not show much variation among the mono-fluorinated amino acids investigated, nor did they change notably with temperature.

Several different amino acids carrying a CF_3-substituent were also investigated, in analogy to the characterization of mono-fluorinated amino acids. Initially, the CF_3-group posed the experimental problem of finding a proper pulse sequence able to refocus both CSA and dipolar interactions, which are present at comparable magnitude in the CF_3-group. To address this problem, various standard and custom-tailored pulse sequences were tested. Contrary to common belief, the simple single-pulse experiment proved to be feasible on a modern spectrometer, and should be preferred in all experiments. Having solved the problem of the adequate pulse sequence, it was possible to extract CSA principal tensor and dipolar coupling values from the CF_3-labeled amino acids. T_1 relaxation times are on the order of 1 s, and displayed interesting temperature dependence in the range of –60° to +60°C. T_2 values are very similar for all substances and do not vary with temperature.

Three small organic molecules each carrying two CF_3-substituents in close spatial proximity were investigated in macroscopically aligned lipid bilayers. These 'six-spin' systems on the one hand serve as a model for two interacting CF_3-labels. At the same time, they can serve as small non-perturbing reporters of lipid bilayer properties. They insert and orient readily in model membranes, and show complex ^{19}F-NMR spectra in demanding CPMG experiments. This complexity may be a serious obstacle against the usage of interacting CF_3-groups as reporters in peptides. However, the complicated spectra were successfully deconvoluted, and precise coupling values were determined for both intra- and inter-CF_3 dipolar couplings. Structural analysis of the coupling values revealed that small organic compounds behave qualitatively different from larger molecules (e.g. peptides) in lipid bilayers. Larger systems tend to have a well-defined orientation in the lipid bilayer, with molecular mobility having only minor amplitudes and little influence on their structural description. In contrast, the

small six-spin systems are characterized by strong and significantly anisotropic mobility. Their behavior is very similar to that of small solutes in nematic liquid crystals, which have been extensively studied in the past. This work has thus transferred an application of those earlier studies to the investigation of lipid membrane systems. Applying the appropriate framework for interpretation eventually does make two interacting CF_3-groups highly interesting as reporters in a biomolecular system, since motional properties of membrane-associated systems are of as much biophysical interest as structural ones.

In contrast to the sixspin situation just described, when turning to larger membrane-bound peptide molecules it proved in all cases possible to determine an unambiguous molecular orientation from three or more fluorine labels. To determine the structure and orientation of the fusogenic peptide B18 and the antimicrobial peptide gramicidin S, data obtained on 4F-Phg labels was analyzed in terms of model theory and best-fit analysis. Prerogative of such analysis is the knowledge of or a reasonable assumption for local secondary structure. Data analysis of this ^{19}F-label has to rely heavily on the side chain torsion angle χ_1, which needs to be determined from other sources. Values determined from basic molecular modeling and MD simulations were found to be sufficiently reliable to overcome the problem of unknown side chain conformation. In addition, restricted rotation of the fluoro-phenyl side chain around the C_α-C_β-bond had to be taken into account by introducing a rotational order parameter.

The geometrical shape in which the fusogenic peptide B18 binds to model lipid bilayers was thus characterized. It was found to assume a helix-loop-helix conformation, reminiscent of a boomerang, where the more hydrophobic helix inserts into the lipid bilayer, while the more amphiphilic one floats peripherally on the bilayer surface. This novel mode of binding gives a direct explanation of how B18 can disturb the lipid bilayer core and at the same time dehydrate the headgroup region. Both effects represent well-known modes of bilayer destabilization and are a prerogative for membrane fusion.

For the antimicrobial peptide gramicidin S, data from only two 4F-Phg labeling sites was available. By additional use of two ^{15}N isotope labels, it was nonetheless possible to determine unambiguously the orientation in the lipid membrane. Owing to the high sensitivity of ^{19}F-NMR, a concentration-dependent re-alignment could be comprehensively characterized. Orientational analysis yielded a structural model for a novel membrane-inserted state, which appears to be connected to the membrane-permeabilizing properties of the peptide. Based on these structural results, we propose the formation of an oligomeric peptidic pore to explain membrane permeabilization.

Using another antimicrobial peptide, PGLa, CF_3-labeling was for the first time shown to be a viable approach to determine the orientation of a membrane-active peptide. The CF_3-group proved to have superior properties for data analysis compared to the single ^{19}F-substituent on 4F-Phg. However, the ^{19}F-NMR spectra are disturbed by the effect of differential relaxation, a fact that is aesthetically unfavorable at the moment but may turn out to be an important source of information when examined more closely. Data analysis again allowed for a comprehensive determination of peptide alignment, which was additionally scrutinized by testing the influence of various model structures on the results. Good agreement was found between results from CF_3-labels and more common ^{2}H and ^{15}N isotope labels. Again, a concentration-dependent re-alignment process was found, which, however, can not be readily understood in terms of the two-state model of antimicrobial action.

On all three investigated membrane-active peptide systems, it proved possible to unambiguously determine their molecular orientation from only a handful of NMR constraints, given that the peptides' secondary structures are known. Influence of side chain torsion as well as of slight variations in model structure were examined. Data acquired on ^{19}F-labels was
STOP
found to give similar information as ^{2}H-labels at markedly increased sensitivity and without compromising accuracy, since molecular structure is not significantly disturbed. Information from ^{15}N-labels was found to be 'orthogonal' to ^{19}F- and ^{2}H-information, substantially aiding structural data analysis. Thus, by means of solid-state ^{19}F-NMR, the orientational behavior of the three membrane-active peptides B18, gramicidin S, and PGLa could be studied. Exciting insight was gained into their action, namely a structural model for the fusogenic peptide B18 was obtained for the first time for this class. A concentration-dependent re-orientation and indications for dimer formation were detected and thoroughly characterized, also for the first time in such detail, in two different antimicrobial peptides, gramicidin S and PGLa. Although the chosen concentrations at which the novel alignments were detected may seem exceedingly high, they are not. Under physiological conditions of antimicrobial action *in vivo*, comparable or even far higher concentrations are expected. Therefore, it is concluded that the observed re-alignment processes are indicative of a functional state of the peptides.

On the whole, the present thesis gained substantial experience with the method of solid-state ^{19}F-NMR by characterizing polycrystalline monofluorinated and CF_3-labeled amino acids, by examining doubly CF_3-labeled model substances in lipid bilayers, and by developing and evaluating methods for data analysis on biologically relevant ^{19}F-labeled peptides. For structural biomolecular studies, both 4F-Phg and CF_3-Phg were shown to be viable reporter groups for synthetic peptides, with CF_3-Phg being the superior label in view of data analysis. Additional advantages of the CF_3-label include increased sensitivity and the possibility of dipolar coupling sign determination. Data analysis from ^{19}F- and CF_3-labeled peptides can now be carried out routinely using the best-fit analysis approach that was implemented, tested, and applied here.

APPENDICES

A. List of abbreviations
B. Sample *Mathematica* notebook
C. Publication on B18 in *Magnetic Resonance in Chemistry*
D. Publication on PGLa in *Journal of Magnetic Resonance*
E. Publication on PGLa in *Biophysical Journal*
F. Statement of contributions
G. Curriculum vitae
H. Acknowledgements

A. List of abbreviations

4F-Phg	4-fluoro-phenylglycine
Ala-d_3	3,3,3-trideutero-alanine
CF_3-Phg	4-CF_3-phenylglycine
CP	cross polarization
CSA	chemical shift anisotropy
DD	dipolar coupling
DLPC	dilaureoylphosphatidylcholine
DMPC	dimyristoylphosphatidylcholine
DMPG	dimyristoylphosphatidylglycerol
DPPC	dipalmitoylphosphatidylcholine
FID	free induction decay
LAB	laboratory coordinate system
MAS	magic angle sample spinning
MD	molecular dynamics
MLV	multi-lamellar vesicle
MOL	molecular coordinate system
NMR	nuclear magnetic resonance
PAS	principal axis coordinate system
PPL	peptide plane coordinate system
RF	radio frequency
rmsd	root mean square deviation
SNR	signal-to-noise ratio

B. Sample *Mathematica* notebook

Simplified sample *Mathematica* notebook as used in analysis of ^{19}F data acquired on macroscopically aligned lipid bilayer samples of 4F-Phg labeled analogues of gramicidin S.

Appendices

gramicidin S
Best-fit analysis of 19F data

Simplified sample *Mathematica* notebook as used in analysis of 19F data acquired on macroscopically aligned lipid bilayer samples

UD, May 2004

■ Prepare notebook

This cell needs to be run first, in order to initialize the notebook by providing necessary functions

```
In[1]:= Clear["Global`*"];
        Print["loading Mathematica packages"];
        << Calculus`VectorAnalysis`;
        << LinearAlgebra`Orthogonalization`;
        Print["loading mathematical routines"];
        << "E:\user\ulli\mathlib\euler-new.m";
```

```
loading Mathematica packages

loading mathematical routines

EulerMatrix[a_,b_,g_]

  active Euler rotation matrix as given by Melinda Duer (2002):

  EulerMatrix[α,β,γ] :=
```

$$\begin{pmatrix} \cos[\alpha]\cos[\beta]\cos[\gamma]-\sin[\alpha]\sin[\gamma] & -\cos[\gamma]\sin[\alpha]-\cos[\alpha]\cos[\beta]\sin[\gamma] & \cos[\alpha]\sin[\beta] \\ \cos[\beta]\cos[\gamma]\sin[\alpha]+\cos[\alpha]\sin[\gamma] & \cos[\alpha]\cos[\gamma]-\cos[\beta]\sin[\alpha]\sin[\gamma] & \sin[\alpha]\sin[\beta] \\ -\cos[\gamma]\sin[\beta] & \sin[\beta]\sin[\gamma] & \cos[\beta] \end{pmatrix}$$

```
  argument angles a,b,g in radians

EulerRotate[Matrix_,a_,b_,g_]

  returns transform of matrix M according to M'= R.M.Rt

  argument angles a,b,g in radians

AveDia[diamatrix_,S_]

  returns diagonal matrix diamatrix, all components scaled by order parameter S

RotDia[diamatrix_,S_]

  returns diagonal matrix diamatrix, 1 and 2 component scaled by order parameter S
```

■ Generate transformation matrices PPL->MOL

Transformation matrices PPL->MOL are generated from atomic coordinates for residues Val1, Leu3, Val6, and Leu8 (as extracted from e.g. pdb or COSMOS format data files). Phenyl torsion angle chi 1 is introduced as independent parameter.

```
In[3]:= (*atomic coordinates characterizing PPL
          coordinate system in each fluorine label   (i.e. Ce, F, Cd1, Cd2)*)
        Print["Model:   Xu et al."];
        coord1F = {{3.847,  0.982,  -5.518}, {3.992,  0.542,  -6.765},
          {4.81888,  0.69784, -4.56237}, {2.72272,  1.73001, -5.17004}};
        coord3F = {{-3.026,  1.594,  -5.488}, {-2.919 ,  1.297,  -6.780},
          {-1.986,  1.281,  -4.614}, {-4.177,  2.217,  -5.009}};
        coord6F = {{-3.811,  -1.705,  -5.337}, {-3.949,  -1.455,  -6.636},
          {-4.811,  -1.324,  -4.444}, {-2.666,  -2.347,  -4.868}};
        coord8F = {{3.062,  -2.304,  -5.176}, {2.963 , -2.203,  -6.498},
          {2.018,  -1.864,  -4.363}, {4.210,  -2.849,  -4.602}};

        (*Xu et al.' s definition of
          MOL is 90 degree turned from ours, this needs to be fixed*)
        Rco = EulerMatrix[90 Degree, 0, 0];
        For[i = 1, i <= 4, i++,
         coord1F[[i]] = Rco . coord1F[[i]];
         coord3F[[i]] = Rco . coord3F[[i]];
         coord6F[[i]] = Rco . coord6F[[i]];
         coord8F[[i]] = Rco . coord8F[[i]];
        ];

        (*switch between analysis of gS-1/1' and gS-3/3' data*)
        coordSETval = {coord1F, coord6F};
        coordSETleu = {coord3F, coord8F};
        coordSET = coordSETval;
        coordN = Length[coordSET];

        (*calculate normalized axis vectors for PPL coordinate system in MOL*)
        system = Table[, {i, coordN}, {j, 4}];
        (*allow ambiguity in x definition*)
        directorSET = {-1, -1, 1, -1};
        For[i = 1, i <= coordN, i++,
         system[[i, 1]] = coordSET[[i,
            1]];
         (* fluorine position as origin*)
         system[[i, 2]] = Normalize[
           directorSET[[i]] (coordSET[[i, 3]] - coordSET[[i, 4]])];        (*xPPL in MOL*)
         system[[i, 4]] = Normalize[
           coordSET[[i, 2]] - coordSET[[i, 1]]];                             (*zPPL*)
         system[[i, 3]] = Normalize[
           CrossProduct[system[[i, 4]], system[[i, 2]]]]                   (*yPPL*)
        ];
        Print["\nnormalized PPL coordinate vectors in MOL:"];
        Print[MatrixForm[system]];

        (*construct transformation matrices*)
        T = Table[, {i, coordN}];
        For[i = 1, i <= coordN, i++,
         T[[i]] = Transpose[{system[[i, 2]], system[[i, 3]], system[[i, 4]]}];
         ];
        Print["\ntransformation matrices (active PAS-MOL):"];
        Print[MatrixForm[T[[1]]]];
        Print[MatrixForm[T[[2]]]];
```

```
Model:   Xu et al.

normalized PPL coordinate vectors in MOL:
```

$$\begin{pmatrix} \begin{pmatrix} -0.982 \\ 3.847 \\ -5.518 \end{pmatrix} & \begin{pmatrix} -0.427535 \\ -0.868251 \\ -0.251703 \end{pmatrix} & \begin{pmatrix} -0.841333 \\ 0.484024 \\ -0.24058 \end{pmatrix} & \begin{pmatrix} 0.330758 \\ 0.109 \\ -0.9374 \end{pmatrix} \\ \begin{pmatrix} 1.705 \\ -3.811 \\ -5.337 \end{pmatrix} & \begin{pmatrix} 0.42378 \\ 0.888572 \\ -0.175643 \end{pmatrix} & \begin{pmatrix} 0.886074 \\ -0.446913 \\ -0.123052 \end{pmatrix} & \begin{pmatrix} -0.187968 \\ -0.103758 \\ -0.976679 \end{pmatrix} \end{pmatrix}$$

```
transformation matrices (active PAS-MOL):
```

$$\begin{pmatrix} -0.427535 & -0.841333 & 0.330758 \\ -0.868251 & 0.484024 & 0.109 \\ -0.251703 & -0.24058 & -0.9374 \end{pmatrix}$$

$$\begin{pmatrix} 0.42378 & 0.886074 & -0.187968 \\ 0.888572 & -0.446913 & -0.103758 \\ -0.175643 & -0.123052 & -0.976679 \end{pmatrix}$$

■ Visualization of molecular model

Transformation matrices Ti generated above are used for vectorial transformation of PPL basis vectors, providing visual control of the above calculations. Backbone Calpha positions are shown additionally to give an idea of the structure. Used to generate figure 2.6 in Ph.D. thesis

```
In[38]:= (*GRAPHICS FOR PPL COORDINATE SYSTEMS*)

         (*PPL coordinate vectors before transformation, i.e. coinciding with LAB*)
         xPPL = {1, 0, 0};
         yPPL = {0, 1, 0};
         zPPL = {0, 0, 1};

         chi1 = 30;

         label = Table[, {j, coordN}];
         For[i = 1, i <= coordN, i++,
           Module[{Ti, xT, yT, zT, origin}, {
            (*matrices giving chi1 torsion*)
            Tchip = EulerMatrix[chi1 Pi / 180, 0, 0];
            Tchim = EulerMatrix[-chi1 Pi / 180, 0, 0];
            (*transformation PPL-MOL from above*)
            Ti = T[[i]];
            Print["current transformation matrix Ti=", MatrixForm[Ti]];
            xT = Ti . Tchip . xPPL;
            yT = Ti . Tchip . yPPL;
            zT = Ti . Tchip . zPPL;
            origin = system[[i, 1]];
            (*generate graphics objects for coordinate threepods*)
            stretch = 2;
            label[[i]] = {
             Graphics3D[{Thickness[.012], RGBColor[0, 0, 0],
                Line[{origin, origin + stretch xT}]}],
             Graphics3D[{Thickness[.012], RGBColor[0, 0.6, 0],
                Line[{origin, origin + stretch yT}]}],
             Graphics3D[{Thickness[.012], RGBColor[1, 0, 0],
```

```
        Line[{origin, origin + stretch zT}]}]
      };
    }]
   ];


  (*GRAPHICS FOR BACKBONE DISPLAY*)

  (*Calpha positions*)
  Calpha = {{3.376,  2.409,  -1.476},
     {  0.043,    2.271,    0.317},
     {-3.371,    2.556 , -1.298},
     {-6.270,    1.580,    0.944},
     {-6.391,  -2.193,    1.220},
     {-3.363,  -2.515,  -1.124},
     {-0.041,  -2.109,    0.648},
     {  3.383,  -2.630,  -0.887},
     {  6.271,  -1.327,    1.203},
     {  6.389,    2.444,    0.916}
   };
  Nres = Length[Calpha];
  For[i = 1, i <= Nres, i++, Calpha[[i]] = Rco . Calpha[[i]]];

  (*graphics objects*)
  backbone = Table[, {j, Nres}];
  For[i = 1, i < Nres, i++,
   backbone[[i]] = {
      (*Graphics3D[{PointSize[0.03],RGBColor[0,0,0],Point[Calpha[[i]]]}],*)
     Graphics3D[{Thickness[.012], RGBColor[0, 0, 0],
       Line[{Calpha[[i]], Calpha[[i + 1]]}]}]
    };
  ];
  backbone[[Nres]] = {
     (*Graphics3D[{PointSize[0.03],RGBColor[0,0,0],Point[Calpha[[i]]]}],*)
    Graphics3D[{Thickness[.012], RGBColor[0, 0, 0],
      Line[{Calpha[[Nres]], Calpha[[1]]}]}]
   };


  (*GENERATE PLOTS*)

  gsmodel = {label, backbone};
  a = 8; b = 3;
  (*default:  ViewPoint→{1.3,-2.4,2}*)
  pic1 = Show[gsmodel, PlotLabel → "default:  ViewPoint->{1.3,-2.4,2}",
    Axes → True, AxesLabel → {x, y, z},
    PlotRange → {{-a, a}, {-a, a}, {-a, b}}, DisplayFunction → Identity];
  (*directly in front*)
  pic2 = Show[gsmodel, PlotLabel → "directly in front", Axes → True,
    AxesLabel → {x, y, z}, PlotRange → {{-a, a}, {-a, a}, {-a, b}},
    ViewPoint → {0, -2, 0}, DisplayFunction → Identity];
  (*down helix axis*)
  pic3 = Show[gsmodel, PlotLabel → "down symmetry axis", Axes → True,
    AxesLabel → {x, y, z}, PlotRange → {{-a, a}, {-a, a}, {-a, b}},
    ViewPoint → {0, 0, 2}, DisplayFunction → Identity];
  (*from right side*)
  pic4 = Show[gsmodel, PlotLabel → "from right side", Axes → True,
    AxesLabel → {x, y, z}, PlotRange → {{-a, a}, {-a, a}, {-a, b}},
    ViewPoint → {2, 0, 0}, DisplayFunction → Identity];
  allpic = Show[GraphicsArray[{{pic3, pic2}, {pic1, pic4}}],
    ImageSize -> 400, ImageResolution -> 600];
  Print["chi1=", chi1];
  Print["x  black\ty  green\tz  red"];
```

current transformation matrix Ti= $\begin{pmatrix} -0.427535 & -0.841333 & 0.330758 \\ -0.868251 & 0.484024 & 0.109 \\ -0.251703 & -0.24058 & -0.9374 \end{pmatrix}$

current transformation matrix Ti= $\begin{pmatrix} 0.42378 & 0.886074 & -0.187968 \\ 0.888572 & -0.446913 & -0.103758 \\ -0.175643 & -0.123052 & -0.976679 \end{pmatrix}$

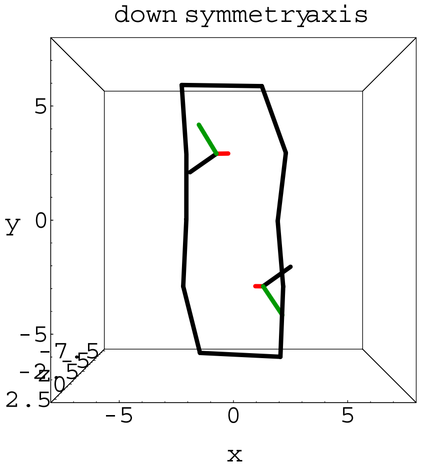

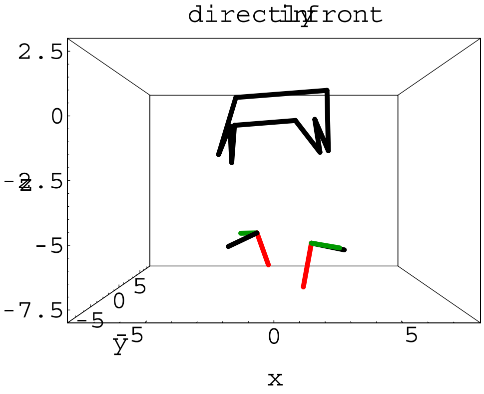

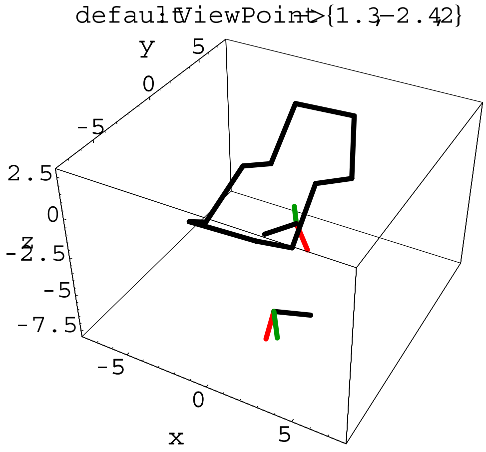

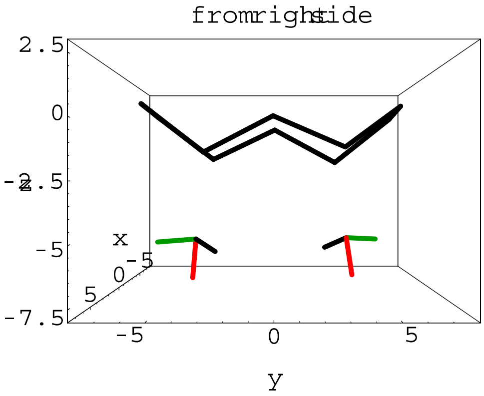

chi1=30

x black y green z red

■ Generate chi-square plots

Transformation matrices Ti generated above are used for tensorial transformation of CSA tensor from its PAS frame of reference into LAB, ultimatively allowing prediction of expected 19F-NMR resonance frequency. This enters chi-square function, which is shown in rho-tau-plot to allow for visual inspection. Used to generate figure 7.4 in Ph.D. thesis.

```
In[35]:= (*rigid fluorine CSA tensor as measured on gS-3/3' lyophilate*)
fluorinePAS = DiagonalMatrix[{-65.5, -153, -126.5}];

(*experimental resonances observed for I-state in main lipid phase transition*)
fexp = {-86.0, -65.0, -86.0, -77.5};

(*function
  to calculate resonance frequency after transforming CSA tensor to LAB*)
f[i_, rho_, tau_, Smol_, Srot_] :=
 Module[{fmod, Ti, Titr, M, Mtr, sigmaWOB, sigmaROT, sigmaMOL, sigmaLAB}, (
   sigmaPAS = fluorinePAS;
   (*wobble routines for Smol and Srot*)
   sigmaWOB = AveDia[sigmaPAS, Smol];
   sigmaROT = RotDia[sigmaWOB, Srot];
   (*introduce chi1 torsion*)
   Tchip = EulerMatrix[chi1 Degree, 0, 0];
   Tchiptr = Transpose[Tchip];
   Ti = T[[i]];
   Titr = Transpose[Ti];
   (*transformation PAS-MOL*)
   sigmaMOL =
    Ti . Tchip . sigmaROT . Tchiptr . Titr;                 (*xT=Ti.Tchip.xPAS;*)
   (*transformation MOL-LAB*)
   M = EulerMatrix[0, tau, rho];
   Mtr = Transpose[M];
   sigmaLAB = M . sigmaMOL . Mtr;
   (*resonance frequency is 33-component of LAB tensor*)
   fmod = sigmaLAB[[3, 3]];
   Return[fmod];
)];

(*chi-square function*)
error = 2;
chisq[rho_, tau_, Smol_, Srot_] := Module[{value = 0.0, i}, (
  For[i = 1, i <= coordN, i++, value += (f[i, rho, tau, Smol, Srot] - fexp[[i]])^2];
   Return[value / (error^2)];
  )];


(*OUTPUT SECTION*)

Print["Model:  Xu et al."];
Switch[coordSET,
 coordSETval, (fexp = {fexp[[3]], fexp[[1]]}; Print["analyzing VgS"];),
 coordSETleu, (fexp = {fexp[[4]], fexp[[2]]}; Print["analyzing LgS"];)];
Print["experimental resonances at ", fexp[[1]], "ppm and ", fexp[[2]], "ppm"];
Smol = 1.0;
Srot = 1.0;
Print["Smol=", Smol, ", Srot=", Srot];

(*generate an array of chi-square plots*)
   allpic = Table[, {10}];
cont = {-2, -4, -6};
resol = 75;
chi1 = -80.0;
```

```
For[i = 1, i ≤ 10, i++, (
  allpic[[i]] =
   ContourPlot[
     -chisq[rho Pi / 180, tau Pi / 180, Smol, Srot], {rho, -90, 90}, {tau, 45, 135},
    ContourShading -> False,
    Contours -> cont,
    PlotPoints -> resol,
    AspectRatio -> 0.5,
    FrameTicks -> {{-90, -60, -30, 0, 30, 60, 90, 120, 150, 180},
        {0, 30, 60, 90, 120, 150, 180}, {}, {}},
    DisplayFunction → Identity];
    chi1 += 20;
    )];
panel = Partition[allpic, 5];
picchi1 = Show[GraphicsArray[Transpose[panel]], ImageSize -> 400];
```

```
Model:  Xu et al.

analyzing VgS

experimental resonances at  - 86.ppm and  - 86.ppm

Smol=1., Srot=1.
```

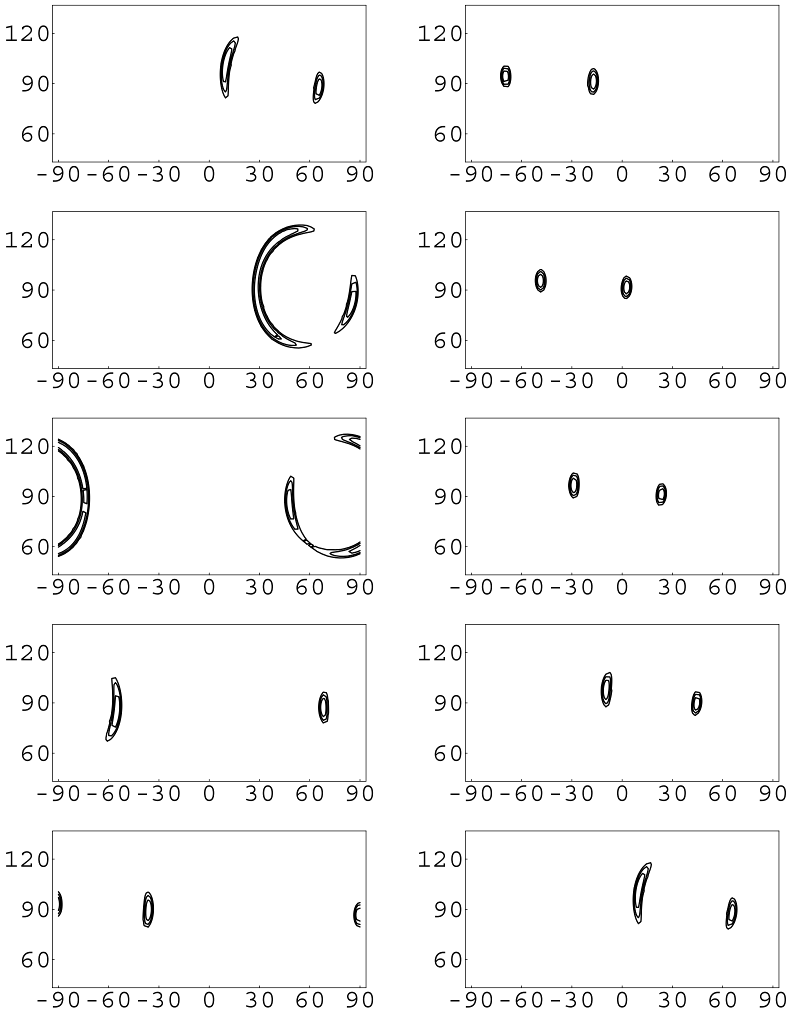

■ Search for minimum

Minimum search routine provided by *Mathematica* allows for exact determination of minima found in chi-square function.
Used to generate table 7.4 in Ph.D. thesis

```
Clear[S];
Smol = 1.0;
Srot = 1.0;

chi1 = 40;
tau0 = 90;

rho0 = -40;
FindMinimum[chisq[rho Degree, tau Degree, Smol, Srot],
 {rho, rho0}, {tau, tau0}, MaxIterations -> 100]
rho0 = 20;
FindMinimum[chisq[rho Degree, tau Degree, Smol, Srot], {rho, rho0},
 {tau, tau0}, MaxIterations -> 100]
```

$\{1.40114\times10^{-14}, \{rho \to -48.8399, tau \to 95.5254\}\}$

$\{6.60817\times10^{-21}, \{rho \to 2.80382, tau \to 91.6434\}\}$

C. Publication on B18 in *Magnetic Resonance in Chemistry*

Afonin, S., U. H. N. Dürr, R. W. Glaser, A. S. Ulrich

'Boomerang'-like insertion of a fusogenic peptide in a lipid membrane revealed by solid-state ^{19}F-NMR

Magnetic Resonance in Chemistry **2004**, ***42***, 195-203.

Appendices

MAGNETIC RESONANCE IN CHEMISTRY
Magn. Reson. Chem. 2004; **42**: 195–203
Published online in Wiley InterScience (www.interscience.wiley.com). DOI: 10.1002/mrc.1340

MRC

'Boomerang'-like insertion of a fusogenic peptide in a lipid membrane revealed by solid-state ^{19}F NMR

Sergii Afonin,[1] Ulrich H. N. Dürr,[2] Ralf W. Glaser[3] and Anne S. Ulrich[1,2]*

[1] Forschungszentrum Karlsruhe, IFIA, POB 3640, 76021 Karlsruhe, Germany
[2] University of Karlsruhe, Institute of Organic Chemistry, Fritz-Haber-Weg 6, 76131 Karlsruhe, Germany
[3] University of Jena, Institute of Biochemistry & Biophysics, Hans-Knöll-Strasse 2, 07745 Jena, Germany

Received 22 May 2003; Revised 25 July 2003; Accepted 25 July 2003

Solid state ^{19}F NMR revealed the conformation and alignment of the fusogenic peptide sequence B18 from the sea urchin fertilization protein bindin embedded in flat phospholipid bilayers. Single ^{19}F labels were introduced into nine distinct positions along the wild-type sequence by substituting each hydrophobic amino acid, one by one, with L-4-fluorophenylglycine. Their anisotropic chemical shifts were measured in uniaxially oriented membrane samples and used as orientational constraints to model the peptide structure in the membrane-bound state. Previous ^{1}H NMR studies of B18 in 30% TFE and in detergent micelles had shown that the peptide structure consists of two α-helical segments that are connected by a flexible hinge. This helix–break–helix motif was confirmed here by the solid-state ^{19}F NMR data, while no other secondary structure (β-sheet, 3_{10}-helix) was compatible with the set of orientational constraints. For both α-helical segments we found that the helical conformation extends all the way to the respective N- and C-termini of the peptide. Analysis of the corresponding tilt and azimuthal rotation angles showed that the N-terminal helix of B18 is immersed obliquely into the bilayer (at a tilt angle $\tau \approx 54°$), whereas the C-terminus is peripherally aligned ($\tau \approx 91°$). The azimuthal orientation of the two segments is consistent with the amphiphilic distribution of side-chains. The observed 'boomerang'-like mode of insertion into the membrane may thus explain how peptide binding leads to lipid dehydration and acyl chain perturbation as a prerequisite for bilayer fusion to occur. **Copyright © 2004 John Wiley & Sons, Ltd.**

KEYWORDS: solid-state ^{19}F NMR; fluorine chemical shift anisotropy; uniaxially oriented sample; 4-fluorophenylglycine; membrane fusion; fusogenic peptide; tilted alignment; azimuthal rotation; helix–break–helix motif

INTRODUCTION

Membrane fusion is a fundamental process in many intra- and intercellular events such as fertilization, viral infection, vesicular traffic and synaptic transmission.[1–3] Complex protein machineries control the recognition between the two apposing membranes, and trigger their fusion at the correct point in time and space.[4,5] Short amphiphilic protein sequences, so-called fusion peptides, mediate the actual merging between the bilayers.[6–10] Even as isolated peptides these fusogenic sequences are able to induce vesicle fusion *in vitro*, hence their structural description promises a better understanding of the fundamental mechanism. From theoretical considerations it has been proposed that many fusion peptides adopt a continuous α-helix that inserts obliquely into the membrane, thereby leading to a considerable perturbation of the lipid acyl chains.[11,12] Experimentally, however, it is not trivial to determine the peptide alignment at high resolution, as there exists no straightforward and unambiguous method for investigating protein structures in the membrane-bound state. The conformation and alignment of fusion peptides have been qualitatively described by indirect methods such as ESR, neutron diffraction and IR spectroscopy, in addition to many functional studies.[13–16] One of the few techniques able to resolve three-dimensional structural details of membrane-associated peptides is provided by solid-state NMR,[17–19] but no fusogenic sequence has yet been solved using this approach.

Solid-state NMR studies of membrane-associated peptides generally suffer from low sensitivity of the isotope labels that are commonly incorporated and observed. The ^{19}F nucleus, on the other hand, has an exquisitely high NMR sensitivity,[20,21] which saves material and instrument time up to several orders of magnitude compared with ^{2}H, ^{13}C or ^{15}N.[22] Only small amounts of ^{19}F-labeled peptide (down to 20 nmol) need to be incorporated in macroscopically oriented membrane samples to be observable in short acquisition times (minutes to hours).[23] As the fluorine nucleus is normally absent in proteins, there is no natural abundance background. On the other hand, it is necessary to introduce non-natural ^{19}F-labeled amino acids chemically or biosynthetically.[20] We have recently demonstrated that

*Correspondence to: Anne S. Ulrich, Forschungszentrum Karlsruhe, POB 3640, 76021 Karlsruhe, Germany.
E-mail: anne.ulrich@ifia.fzk.de
Contract/grant sponsor: Deutsche Forschungsgemeinschaft; Contract/grant number: SFB196/TPB13; SFB604/TPB6.

Copyright © 2004 John Wiley & Sons, Ltd.

L-4-fluorophenylglycine (4F-Phg) is a suitable ^{19}F NMR label in peptides for structural studies, causing little perturbation of the conformation and biological function when substituted for a hydrophobic amino acid.[22,24–26] This particular non-natural amino acid was chosen because the ^{19}F substituent on the 4F-Phg side-chain is stiffly connected to the peptide backbone in a well-defined geometry. Provided that the N—C_α—C_β—C_γ torsion angle of the phenyl group is known, the anisotropic ^{19}F chemical shift provides information about the alignment of the labeled segment relative to the membrane normal (C_α—C_β being collinear with the C_ε—F bond). A few of these orientational constraints are then sufficient to deduce directly the backbone alignment of any well-defined secondary structure element, such as an idealized α-helix or a β-sheet[25] or any independently determined tertiary fold.[27,28] Our strategy using oriented samples is thus (i) to measure the chemical shifts of several individually 4F-Phg substituted positions along the peptide sequence, (ii) to confirm whether they are compatible with any one type of common secondary structure and (iii) to determine the overall alignment of the folded peptide from these ^{19}F NMR constraints.

The fusion peptide investigated here, B18 (NH_2 – L^{103}GLLLRHLRHHSNLLANI^{120}-COOH, numbering according to *Strongylocentrotus purpuratus*), stems from the fully conserved membrane-interacting region of the acrosomal sea urchin protein bindin, which is responsible for merging the membranes of sperm and egg during fertilization.[29,30] The peptide represents the minimal sequence that retains the fusogenic properties of the parent protein, and it has many features in common with viral fusion peptides.[10,31–33] ^{1}H NMR and circular dichroism (CD) studies showed that under functionally relevant conditions B18 assumes a helical structure with a central break.[32] By attenuated total reflection (ATR) IR spectroscopy the helix was observed to bind peripherally to membranes at a tilted angle, leading to significant dehydration of the lipid headgroups.[33] In the present study, a more detailed B18 structure was assembled from a series of orientational constraints that were obtained from 4F-Phg-labeled peptides. The fusion activity of these analogues was monitored by a fluorescence dequenching assay and their conformation was examined by CD. All labeled peptides retained the fusogenic functionality and structural integrity of the wild type.[24] Hence they are well suited for structure analysis.

By solid-state ^{19}F NMR we have now resolved the local conformation and overall alignment of the fusion peptide B18 in a flat lipid bilayer, with the aim of drawing some conclusions on the general mechanism of membrane fusion.

EXPERIMENTAL

^{19}F-labeled peptides

Nine 4F-Phg-labeled peptide analogues of B18 were synthesized by standard solid-phase Fmoc chemistry, as summarized in Table 1. They were purified by reversed-phase high-performance liquid chromatography (RP-HPLC) on Vydac C18 columns with 5 mM HCl–acetonitrile gradients, to remove by-products and traces of trifluoroacetic acid from the cleavage reaction. Given that 4F-Phg tends to racemize under the basic coupling conditions, the HPLC fractions containing the all-L-isomeric peptides were identified using Marfey's reagent.[24] Molecular masses were confirmed by standard matrix-assisted laser desorption/ionization time-of-flight or electrospray ionization mass spectrometry. The secondary structures of the ^{19}F-labeled analogues were confirmed by CD spectroscopy, and their fusion activities were validated by fluorescence spectroscopy, as outlined previously.[24,31,32]

Solid-state NMR experiments

The lipid mixture used in the study was 1,2-dimyristoyl-*sn*-glycero-3-phosphocholine–1,2-dimyristoyl-*sn*-glycero-3-[phospho-*rac*-(1-glycerol)] [DMPC–DMPG (80 : 20, mol/mol)] from Avanti Polar Lipids (Alabaster, AL, USA). To prepare oriented NMR samples, a 70% methanol solution containing peptide (typically 0.5 mg) and lipids in the desired ratio (usually 1 : 150) was deposited on glass slides (0.06 × 7.5 × 18 mm) (Marienfeld, Landa-Königshofen, Germany) and dried to completion.[22,24–26] About 17 membrane-coated glass slides were stacked, covered with an empty slide and re-hydrated for 1–4 days at 48 °C over saturated K_2SO_4 solution (~98% relative humidity at 20 °C), wrapped and immediately used for NMR measurement.

Solid-state NMR experiments were carried out on a wide-bore Unity Inova 500 spectrometer (Varian, Palo Alto, CA, USA), as described previously.[22,24,26,34,35] For ^{19}F NMR, a ^{19}F/^{1}H double-tuned flat-coil probehead with a goniometer (Doty Scientific, Columbia, SC, USA) and an external 470 MHz high-power amplifier (Creative Electronics, Los Angeles, CA, USA) were used. ^{31}P NMR experiments were performed on a laboratory-built ^{1}H/X probe equipped with a flat coil. ^{1}H-decoupled ^{19}F NMR spectra were acquired at 35 °C with typically 2000 transients, and referenced externally with 100 mM NaF in 10 mM HEPES, pH 7.5 (measured at 35 °C and taken as −120.4 ppm).[23,26] ^{1}H-decoupled ^{31}P NMR spectra were recorded to judge the quality of lipid orientation in the samples. The static ^{19}F CSA tensor elements were determined by fitting the powder spectra of the lyophilized peptides with a self-written C^{++} program and DMfit.[36] Composite pulses[37,38] and long echo delay times were used to obtain ^{19}F NMR spectra free from off-resonance distortions.

Modeling of secondary structure elements

To test whether different types of secondary structure elements are compatible with the NMR constraints, we assumed various ideal backbone conformations for an α-helix, 3_{10}-helix and β-sheet. An ideal right-handed α-helix was modeled according to the IUPAC–IUB-recommended values $\varphi = -57°$, $\psi = -47°$, $\omega = 180°$, or using $\varphi = -65°$, $\psi = -40°$, $\omega = 180°$ as suggested by Morris *et al.*[39] An ideal β-sheet was modeled either in a parallel ($\varphi = -119°$, $\psi = 113°$, $\omega = 180°$) or anti-parallel ($\varphi = -139°$, $\psi = 135°$, $\omega = -178°$) conformation. For the 3_{10}-helix the torsion angles were taken as $\varphi = -49°$, $\psi = -26°$, $\omega = 180°$.

To determine the relevant side-chain torsion angle χ_1 (see inset in Fig. 1) of 4F-Phg in the different backbone environments, we placed this label into each secondary

Copyright © 2004 John Wiley & Sons, Ltd.

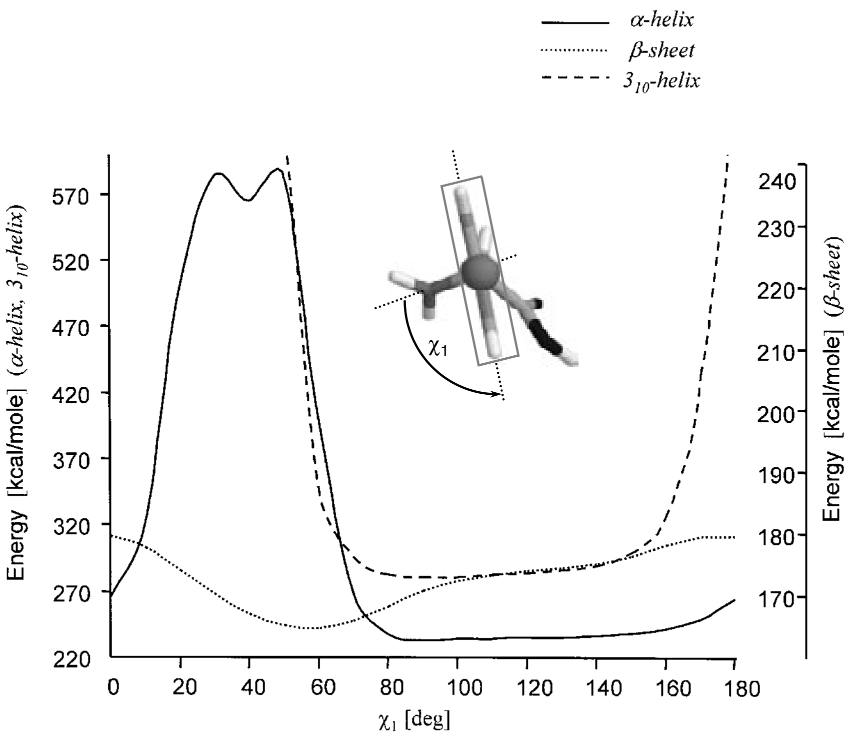

Figure 1. Energy profile of the N — Cα — Cβ — Cγ torsion angle χ_1 of the 4F-Phg side-chain in different peptide conformations (α-helix, β-sheet, 3_{10}-helix). The molecules were constructed as AAAA-[4F-Phg]-AAAA and analyzed with the cvff.frc force field.

structure model and calculated the total molecular energy as a function of χ_1. Standard force fields were used with varying impact on steric interactions, as implemented in the InsightII (Accelrys, San Diego, CA, USA), SYBYL (Tripos, St. Louis, MO, USA) and COSMOS (COSMOS Software, Jena, Germany) molecular modeling software packages. In these calculations we tested model peptides of different length [3-, 5-, 7-, 9- and 11-mers of the type $X_{(n)}$-4F-Phg-$X_{(n)}$] to assess short- and long-range steric effects. The energy profiles in Fig. 1 show the most appropriate χ_1 angle to be 110° for an α-helix, 115° for a 3_{10}-helix and 65° for a β-sheet. These numbers represent the mean values after restricted rotational averaging (discussed below) and were used as input parameters for calculating the peptide alignment.

Calculation of peptide alignment

The alignment of any well-defined secondary structure element in the membrane is found by systematically tilting and rotating this rigid body to find the minimum root mean square deviation (r.m.s.d.) between the predicted ^{19}F NMR chemical shifts of the labels and the experimental set of data.[22] In the case of B18 we started off by analyzing simultaneously the ^{19}F CSA tensors of three consecutive labeled positions, which fortuitously occur as a hydrophobic stretch within each half of the sequence (L105–L106–L106 in the N-terminal segment and L116–L117–A118 in the C-terminal segment). The same approach was then used to examine longer stretches of the peptide (including further labeled sites: L103, L110 and/or L120).

Figure 2(a) shows the known orientation of the ^{19}F chemical shift anisotropy (CSA) tensor within the rigid framework of the 4F-Phg side-chain,[22,25] which was placed into each

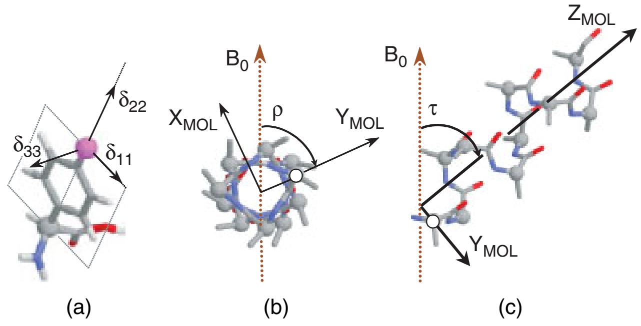

Figure 2. Assignment of the ^{19}F CSA tensor elements δ_{11}, δ_{22} and δ_{33} in 4F-Phg (a) and definition of the coordinate system associated with the α-helical molecule, viewed along the $+z_{MOL}$ axis (b) and from the side (c). The direction of the magnetic field B_0 is indicated by the dotted lines to illustrate the definition of the tilt angle τ and the azimuthal rotation ρ.

type of idealized secondary structure (α-helix, 3_{10}-helix or β-strand) using the appropriate χ_1 torsion angle. The molecular coordinate frame was defined such that the long axis of the secondary structure element running from N- to C-terminus is the z-axis (z_{MOL}); the direction of y_{MOL} was defined as the axis perpendicular to z_{MOL} that projects through C_α of the first residue of the three consecutively labeled sites; x_{MOL} follows to be orthogonal to y_{MOL} and z_{MOL} [Fig. 2(b) and (c)]. The angle between z_{MOL} and the membrane normal is denoted as the tilt angle τ of the secondary structure element, and the azimuthal rotation ρ defines its polarity with respect to the origin of y_{MOL} [Fig. 2(b) and (c)]. As a starting point, the structured peptide was placed into the laboratory frame such that z_{MOL} was parallel to the membrane normal, then a systematic

Copyright © 2004 John Wiley & Sons, Ltd.

rotation throughout the entire Euler space was performed. At every rotational step the orientation-dependent chemical shifts were calculated for all relevant ^{19}F CSA tensors and compared with the corresponding experimental values. The quality of fit was finally represented by an r.m.s.d. map as a function of τ and ρ. All calculations were automated and performed using the self-written Mathematica notebooks (Wolfram Research, Champaign, IL, USA). The resulting alignment of the peptide was visualized with MOLMOL[40] and DS ViewerPro 5.0 (Accelrys) software.

Aspects of molecular mobility

A monomeric peptide the size of B18 is expected to exhibit considerable mobility in a liquid-crystalline bilayer,[25,41,42] besides the long-axial rotation around the membrane normal that is taken for granted here. In order to take into account any librational motions within the peptide backbone and any wobble of the entire secondary structure element in the bilayer,[25] we introduced an isotropic molecular order parameter S_{mol}. In our calculations the effect of $0 < S_{mol} < 1$ leads to a proportional reduction of all three principal CSA tensor elements towards the isotropic chemical shift value of 4F-Phg.[25] A second order parameter S_{Phg} is introduced to account for the local 4F-Phg side-chain mobility. It is known that the energy barrier for phenyl rotation can vary significantly in organic molecules [e.g. 0.23–226.5 kcal mol^{-1} (1 kcal = 4.184 kJ)].[43] In a folded peptide structure, rotation of the 4F-Phg side-chain may be restricted to different degrees, depending on the environment. As illustrated by Fig. 1, a helical backbone conformation gives the 4F-Phg side-chain a restricted rotational freedom about χ_1 within a relatively flat and broad potential well. This motion does not affect the position of the ^{19}F label, but the degree of averaging and the choice of χ_1 have significant impact on the effective magnitude of the CSA tensor and its alignment with respect to the peptide backbone. We therefore describe a restricted rotation around C_α—C_β by the side-chain order parameter S_{Phg}, which accounts for a partial averaging of the δ_{11} and δ_{33} components of the static CSA tensor (see Fig. 2). An immobile phenyl ring would correspond to $S_{Phg} = 1$, while unrestricted rotation with $S_{Phg} = 0$ would yield an axially symmetric CSA tensor.

In the structure analysis an entire family of r.m.s.d. maps was thus systematically constructed from the ^{19}F NMR data as a function of both S_{mol} and S_{Phg}, and the lowest minimum of all was considered the best solution. Even though the separate treatment of isotropic peptide wobble and axially restricted side-chain rotation introduces one additional degree of freedom in the data analysis, the extra parameter does not generate false positives if the r.m.s.d. maps are cautiously interpreted. That is because S_{mol} and S_{Phg} have a qualitatively similar effect on the CSA tensor for reasonable values $0 < S < 1$, as both of them act most strongly on δ_{11} and δ_{33}.

RESULTS

Structural assumptions

Like many other fusion peptides, B18 exhibits a pronounced conformational plasticity, which raises the question as to which structure is biologically relevant in the membrane-bound state. Depending on the experimental conditions (concentration, solvent composition, pH, presence of divalent cations, detergent micelles, type of lipid, etc.), the peptide changes its aggregation state (monomer, or self-assembled amyloid fibril) and conformation (random coil, α-helix or β-sheet).[31–33,44] The ^{1}H NMR structure of B18 in membrane-mimicking environments such as 30% TFE, SDS or DPC micelles shows two separate α-helical segments.[32] The pronounced break in the central histidine-rich motif proved to be a flexible hinge. Its position is clearly visible in Fig. 3, where the chemical shifts of the H_α protons are depicted by their difference with respect to the random coil values from the literature. From our previous NOE analysis, the N-terminal α-helix was unambiguously defined over the segment L105–L110. The C-terminal segment N115–A118 was also found to be α-helical, but showing in some of the calculations features of a 3_{10}-helix. No contacts were observed between the two helical parts in the high-resolution NMR study of B18. Therefore, in the present solid-state ^{19}F NMR analysis we treat the two N- and C-terminal segments of the peptide as two mutually independent structural units.

To resolve the three-dimensional membrane-bound structure of B18 by solid-state ^{19}F NMR, nine peptide analogues were synthesized.[24] Each one contains as a single ^{19}F label the non-natural amino acid 4F-Phg, which preserves the amphiphilicity profile of the peptide when substituted for a hydrophobic amino acid.[24,25] The positions of these labels allowed us to address significant regions throughout the full length of the peptide, as illustrated by the framed areas in Fig. 3. Each of the two helical parts of B18 contains three consecutive labeling sites (L105, L106, L107 and L116, L117, A118), one 4F-Phg residue is situated near the flexible hinge (L110) and one label each is located at the N- and C-terminal positions (L103 and I120). In addition to trying to determine the alignment of the two representative tripeptide units constructed as ideal α-helices, we also considered the possibility of these segments adopting either a β-sheet or 3_{10}-helical conformation. If any one of these models were

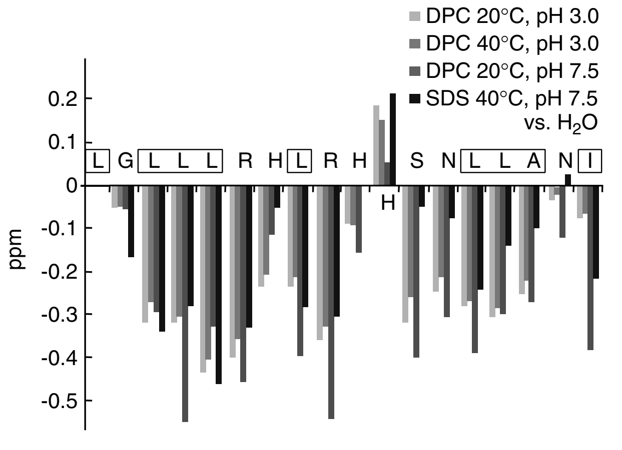

Figure 3. High-resolution ^{1}H NMR data adapted from Ref. 32, demonstrating the isotropic Hα chemical shifts of the wild-type B18 peptide in detergent micelles under various conditions. The values for the deprotonated histidines (above pH 7) are corrected for the corresponding shifts.

Copyright © 2004 John Wiley & Sons, Ltd.

compatible with the experimental data, the labeling scheme allowed us to find out whether the corresponding secondary structure element is extended towards the respective N- and C-terminus or the hinge region.

^{19}F NMR spectra of the membrane-bound peptides

To study reconstituted membrane systems, it is essential to choose an appropriate peptide concentration. Hydrophobic sequences have a high tendency to aggregate and may change their conformational and functional state, as was observed for B18, which can self-assemble as an inactive β-sheet amyloid fibril.[44] Therefore, a sufficiently low peptide concentration is essential to preserve it in a non-aggregated functional state, while the NMR sensitivity calls for the highest amount possible. Fortunately, ^{19}F labels are sensitive enough to examine lipid : peptide ratios over a range from 3000 : 1 to 8 : 1.[23,26] The spectra of B18 showed that it aggregated severely in the membrane below a lipid : peptide ratio of 100 : 1, even though the lipids were highly oriented according to ^{31}P NMR. Peptide aggregation was also associated with sample aging. Above 100 : 1, however, the fresh samples were well oriented and homogeneous, indicating that B18 assumes a unique orientation in liquid-crystalline DMPC–DMPG (80 : 20) bilayers.

The representative ^{19}F NMR spectra shown in Fig. 4 consist of a single narrow resonance (linewidth 400–900 Hz), whose frequency $\nu(\theta)$ is modulated by the sample tilt angle θ according to $(3\cos^2\theta - 1)/2$. Such simple anisotropic behavior indicates that the peptide undergoes fast motional averaging around the membrane normal.[22,25,41] When the oriented sample is aligned with its normal either parallel ($\theta = 0°$) or perpendicular ($\theta = 90°$) to the external magnetic field, the uniaxially averaged CSA tensor is defined by the two respective resonance frequencies $\nu_\parallel$ and $\nu_\perp$, which are summarized in Table 1. The respective isotropic chemical shifts ν_{iso} were calculated for each labeled position, together with the corresponding anisotropy parameters $\Delta^{obs} = \nu_\parallel - \nu_{iso}$. It is known that the isotropic chemical shifts of ^{19}F substituents vary to some extent with the chemical and solvent environment, hence the deviations seen here are not surprising (e.g. of the N-terminal amino acid that is not engaged in another peptide bond). To achieve the highest possible accuracy in our data analysis of ± 1 ppm, we explicitly take this variation into account by referring to the chemical shift differences Δ^{obs} rather than the absolute frequencies $\nu_\parallel$ and $\nu_\perp$. We also note that the same data could in principle also be obtained from non-oriented powder samples of reconstituted liposomes,[27] but the oriented samples provide much higher sensitivity and accuracy.

^{19}F CSA tensor elements in 4F-Phg

Owing to the symmetry of the 4F-substituted phenyl ring, the principal axis system of the static CSA tensor is unambiguously positioned in the aromatic framework,[22,25] as shown in Fig. 2(a). A previous study on 4F-Phg had been carried out on a β-sheet peptide,[25] but not in an α-helix. Therefore, to obtain statistically relevant starting values for the structure analysis, we determined the principal CSA axis

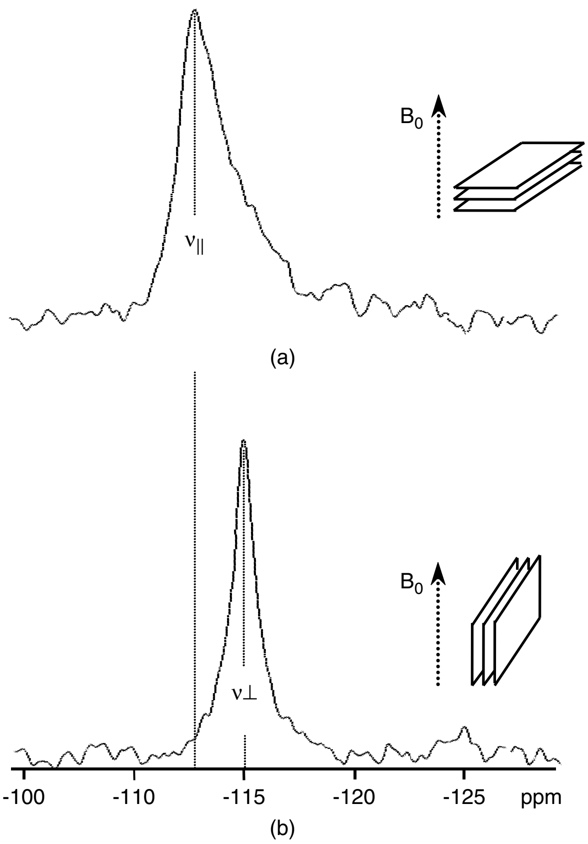

Figure 4. Representative solid-state ^{19}F NMR spectra of the ^{19}F-labeled analogue B18–L106 embedded in uniaxially oriented DMPC–DMPG membranes with a B18–L106 : DMPC : DMPG molar ratio of 1 : 120 : 30. The sample is aligned with its normal either parallel (a) or perpendicular (b) to B_0, yielding a linewidth at half height of 952 and 388 Hz, respectively. About 250 nmol of peptide were used, with an NMR acquisition time of 80 min (ca 2000 transients).

values from the lyophilized powders of most of the labeled B18 analogues, as summarized in Table 1. The static tensor elements of all 4F-Phg labels are rather similar, hence the subsequent data interpretation was based on the following values: $\delta_{11} = -60.1 \pm 2.2$ ppm, $\delta_{22} = -124.3 \pm 0.3$ ppm and $\delta_{33} = -155.3 \pm 1.2$ ppm, corresponding to a mean isotropic value of $\delta_{iso} = -113.2 \pm 2.2$ ppm.

An important aspect in the structure analysis of B18 concerns the question whether the 4F-Phg side-chains are able to rotate freely around the C_α—C_β bond, as this would eliminate the need to set the side-chain torsion angle χ_1 to any preferred mean value. Free rotational averaging of the phenyl ring alone would yield an axially symmetric tensor defined by $\delta_\perp = (\delta_{11} + \delta_{33})/2 = -107.7$ ppm and $\delta_\parallel = \delta_{22} = -124.3$ ppm, with a residual CSA anisotropy of $\Delta^{rot} = \delta_\parallel - \delta_{iso} = -11.1$ ppm. Being placed into a liquid-crystalline lipid bilayer, long-axial diffusion of the peptide around the bilayer normal will lead to further motional averaging of the effective CSA tensor by up to a factor of 2, depending on its alignment with respect to the membrane normal. Therefore, if free phenyl rotation occurs, the expected values of $\Delta^{obs} = \nu_\parallel - \nu_{iso}$ would be restricted

Copyright © 2004 John Wiley & Sons, Ltd.

Table 1. Experimentally determined ^{19}F NMR chemical shifts of the different 4F-Phg-labeled B18 analogues[a]

Synthetic B18 peptide analogues		Lyophilized powder			Oriented membranes			
Sequence	Name	δ_{11} (ppm)	δ_{22} (ppm)	δ_{33} (ppm)	$\nu_{\parallel}$ (ppm)	$\nu_{\perp}$ (ppm)	ν_{iso} (ppm)	Δ^{obs} (ppm)
[4F-Phg]-GLLLRHLRHHSNLLANI	B18–103 (Leu/4F-Phg)				−115.0	−111.1	−112.4	−2.6
LG-[4F-Phg]-LLRHLRHHSNLLANI	B18–105 (Leu/4F-Phg)	−63.0	−124.5	−154.0	−110.1	−118.0	−115.4	+5.3
LGL-[4F-Phg]-LRHLRHHSNLLANI	B18–106 (Leu/4F-Phg)	−63.0	−124.5	−154.0	−112.7	−115.1	−114.3	+1.6
LGLL-[4F-Phg]-RHLRHHSNLLANI	B18–107 (Leu/4F-Phg)	−59.0	−124.8	−157.0	−116.2	−114.8	−115.3	−0.9
LGLLLRH-[4F-Phg]-RHHSNLLANI	B18–110 (Leu/4F-Phg)				−120.0	−111.1	−114.1	−5.9
LGLLLRHLRHHSN-[4F-Phg]-LANI	B18–116 (Leu/4F-Phg)	−58.7	−124.0	−155.5	−112.6	−116.7	−115.3	+2.7
LGLLLRHLRHHSNL-[4F-Phg]-ANI	B18–117 (Leu/4F-Phg)	−58.6	−124.0	−155.8	−109.0	−118.6	−115.4	+6.4
LGLLLRHLRHHSNLL-[4F-Phg]-NI	B18–118 (Ala/4F-Phg)	−58.5	−124.1	−155.6	−118.2	−113.6	−115.1	−3.1
LGLLLRHLRHHSNLLAN-[4F-Phg]G	B18–120 (Ile/4F-Phg)				−121.3	−111.1	−114.5	−6.8

[a] The static CSA tensor values δ_{11}, δ_{22} and δ_{33} were measured for the peptides in lyophilized powders. Uniaxially oriented membrane samples aligned either parallel or perpendicular to B_0 were used to measure the frequencies $\nu_{\parallel}$ and $\nu_{\perp}$, which define the axially symmetric ^{19}F CSA tensor that is averaged by peptide rotation around the bilayer normal. From these values the isotropic chemical shift ν_{iso} and the anisotropy parameter $\Delta^{obs} = \nu_{\parallel} - \nu_{iso}$ were calculated.

to lie between +5.5 ppm (downfield of ν_{iso}) and −11.1 ppm (upfield). To find out whether the 4F-Phg side-chains rotate freely in B18, we collected and compared the observed tensor anisotropies $\Delta^{obs} = \nu_{\parallel} - \nu_{iso}$ of 21 different B18 analogues, including epimers[24] and doubly labeled peptides in oriented membranes. The values of Δ^{obs} were repeatedly found to be wider than or near the limit of Δ^{rot} that would remain accessible after free phenyl rotation (see Table 1, e.g. B18–105 and B18–117). Hence we conclude that the 4F-Phg side-chains cannot rotate freely in this lipid–peptide system.

A restricted rotation of the phenyl ring, on the other hand, would only lead to partial narrowing of Δ^{static} by a concerted shift of δ_{11} and δ_{33} towards $\delta_{\perp}$, which we quantify by the side-chain order parameter S_{Phg}. By assuming a uniform S_{Phg} for all labeled positions, the desired alignment of the partially averaged CSA tensor in the membrane is accessible. Also in this scenario, long-axial rotation of the peptide about the membrane normal leads to further motional narrowing and make the effective CSA tensor axially symmetric under all circumstances. Hence the observed range of chemical shifts becomes rather narrow, and it was essential to apply careful chemical shift referencing to minimize susceptibility-induced errors in the oriented samples.[23,26] For this reason, we recorded both $\nu_{\parallel}$ and $\nu_{\perp}$ to obtain Δ^{obs} accurately within ±1 ppm, as opposed to measuring only $\nu_{\parallel}$ and relying on the isotropic chemical shift δ_{iso} that had been deduced as a mean value from the static CSA tensors.

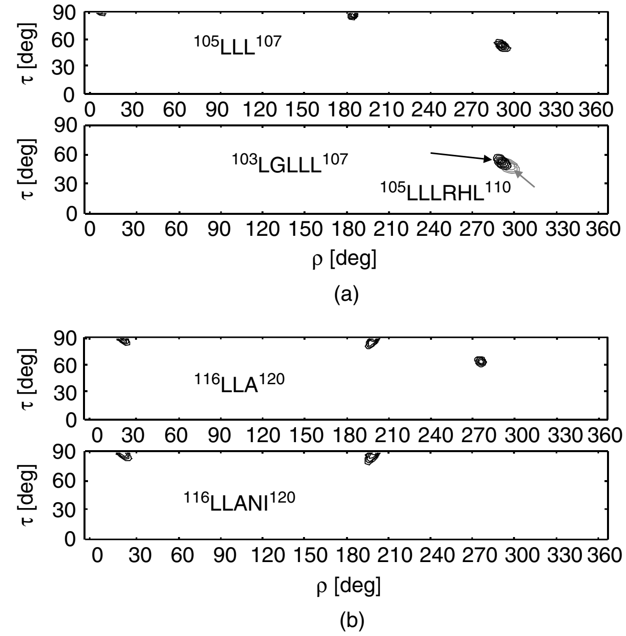

Figure 5. Contour plots of the r.m.s.d. between the experimental and predicted chemical shifts when the α-helical peptide segment is systematically rotated about τ and ρ. The minimal tripeptide of the N-terminal part of B18 in (a), upper panel gives two minima, but the longer sequences with additional orientational constraints shown underneath provide a unique solution in τ and ρ. The overlapping regions provide good evidence that the N-terminal α-helix extends from L103 all the way to L110. The C-terminal part (b) was analyzed correspondingly. Contour lines are spaced with 0.2 ppm and shown for r.m.s.d. below 1.2 ppm.

Determination of peptide conformation and alignment

The alignment of a secondary structure element of B18 with respect to the membrane normal is defined by its tilt angle τ and azimuthal rotation angle ρ (see Fig. 2). The best-fit values are found as an r.m.s.d. minimum between the set of observed chemical shifts and the frequencies predicted for the respective geometry[22] (as illustrated in Fig. 5). Table 2 summarizes the results of the r.m.s.d. analysis that was performed for three types of hypothetical secondary structures (ideal α-helix, β-sheet, 3_{10}-helix), fitted to three, four or five orientational constraints. The absolute r.m.s.d. values contain useful information, as a deviation of more than 1 ppm in the predicted chemical shifts would be readily discernible by eye. These calculations clearly favor the α-helical model over the other hypothetical conformations.

Copyright © 2004 John Wiley & Sons, Ltd.

Table 2. Calculated structural and dynamic parameters for the N- and C-terminal peptide segments containing three, four or five labeled sites, when modeled with different secondary structures (α-helix, β-sheet, 3_{10}-helix)[a]

Sequence stretch	r.m.s.d.	S_{mol}	S_{Phg}	$\tau(^\circ)$	$\rho(^\circ)$
N-terminal segment—					
	α-Helix				
	(0.04)	(0.3)	(0.8)	(83.5)	(13.7)
^{105}LLL^{107}	**0.01**	**0.6**	**0.4**	**60.2**	**−72.6**
^{103}LGLLL^{107}	**0.48**	**0.9**	**0.2**	**48.6**	**−64.2**
^{105}LLLRHL^{110}	**0.08**	**0.9**	**0.3**	**53.0**	**−69.1**
^{103}LGLLLRHL^{110}	**0.99**	**0.8**	**0.2**	**53.5**	**−66.9**
	β-Sheet				
^{105}LLL^{107}	2.5	—	—	—	—
^{103}LGLLL^{107}	2.97	—	—	—	—
^{105}LLLRHL^{110}	4.07	—	—	—	—
	3_{10}-*Helix*				
^{105}LLL^{107}	0.05	0.7	0.1	35.9	80.6
^{103}LGLLL^{107}	1.49	0.2	0.8	42.6	193.1
^{105}LLLRHL^{110}	1.77	0.4	0.4	46.3	130.1
C-terminal segment—					
	α-Helix				
	(0.2)	(0.8)	(0.35)	(112.5)	(95.0)
^{116}LLA^{118}	**0.03**	**0.8**	**0.35**	**89.2**	**22.6**
^{116}LLANI^{120}	**0.14**	**0.5**	**0.6**	**91.3**	**19.3**
^{110}LRHHSNLLA^{118}	1.42	1.0	0.4	118.2	100.0
	β-Sheet				
^{116}LLA^{118}	2.4	—	—	—	—
^{110}LRHHSNLLA^{118}	15.22	—	—	—	—
^{116}LLANI^{120}	5.07	—	—	—	—
	3_{10}-*Helix*				
^{116}LLA^{118}	0.02	0.5	0.35	42.8	50.4
^{110}LRHHSNLLA^{118}	3.04	—	—	—	—
^{116}LLANI^{120}	4.66	—	—	—	—

[a] The tilt angle τ and the azimuthal rotation ρ describe the alignment of the respective secondary structure element in the membrane. The molecular order parameter S_{mol} accounts for global peptide wobble and the 4F-Phg side-chain order parameter S_{Phg} quantitates the degree of partial phenyl averaging about Cα—Cβ. The lowest r.m.s.d.s are obtained for the α-helical conformation, being the only structure that yields self-consistent solutions (bold font) for each of the segments with increasing length. Of the two minima that are observed for the α-helical conformation modeled with three constraints (see Fig. 5), the parameters corresponding to the inappropriate minimum with the higher r.m.s.d. are included in parentheses.

It is, in fact, obvious that the peptide structure is not compatible with a β-sheet conformation in either the N- or C-terminus, not even as tripeptide segments. This is evident from the raw ^{19}F NMR data, since every $i+2$ residue in a β-sheet is aligned the same way and should give rise to nearly identical resonance frequencies, which is not observed. For the case of a 3_{10}-helical conformation, the r.m.s.d. values are worse than for an α-helix, and the 3_{10}-helical H-bonding pattern would also be less favorable, especially in a hydrophobic membrane environment. These arguments suggest that both segments of B18 assume an α-helical structure, in good agreement with the ^{1}H NMR study in solution.

When modeled as an α-helix, the tripeptide segments L105–L106–L107 [top panel in Fig. 5(a)] and L116–L117–A118 [upper panel in Fig. 5(b)] show two minima each (with $[\rho, \tau] = [180 + \rho, 180 - \tau]$). By including one or two additional labeled positions in the analysis, only one of the respective minima remains [lower panels in Fig. 5(a) and (b)]. These unique solutions thus define the most likely alignment of the contiguous stretch of eight amino acids in the α-helical N-terminus of B18 [L103–L110, lower panel in Fig. 5(a)] and of five consecutive amino acids in the α-helical C-terminus [L116–I120, lower panel in Fig. 5(b)]. It is interesting that any attempt to define residue L110 as a hypothetical part of the C-terminal helix did not yield an acceptable r.m.s.d., meaning that the α-helical conformation must be disrupted between L110 and L116. Taken together, all these observations suggest that the structure of the membrane-associated B18 peptide is indeed compatible with (i) an α-helical conformation, (ii) the same helix–break–helix motif as observed by ^{1}H NMR and (iii) well-folded termini (i.e. no frayed ends).

Copyright © 2004 John Wiley & Sons, Ltd.

MRC

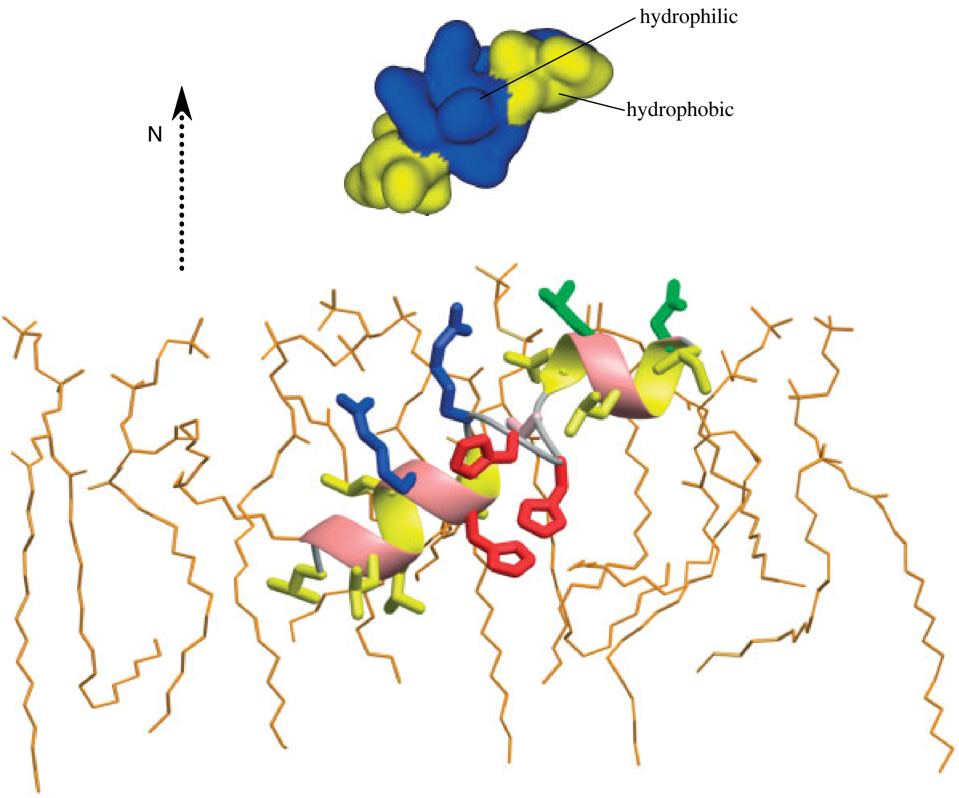

Figure 6. Structural model of the fusogenic B18 peptide in a flat lipid bilayer in the liquid-crystalline state. The illustration of the van der Waals surfaces is colored according to hydrophobicity, and the black arrow denotes the membrane normal. The molecular representation as a ribbon diagram shows hydrophobic amino acids in yellow.

The resulting picture of B18 in the lipid bilayer is illustrated in Fig. 6, suggesting that the peptide binds to the membrane in a 'boomerang'-like fashion. The N-terminal helix is inserted into the lipid bilayer with a tilt angle of $\tau \approx 54 \pm 10°$ (angle between helical axis and the membrane normal), whereas the C-terminal helix is aligned almost parallel to the membrane surface with $\tau \approx 91 \pm 10°$. The azimuthal rotation $\rho \approx -67 \pm 10°$ of the N-terminus and $\sim 19 \pm 10°$ of the C-terminus are consistent with the amphiphilic profile of the membrane, as one would intuitively anticipate. Note that the N-terminal helix is considerably more hydrophobic, especially over the first few residues, than the C-terminal helix that is horizontally bound. The central region of B18, which is presumably unstructured as a hinge, contains several charged or polar amino acids, of which the long arginines may be able to 'snorkel' to the bilayer surface even from a deeper point of immersion.[45]

Motional averaging of the structure

In Fig. 5 we have already moved one step ahead, as the order parameters S_{Phg} and S_{mol} had also been implicitly optimized. It is clear that a blind fit of four variables (τ, ρ, S_{Phg}, S_{mol}) to only three values ($\nu_{\|}$ for three labeled positions) will not give a unique result. However, to evaluate the contributions of restricted side-chain rotation (S_{Phg}) and overall peptide wobble (S_{mol}), we applied the criterion that a reasonable solution for τ and ρ must be found in the range $0 < S < 1$, namely that the r.m.s.d. should not decrease beyond these limiting values of S_{mol} or S_{Phg}. This condition left us with two minima for each of the helical tripeptide segments [upper panels in Fig. 5(a) and (b)]. By repeating the calculation with additional orientational constraints, the elongated peptide segments yielded the same combination of τ and ρ as the tripeptides. This self-consistent solution gives us confidence in the final structural model, also in view of the very reasonable azimuthal rotation angles found.

The optimized molecular order parameters S_{mol} and S_{Phg} shown in Table 2 are 0.8 and 0.2 for the N-terminal helix and 0.5 and 0.6 for the C-terminus, respectively. Very similar peptide structures with almost as low r.m.s.d. are indeed obtained when one order parameter is allowed to increase at the expense of the other. This family of results suggests a significant global wobble of B18 in the membrane and a local mobility of the 4F-Phg side-chains about χ_1, in addition to the long-axial peptide rotation in the liquid-crystalline bilayer. Error analysis shows that τ and ρ are accurate to about $\pm 10°$ for the observed chemical shifts with ± 1.0 ppm. The error introduced by choosing a certain set of backbone torsion angles for an idealized α-helix (allowing ϕ and φ to differ by 7°)[46] is within $\pm 5°$. Allowing a change in χ_1 from 100° to 120° (cf. Fig. 1) translates into an error in τ and ρ below $\pm 10°$.

DISCUSSION

The unusual 'boomerang'-like membrane-association of B18 suggests how this structure may fulfil the two main criteria necessary to induce membrane fusion. An oblique penetration of the peptide into the hydrophobic bilayer core had already been observed by ATR IR spectroscopy.[33]

Copyright © 2004 John Wiley & Sons, Ltd.

The tilted N-terminal helix thus leads to considerable perturbation of the lipid acyl chains, which lowers the energy barrier for merging the monolayers.[10] The amphiphilic C-terminus of B18 is presumably bound at the bilayer surface, as it has been shown to replace water molecules from the lipid headgroups.[33] As a consequence, the hydration repulsion between apposing membranes is decreased, which favors vesicle aggregation and fusion.

Previous studies of various fusion peptides have shown that they often assume an α-helical conformation upon interacting with lipid bilayers.[31,47] Theoretical analysis of their amphiphilic surfaces suggested that they would insert as a continuous helix into the membrane under an oblique angle.[10–12,16] More recently, the fusion peptide derived from the influenza virus hemagglutinin A was found to exhibit a pronounced kink in its ^1H NMR structure in detergent micelles.[48,49] Under the assumption that this helix–break–helix structure would maintain its angled shape, it was docked on to a lipid bilayer and shown to be consistent with the behavior of several ESR labels placed along the peptide sequence.[48] By measuring the tilt angle indirectly via the depth of side-chain penetration into the bilayer, this ESR study thus suggested for the first time a 'boomerang'-like mode of insertion for the influenza fusion peptide. Our ^{19}F NMR study of a different fusogenic peptide has now confirmed the same helix–break–helix motif by directly measuring orientational constraints in a flat lipid bilayer, revealing a similar mode of insertion. Comparing these experimental structural models of two unrelated peptides, it is tempting to speculate that a 'boomerang'-like membrane insertion could be a common functional motif for other fusogenic peptides also.

Acknowledgments

We acknowledge W. Scheiding and M. Dörr for assistance with peptide synthesis and purification, S. Reichard for assistance with fluorescence measurements and S. L. Grage and G. Glabe for fruitful discussions. This research was supported by the Deutsche Forschungsgemeinschaft within SFB196/TPB13 and SFB604/TPB6.

REFERENCES

1. Jahn R, Südhof TC. *Annu. Rev. Biochem.* 1999; **68**: 863.
2. Blumental R, Clague MJ, Durell SR, Epand RM. *Chem. Rev.* 2003; **103**: 53.
3. Jahn R, Lang T, Südhof TC. *Cell* 2003; **112**: 519.
4. Eckert DM, Kim PS. *Annu. Rev. Biochem.* 2001; **70**: 777.
5. Mayer A. *Annu. Rev. Cell Dev. Biol.* 2002; **18**: 289.
6. Martin I, Ruysschaert JM. *Biosci. Rep.* 2000; **20**: 483.
7. Tamm KL, Han X, Li Y, Lai AL. *Biopolymers* 2003; **66**: 249.
8. Tamm LK, Han X. *Biosci. Rep.* 2000; **20**: 501.
9. Durell SR, Martin I, Ruysschaert JM, Shai Y, Blumenthal R. *Mol. Membr. Biol.* 1997; **14**: 97.
10. Pecheur EI, Sainte-Marie J, Bienvenüe A, Hoekstra D. *J. Membr. Biol.* 1999; **167**: 1.
11. Lins L, Charloteaux B, Thomas A, Brasseur R. *Proteins* 2001; **44**: 435.
12. Brasseur R. *Mol. Membr. Biol.* 2000; **17**: 31.
13. Hristova K, Wimley WC, Mishra VK, Anantharamiah GM, Segrest JP, White SH. *J. Mol. Biol.* 1999; **290**: 99.
14. Torres J, Kukol A, Arkin IT. *Biophys. J.* 2000; **79**: 3139.
15. Houbiers MC, Wolfs CJ, Spruijt RB, Bollen YJ, Hemminga MA, Goormaghtigh E. *Biochim. Biophys. Acta* 2001; **1511**: 224.
16. Bradshaw JP, Darkes MJ, Harroun TA, Katsaras J, Epand RM. *Biochemistry* 2000; **39**: 6581.
17. Cross TA. *Methods Enzymol.* 1997; **289**: 672.
18. Castellani F, van Rossum B, Diehl A, Schubert M, Rehbein K, Oschkinat H. *Nature (London)* 2002; **420**: 98.
19. Ketchem RR, Lee KC, Huo S, Cross TA. *J. Biomol. NMR* 1996; **8**: 1.
20. Gerig JT. *Prog. Nucl. Magn. Reson. Spectrosc.* 1994; **26**: 293.
21. Ulrich AS. In *Encyclopedia of Spectroscopy and Spectrometry*, Lindon JC, Tranter GE, Holmes JL (eds). Academic Press: London, 2000.
22. Grage SL, Wang J, Cross TA, Ulrich AS. *Biophys. J.* 2002; **83**: 3336.
23. Ulrich R, Glaser RW, Ulrich AS. *J. Magn. Reson.* 2003; **164**: 115.
24. Afonin S, Glaser RW, Berditchevskaia M, Wadhwani P, Gührs KH, Möllmann U, Perner A, Ulrich AS. *ChemBioChem* 2003; **4**: 1151.
25. Salgado J, Grage SL, Kondejewski LH, Hodges RS, McElhaney RN, Ulrich AS. *J. Biomol. NMR* 2001; **21**: 191.
26. Glaser RW, Ulrich AS. *J. Magn. Reson.* 2003; **164**: 104.
27. Mesleh MF, Valentine KG, Opella SJ, Louis JM, Gronenborn AM. *J. Biomol. NMR* 2003; **25**: 55.
28. Yamaguchi S, Hong T, Waring A, Lehrer RI, Hong M. *Biochemistry* 2002; **41**: 9852.
29. Hofmann A, Glabe CG. *Semin. Dev. Biol.* 1994; **5**: 233.
30. Vacquier VD, Swanson WJ, Hellberg ME. *Dev. Growth Differ.* 1995; **73**: 1.
31. Ulrich AS, Otter M, Glabe D, Hoekstra D. *J. Biol. Chem.* 1998; **273**: 16 748.
32. Glaser RW, Grüne M, Wandelt C, Ulrich AS. *Biochemistry* 1999; **38**: 2560.
33. Binder H, Arnold K, Ulrich AS, Zschörnig O. *Biochim. Biophys. Acta* 2000; **1468**: 1345.
34. Grage SL, Ulrich AS. *J. Magn. Reson.* 1999; **138**: 98.
35. Grage SL, Ulrich AS. *J. Magn. Reson.* 2000; **146**: 81.
36. Massiot D, Fayon F, Capron M, King I, Le Calvé S, Alonso B, Durand JO, Bujoli B, Gan Z, Hoatson G. *Magn. Reson. Chem.* 2002; **40**: 70.
37. Levitt MH, Freeman R. *J. Magn. Reson.* 1979; **33**: 473.
38. Freeman R, Kempsell SP, Levitt MH. *J. Magn. Reson.* 1980; **38**: 453.
39. Morris AL, MacArthur MW, Hutchinson EG, Thornton JM. *Proteins* 1992; **12**: 345.
40. Koradi R, Billeter M, Wüthrich K. *J Mol Graphics* 1996; **14**: 51.
41. Yamaguchi S, Huster D, Waring A, Lehrer RI, Kearney W, Tack BF, Hong M. *Biophys J.* 2001; **81**: 2203.
42. Han X, Steinhauser DA, Wharton SA, Tamm LK. *Biochemistry* 1999; **38**: 15 052.
43. Khare R, Paulaitis EA. *Macromolecules* 1995; **28**: 4495.
44. Ulrich AS, Tichelaar W, Forster G, Zschörnig O, Weinkauf S, Meyer HW. *Biophys J.* 1999; **77**: 829.
45. Killian AJ, von Heijne G. *Trends Biochem. Sci.* 2000; **25**: 429.
46. Kim S, Cross TA. *Biophys. J.* 2002; **83**: 2084.
47. Schanck PJ, Lins L, Brasseur R. *J. Theor. Biol.* 1999; **198**: 173.
48. Han X, Bushweller JH, Cafiso DS, Tamm LK. *Nat. Struct. Biol.* 2001; **8**: 715.
49. Hsu CH, Wu SH, Chang DK, Chen C. *J. Biol. Chem.* 2002; **277**: 22 725.

Copyright © 2004 John Wiley & Sons, Ltd.

Appendices

D. Publication on PGLa in *Journal of Magnetic Resonance*

Glaser, R. W., C. Sachse, U. H. N. Dürr, P. Wadhwani, A. S. Ulrich

Orientation of the antimicrobial peptide PGLa in lipid membranes determined from ^{19}F-NMR dipolar couplings of 4-CF_3-phenylglycine labels

Journal of Magnetic Resonance **2004**, ***168***, 153-163.

Appendices

Available online at www.sciencedirect.com
SCIENCE DIRECT®
Journal of Magnetic Resonance 168 (2004) 153–163
JMR Journal of Magnetic Resonance
www.elsevier.com/locate/jmr

Orientation of the antimicrobial peptide PGLa in lipid membranes determined from ^{19}F-NMR dipolar couplings of 4-CF_3-phenylglycine labels

Ralf W. Glaser,[a] Carsten Sachse,[a] Ulrich H.N. Dürr,[b] Parvesh Wadhwani,[c] and Anne S. Ulrich[b,c,*]

[a] *Institute of Biochemistry and Biophysics, Friedrich-Schiller-Universität Jena, Hans-Knöll-Str. 2, 07745 Jena, Germany*
[b] *Institute of Organic Chemistry, University of Karlsruhe, Fritz-Haber-Weg 6, 76131 Karlsruhe, Germany*
[c] *Forschungszentrum Karlsruhe, IFIA, POB 3640, 76021 Karlsruhe, Germany*

Received 5 December 2003; revised 2 February 2004

Abstract

A highly sensitive solid state ^{19}F-NMR strategy is described to determine the orientation and dynamics of membrane-associated peptides from specific fluorine labels. Several analogues of the antimicrobial peptide PGLa were synthesized with the non-natural amino acid 4-trifluoromethyl-phenylglycine (CF_3-Phg) at different positions throughout the α-helical peptide chain. A simple 1-pulse ^{19}F experiment allows the simultaneous measurement of both the anisotropic chemical shift and the homonuclear dipolar coupling within the rotating CF_3-group in a macroscopically oriented membrane sample. The value and sign of the dipolar splitting determines the tilt of the CF_3-rotational axis, which is rigidly attached to the peptide backbone, with respect to the external magnetic field direction. Using four CF_3-labeled peptide analogues (with L-CF_3-Phg at Ile9, Ala10, Ile13, and Ala14) we confirmed that PGLa is aligned at the surface of lipid membranes with its helix axis perpendicular to the bilayer normal at a peptide:lipid ratio of 1:200. We also determined the azimuthal rotation angle of the helix, which agrees well with the orientation expected from its amphiphilic character. Peptide analogues with a D-CF_3-Phg label resulting from racemization of the amino acid during synthesis were separately collected by HPLC. Their spectra provide additional information about the PGLa structure and orientation but allow only to discriminate qualitatively between multiple solutions. The structural and functional characterization of the individual CF_3-labeled peptides by circular dichroism and antimicrobial assays showed only small effects for our four substitutions on the hydrophobic face of the helix, but a significant disturbance was observed in a fifth analogue where Ala8 on the hydrophilic face had been replaced. Even though the hydrophobic CF_3-Phg side chain cannot be utilized in all positions, it allows highly sensitive NMR measurements over a wide range of experimental conditions and dynamic regimes of the peptide.
© 2004 Elsevier Inc. All rights reserved.

Keywords: Solid state ^{19}F-NMR; Orientational constraints; Lipid bilayer membrane; Antimicrobial peptide PGLa; 4-Trifluoromethyl-phenylglycine

1. Introduction

Structure analysis of membrane-associated peptides and proteins still presents a challenge to the NMR-spectroscopist, given that isotope labeling is necessary to resolve, assign, and interpret the signals from individual molecular segments. Uniform ^{15}N- or ^{13}C-labeling has the obvious advantage of obtaining all information on a single sample, but the data analysis can be rather demanding [1,2]. On the other hand, there are many instances where a small number of selective labels suffice to reveal the 3D-structure of a peptide together with its alignment and dynamics in the lipid membrane [3–5]. A simple α-helical or rigid β-stranded peptide can be described by three structural parameters only, namely its tilt angle τ, its azimuthal rotation angle ρ, and an order parameter S_{mol} representing its wobble. In such cases it is desirable to obtain the necessary parameters by solid state NMR with the highest possible sensitivity, and with maximum accuracy and experimental ease.

* Corresponding author. Fax: +49-721-608-4823.
E-mail address: anne.ulrich@ifia.fzk.de (A.S. Ulrich).

1090-7807/$ - see front matter © 2004 Elsevier Inc. All rights reserved.
doi:10.1016/j.jmr.2004.02.008

We have recently proposed a selective labeling scheme based on incorporation of the non-natural amino acid 4-fluoro-phenylglycine (4F-Phg) in the place of any hydrophobic amino acid [6]. Because of the high gyromagnetic ratio of the ^{19}F-nucleus, this has the advantage of requiring very little material and measurement time. The idea behind using 4F-Phg is that the fluorine CSA tensor of the stiff aromatic side chain is located in a well-defined position with respect to the peptide backbone. Its anisotropic chemical shift in a macroscopically aligned membrane sample can thus be directly translated into the individual side chain orientation. From three or more such orientational constraints the overall peptide structure and tilt angle can then be calculated. The only input required for such analysis is the peptide secondary structure (i.e., a postulated model structure may thus be confirmed or rejected), and the side chain torsion angle of 4F-Phg about the C_α–C_β bond needs to be known. In a number of previous membrane-bound peptide structures that were successfully resolved, namely of the antimicrobial gramicidin S and the fusogenic B18 [5,7], the most ambiguous assumption concerned the exact value of this torsion angle. That is because molecular modeling showed the bulky 4F-Phg side chain to prefer different torsion angles depending on both its local environment and the global secondary structure [7,8]. In addition to this source of error it may be difficult to extract the accurate chemical shift values of 4F-Phg: not only is there no easy ^{19}F-NMR referencing procedure available, but bulk magnetic susceptibility effects may furthermore lead to intrinsic lineshifts and broadenings in macroscopically oriented samples. We have recently demonstrated that errors up to 10 ppm may arise if these effects are not taken into account [9,10].

Here, we suggest a more convenient and robust strategy for peptide structure analysis, combining the high sensitivity of ^{19}F-NMR with virtually non-disturbing side chain labeling. Instead of a single fluorine reporter as in 4F-Phg, a trifluoromethyl-group is introduced via the side chain of 4-CF_3-phenylglycine. A simple 1-pulse experiment yields a triplet signal, whose splitting represents the anisotropic intramolecular dipolar coupling within the CF_3-group [11]. As this value is accurately obtained (with no need for chemical shift referencing) it can then be directly translated into the desired side chain alignment. The indispensable sign of the dipolar splitting is available from the anisotropic chemical shift, which moves the triplet signal the same way as the dipolar coupling is being scaled. Another potential advantage of the labeling scheme introduced here, lies in the possibility to extract two orientational constraints about the same peptide plane by analyzing both the L- and D-enantiomer of the 4-CF_3-Phg label.

To illustrate and verify this new dipolar ^{19}F-NMR approach experimentally, we have chosen the antimi-

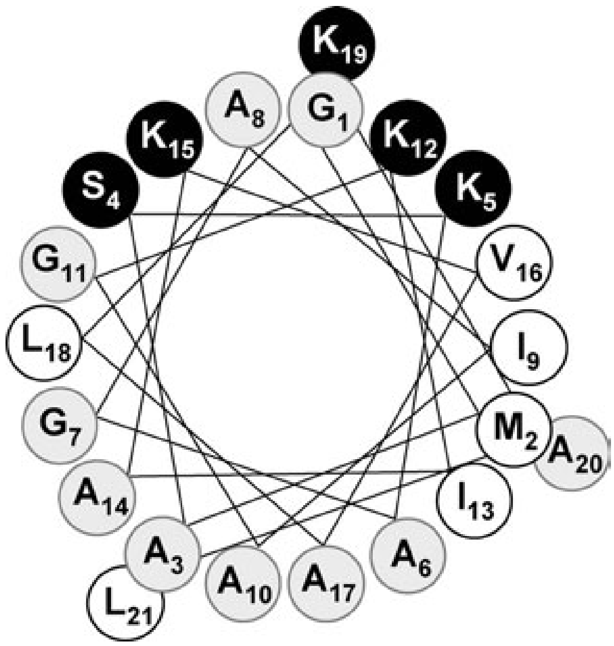

Fig. 1. Helical wheel representation of PGLa with hydrophilic residues in black and hydrophobic residues in white.

crobial peptide PGLa, which has a well-characterized α-helical structure in lipid model membranes and detergent micelles [12,13]. Previous solid state NMR studies on a series of selectively ^{15}N-labeled samples have demonstrated that the helix axis is aligned parallel to the membrane surface ($\tau = 90 \pm 30°$), as expected from its amphiphilic character. Even though the azimuthal rotation angle ρ was not available from this previous analysis, the distribution of cationic and hydrophobic side chains allows a straightforward prediction of how the peptide should be rotationally positioned within the lipid bilayer (Fig. 1). Our aim of this ^{19}F-NMR study is (i) to judge the potentially disturbing effect of the 4-CF_3-Phg side chain on the PGLa secondary structure and its biological function, (ii) to hopefully verify the peripheral alignment of PGLa and determine its azimuthal rotation angle, (iii) to assess the accuracy of the dipolar ^{19}F-NMR analysis and its potential sources of error, and (iv) to discuss the advantages and disadvantages of this new approach in comparison to established labeling methods that can in principle yield the same results.

2. Materials, methods, and theory

2.1. Peptide synthesis and purification

PGLa (peptidyl-glycylleucine-carboxyamide) and a series of ^{19}F-labeled 4-trifluoromethyl-phenylglycine (CF_3-Phg) analogues were produced the same way as previously reported for 4F-Phg [6]. Within the sequence GMASKAG***AIA***GK***IA***KVALKAL-carboxyamide we

incorporated a single CF_3-Phg at the position of either Ala8, Ile9, Ala10, Ile13, or Ala14. We used a racemic mixture of CF_3-Phg (ABCR, Karlsruhe, Germany). The peptides were synthesized on an Applied Biosystems 433A instrument using standard solid phase Fmoc protocols. The amino acid composition was confirmed by mass spectrometry. The epimers were separated under standard reverse phase HPLC conditions [6]. For each of the five peptide analogues we obtained two clearly separated peaks for the epimers containing L- and D-CF_3-Phg. A second HPLC run with an acetonitrile/water gradient containing 5 mM HCl in the aqueous phase was subsequently performed to remove TFA and avoid any ^{19}F-NMR background, which increased the purity of the peptide to >95%.

2.2. Circular dichroism spectroscopy and antimicrobial activity assays

Circular dichroism spectra were recorded on a Jasco 710 instrument with a 2 mm cuvette in aqueous buffer containing 1 mM NaH_2PO_4/Na_2HPO_4, pH 7.0. To adjust a uniform and accurate peptide concentration for all analogues, UV spectra of both the 1 mg/ml peptide stock solution and the final CD sample were measured. In the stock solution the UV absorption of the CF_3-Phg side-chain at 263 nm was evaluated, and in the CD sample the absorption of the peptide backbone at 190–220 nm was checked. For CD measurements of peptides interacting with model membranes, the lipids (DMPC:DMPG, 60:40) were dissolved and mixed in chloroform/methanol/water, dried under a nitrogen stream, and resuspended in buffer. Small unilamellar vesicles were then produced by ultrasonification. PGLa is virtually fully bound to negatively charged lipid vesicles at low ionic strength when the total negative charge of the lipids exceeds the total positive charges of the peptides [6]. Here we used an 80-fold concentration of negatively charged lipids compared to the concentration of PGLa (25 μM in 2 mm cuvette).

Antimicrobial inhibition assays (both radius of inhibition and MIC determination) were performed as described by Afonin et al. [6].

2.3. NMR sample preparation

For oriented samples a 1:200 peptide:lipid mixture of PGLa and DMPC was prepared and deposited on thin glass slides ($7.5 \times 18 \times 0.08\ mm^3$) as described before [5–7,9]. The peptide (typically 0.25 mg) was dissolved in water, and the lipid in methanol. Both components were mixed to give a 70% methanol solution, and 30 μl drops of the solution were spread onto one side of each glass plate. The membrane films were dried under vacuum, stacked, and hydrated for 2 days at 48 °C in an atmosphere of about 98% relative humidity over a saturated K_2SO_4 solution, such that the membranes spontaneously orient themselves. The stack was immediately wrapped in several layers of parafilm and polyethylene sheet. The quality of orientation of the lipid bilayers was determined with ^{31}P-NMR [14]. Typically 80–90% of the lipid was well aligned between the glass plates.

2.4. Solid state NMR measurements

Measurements were performed on a 500 MHz wide-bore Unity Inova spectrometer (Varian, Palo Alto, CA) with an external 470 MHz high power amplifier (Creative Electronics, Los Angeles, CA) and a ^{19}F/^{1}H double-tuned flatcoil probe (Doty Scientific, Columbia, SC) [5–7,11,15]. Sample and coil can be manually rotated, but usually the layered sample is aligned horizontally such that the membrane normal is parallel to B_o. Due to technical limitations of the probe ^{1}H-decoupling was limited to about 10–15 kHz, which was sufficient to observe the ^{19}F-labeled peptides in liquid crystalline samples.

2.5. ^{19}F–^{19}F dipolar coupling within the CF_3-group

The general lineshapes of CF_3-labeled groups in powder samples and oriented membranes have been discussed previously [11]. To be able to analyze the dipolar splittings quantitatively, we need to know the static coupling constant of 4-CF_3-Phg. This value was estimated from the distance between the fluorine atoms, given an average C–F bond distance of 1.322 ± 0.015 Å in comparable compounds [16]. Assuming an ideal tetrahedral geometry, the F–F distance is $r_{12} = 2.159 \pm 0.024$ Å. The general dipolar coupling

$$\Delta = \left| 3\hbar\gamma_1\gamma_2 \frac{\mu_0}{4\pi} \frac{1}{r_{12}^3} \frac{3\langle\cos^2\theta\rangle - 1}{2} \right|, \quad (1)$$

between static equivalent spins with $\gamma_F = 2.52 \times 10^8$ rad $T^{-1}\,s^{-1}$ thus yields a maximum splitting of $\Delta = 31.7 \pm 1.1$ kHz (for $\theta = 0°$). All measurements that we made with CF_3-labeled groups in solid compounds, in lipid membranes, and in solution, are consistent with the assumption that the three fluorines in the CF_3-group give rise to equivalent signals, i.e. they are in fast chemical exchange on the NMR time-scale. This rotational motion around the three-fold symmetry axis of the CF_3-group has to be taken into account by introducing an order parameter $S_{rot} = -1/2$, which makes the maximum observable splitting $\Delta^0_{CF_3} = 15.8$ kHz. Whether the CF_3-group rotates or undergoes 120° jumps or anything in between, does not make a difference. We had previously measured the maximum splitting $\Delta^0_{CF_3}$ within a related aromatic CF_3-group to be about 16 kHz [11], and the corresponding dipolar splitting within a CF_2-segment was reported as 15.5 kHz [17,18].

In an oriented sample (aligned with its normal parallel to B_0) the experimentally observed dipolar splitting Δ_{CF_3} depends directly on the time-averaged value of the angle θ between the CF_3-axis and the membrane normal:

$$\Delta_{CF_3} = \left| \frac{3\langle \cos^2\theta \rangle - 1}{2} \right| \Delta^0_{CF_3}. \quad (2)$$

The time-averaged term $\langle 3\cos^2\theta - 1 \rangle$ results from local oscillations of the side chain and a wobble of the entire peptide within the lipid bilayer. If we approximate these modes as fast isotropic motions, we may then summarize the overall effect of motional averaging by a generalized molecular order parameter $1.0 \geqslant S_{mol} \geqslant 0$, to get

$$\Delta_{CF_3} = \left| \frac{3\cos^2\theta - 1}{2} \right| S_{mol} \times \Delta^0_{CF_3}, \quad (3)$$

where θ is now the effective orientation of the CF_3-axis (which is equivalent to the C_α–C_β bond vector in CF_3-Phg). Note that the dipolar splitting of a horizontally aligned sample cannot tell whether the peptide is undergoing rotation around the membrane normal, as this will only be revealed when the sample is measured at a different tilt angle.

2.6. Determining the sign of the dipolar coupling

When the CF_3-label on the peptide is aligned parallel to the membrane normal ($\theta = 0°$) the maximum dipolar splitting is observed in the triplet signal [11]. As θ approaches the magic angle, the splitting becomes zero, and for $\theta > 54.7°$ it increases again but with a negative sign. Thus any dipolar splitting $|\Delta_{CF_3}| < ((1/2)S_{mol} \times \Delta^0_{CF_3})$ will yield two solutions for the angle θ, one for positive and one for negative dipolar couplings. The sign of a dipolar coupling cannot be measured from the splitting [19], but is readily deduced from the anisotropic chemical shift of the oriented sample. Due to the rotation of the three equivalent fluorine atoms, the ^{19}F CSA tensor is axially symmetric, and the anisotropic chemical shift is also a function of $\cos^2\theta$. Therefore, we could in principle also use the anisotropic chemical shift alone to determine θ, but this is more problematic in view of the need for chemical shift referencing and bulk magnetic susceptibility effects [9,10]. Consequently, we recommend to determine θ accurately from the dipolar splitting, and to use the chemical shift of the triplet signal only to resolve the degeneracy between tilt angles θ above and below the magic angle.

The principal axis values of the CSA tensor of a rotating CF_3-group are not available from the literature but can be estimated from our samples. We found that the most deshielded value lies along the rotational axis. This was concluded from the ^{19}F-NMR spectra of the PGLa-10D-CF_3-Phg analogue in oriented samples, which showed a dipolar splitting of about 11 kHz with a chemical shift of −38 ppm for the central peak of the CF_3-triplet, while the isotropic chemical shift was at −63 ppm. According to Eq. (3), any splitting above 8 kHz can only arise from orientations $0° \leqslant \theta \leqslant 35.3°$. Therefore, anisotropic chemical shifts downfield of the isotropic value correspond to $0° \leqslant \theta \leqslant 54.7°$, and upfield shifts correspond to $54.7° < \theta \leqslant 90°$. We thus define the signed dipolar splitting $\Delta^0_{CF_3}$ to be positive for downfield and negative for upfield chemical shifts, so that from Eq. (3) we get

$$\theta = \arccos\sqrt{\frac{2\Delta_{CF_3}}{3S_{mol}\Delta^0_{CF_3}} + \frac{1}{3}}. \quad (4)$$

The sign of Δ_{CF_3} is the true sign of the dipolar coupling, as the negative sign of the dipolar coupling constant and the negative sign of the rotational order parameter S_{rot} compensate each other [20].

2.7. Determining the orientational constraints

To describe the alignment of PGLa, we defined a molecular frame in which the z-axis is the helix axis of the peptide and the C_α atom of Lys12 lies radially on the y-axis. The helix tilt angle, τ, and the azimuthal rotation of the helix, ρ, define a set of Euler angles $\{0, \tau, \rho\}$ that describes the orientation of the molecule in the laboratory frame, i.e., in the oriented membrane sample. The relative arrangement of the individual labeled CF_3-groups in the molecular frame is given by the assumed molecular model structure. The signed dipolar couplings Δ_{CF_3} of these individual labels are predicted as a function of τ, ρ, and S_{mol}. For all labeled positions, the sum of squared deviations to the experimentally determined couplings, χ^2, is then minimized by a grid search in the region $0 \leqslant \tau < 180°$, $0 \leqslant \rho < 180°$, and $0.5 \leqslant S_{mol} \leqslant 1$. The calculations were done with MATHEMATICA (http://www.wolfram.com), structures were modeled with SYBYL (Tripos, St. Louis, MO) and visualized with MOLMOL [21]. Further details of the procedure are described on our website http://www-ifia.fzk.de/IFIA_Webseiten/Webseiten_Ulrich/index.html, where programs and other scripts that were used for the calculation are publicly available.

3. Results and discussion

3.1. Effect of the CF_3-phenylglycine side chain on peptide properties

It is essential for our investigation that the introduction of a CF_3-label into the PGLa molecule does not change its structural or functional properties. Therefore, we compared the secondary structure of the various labeled PGLa analogues with the wild type peptide by

circular dichroism spectroscopy (CD), and we determined their antimicrobial activities against various strains of bacteria.

Circular dichroism spectra of the peptides were acquired in the presence of negatively charged DMPC/DMPG vesicles (Fig. 2). Its interaction with the lipid membrane transforms the peptide from a random coil conformation to a helical structure. For wild type PGLa and most of the analogues we found a helix content of about 50–60%, in agreement with earlier studies [12]. It did not differ significantly for the analogues with either L- or D-CF_3-Phg labels (Table 1). However, an accurate determination of the helical content depends critically on the peptide concentration in the solution. While the concentration of the labeled peptides could be determined rather exactly from UV absorption of the aromatic ring at 263 nm, this was not possible for the wild type peptide. The apparent difference between wild type PGLa and the labeled peptides is therefore not really significant.

Interestingly, a considerable reduction in helical content was observed for the L- and D-epimers labeled at position Ala8. These peptides also exhibited a visibly

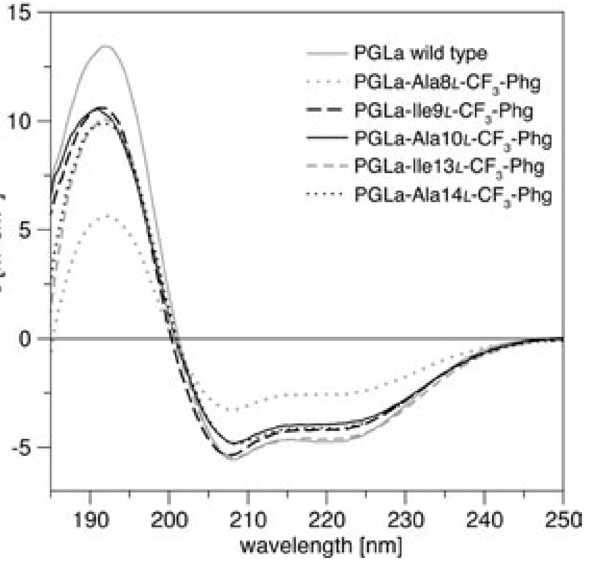

Fig. 2. Circular dichroism spectra of wild type PGLa and its analogues labeled with a single L-CF_3-Phg in position 8,9,10,13, or 14 in the presence of small unilamellar vesicles at a molar ratio of peptide:DMPC:DMPG = 1:120:80.

Table 1
Helix content of PGLa and its CF_3-Phg-labeled analogues (%)

Position/replaced with	L-CF_3-Phg	D-CF_3-Phg
Ala 8	38	19
Ile 9	53	53
Ala 10	48	51
Ile 13	54	48
Ala 14	48	50
Wild type	60	

reduced solubility. In contrast to all other labeled positions, Ala8 is situated on the hydrophilic face of the helix, as illustrated in Fig. 1. The large hydrophobic CF_3-Phg sidechain in this position thus seems to disturb the amphiphilic character of the peptide that is necessary for helix formation. The fact that Ala8 is close to the less structured N-terminal part of PGLa may also contribute to this structural deviation. We had previously observed that the somewhat less hydrophobic fluoro-phenylglycine label in position Ala8 did not disturb the structure to such extent [6].

Antimicrobial activity against 7 Gram-positive and 5 Gram-negative strains of bacteria was tested with agar diffusion assays. Again, PGLa labeled in position Ala8 showed a considerably reduced activity for both L- and D-forms. All other analogues showed an antimicrobial activity similar to wild type PGLa (Fig. 3). Some of the labeled peptides even showed a higher activity than the wild type—in particular the activity of PGLa-10-CF_3-Phg and PGLa-14-CF_3-Phg against two strains of *Pseudomonas aeruginosa* was increased. A similar but less pronounced increase had been previously observed for PGLa-10-fluoro-phenylglycine [6], suggesting that the increased activity is due to the higher overall hydrophobicity of the aromatic side chain in place of Ala. Generally, the D-CF_3-Phg epimers had a lower activity compared to the respective L-CF_3-Phg epimers. Although the differences were small, this was highly significant ($p < 10^{-7}$ in paired t test) for all measurements taken together.

In addition, the minimal inhibitory concentrations of PGLa wild type and the CF_3-Phg analogues were measured for *Escherichia coli* ATCC 25922 and for *Staphylococcus aureus* SG 511 with a standard microbroth dilution method. Between the eight L- and D-analogues

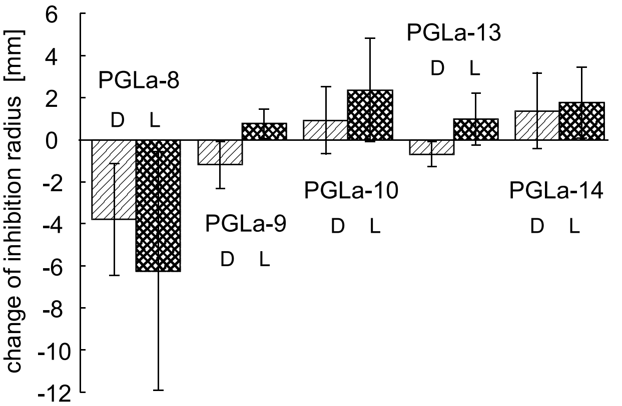

Fig. 3. Effect of the L- and D-CF_3-Phg label on antibacterial activity. Wild type PGLa and its analogues with L- and D-CF_3-Phg in position 8,9,10,13, or 14 were studied by agar diffusion assays. Of the 12 strains of bacteria tested, two were resistant and one gave ambiguous results. For the remaining 9 bacterial strains the average change in the radius of inhibition compared to wild type PGLa is shown together with the standard deviation.

labeled in positions 9,10,13, and 14 and the wild type PGLa the differences in minimal inhibitory concentration were no more than one dilution step of factor 2.

These results justify the use of PGLa analogues with CF_3-Phg labels in positions 9,10,13, or 14 to study the orientation and dynamics of PGLa in the membrane. We did not, however, employ any peptide with a CF_3-Phg label in position 8 for any further experiments.

3.2. Different relaxational behavior of dipolar peaks

The signal of the three equivalent fluorines of the CF_3-group is split into a triplet under the influence of the homonuclear dipolar coupling, which is scaled by fast rotation around the tilted C_ϵ–C_ζ axis and any further molecular wobble. The expected three narrow signals with peak intensities of 1:2:1 are not as well resolved in these samples as they had been previously described for small and highly mobile organic molecules in oriented membranes [11]. In this case of a less mobile peptide, the triplet is always asymmetric with a narrow intense peak near the isotropic chemical shift, and with the broadest peak at the furthest distance away from the isotropic value (Fig. 4). We attribute this asymmetry to a differential transverse relaxation rate of the three signal components, which is modulated by fluctuations of the angle θ between the CF_3-axis and the static magnetic field on the time-scale of the experiment. The anisotropic chemical shift and the homonuclear dipolar coupling in the rotating CF_3-group are both proportional to $3\cos^2\theta - 1$, and at a magnetic field of 11.7 T they have approximately the same magnitude. In one of the three spectral components these two orientation-dependent effects have opposite signs and partially compensate one another. The resonance frequency of this component is therefore close to the isotropic chemical shift value. The central component of the triplet appears at the pure anisotropic chemical shift, as the dipolar contribution is zero. In the third component the two orientation-dependent effects add up, hence the chemical shift of this component depends most strongly on the instantaneous orientation of the CF_3-axis. Consequently, any slow fluctuations in the local tilt angle of the CF_3-group lead to a very different T_2-broadening of the three spectral components. Thus, the observed peak broadening is attributed to slow dynamics rather than insufficient proton decoupling. As we are interested in the orientation-dependence of the signal we cannot make constructive use of this effect. For future analysis of the interaction of a CF_3-group with other nuclei, however, it may be worthwhile considering the development of TROSY experiments [22].

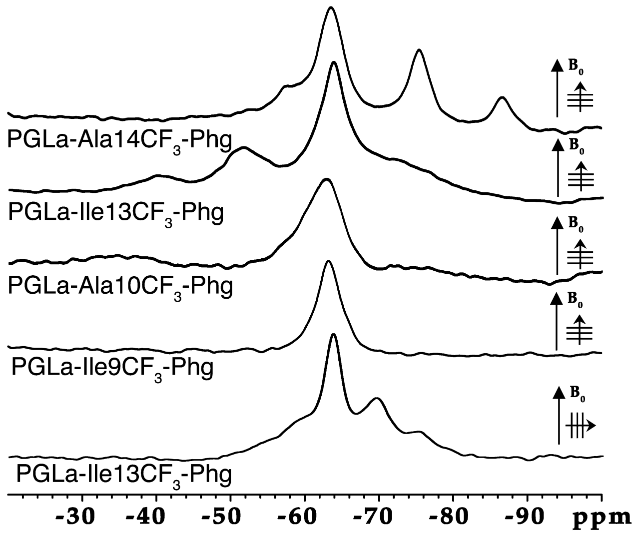

Fig. 4. ^{19}F-NMR spectra of oriented samples of PGLa analogues labeled with L-CF_3-Phg in position 9,10,13, or 14 with a molar ratio of peptide:DMPC = 1:200. 1-pulse spectra were recorded for 1–3 h at 35 °C, with ^{1}H decoupling of 10 kHz. All samples are oriented with the membrane normal parallel to the field, and the PGL-13-CF_3-Phg sample is also shown in the perpendicular orientation. Despite the fast relaxation of some signal components it is possible to read the splitting due to the homonuclear dipolar coupling within the CF_3-group directly from these triplets:

Position replaced with L-CF_3-Phg	Ile 9	Ala 10	Ile 13	Ala 14
Dipolar coupling (kHz)	0	0	5.6	−5.4

In this work, we determined the signed dipolar coupling from a simple NMR experiment with a 90° ^{19}F-pulse followed by continuous wave ^{1}H-decoupling during acquisition. The gap between the ^{19}F-pulse and the start of acquisition was compensated by first order phase correction or backward linear prediction. This experiment was slightly more sensitive than any echo experiment, which gave nearly identical spectra. We also performed CPMG experiments on the CF_3-groups with the oriented peptide samples [11,23,24]. However, these data did not provide any real advantage, as the accuracy of the dipolar coupling was not critical to determine the orientation of the molecule (see below). On the other hand, the CPMG experiments required very accurate optimization of the pulse length, had a lower sensitivity, and for some samples (with broad peaks in the 1-pulse experiment) they failed to show a recognizable signal after several hours of measurement time.

3.3. Orientation of PGLa in the lipid membrane

To determine the alignment of the PGLa molecule with respect to the lipid bilayer in the liquid crystalline state, we had to make certain assumptions concerning its structure and dynamics. In a first approach we assumed that the molecule has a regular α-helical structure. We used a pitch angle $\omega = 99.8°$ between successive residues in the helical wheel and a side chain orientation of $\alpha = 53.2°$ and $\beta = 121.1°$ (see http://www-ifia.fzk.de/IFIA_Webseiten/Webseiten_Ulrich/index.html),

which corresponds to a poly-Ala helix with $\varphi = -58°$ and $\psi = -47°$ as constructed by SYBYL. The effect of all motions namely of the molecule in the membrane and of the side chain within the molecule are approximated by a single isotropic order parameter S_{mol}, which is supposed to scale all dipolar couplings by the same factor. With these assumptions we searched for the molecular orientation $\{\tau, \rho\}$ and order parameter (S_{mol}) that provide the best fit with the experimentally determined dipolar couplings of the four PGLa analogues labeled with L-CF_3-Phg (Fig. 5). We found a global minimum for the sum of squared deviations between experimental and simulated data with $\chi^2 = 0.4\,kHz^2$, which was a very acceptable fit. The corresponding peptide tilt angle of $\tau = 89°$ is in good agreement with previous ^{15}N-NMR data on PGLa [13], and the azimuthal rotation angle $\rho = 106°$ agrees well with the expected alignment of the amphiphilic helix (Fig. 6).

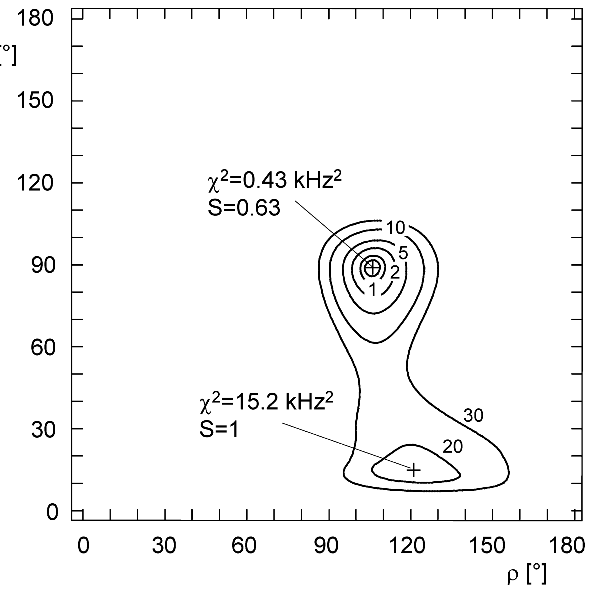

Fig. 5. Fit between the four experimentally measured dipolar splittings (see Fig. 4) and the simulated values that are obtained by systematically rotating the molecule through all possible orientations τ (helix tilt angle) and ρ (azimuthal rotation angle). The molecule is modelled as a regular α-helix with $\omega = 100°$, $\alpha = 53°$, and $\beta = 121°$. For every combination of angles $\{\tau, \rho\}$ the minimum of χ^2 in the complete range of feasible order parameters $0.5 < S_{mol} < 1.0$ is determined and displayed as a contour plot.

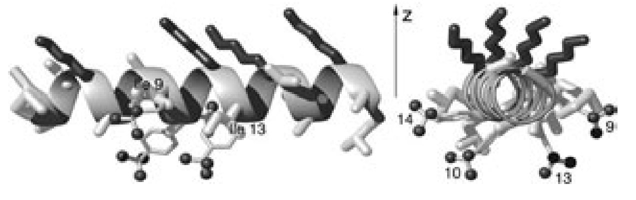

Fig. 6. Regular α-helical model of PGLa in the best fit orientation with $\tau = 89°$, $\rho = 106°$. The charged lysine side chains are shown in dark grey. The z-axis marks the direction of the membrane normal.

The order parameter of $S_{mol} = 0.6$ indicates that the peptide is reasonable mobile in the liquid crystalline lipid bilayer at the low peptide:lipid ratio of 1:200, as seen before for other comparable systems [5,7]. There is only one further local minimum observed ($\tau = 14°$, $\rho = 121°$, $S_{mol} = 1$), but it has a much higher χ^2 deviation of $15.7\,kHz^2$ and can be safely ignored.

In a second approach we constructed the four PGLa analogues with individual L-CF_3-Phg labels as α-helices ($\varphi = -58°$; $\psi = -47°$) and performed a simple energy-minimization to relax the respective local structure and accommodate the bulky L-CF_3-Phg side chains. The orientations of the four C_ϵ–C_ζ axes were again used to determine the overall peptide alignment. With these molecular models we obtained unexpectedly a very good fit for a tilted transmembrane orientation of the helix. This search revealed another minimum for a slightly rotated peripheral orientation although its fit with $\chi^2 = 1.9\,kHz^2$ was not as good (Table 2).

We are able to exclude the unexpected and artefactual solution corresponding to a tilted transmembrane orientation of PGLa, because it is not compatible with the coupling data measured for the corresponding D-CF_3-Phg analogues as discussed below. Nevertheless, the comparison between the different structural models (ideal α-helix versus relaxed conformations) shows that the calculations are sensitive to small changes in the molecular structure. Therefore, we have to consider the effect of any subtle structural changes on the calculation of the molecular orientation very carefully.

3.4. Variation in the model structure

We will now discuss the assumptions made to determine the orientation of the PGLa molecule, and how this result is affected by any deviations from these assumptions.

(a) For the orientational analysis we assume a known molecular structure. It is evident from CD measurements that PGLa assumes a helical structure upon interaction with lipid membranes. High resolution ^1H-NMR studies in micelles have shown that the helix is quite rigid in the central and C-terminal part, while the N-terminus is more flexible [13]. These studies did not provide a sufficiently well-resolved structure that would have allowed us to reliably derive the side chain orientations in the molecular coordinate system. In addition, even though our CD measurements have shown very little changes in helicity, the introduction of a CF_3-Phg label may slightly modify the local structure.

(b) We assume that the hydrophobic CF_3-Phg label has no effect on the orientation of the molecule in the lipid bilayer, when substituted for another hydrophobic side chain. The microbial inhibition assays have indeed shown that the labels do not lead to any principal changes in the interaction of the molecules with the

Table 2
Best fit orientations for various model structures of PGLa

Structure				Orientation			
	ω	α (°)	β (°)	χ^2 (kHz^2)[d]	τ (°)	ρ (°)	S_{mol}
α-Helix, standard[a]	99.8	53.2	121.1	**0.39**	**89**	**106**	**0.63**
α-Helix, energy-minimized[b]	91.7– 98.4	43.6–51.9	109.8–111.6	0.10	29	117	0.85
				1.94	**90**	**119**	**0.57**
α-Helix, adapted[c]	100	47	110	0.51	29	113	0.99
				0.97	**98**	**112**	**0.60**
α-Helix, adapted[c]	96	47	110	**0.08**	**99**	**103**	**0.80**
				5.00	29	108	1.00
3_{10}-Helix[a]	119	53.5	111.2	13.90	43	148	1.00
π-Helix[a]	85.3	52.5	131.1	10.40	82	164	0.84
β-Sheet[a]	178.9	28.3	89.2	53.40	142	40	1.00

The peptide orientation is calculated for structural models with the following sidechain arrangements: [a]Secondary structure of poly-Ala chains as constructed in SYBYL with $\varphi = -58°/\psi = -47°$ (α-helix); $\varphi = -50°/\psi = -28°$ (3_{10}-helix); $\varphi = -57°/\psi = -71°$ (π-helix); and $\varphi = -139°/\psi = 135°$ (β-sheet). [b]α-Helix after 500 steps of energy-minimization. [c]Regular α-helices with slightly modified structure (see text). [d]The global minimum of χ^2 and all local minima with $\chi^2 < 10\,\mathrm{kHz}^2$ are shown.

membrane. A variation in the azimuthal rotation angle ρ by several degrees is rather likely, however, as the different retention times of wild type PGLa and the CF_3-Phg analogues in reverse phase HPLC demonstrate that there exist detectable differences in the hydrophobic surfaces of these molecules.

(c) We assume that the fast molecular motions of the peptide (i.e., its deviations from the effective orientation) are not only isotropic, but also that they are identical at all labeled sites. This is most probably not the case, neither for the motion of the whole molecule in the membrane, nor for the internal motion of the respective side chain within the molecule. Consequently, the dipolar couplings of the individual labels will be averaged to a different extent and cannot all be described by exactly the same order parameter S_{mol}. We have to ignore the effects of such anisotropic and non-uniform dynamic modes, because they cannot be described by any simple model.

These limitations of our model assumptions are the major source of uncertainty, compared to which the experimental errors in the dipolar couplings are less critical for an accurate determination of the molecular orientation. Therefore, we have to validate the data evaluation, by (i) systematically examining the deviations resulting from different assumed conformations, (ii) by introducing an error function that takes additional sources of errors into account, and (iii) by including the D-CF_3-Phg peptide analogues in the analysis.

First, we compared the best fitting orientations for different molecular conformations. Energy-minimization had shown that the side chain angle β of L-CF_3-Phg tends to be reduced compared to a poly-Ala helix, and that the angle between two adjacent residues in the helical wheel is rather variable. Hence, we calculated the orientational fits for a large number of regular α-helical structures with ω between 95 and 102°, and β between 105 and 120°. Steps were small enough (1–5°) to see a smooth shift in the results of the fit. Only two of these datasets are shown in Table 2. The side chain angle α was not varied in this series, but a change of α lead to a change of $-\rho$ by the same amount without affecting the quality of the fit. In addition we evaluated four of these structures after energy-minimization. All α-helical structures, both regular and energy-minimized ones, had a local minimum in the range of $\rho = 100$–$120°$, and $\tau = 88$–$99°$. This indicated an uncertainty in the molecular orientation of about 10–20° resulting from small variations in molecular structure. The uncertainty due to experimental inaccuracy (about ±0.5 kHz) was considerably smaller.

We also examined structures other than α-helix. Even though it is clear that a 3_{10}- or π-helical structure is incompatible with an amphiphilic distribution of side chains in PGLa, we tested whether they would fit the experimental data. For these regular helical structures we obtained minima with rather high χ^2 (Table 2). Nonetheless, after locally adjusting certain side chain orientations by less than 10° accurate fits could be obtained (not shown). A putative β-sheet structure was altogether incompatible with the experimental data. Generally, we found that small changes in the model structure have a large influence on the quality of the best fit. Nevertheless, it is impossible to determine the exact structure of the molecule from these data, as there are too many parameters for fine-adjustment. We can rather hope to find a possible range of orientations for certain groups of structures, thereby, excluding some other groups of structures that are not compatible with the

data. It should be noted that each individual side chain can generally fit the measured dipolar coupling in four different azimuthal orientations ρ for any given set of τ and S_{mol} values. Therefore a "false" structure in a "false" orientation may also happen to fit the experimental data very well.

This first strategy could not account for deviations like variations in peptide alignment as discussed under (b) above. Following a second strategy, therefore, we assigned an estimated error both to the experimentally determined dipolar couplings and to the orientation of each individual side chain, i.e., to the angle between each CF_3-axis and the membrane normal. The deviation χ^2 is normalized on the basis of these error estimates (http://www-ifia.fzk.de/IFIA_Webseiten/Webseiten_Ulrich/index.html). χ^2 is expected to increase with the number of experimental constraints and to decrease with the number of fitted parameters. An objective criterion as to which χ^2 values represent acceptable solutions cannot be stated, because the error estimates are subjective and neither the couplings nor the parameters form sets of independent data. We may consider sets ρ, τ, S_{mol} with $\chi^2 < 10$ as possible solutions and sets with $\chi^2 < 1$ as a good agreement with the experiment. This strategy has several advantages. It allows to assign different error margins to individual labels, and conformational errors are correctly translated into couplings with the $\cos^2$ function. Basically, this second strategy led to the same conclusions as the first one, as shown in Fig. 7A.

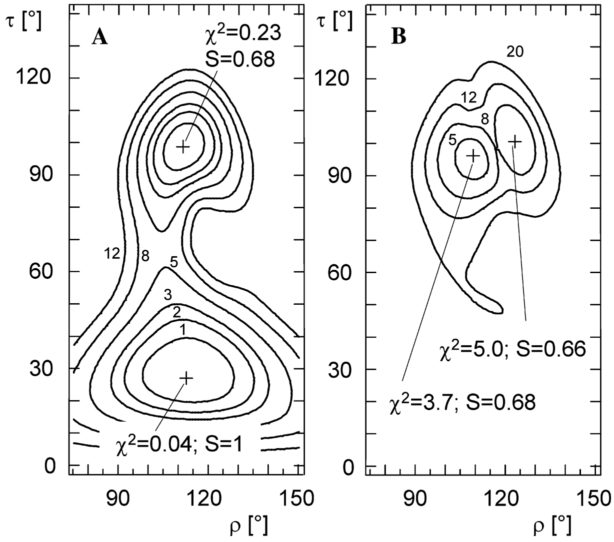

Fig. 7. Fit between the measured and simulated dipolar splittings as a function of τ and ρ for order parameters $0.5 < S_{mol} < 1.0$. In (A) the dipolar couplings of the L-CF_3-Phg labels in position 9,10,13, and 14 are used, while in (B) the couplings of both L- and D-CF_3-Phg labels in these positions are used. In contrast to Fig. 4, $\omega = 99.9°$, $\alpha = 47.3°$ (L) and $-40.1°$ (D), $\beta = 110.7°$ (L) and $70.1°$ (D). χ^2 is normalized to the following scaling factors: all couplings to 0.5 kHz, the angle to the membrane normal to 10° for L- and 20° for D-CF_3-Phg analogues, except for 14L, 9D, and 13D with an additional 5° or 10° uncertainty due to changes of hydrophobic moment.

3.5. Peptide analogues with D-CF_3-phenylglycine

As a by-product of the purification of the labeled all-L-PGLa analogues we had also obtained peptides with a single D-CF_3-Phg side chain. We analyzed their ^{19}F-NMR spectra in DMPC membranes (Table 3) to evaluate their potential for structure analysis. In case they turn out to be reliable sources of information, this would double the number of independent parameters for calculating the overall peptide alignment. To interpret the corresponding data, the local structure of the D-CF_3-Phg label in the molecule has to be known. Major distortions of the α-helical structure are not expected for the following reasons: first, circular dichroism detected no significant reduction of the overall helicity (Fig. 2). Second, by high resolution ^{1}H-NMR we have previously shown that a ^{19}F-labeled amino acid with very similar steric restrictions, D-4-fluoro-phenylglycine, substituted at position Ala10 of PGLa does not cause a local break in the helix [6]. Third, computer modeling shows that in none of the labeled positions in PGLa the D-CF_3-Phg side chain would require major structural rearrangements to relax the surrounding steric contacts. That is, energy-minimization of the D-analogues changed the orientation of the CF_3-axis in the molecule by less than 6° starting from a regular α-helix with $\varphi = -58°$; $\psi = -47°$. On the other hand, a statistical analysis had reported an undisturbed α-helical structure to be quite rare for any D-amino acid situated between two L-amino acids [25]. We also observed a slightly reduced antimicrobial activity for the D-CF_3-Phg analogues compared to the respective L-CF_3-Phg epimers. Taken together, we expect the D-CF_3-Phg side chains to assume a local conformation that does not differ much from an α-helix, but we cannot predict the exact conformational deviation.

As a first observation we note that the dipolar coupling data from the D-CF_3-Phg analogues are not fully compatible with a regular α-helical structure. The best fit has a χ^2 of 26 kHz^2 and gives $\tau = 102°$, $\rho = 139°$, and $S_{mol} = 0.8$. Starting from an energy-minimized structure, we found a minimum of $\chi^2 = 23$ kHz^2 for $\tau = 97°$, $\rho = 138°$ and $S_{mol} = 0.8$. By slightly varying the angles of a regular α-helical structure we did not achieve any acceptable reduction of χ^2 either. These data thus suggest that some considerable local deviations from the α-helical model are induced by D-CF3-Phg, after all.

Table 3
Dipolar coupling of PGLa analogues with D-CF_3-Phg label

Position replaced with D-CF_3-Phg	Ile 9	Ala 10	Ile 13	Ala 14
Dipolar coupling (kHz)[a]	0	12.1	−3.5	8.2

[a] Couplings were measured in oriented samples with a 1:200 molar peptide:DMPC ratio at 35 °C.

Although no reliable stand-alone solution is found, nevertheless, the tilt angle τ of the best fit solutions is close to the expected alignment of PGLa. We also believe that the apparent increase in ρ compared to the azimuthal orientation of the L-CF_3-Phg analogues may be rationalized by two arguments. First, the D-CF_3-Phg side chains are in close contact with the i + 3rd residues. The entropy of such a conformation is very low, and in view of the high flexibility of the peptide the average distance between these side chains will probably be larger than that of the single energy-minimized structure. For some more realistic structural models with larger α we indeed found fits with lower ρ values (not shown). Second, the extended hydrophobic CF_3-Phg side chain in the D-enantiomer is expected to modify the hydrophobic moment of the peptide compared to the wild type or L-CF_3-Phg analogues. If this effect is visualized in a lipid environment, the helix would indeed become rotated towards the direction of larger ρ values.

Despite the uncertainty concerning the exact conformation of the D-CF_3-Phg analogues, their experimental data are useful to exclude certain putative solutions that have emerged from the analysis of the L-CF_3-Phg labels alone. Namely, for several α-helical structures and the 3_{10}-helix a second local minimum have suggested a solution with a low τ value, corresponding to a tilted transmembrane orientation rather than a peripheral peptide alignment (Table 2). In any model with such small tilt angle, it is clear that the set of individual side chains must show similar dipolar couplings. The couplings of the D-CF_3-Phg analogues, however, gave values between −3.5 and +12.1 kHz (Table 3), which clearly excluded such transmembrane orientation.

A more quantitative approach was used to include the data from the D-CF_3-Phg analogues into the orientational fit. We followed the second strategy discussed above and simply assigned large error estimates to the side chain angle α of the D-CF_3-Phg analogues. For the α-helical structures the peripheral orientation now emerges as a unique solution (Fig. 7B). The 3_{10}-helix model can also be excluded by this strategy, as it does not yield any acceptable solution (not shown).

3.6. Interaction of PGLa with gel phase membranes

The robustness of the ^{19}F 1-pulse experiment allowed us to measure the dipolar couplings under a wide range of experimental conditions and to monitor the behavior of the peptide throughout the lipid phase transition of the DMPC membranes. In the lipid gel phase at 15 °C, we found a slight increase in all dipolar couplings, when the sample was measured in the standard orientation with the membrane normal parallel to the magnetic field. The orientational fit for the regular α-helix has a minimum at virtually the same orientation as in the liquid crystalline phase, but with an order parameter that is increased by about 12% (to $S_{mol} = 0.71$ for the regular standard helix shown in Table 2). When the sample was measured with the membrane normal perpendicular to the field, the signals of the peptide in the fluid and gel phases of the lipid differed qualitatively. In the fluid phase membrane the anisotropic chemical shift and dipolar coupling were scaled with respect to the horizontal membrane alignment by an order parameter of $-1/2$, as expected for fast rotation of the peptide around the membrane normal (Fig. 4). Experiments with vertically tilted samples in the gel phase showed only a broad component around the isotropic position. The rotation of the peptide obviously stops or becomes so slow that the different orientations of the label are not averaged, and the other components of the signal are broadened and disappeared in the background. Thus, we conclude that the interaction of PGLa with DMPC does not depend on the phase state of the lipid. The observed increase in the order parameter very likely reflects a reduced overall mobility of the peptide in the more rigid gel phase membrane. The fast rotation around the membrane normal is stopped as expected for an inserted peptide.

4. Conclusions

The high intrinsic sensitivity of the ^{19}F nucleus and the simple 1-pulse NMR sequence make the proposed dipolar approach very robust under a wide range of experimental conditions. Analogous experiments with membrane-active peptides based on ^{15}N labeling suffer from several limitations. Fast motion makes the ^{1}H–^{15}N cross polarization inefficient. Slow motion leads to fast transverse relaxation and reduces the sensitivity, which is anyway not very high for ^{15}N. With the CF_3-label, on the other hand, we measured dipolar couplings from 0.25 μmol of peptide in 2 h. Only some small dipolar couplings are virtually obscured by the linewidth itself and have to be approximated. Our general conclusions are summarized as follows:

- ^{19}F homonuclear dipolar couplings within the CF_3-group of 4-trifluoromethyl-phenylglycine provide a very accurate measure of the orientation of the amino acid side chain, which is rigidly attached to the peptide backbone.
- A simple 1-pulse ^{19}F-NMR experiment allows the simultaneous determination of the anisotropic chemical shift and the homonuclear dipolar coupling, thus, uniquely defining the effective tilt angle of the CF_3-axis with respect to the external field.
- Using four CF_3-labeled peptide analogues we could confirm that PGLa is aligned at the surface of DMPC bilayers at a peptide:lipid ratio of 1:200, with the helix axis perpendicular to the membrane normal.

- We have measured the azimuthal rotation angle of the PGLa helix, which agrees well with the orientation expected from its amphiphilic character.
- Peptide analogues with a D-CF_3-Phg label provide only qualitative information about the peptide structure and orientation, which can be used to supplement the more reliable data from the L-CF_3-Phg labels.
- The CF_3-Phg side chain is not compatible with all hydrophobic positions along a peptide sequence, hence the labeled analogues have to be critically tested for an intact conformation and biological function.
- The simple 1-pulse ^{19}F-NMR experiment allows highly sensitive measurements over a wide range of conditions (such as very low peptide concentration [9]) and dynamic regimes. This makes it both an attractive alternative and a complement to conventional NMR experiments based on ^{15}N- or ^{2}H- labeling to monitor the orientation and dynamics of peptides and proteins in the membrane.

Acknowledgments

We thank Ulrich Sternberg (Forschungszentrum Karlsruhe) for discussion of the CF_3-group geometry, Ute Möllmann (HKI Jena) for her help with antimicrobial inhibition assays, and Karl-Heinz Gührs (IMB Jena) for access to mass spectrometry. This work was supported by SFB 604 (TP B6) of the Deutsche Forschungsgemeinschaft.

References

[1] F. Castellani, B. van Rossum, A. Diehl, M. Schubert, K. Rehbein, H. Oschkinat, Structure of a protein determined by solid-state magic-angle-spinning NMR spectroscopy, Nature 420 (2002) 98–102.

[2] S.J. Opella, Membrane protein NMR studies, Methods Mol. Biol. 227 (2003) 307–320.

[3] R. Fu, T.A. Cross, Solid-state nuclear magnetic resonance investigation of protein and polypeptide structure, Annu. Rev. Biophys. Biomol. Struct. 28 (1999) 235–268.

[4] F.M. Marassi, S.J. Opella, NMR structural studies of membrane proteins, Curr. Opin. Struct. Biol. 8 (1998) 640–648.

[5] J. Salgado, S.L. Grage, L.H. Kondejewski, R.S. Hodges, R.N. McElhaney, A.S. Ulrich, Membrane-bound structure and alignment of the antimicrobial beta-sheet peptide gramicidin S derived from angular and distance constraints by solid state 19F-NMR, J. Biomol. NMR 21 (2001) 191–208.

[6] S. Afonin, R.W. Glaser, M. Berditchevskaia, P. Wadhwani, K.H. Gührs, U. Möllmann, A. Perner, A.S. Ulrich, 4-Fluorophenylglycine as a label for 19F NMR structure analysis of membrane-associated peptides, Chembiochem. 4 (2003) 1151–1163.

[7] S. Afonin, U.H.N. Dürr, R.W. Glaser, A.S. Ulrich, Boomerang-like insertion of a fusogenic peptide in a lipid membrane revealed by solid state ^{19}F-NMR, Magn. Reson. Chem. 42 (2004) 195–203.

[8] S. Afonin, PhD thesis, Friedrich-Schiller-Universität Jena (2003).

[9] R.W. Glaser, A.S. Ulrich, Susceptibility corrections in solid state NMR experiments with oriented membrane samples. Part I: applications, J. Magn. Reson. 164 (2003) 104–114.

[10] R. Ulrich, R.W. Glaser, A.S. Ulrich, Susceptibility corrections in solid state NMR experiments with oriented membrane samples. Part II: theory, J. Magn. Reson. 164 (2003) 115–127.

[11] S.L. Grage, A.S. Ulrich, Orientation-dependent ^{19}F dipolar couplings within a trifluoromethyl group are revealed by static multipulse NMR in the solid state, J. Magn. Reson. 146 (2000) 81–88.

[12] A. Latal, G. Degovics, R.F. Epand, R.M. Epand, K. Lohner, Structural aspects of the interaction of peptidyl-glycylleucine-carboxyamide, a highly potent antimicrobial peptide from frog skin, with lipids, Eur. J. Biochem. 248 (1997) 938–946.

[13] B. Bechinger, M. Zasloff, S.J. Opella, Structure and dynamics of the antibiotic peptide PGLa in membranes by solution and solid-state nuclear resonance spectroscopy, Biophys. J. 74 (1998) 981–987.

[14] A.S. Ulrich, M.P. Heyn, A. Watts, Structure determination of the cyclohexane ring of retinal in bacteriorhodopsin by solid state deuterium NMR, Biochemistry 31 (1992) 10390–10399.

[15] S.L. Grage, A.S. Ulrich, Structural parameters from 19F homonuclear dipolar couplings, obtained by multipulse solid-state NMR on static and oriented systems, J. Magn. Reson. 138 (1999) 98–106.

[16] W. Martienssen (Ed.), Landolt-Börnstein Numerical Data and Functional Relationships in Science and Technology, Springer, Berlin, 1997.

[17] S.R. Dowd, V. Simplaceanu, C. Ho, Fluorine-19 nuclear magnetic resonance investigation of fluorine-19-labeled phospholipids. 2. A line-shape analysis, Biochemistry 23 (1984) 6142–6146.

[18] M. Engelsberg, S.R. Dowd, V. Simplaceanu, B.W. Cook, C. Ho, Nuclear magnetic resonance line-shape analysis of fluorine-19-labeled phospholipids, Biochemistry 21 (1982) 6985–6989.

[19] A.S. Ulrich, S.L. Grage, in: I. Ando, T. Asakura (Eds.), Solid State 2H-NMR in Solid State NMR of Polymers, Elsevier Science, The Netherlands, 1998, pp. 190–211.

[20] M.H. Levitt, The signs of frequencies and phases in NMR, J. Magn. Reson. 126 (1997) 164–182.

[21] R. Koradi, M. Billeter, K. Wüthrich, MOLMOL: a program for display and analysis of macromolecular structures, J. Mol. Graphics 14 (1996) 51–55.

[22] K. Pervushin, R. Riek, G. Wider, K. Wüthrich, Attenuated T2 relaxation by mutual cancellation of dipole-dipole coupling and chemical shift anisotropy indicates an avenue to NMR structures of very large biological macromolecules in solution, Proc. Natl. Acad. Sci. USA 94 (1997) 12366–12371.

[23] H.Y. Carr, E.M. Purcell, Effects of diffusion on free precession in nuclear magnetic resonance experiments, Phys. Rev. 94 (1954) 630–638.

[24] S. Meiboom, D. Gill, Modified spin-echo method for measuring nuclear relaxation times, Rev. Sci. Instrum. 29 (1958) 688–691.

[25] J.B. Mitchell, J. Smith, D-amino acid residues in peptides and proteins, Proteins 50 (2003) 563–571.

Appendices

E. Publication on PGLa in *Biophysical Journal*

Glaser, R. W., C. Sachse, U. H. N. Dürr, P. Wadhwani, S. Afonin, E. Strandberg, A. S. Ulrich

Concentration-dependent realignment of the antimicrobial peptide PGLa in lipid membranes observed by solid-state ^{19}F-NMR

Biophysical Journal **2005**, ***88***, 3392-3397.

Appendices

Biophysical Journal Volume 88 May 2005 3392–3397

Concentration-Dependent Realignment of the Antimicrobial Peptide PGLa in Lipid Membranes Observed by Solid-State ^{19}F-NMR

Ralf W. Glaser,* Carsten Sachse,* Ulrich H. N. Dürr,† Parvesh Wadhwani,‡ Sergii Afonin,‡ Erik Strandberg,‡ and Anne S. Ulrich†‡

*Institute of Biochemistry and Biophysics, University of Jena, Jena, Germany; †Institute of Organic Chemistry, University of Karlsruhe, Karlsruhe, Germany; and ‡Forschungszentrum Karlsruhe, Karlsruhe, Germany

ABSTRACT The membrane-disruptive antimicrobial peptide PGLa is found to change its orientation in a dimyristoylphosphatidylcholine bilayer when its concentration is increased to biologically active levels. The alignment of the α-helix was determined by highly sensitive solid-state NMR measurements of ^{19}F dipolar couplings on CF_3-labeled side chains, and supported by a nonperturbing ^{15}N label. At a low peptide/lipid ratio of 1:200 the amphiphilic peptide resides on the membrane surface in the so-called S-state, as expected. However, at high peptide concentration ($\geq$1:50 molar ratio) the helix axis changes its tilt angle from $\sim$90° to $\sim$120°, with the C-terminus pointing toward the bilayer interior. This tilted "T-state" represents a novel feature of antimicrobial peptides, which is distinct from a membrane-inserted I-state. At intermediate concentration, PGLa is in exchange between the S- and T-state in the timescale of the NMR experiment. In both states the peptide molecules undergo fast rotation around the membrane normal in liquid crystalline bilayers; hence, large peptide aggregates do not form. Very likely the obliquely tilted T-state represents an antiparallel dimer of PGLa that is formed in the membrane at increasing concentration.

INTRODUCTION

PGLa (GMASKAGAIAGKIAKVALKAL-NH_2) is an antibiotic peptide found in frog skin (Hoffmann et al., 1983; Richter et al., 1985; Soravia et al., 1988; Latal et al., 1997). As a member of the magainin family it assumes an amphiphilic α-helical structure upon membrane binding (Bechinger et al., 1998). The cationic peptide has a high affinity for bacterial membranes and is able to permeabilize them. A specific receptor is not involved in this antimicrobial action (Wade et al., 1990); hence, it is unlikely that bacteria develop resistance against such peptides. Several different models of antimicrobial action have been proposed (McElhaney and Prenner, 1999; Shai, 1999; Matsuzaki, 1999; Huang, 2000; Zasloff, 2002; Strandberg and Ulrich, 2004). Initially, amphiphilic peptides are supposed to bind flat to the membrane surface in the so-called ''S-state''. Above a threshold concentration the membrane may then get disrupted nonspecifically by the high surface density, as in the carpet mechanism. Alternatively, a realignment of the peptide molecules into a membrane-inserted ''I-state'' has been demonstrated, leading to the formation of oligomeric pores. Here, it is appropriate to differentiate between the ''barrel-stave'' model in which the pore is exclusively made up of peptide molecules, and the ''toroidal wormhole'' model in which anionic lipids contribute to the pore lining. A better understanding of the structural basis for these different functional mechanisms may help to improve the activity and specificity of antimicrobial peptides.

We have recently developed a highly sensitive solid-state ^{19}F-NMR strategy for characterizing the orientation and dynamics of membrane-bound peptides, based on collecting a number of orientational constraints (Salgado et al., 2001; Afonin et al., 2003, 2004; Glaser and Ulrich, 2003; Glaser et al., 2004; Ulrich, 2005; Ulrich et al., 2005). The most appropriate label for obtaining these structural data is L-4-trifluoromethyl-phenylglycine (CF_3-Phg), when substituted for a single nonpolar amino acid in the peptide sequence. The anisotropic ^{19}F-^{19}F dipolar coupling within the CF_3 group is resolved by ^{19}F-NMR measurements using macroscopically aligned membrane samples (Glaser et al., 2004). The dipolar splittings from several individual labels serve as experimental constraints to determine the orientation of the peptide within the lipid bilayer. For PGLa reconstituted in DMPC (dimyristoyl-phosphatidylcholine) at a peptide/lipid molar ratio (P/L) of 1:200 we have previously demonstrated that the helix is aligned flat in the plane of the membrane. The tilt angle of $\sim$90° between the helix axis and the membrane normal corresponds to the surface-bound S-state, as expected from the amphiphilic character of the peptide. We have now studied PGLa at higher concentration (P/L $\geq$ 1:50), since antimicrobial peptides tend to become biologically active only above such threshold value (Blazyk et al., 2001). Here, we observed an unexpected realignment of the peptide, whereby the helix axis assumes an oblique tilt angle. This new orientation is clearly distinct from a transmembrane alignment, and it does not correspond to an I-state, which would have been expected for such peptides when a pore is formed (Huang, 2000). Instead, it appears that PGLa is able to self-assemble as a dimer on the bilayer surface at high peptide concentration, which would explain how its tilted orientation in the membrane is stabilized as a distinct state.

Submitted November 17, 2004, and accepted for publication January 27, 2005.

Address reprint requests to Anne S. Ulrich, Institute of Organic Chemistry, University of Karlsruhe, Fritz-Haber-Weg 6, 76131 Karlsruhe, Germany. E-mail: anne.ulrich@ifia.fzk.de.

© 2005 by the Biophysical Society

0006-3495/05/05/3392/06 $2.00

doi: 10.1529/biophysj.104.056424

MATERIALS AND METHODS

^{19}F-NMR analysis

A series of CF_3-Phg labeled PGLa analogs were synthesized, purified, and characterized to be functionally fully intact, as previously reported (Afonin et al., 2003; Glaser et al., 2004). A single label was introduced either at position Ile-9, Ala-10, Ile-13, or Ala-14. Macroscopically oriented samples with a mixture of 0.2–0.5 mg peptide plus lipid in different molar ratios were prepared as previously described, and one-pulse ^{19}F-NMR spectra were acquired on a 500-MHz wide-bore Unity Inova spectrometer (Varian, Palo Alto, CA) with a ^{19}F/^{1}H double-tuned flat-coil probe (Doty Scientific, Columbia, SC) that can be manually rotated and allows ^{1}H decoupling with 10–15 kHz (Glaser et al., 2004).

^{15}N-NMR analysis

^{15}N-labeled PGLa was synthesized by standard Fmoc solid phase synthesis with ^{15}N-glycine at Gly-11. For the sample with P/L = 1:200, ~1 mg of peptide plus 70 mg DMPC were oriented on 25 glass plates, and 2.7 mg PGLa plus 47 mg lipid were used for the P/L 1:50 sample. ^{15}N-NMR experiments were performed at 50.68 MHz on a Bruker Avance 500 MHz NMR spectrometer with a fixed flat-coil triple-resonance probe (Bruker, Karlsruhe, Germany). We used a ramped cross-polarization sequence with a power of 40 kHz, 2.5 s relaxation delay time, 100 kHz spectral width, 2048 data points, and tppm20 proton decoupling. The contact time was 1 ms in hydrated samples, and 2 ms for the lyophilized peptide. Between 30,000 and 200,000 scans were collected. Spectra were referenced to $^{15}NH_4NO_3$ by setting the signal of solid $^{15}NH_4Cl$ to 18.0 ppm. We determined the principal axis values of the ^{15}N chemical shift anisotropy (CSA) tensor as $\sigma_{11} = 14$, $\sigma_{22} = 33$, and $\sigma_{33} = 197$ ppm by fitting the lineshape to the experimental spectrum of the lyophilized peptide powder. We used an orientation of the ^{15}N tensor of the labeled glycine with σ_{33} tilted 17° from N-H toward the N-C′ bond, and σ_{11} normal to the plane of the peptide bond (Sternberg et al., 2004).

RESULTS AND DISCUSSION

Concentration-dependent realignment of PGLa in DMPC

The one-pulse ^{19}F-NMR spectra of the four different labeled PGLa analogs were measured at different peptide/lipid ratios in DMPC membranes at 35°C (Fig. 1). At low peptide concentration, i.e., between 1:1000 and 1:200, the dipolar analysis yielded a surface alignment as previously described

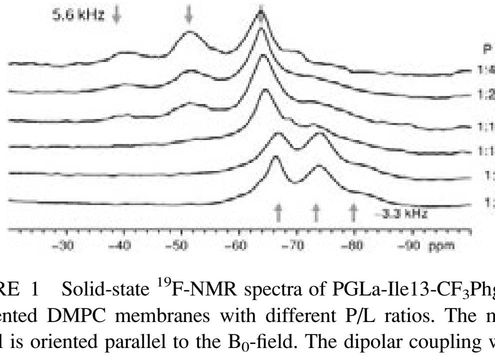

FIGURE 1 Solid-state ^{19}F-NMR spectra of PGLa-Ile13-CF_3Phg at 35°C in oriented DMPC membranes with different P/L ratios. The membrane normal is oriented parallel to the B_0-field. The dipolar coupling within the CF_3-group is read from the splitting of the triplet, and its sign is taken from the chemical shift. The asymmetric shape of the triplet results from differential relaxation properties (Glaser et al., 2004).

TABLE 1 ^{19}F dipolar couplings (in kHz) of CF_3-Phg-labeled PGLa

Labeled position	Ile-9	Ala-10	Ile-13	Ala-14
P/L ratio 1:200	0	0	5.6	−5.4
P/L ratio 1:50	−4.7	−3.1	−3.3	−5.3

(Glaser et al., 2004). Upon increasing the P/L to 1:50 and beyond, the chemical shift and dipolar couplings of the labels changed (Table 1). In the following, we will analyze and interpret the structural meaning of these spectral changes, providing new insight into the peptide-lipid interactions of antimicrobial peptides. A similar observation of a concentration-dependent change in NMR parameters had been reported for a 4F-Phg labeled PGLa (Glaser and Ulrich, 2003) as well as a related model peptide K3 (Toke et al., 2004). At that time, no structural interpretation had been possible in these systems.

Using ^{31}P-NMR, we confirmed that the phospholipids remain in a lamellar bilayer phase at all concentrations, irrespective of the peptide orientation (Sachse, 2003). We observed a slight smooth change of the anisotropic ^{31}P chemical shift of the lipids, roughly proportional to peptide concentration. Such a qualitative reduction of lipid headgroup order was also observed with many other molecules dissolved in membranes (Zidovetzki et al., 1988). There was no indication of phase separation between bound and free lipids, nor between peptide-rich and peptide-depleted regions. The uncharged lipid DMPC allowed a highly reproducible preparation of samples with well-oriented bilayers. As the oriented samples contain no excess bulk water, anionic lipids are not necessary to attract the peptides to the membranes.

Confirmation of realignment in DMPC/DMPG (dimyristoyl-phosphatidylglycerol)

To determine the alignment of PGLa in the membrane from the local orientational constraints of its four labels, the peptide secondary structure has to be verified. Circular dichroism was used to confirm that the helix content of all four analogs is comparable to that of the wild-type peptide in the presence of small unilamellar vesicles at a P/L of 1:50 and 1:200 (see Supplementary Material). Unlike the solid-state ^{19}F-NMR experiments above, circular dichroism (CD) measurements are performed on vesicles in dilute suspension. Hence, negatively charged lipids are required to attract the cationic PGLa to the membrane. Under those conditions we have previously shown by solution-state ^{19}F-NMR that the fraction of membrane-bound PGLa increases when negatively charged dimyristoyl-phosphatidylglycerol (DMPG) is mixed into the vesicles of DMPC (Afonin et al., 2003). Once the overall negative charge of the lipids exceeded the positive charge of PGLa (+5 at neutral pH), virtually all PGLa was associated to the membrane and the concentration in bulk solution became immeasurably small.

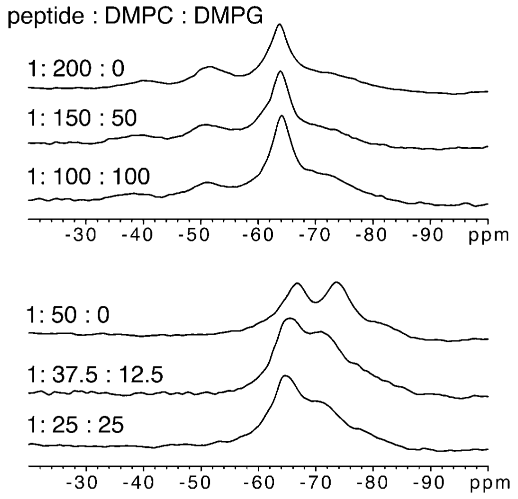

FIGURE 2 ^{19}F-NMR spectra of PGLa (as in Fig. 1) in oriented membranes with different mixtures of DMPC and DMPG.

To test the influence of negative lipid charge on peptide orientation and to justify the CD-derived secondary structure information, we acquired further solid-state ^{19}F-NMR spectra of a labeled PGLa analog in mixtures of DMPC and DMPG. Measurements in oriented membranes were performed at 1:200 and 1:50 molar peptide/lipid ratio (Fig. 2). The linewidth on these spectra was higher than in samples containing only DMPC. The reason for the line broadening is not clear at this point, but differences in hydration properties and ^{1}H decoupling are likely. Nevertheless, for 3:1 and 1:1 DMPC/DMPG we found the same qualitative changes in the spectra as in DMPC alone, which is clearly indicative of a reorientation from the S-state at 1:200 to a new state at 1:50. Given that the conformation of PGLa remains α-helical in all cases, the observed changes in the ^{19}F-NMR spectra must therefore be attributed to a concentration-induced realignment of PGLa in the membrane.

Calculation of helix tilt angle

The orientation of PGLa in the bilayer can be calculated from the signed dipolar splittings of the individual CF_3-Phg labels (see Supplementary Material). The peptide orientation is fully described by two angles: the tilt angle τ between the helix axis and the membrane normal, and the azimuthal rotation angle ρ around the helix axis. With our definition of C_α of Lys-12 and the helix axis as the base of the molecular coordinate system, $\tau \approx 0°$ corresponds to an inserted orientation (I-state), and $\tau \approx 90°$, $\rho \approx 80 \ldots 120°$ corresponds to a surface orientation according to the amphiphilic side-chain distribution of the peptide. Additionally, the degree of motional averaging is described by a molecular order parameter S_{mol}. These three parameters, τ, ρ, and S_{mol} are derived from the four dipolar couplings by means of a least-squares fit (Glaser et al., 2004; Afonin et al., 2004). For PGLa at P/L = 1:200 the minimum in the resulting ρ/τ map corresponds to the S-state, with $\tau \approx 89°$, $\rho \approx 106°$, and $S_{mol} \approx 0.6$ (Fig. 3 *A*), as described before (Glaser et al., 2004). At P/L = 1:50, on the other hand, we find that the allowed region in the ρ/τ map has moved to $\tau \approx 123°$, $\rho \approx 85°$, with $S_{mol} \approx 0.6$ (Fig. 3 *B*). Now the helix axis is tilted at an oblique angle, with the C-terminus of PGLa more deeply inserted into the lipid bilayer than the N-terminus. The azimuthal angle has also changed to some extent, though the amphiphilicity profile of PGLa is still compatible with the charged side chains reaching up toward the aqueous layer. We shall name this novel tilted state the ''T-state''.

In a concentration-dependent series of experiments from 1:400 to 1:35, at low peptide concentration (1:400–1:150) the splitting in Fig. 1 is +5.6 kHz, whereas at high concentration (1:50, 1:35) the splitting is −3.3 kHz. There is not a gradual change of the splitting, which indicates that there is not a gradual change of peptide orientation. At intermediate concentration the spectra are broadened to such an extent that the two outer peaks of the triplet are not detectable, i.e., the peptide changes between the S- and T-states in the timescale of the NMR experiment. The same concentration-dependent change between two distinct states has also been observed for PGLa labeled with 4F-phenylglycine, when an extensive concentration range was studied from 1:3000 to 1:8. Here, the chemical shift underwent a distinct change at a limiting threshold concentration of around 1:100 (Glaser and Ulrich, 2003).

Peptide mobility in the membrane

The orientational analysis above yielded an order parameter of $S_{mol} \approx 0.6$ for PGLa in both the S- and the T-states in liquid crystalline DMPC. On a scale of 1.0 (no averaging) to

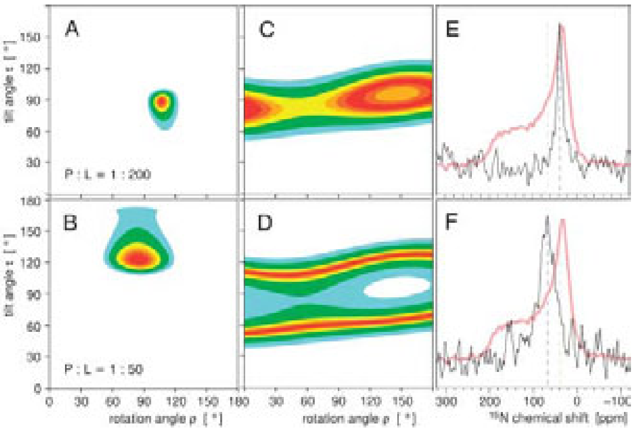

FIGURE 3 Orientation of the PGLa helix in a DMPC bilayer at a 1:200 (*upper panels*) and 1:50 (*lower panels*) molar peptide/lipid ratio. The contour plots *A–D* show the sum of squared deviations between the experimental data and calculated values as a function of the helix tilt angle τ and the azimuthal rotation ρ, with best-fitting orientations in dark red. (*A* and *B*) Summary of the ^{19}F-NMR analysis based on four CF_3-Phg labels, and (*C* and *D*) a single ^{15}N label. The corresponding ^{15}N spectra are shown in *E* and *F*, with the powder lineshape of the lyophilized peptide superimposed.

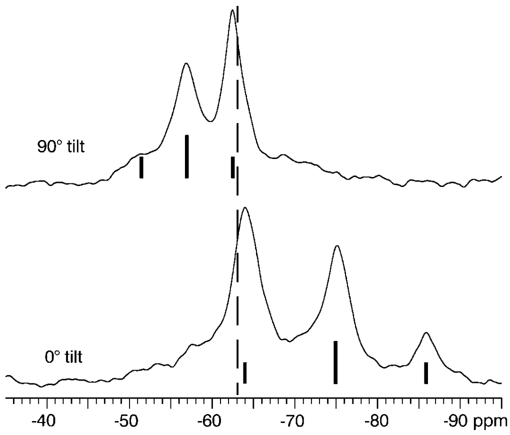

FIGURE 4 ^{19}F-NMR spectra of PGLa (as in Fig. 1) at a P/L of 1:50 in oriented DMPC membranes acquired with two different sample orientations. Upper spectrum with the membrane normal aligned perpendicular to the magnetic field (90° tilt), and lower spectrum with the membrane normal parallel to the magnetic field (0° tilt). In addition, the idealized triplet structure of the spectrum along with the isotropic chemical shift of CF_3-Phg (*dotted line*) are indicated.

0.0 (isotropic tumbling) this value accounts for both the global orientational mobility of the peptide with respect to the membrane normal and the local wobbling motion of the label.

Rotational diffusion of PGLa around the membrane normal is not visible in the spectra acquired with the membrane normal aligned parallel to the static magnetic field direction, but it is revealed when the sample is positioned at a 90° angle, i.e., with the membrane normal perpendicular to the field (Salgado et al., 2001; Ulrich, 2004; Glaser et al., 2004). All spectra at P/L ratios of 1:200 and 1:50 were found to scale around the isotropic chemical shift by a factor of $-1/2$ compared to the respective spectrum acquired at 0° angle, and no powder pattern or signal broadening was observed (Fig. 4). This indicates that all NMR interactions are averaged around the sample axis on the timescale of the experiment (10 kHz spectral width). Thus, the PGLa molecules rotate freely around the membrane normal, in both the S- and T-states.

We can furthermore exclude that PGLa rotates around its helical axis, since this would lead to identical dipolar splittings for all labeled positions. Especially the dipolar couplings of the epimeric D-CF_3-Phg labels (see Supplementary Material) are incompatible with such motion, which besides would be energetically very unfavorable in view of the amphiphilic character of PGLa.

Verification of the peptide tilt angle by ^{15}N-NMR

To decide whether the observed spectral changes at high peptide concentration are genuinely due to an oblique tilt of PGLa, we studied a peptide labeled with ^{15}N at Gly-11. ^{15}N-NMR experiments have a much lower sensitivity compared to ^{19}F-NMR experiments (Afonin et al., 2003), but we can be sure that this label does not perturb the local peptide conformation nor its interactions with other molecules. At low peptide concentration (P/L = 1:200) the ^{15}N signal of an oriented sample is at 40 ppm, and at high concentration (1:50) it moves to 68 ppm (Fig. 3, *E* and *F*). To find out which alignments of the peptide helix are compatible with these data, the principal axis values of the ^{15}N CSA tensor need to be known. As Gly differs slightly from other amino acids (Sternberg et al., 2004), the values were determined from the lyophilized peptide powder, which is shown superimposed over the oriented spectra.

Orientational analysis of the ^{15}N data in terms of τ yielded a tilt angle of 90° for a P/L of 1:200, confirming the S-state, as expected (Fig. 3 *C*). At a high peptide concentration of 1:50, we determined a helix tilt of about $\tau \approx 65°$ or 115°, which is also in full agreement with the ^{19}F analysis (Fig. 3 *D*). This orientational analysis was performed with $S_{mol} = 0.7$. For the ^{15}N label in the backbone, a slightly higher order parameter than 0.6 was chosen to compensate for any extra wobble of the CF_3-Phg side chain and any motion in the lyophilized peptide. The signal lies close to (but not at) the isotropic position of ^{15}N, but free tumbling or micellarization of the peptide can be excluded in view of the ^{19}F- and ^{31}P-NMR data on equivalent samples. For any reasonable choice of $0.5 < S_{mol} < 1$ only an oblique helix tilt can explain the ^{15}N data at P/L = 1:50. The evaluation of an oblique helix tilt angle thus unequivocally confirms the self-consistent picture derived above by ^{19}F-NMR.

We note that the ^{15}N-NMR signal at 40 ppm of the 1:50 sample is significantly broader than the signal of the 1:200 sample at 68 ppm. This is an inevitable consequence of the differential effect of the mosaic spread on the ^{15}N chemical shift in the different CSA tensor orientations. Namely, the same mosaic spread produces an apparent linewidth that is ~3 times smaller near the high-field and low-field edge of the CSA range (S-state) than in the middle of the CSA range (T-state).

Further evidence for a realignment of PGLa from an S-state to a T-state stems from analyzing the epimeric byproducts of our peptide synthesis, namely those PGLa analogs carrying a D-CF_3-Phg label (see Supplementary Material). The bulky and stiff D-amino acid is expected to cause slight changes in the structure and in the hydrophobic surface of the peptide; therefore, the dipolar couplings only provide qualitative information about the orientation of the peptide (Glaser et al., 2004). Nevertheless, these measurements also confirmed the obliquely tilted orientation of PGLa at high concentration in the membrane, and they clearly excluded the possibility of a transmembrane orientation of the PGLa helix.

Interpretation in terms of peptide dimerization

Notably, the concentration-dependent series of experiments never showed a gradual shift of the signals (e.g., Fig. 1) (as

also observed in Glaser and Ulrich, 2003). At peptide/lipid ratios around 1:100, the NMR signal deteriorates because of exchange between the two populations in the intermediate timescale. This is taken as evidence for the presence of two distinct populations of peptides in different orientational states, separated by an energy barrier. A tilted state with $\tau = 120°$ would not seem to be a particularly favorable alignment for a monomer of PGL, which is already perfectly stable in a flat alignment (S-state). Hence, the change from the S- to the T-state must involve more than just a change in orientation with respect to the membrane. Significant conformational changes were excluded by CD experiments, and are very unlikely since our NMR data fits well with a helical conformation in both states. The formation of large peptide aggregates can also be excluded in view of the observed fast rotation around the membrane normal and the same S_{mol} at low concentration. Therefore, although we have no direct experimental evidence, the most probable explanation for the occurrence of the T-state is the formation of peptide dimers upon increasing the PGLa concentration in the membrane. Indeed, PGLa is known to form dimers in a lipid monolayer at the air-water interface (Konovalov et al., 2002). Dimerization in the membrane has even been described for related antimicrobial peptides: REDOR distance measurements on the model peptide K3 showed parallel dimers (Toke et al., 2004), transferred NOE of a magainin analog indicated antiparallel dimers (Wakamatsu et al., 2002), and PGLa was found to associate with magainin as an antiparallel heterodimer (Hara et al., 2001). The tilt angle of such peptide dimers in the membrane has not yet been determined, as these experiments provided distance constraints but no orientational information. In our case of PGLa, the homodimers in DMPC must be rotationally symmetric with respect to the membrane normal, since we observe only a single set of NMR signals. The tilt of the monomer is then a consequence of the dimer orientation according to its overall amphiphilic shape. Self-assembly of PGLa into antiparallel dimers may thus account for the observation of the distinctly tilted T-state, as schematically illustrated in Fig. 5.

Assessment of error margins

An experimental inaccuracy of ± 0.5 kHz in the dipolar splitting translates into an intrinsic error in τ and ρ of $< \pm 10°$ (Glaser et al., 2004). Nevertheless, this margin includes the ambiguity of choosing one or another helical conformation for the data analysis, as demonstrated by our systematic analysis of different conformational models (see Supplementary Material). Since the L-CF_3-Phg labels used to replace Ile or Ala may induce slight distortions in the peptide backbone, the error margins should be considered more generously, say at $\pm 20°$. Especially in the T-state, which appears to involve specific peptide-peptide interactions, the stiff CF_3-Phg labels might be more problematic than in the monomeric S-state.

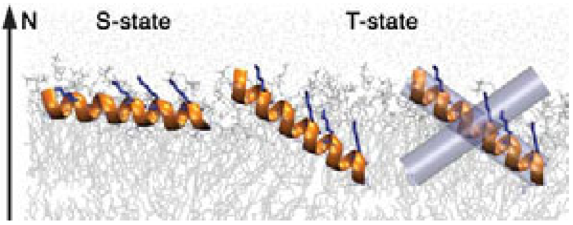

FIGURE 5 Illustration of the observed realignment of PGLa in a DMPC membrane. At low peptide concentration, the amphiphilic helix lies flat on the surface in the S-state. With increasing concentration, it assumes a tilted T-state, which appears to involve the formation of antiparallel peptide dimers.

The information from a single nonperturbing ^{15}N-label is not very accurate either (about $\pm 20°$ in τ, and ρ is generally not accessible by ^{15}N CSA analysis of single labels). Nonetheless, the distinct changes in the ^{19}F dipolar couplings and in the ^{15}N chemical shift unequivocally show that PGLa undergoes a concentration-dependent realignment.

With a small number of orientational constraints we can only test whether a certain helix conformation and orientation is compatible with the NMR data. In fact, the four constraints from the L-CF_3-Phg labels alone would also be compatible with a distorted helix that is slightly tilted away from a transmembrane orientation (see Supplementary Material). However, the independent additional constraints (1× ^{15}N-Gly, 4× D-CF_3-Phg) supporting the oblique tilt of the central helical segment of PGLa make any alternative interpretation of the data very unlikely.

CONCLUSIONS

The tilted T-state of PGLa exhibits quite unexpected properties that do not fit well into the currently discussed structural models of antimicrobial action (Shai, 1999; Matsuzaki, 1999; Huang, 2000; Zasloff, 2002; Strandberg and Ulrich, 2004). It is clearly not compatible with a barrel-stave pore, and the rotational diffusion of the peptide around the membrane normal does not support the carpet model either. The oblique tilt with an order parameter nearly identical to that of the S-state is also not compatible with a toroidal wormhole. Although the high peptide concentration of the T-state may appear to correlate with the threshold for pore formation (Wieprecht et al., 2000), there is no evidence from our experiments that this state should be directly responsible for the destruction of the membrane barrier. Dimerization of PGLa at the membrane surface is a plausible hypothesis to explain our data in light of observations from similar amphiphilic helical membrane peptides from the same family. The T-state may thus be an intermediate in the formation of pores on the way from the monomeric S-state toward a cooperative I-state.

SUPPLEMENTARY MATERIAL

An online supplement to this article can be found by visiting BJ Online at http://www.biophysj.org.

CD experiments, [19]F-NMR experiments with D-CF_3-Phg labeled peptides, and effect of structural variation on peptide orientation are available as supporting material in PDF format; the orientational calculation of τ and ρ is available as MATHEMATICA notebook.

This work was supported by Sonderforschungsbereich 604 (TP B6) and by the Center for Functional Nanostructures of the Deutsche Forschungsgemeinschaft.

REFERENCES

Afonin, S., R. W. Glaser, M. Berditchevskaia, P. Wadhwani, K. H. Gührs, U. Möllmann, A. Perner, and A. S. Ulrich. 2003. 4-Fluorophenylglycine as a label for [19]F-NMR structure analysis of membrane-associated peptides. *ChemBioChem.* 4:1151–1163.

Afonin, S., U. H. N. Dürr, R. W. Glaser, and A. S. Ulrich. 2004. ''Boomerang''-like insertion of a fusogenic peptide in a lipid membrane revealed by solid state [19]F-NMR. *Magn. Reson. Chem.* 42:195–203.

Bechinger, B., M. Zasloff, and S. J. Opella. 1998. Structure and dynamics of the antibiotic peptide PGLa in membranes by solution and solid-state nuclear resonance spectroscopy. *Biophys. J.* 74:981–987.

Blazyk, J., R. Wiegand, J. Klein, J. Hammer, R. M. Epand, R. F. Epand, W. L. Maloy, and U. P. Kari. 2001. A novel linear amphipathic beta-sheet cationic antimicrobial peptide with enhanced selectivity for bacterial lipids. *J. Biol. Chem.* 276:27899–27906.

Glaser, R. W., C. Sachse, U. H. N. Dürr, P. Wadhwani, and A. S. Ulrich. 2004. Orientation of the antimicrobial peptide PGLa in lipid membranes determined from [19]F-NMR dipolar couplings of 4-CF_3-phenylglycine labels. *J. Magn. Reson.* 168:153–163.

Glaser, R. W., and A. S. Ulrich. 2003. Susceptibility corrections in solid state NMR experiments with oriented membrane samples. Part I: Applications. *J. Magn. Reson.* 164:104–114.

Hara, T., Y. Mitani, K. Tanaka, N. Uematsu, A. Takakura, T. Tachi, H. Kodama, M. Kondo, H. Mori, A. Otaka, F. Nobutaka, and K. Matsuzaki. 2001. Heterodimer formation between the antimicrobial peptides magainin 2 and PGLa in lipid bilayers: a cross-linking study. *Biochemistry.* 40:12395–12399.

Hoffmann, W., K. Richter, and G. Kreil. 1983. A novel peptide designated PYLa and its precursor as predicted from cloned mRNA of *Xenopus laevis* skin. *EMBO J.* 2:711–714.

Huang, H. W. 2000. Action of antimicrobial peptides: two-state model. *Biochemistry.* 39:8347–8352.

Konovalov, O., I. Myagkov, B. Struth, and K. Lohner. 2002. Lipid discrimination in phospholipid monolayers by the antimicrobial frog skin peptide PGLa. A synchrotron X-ray grazing incidence and reflectivity study. *Eur. Biophys. J.* 31:428–437.

Latal, A., G. Degovics, R. F. Epand, R. M. Epand, and K. Lohner. 1997. Structural aspects of the interaction of peptidyl-glycylleucine-carboxyamide, a highly potent antimicrobial peptide from frog skin, with lipids. *Eur. J. Biochem.* 248:938–946.

Matsuzaki, K. 1999. Why and how are peptide-lipid interactions utilized for self-defense? Magainins and tachyplesins as archetypes. *Biochim. Biophys. Acta.* 1462:1–10.

McElhaney, R. N., and E. J. Prenner, editors. 1999. Special issue. The interaction of antimicrobial peptides with model lipid bilayers and biological membranes. *Biochim. Biophys. Acta.* 1462:1–234.

Richter, K., H. Aschauer, and G. Kreil. 1985. Biosynthesis of peptides in the skin of *Xenopus laevis*: isolation of novel peptides predicted from the sequence of cloned cDNAs. *Peptides.* 6(Suppl 3):17–21.

Sachse, C. 2003. [19]F-Festkörperuntersuchungen zur Orientierung und Dynamik des antimikrobiellen Peptides PGLa in Lipidmembranen. Diploma thesis, Friedrich-Schiller-University Jena. http://www.db-thueringen.de/servlets/DocumentServlet?id=1898

Salgado, J., S. L. Grage, L. H. Kondejewski, R. S. Hodges, R. N. McElhaney, and A. S. Ulrich. 2001. Membrane-bound structure and alignment of the antimicrobial beta-sheet peptide gramicidin S derived from angular and distance constraints by solid state [19]F-NMR. *J. Biomol. NMR.* 21:191–208.

Shai, Y. 1999. Mechanism of the binding, insertion and destabilization of phopholipid bilayer membranes by α-helical antimicrobial and cell non-selective membrane-lytic peptides. *Biochim. Biophys. Acta.* 1462:55–70.

Soravia, E., G. Martini, and M. Zasloff. 1988. Antimicrobial properties of peptides from *Xenopus* granular gland secretions. *FEBS Lett.* 228:337–340.

Sternberg, U., R. Witter, and A. S. Ulrich. 2004. 3D structure elucidation using NMR chemical shifts. *Annu. Rep. NMR Spectrosc.* 52:53–104.

Strandberg, E., and A. S. Ulrich. 2004. NMR methods for studying membrane-active antimicrobial peptides. *Concepts Magn. Reson.* 23A: 89–120.

Ulrich, A. S. 2005. Solid state [19]F-NMR methods for studying biomembranes. *Prog. Nucl. Magn. Reson. Spectrosc.* In press.

Ulrich, A. S., P. Wadhwani, U. H. N. Dürr, S. Afonin, R. W. Glaser, E. Strandberg, P. Tremouilhac, C. Sachse, M. Berditchevskaia, and S. Grage. 2005. Solid-state [19]F-NMR analysis of membrane-active peptides. *In* NMR Spectroscopy of Biological Solids. H. Ramamoorthy, editor. Marcel Dekker, New York. In press.

Toke, O., R. D. O'Connor, T. K. Weldeghiorghis, W. L. Maloy, R. W. Glaser, A. S. Ulrich, and J. Schaefer. 2004. Structure of $(KIAGKIA)_3$ aggregates in phospholipid bilayers by solid-state NMR. *Biophys. J.* 87:675–687.

Wade, D., A. Boman, B. Wåhlin, C. M. Drain, D. Andreu, H. G. Boman, and R. B. Merrifield. 1990. All-D amino acid-containing channel-forming antibiotic peptides. *Proc. Natl. Acad. Sci. USA.* 87:4761–4765.

Wakamatsu, K., A. Takeda, T. Tachi, and K. Matsuzaki. 2002. Dimer structure of magainin 2 bound to phospholipid vesicles. *Biopolymers.* 64:314–327.

Wieprecht, T., O. Apostolov, M. Beyermann, and J. Seelig. 2000. Membrane binding and pore formation of the antibacterial peptide PGLa: thermodynamic and mechanistic aspects. *Biochemistry.* 39:442–452.

Zasloff, M. 2002. Antimicrobial peptides of multicellular organisms. *Nature.* 415:389–395.

Zidovetzki, R., U. Banerjee, D. W. Harrington, and S. I. Chan. 1988. NMR study of the interactions of polymyxin B, gramicidin S, and valinomycin with dimyristoyllecithin bilayers. *Biochemistry.* 27:5686–5692.

F. Statement about contributions

Chapters III and IV

All simulations were produced by the author, and most of the static and MAS spectra.

Relaxation times were measured equally by the author and Dr. Stephan Grage.

Chapter V

All spectral simulations and orientational analysis were performed by the author.

Sample preparation and NMR measurements were done in close collaboration with Dr. Sergii Afonin.

Dipolar analysis was done by Dr. Giuseppina de Luca, University of Calabria, Rende, Italy.

Molecular dynamics simulations were carried out by Dipl.-Ing. Barbara Hoff, MVM, Universität Karlsruhe (TH).

Chapters VI, VII and VIII

The author developed the entire software approach used in data analysis.

Most of the orientational analysis was done or supervised by the author. The studies on the influence of model imperfection on PGLa analysis were done in close collaboration with Dr. Ralf Glaser.

Peptide synthesis, sample preparation, and NMR measurements were carried out by Dr. Sergii Afonin (B18), by Dr. Parvesh Wadhwani, Dr. Sergii Afonin, and Dr. Jesús Salgado (gS), and by Dr. Parvesh Wadhwani, Dr. Ralf Glaser, Dr. Sergii Afonin, Dipl.-Biochem. Carsten Sachse, and Dipl.-Chem. Pierre Tremouilhac (PGLa).

G. Curriculum vitae

Ulrich Heiner Nikolaus Dürr

Date of birth	June 26, 1972
Place of birth	Hamburg-Eppendorf, Germany
Nationality	German
Marital status	single, no children

Professional experience

Oct. 2002-April 2004	Research assistant, Institute of Organic Chemistry, Biochemistry Dept., Universität Karlsruhe (TH)
May 1999-Sept. 2002	Research assistant, Institute of Molecular Biology, Friedrich-Schiller-Universität Jena
Dec. 1998-Mar. 1999	Research assistant, Institute of Applied Physics, Georg-August-Universität Göttingen
July 1992-Sept. 1993	Mandatory government service time Emergency medical service, Hamburg-Ottensen

Education

since May 1999	Ph.D. student in the group of Prof. Anne S. Ulrich, initially at University of Jena, currently at University of Karlruhe
Oct. 1998	'Diplom'-degree in pysics, grade 'sehr gut'
Feb. 1997-Aug. 1998	Diploma thesis on 'Quasi-elastic light scattering measurements of ethanol-dodecane-mixtures close to the critical de-mixing point'
start Oct.1993	Student of physics, University of Göttingen specialized on applied physics and theoretical physics
June 1992	Graduation from secondary school grade point average 1.5
Aug. 1988-June 1989	Exchange student at Adair-Casey High School, Adair, IA, USA
start Aug. 1982	Secondary school, Hamburg
1978-1982	Elementary school, Hamburg

H. Acknowledgements

To the following people I am deeply indebted and wish to express my sincere thanks:

Prof. Dr. Anne S. Ulrich for supervising this work and her continuous interest in its progress

Dr. Parvesh Wadhwani and Dr. Sergii Afonin for the long and fruitful time of great amicable cooperation both at Jena and Karlsruhe

Dr. Ralf Glaser, Dr. Jesús Salgado, Dr. Stephan Grage, and Dr. Marina Berditchevskaja for the friendly and helpful surroundings of the Jena lab

Dr. Bert Heise, Dr. Matthias Görlach, and Dr. Jörg Leppert for all their support with the frequent technical problems on the spectrometer at Jena

Fritz Haubensak for his help in everyday life and in keeping up the computer network of the Institut für Molekularbiologie

All the people at the Institut für Molekularbiologie, Jena, for the interesting and cooperative environment of that place

Dr. habil. Ulrich Sternberg and Dr. Raiker Witter whose deep understanding of physics and enthusiasm for science were a constant inspiration and greatly helped in completing this work.

All the people at the labs of the University of Karlsruhe and at the Forschungszentrum Karlsruhe for the very friendly and supportive atmosphere at those labs

Dorit Grasnick, Florian Dürr, and Parvesh Wadhwani for proofreading and help in preparing the printout of the manuscript

Vincent v. Borcke for counseling on the staircase of Bahnhof Zoo

My family for continuous support

Appendices

The fluorine nucleus, when introduced as a reporter group in membrane-associated proteins or peptides, offers a highly sensitive alternative to conventional isotope labels in solid-state NMR spectroscopy. The study presented here is concerned with the development of ^{19}F-NMR methods, as well as data analysis schemes to extract the wealth of structural and motional information from the spectra. Valuable methodological ^{19}F-NMR experience was gathered on simple model systems. The most complicated model system treated were small hexafluorinated substances in lipid bilayers. A complete description of their orientational and dynamic behaviour was attained (shown as a cartoon on the front cover). Subsequently, this experience was transferred and applied to more complex membrane-active peptide systems of high biological and pharmaceutical interest. Structural interpretations were achieved for the action of the fusion peptide B18, as well as for two antimicrobial peptides, gramicidin S and PGLa.

ISBN 3-86644-046-4

www.uvka.de